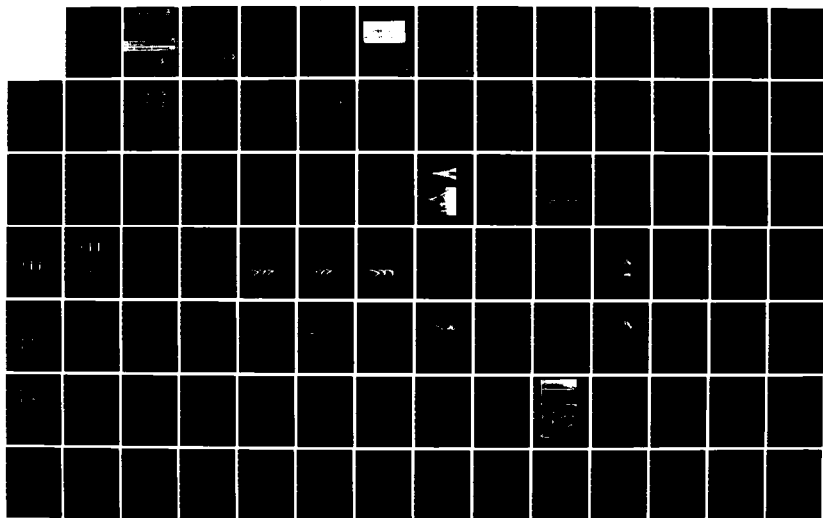INTERNAL GRAVITY WAVES AND SMALL-SCALE TURBULENCE:
PROCEEDINGS OF 'AHA HU..(U) HAWAII INST OF GEOPHYSICS
HONOLULU P MULLER ET AL. 1984 N00014-84-G-0008
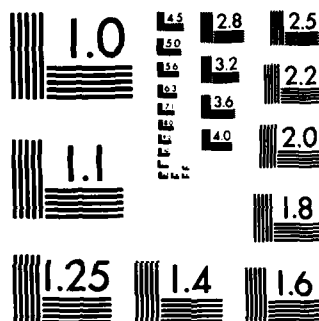
UNCLASSIFIED

F/G 8/3

NL

MICROCOPY RESOLUTION TEST CHART

NATIONAL BUREAU OF STANDARDS-1963-A

'Aha Huliko'a

③

INTERNAL GRAVITY WAVES

AND SMALL-SCALE TURBULENCE

Internal Gravity Waves
And Small-Scale Turbulence

PETER MULLER
RITA PUJALET
editors

PROCEEDINGS
'Aha Huliko'a
Hawaiian Winter Workshop
University of Hawaii at Manoa
January 17-20, 1984

DTIC
ELECTE
DEC 1 1 1984
S
D

D

Acc_____ __r
NT__
D__
Una____
Justi__.

By_____
Distribu:
Availab_____
Avail _____r
Dist   Special

A

ii

FOREWORD

The second annual 'Aha Huliko'a Hawaiian Winter Workshop was convened from January 18 to 20, 1984 to study "Internal Gravity Waves and Small-Scale Turbulence." ('Aha Huliko'a is a Hawaiian phrase meaning an assembly that seeks into the depth of a matter and describes it fully.)

Recognizing the importance of these motions for the distribution of properties in the ocean, the nineteen oceanographers and one meteorologist who gathered in Honolulu reviewed recent developments and discussed plans for future research. Their lectures are published in these proceedings, as submitted in camera-ready form by the authors. The order of presentation loosely follows the agenda of the workshop, progressing from observations to theory. Also included is a summary of the meeting, which appeared in Transactions of the American Geophysical Union.

The workshop, made possible by a grant from the United States Office of Naval Research, was hosted by the Hawaii Institute of Geophysics and the Department of Oceanography of the University of Hawaii. The excellent facilities of the East-West Center and the capable staff directed by James McMahon contributed greatly to the success of the meeting. The local organization and logistical arrangements were ably executed by Vicki Gaynor, without whose help the workshop would not have been possible. Graphic design for the workshop and this volume was by April Kam. Last, but not least, this volume came into existence through the creative thought and dedicated research of the scientists who gathered in Hawaii and provided the articles that follow.

Peter Muller   Department of Oceanography
Rita Pujalet   Hawaii Institute of Geophysics
Editors   University of Hawaii
                                Honolulu, Hawaii 96822

iii

PARTICIPANTS, 'AHA HULIKO'A 1984

Top row, left to right: Charles Eriksen, Frank Henyey, Steven Thorpe, Kenneth Watson, Charles Mader, Peter Muller, Greg Holloway, Thomas Osborn, Eric D'Asaro, Lorenz Magaard, Robert Haney, Christopher Garrett, Dirk Olbers.

Middle row, left to right: Murray Levine, Yves Desaubies, John Dugan

Bottom row, left to right: Dennis Moore, Ann Gargett, Melbourne Briscoe, Michael Gregg, Brent Gallagher, Robert Pinkel, Henry Abarbanel, Tom Spence.

Not present for photograph: Douglas Lilly

CONTENTS :

PREVIOUS PAGE
IS BLANK

PERSISTENT TURBULENT MIXING AND NEAR-INERTIAL INTERNAL WAVES

Michael C. Gregg

Applied Physics Laboratory and School of Oceanography
University of Washington, Seattle, WA 98105

ABSTRACT

Repeated profiles from a drifting ship revealed sustained mixing at the same depth as a near-inertial internal wave. Most of the turbulence occurred in well-stratified sections and produced overturns thinner than 0.2 m, consistent with the local Ozmidov scale. The remaining turbulence was in well-mixed layers, which were as thick as 1 m. Applying criteria determined from laboratory experiments by Stillinger et al. (1983) shows that the turbulence was marginally active in stratified sections and strongly active in well-mixed layers. If the mixing efficiency is assumed to be 25%, 3 hours were required to form the well-mixed layers, a period much longer than the lifetime of random breaking events. Because of the low dissipation rates being found in the upper thermocline, it appears that only near-inertial motions can produce mixing events lasting long enough to cause significant increases in potential energy. It follows that the global distribution of mixing in the upper thermocline is affected by the climatology of near-inertial waves.

1. INTRODUCTION

The vertical fluxes of heat, salt and momentum produced by turbulent mixing are among the least understood components of the large-scale circulation of the ocean, owing to the highly intermittent nature of mixing and the absence of techniques for measuring fluxes directly. The solution to the intermittence problem is collecting more data, an approach that is difficult and tedious, but straightforward. Using a model is the indirect, and more complicated, solution to the lack of measured fluxes. The procedure is to measure the average gradients, $\partial \vec{U}/\partial z$ and $\partial \overline{T}/\partial z$, and the principal components of the rate of entropy generation, ε and χ. The fluxes needed to produce ε and χ are then inferred from the models by assuming that turbulent production and dissipation are in balance. This raises a host of secondary issues, however, mainly concerning the realism of the models. Until these issues are resolved and more extensive sampling is completed, the role of turbulent fluxes in the general circulation will remain uncertain.

Instabilities of internal waves are localized overturns of the ambient stratification, which produce turbulence as they collapse. Away from fronts and salt fingering fields, these instabilities are the only mechanism known to produce vertical turbulent fluxes, although very little evidence exists about how this actually occurs. Information is particularly needed about the following aspects: the rate of energy loss by viscous dissipation; the scales, in space and time, of the energy loss; and the mechanisms of energy loss. Fortunately, direct observations can resolve these issues.

In October 1982, as part of the Drifter cruise, an extensive set of ε, χ, and shear profiles was collected in the California Current. By working alongside a buoy attached to a large canvas drogue, the sampling was done in a tagged body of water. Analysis of one sequence of profiles gives a partial definition of the space and time scales of a sustained mixing event due to internal waves. Comparison with recent laboratory experiments provides a means of determining the relative importance of inertial and buoyancy forces in the turbulence.

2. INSTRUMENTS AND PROCEDURES

The Advanced Microstructure Profiler (AMP) transmits data to the ship via a fiber optic link enclosed in a 2-mm-diameter Kevlar cable (Gregg et al., 1982). Because the cable is very flexible, the AMP falls freely, unaffected by ship motion. The instrument can operate in the upper 300 m, typically falling at 0.45 m/s.

Sequences of drops, termed bursts, were taken as the ship drifted broadside to the sea, i.e., while in the trough--a procedure that prompted the ship's chief engineer to pronounce the AMP group a "fistful of weirdos." Radar ranging on the buoy during burst 6 gave an average spacing of 300 m and an average time of 21 minutes between the 10 drops to 200 m (Fig. 1). The drogue was centered at 100 m.

A Neil Brown conductivity cell, a Thermometrics Fasttip thermistor, and a Setra pressure gauge provided data for computing temperature, salinity, and density. The microstructure was sensed by two airfoil lift probes (Osborn, 1974), a cold film, and a Fasttip thermistor with a high-gain circuit (Gregg et al., 1978). Two accelerometers, one oriented vertically and the other horizontally, monitored vehicle motion.

Values of ε and χ were obtained by computing spectra of velocity and temperature gradients over successive intervals of 0.005 MPa (0.5 m), assuming full spectral isotropy, and integrating to obtain the variances. The integrations were cut off at 20 Hz (44 cpm) for velocity and 30 Hz (67 cpm) for temperature. Using a fixed integration cutoff causes the highest dissipation rates to be slight underestimates and the smallest values to be large overestimates. At a fall rate of 0.5 m/s only 13% of the variance in a universal dissipation spectrum for $\varepsilon = 10^{-7}$ W kg^{-1} occurs at a frequency greater than 20 Hz, but for $\varepsilon < 10^{-10}$ W kg^{-1} the spectra drop to instrument noise levels at frequencies much less than 20 Hz. Because error estimation is difficult owing to variability in low-frequency noise levels, 10^{-10} W kg^{-1} was used as the threshold for significant signals. Dissipation rates were computed for both sets of shear data and compared, as a check for plankton impacts; in cases of large differences, the lower value was retained.
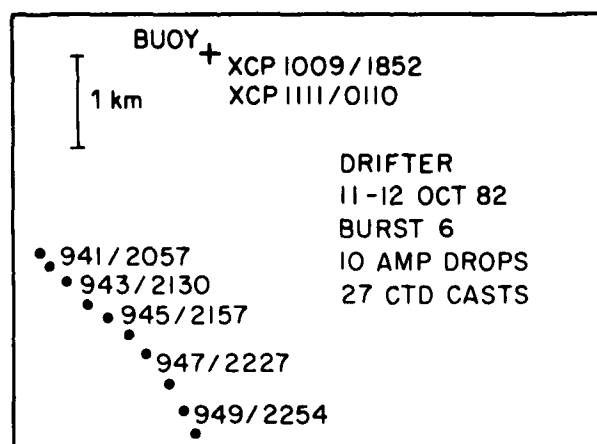
Fig. 1. Locations of AMP profiles in burst 6.
The positions and start times of alternate
AMP profiles are labeled. XCP drops were
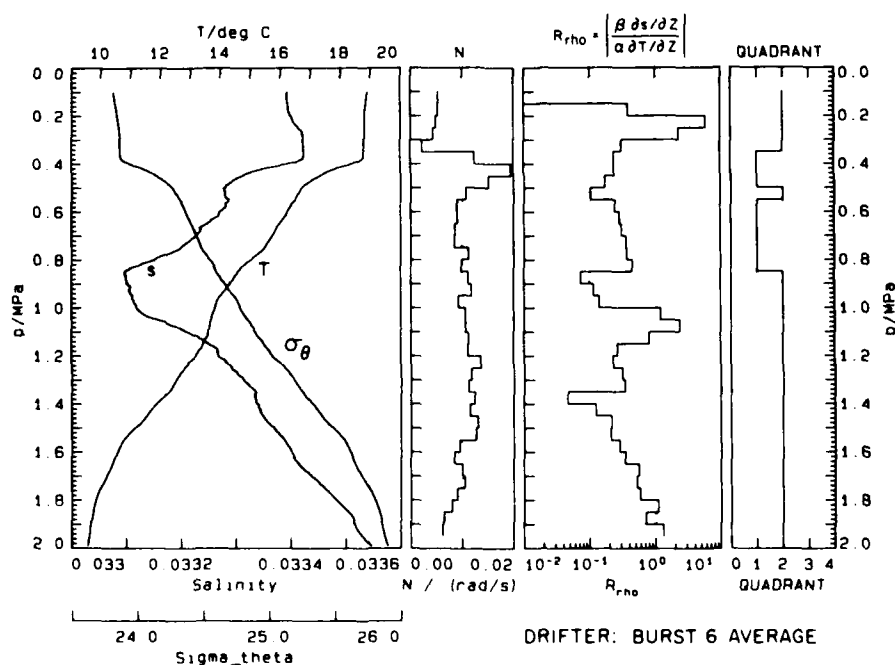taken at the buoy at the times shown.

Fig. 2. Average profile for burst 6. A pressure of 1 MPa corresponds to
a depth of 100 m. The panel on the right gives the quadrant of the
gradient TS diagram; the profile is diffusively stable in quadrant 2.

The noise pattern in χ is similar to that in ε; 10^{-10} K^2 s^{-1} was used as the threshold.

3. BACKGROUND OBSERVATIONS

Typical of the California Current off San Diego (31°N, 121°W), the most conspicuous features in the average profile are a shallow mixed layer and the salinity minimum near 0.8 MPa (Fig. 2). Because R_ρ, the ratio of the stratification due to salinity to that due to temperature, varies from 0.05 to 7, the average temperature gradient alone is not sufficient to determine $\overline{N}$, even over sections as thin as 10 to 20 m. Thermohaline intrusions are common in individual records, particularly between 0.5 and 1.2 MPa, but they had short horizontal scales and do not appear in the average profile. $\overline{N}$ is uniform at 0.01 rad/s; from the base of the mixed layer to 1.8 MPa the variability is less than 20%. Near the bottom of the profile the stratification decreases to values more typical of the main thermocline. The profile is diffusively stable when the gradient-TS relation is in the second quadrant, which occurred in the surface layer and below 1.0 MPa (see fourth panel). Because the profile is diffusively stable and nearly free of intrusions only at pressures greater than 1.4 MPa, this analysis was restricted to that section.

To monitor the internal wave field, Expendable Current Profilers (XCP's) were dropped alongside the buoy every 1/4 inertial period. XCP 1009, taken 2 hours before burst 6, shows several zones with high shear in the upper 2.0 MPa, particularly between 1.4 and 2.0 MPa (Fig. 3). Following the procedure of Leaman and Sanford (1975), all XCP profiles within a day of burst 6 were rotated to a common origin in time, on the assumption that the dominant frequency is 5% above the inertial frequency. The jet-like feature then appears as a steady velocity maximum, between 160 and 170 MPa in Fig. 4, which is a trait of near-inertial waves.

4. AVERAGE MIXING RATES

Averaging the 10 drops between 1.4 and 2.0 MPa yields $\overline{\varepsilon} = 6.8 \times 10^{-10}$ W kg^{-1}, a value that is very low compared with previous dissipation rates measured in strongly stratified profiles. The earlier data are in rough agreement with a universal function, $\overline{\varepsilon} \sim (\overline{N})^\beta$, proposed by Gargett and Holloway (in press), and plotted in Fig. 5 with $\beta = 1$ and 2. The Drifter value is far below this trend; either the other data in Fig. 5 were contaminated by noise or $\overline{\varepsilon}(\overline{N})$ is not a universal function.

Energy was being extracted from the internal wave field at a very slow rate. In a standard thermocline (N = 0.0052 rad/s), the specific energy of the field is 0.003 J/kg (Munk, 1981). For Drifter (N = 0.0095), the specific energy is 0.0055 J/kg, yielding a time for complete decay of

$$\tau = \frac{E}{\varepsilon} = \frac{5.5 \times 10^{-3}}{6.8 \times 10^{-10}} = 94 \text{ days.}$$

By comparison, Lueck et al. (1983) expressed the average dissipation rate between 200 and 1000 m off Vancouver Island as $\overline{\varepsilon} = 1.5 \times 10^{-7} \overline{N}$, yielding $\tau = 50$ days.
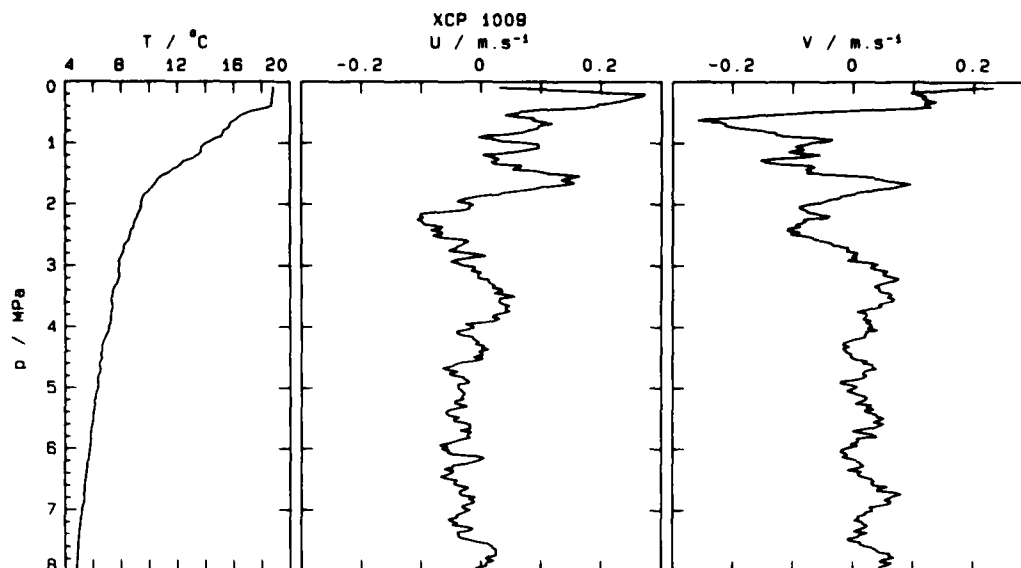
Fig. 3. XCP 1009, taken 2 hours before the beginning of AMP burst 6 at the buoy, which was 3 km away. The jet-like feature with a velocity maximum at 1.6 MPa has a dominant frequency slightly greater than the local inertial frequency.
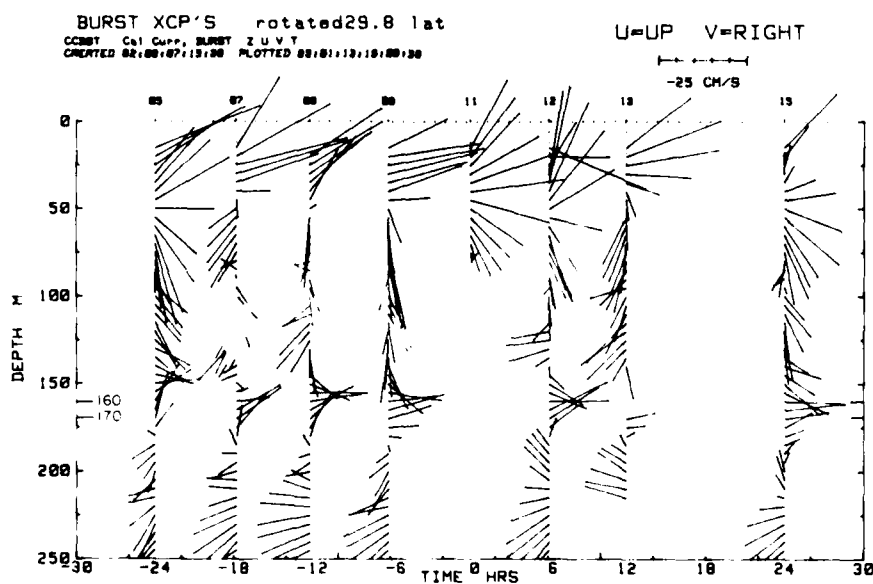
Fig. 4. XCP data plotted as vectors and rotated to a common origin in time, assuming a dominant frequency 5% above the local inertial frequency. The velocity maximum near 1.6 MPa persists throughout this sequence. (This figure kindly supplied by E. D'Asaro.)
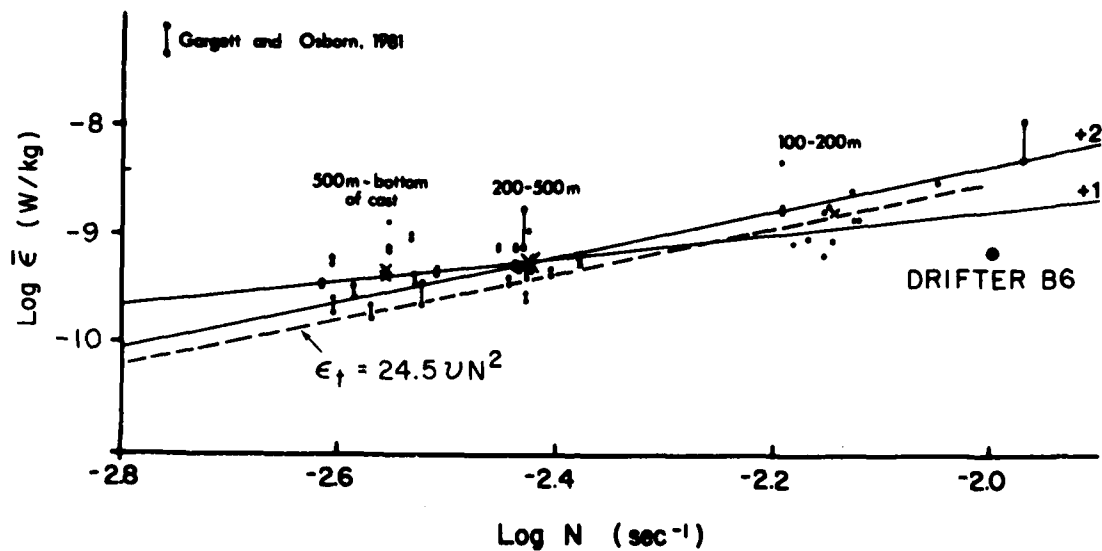
Fig. 5. Values of $\overline{\varepsilon}(\overline{N})$ from Lueck et al. (1983) with Drifter data added. Dashed line is the Stillinger et al. (1983) criterion for active turbulence.
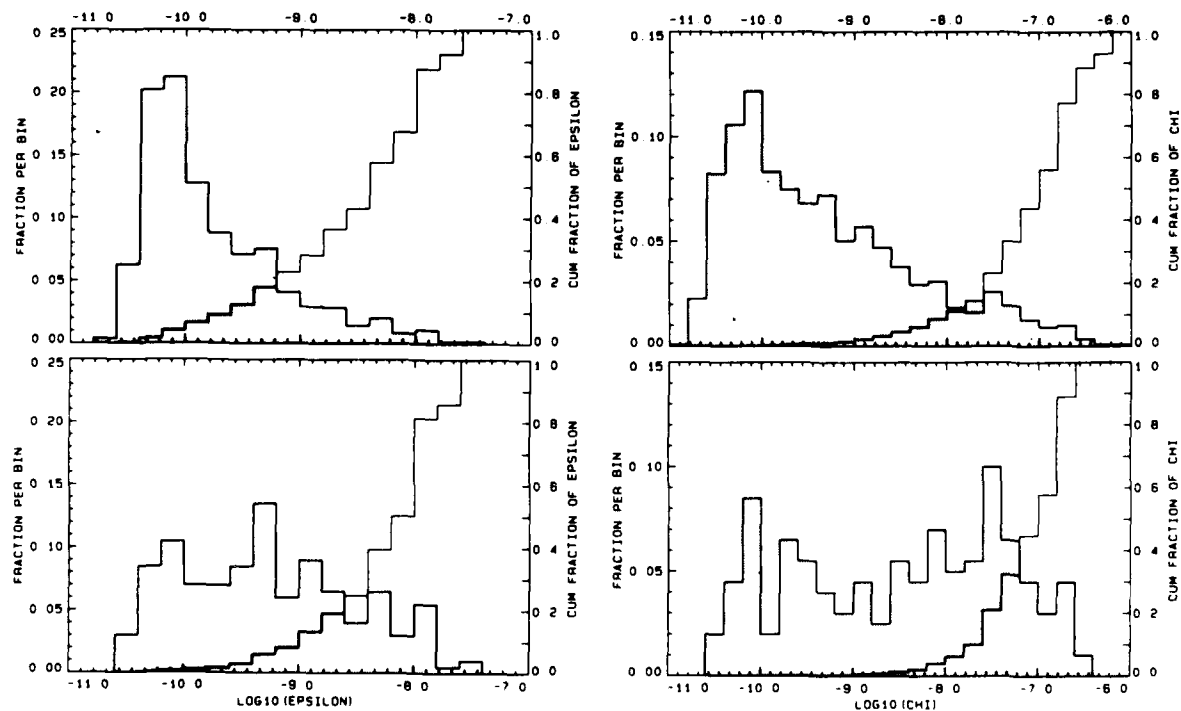
Fig. 6. Histograms (shaded) of 0.5 m values of ε and χ from 1.4 to 2.0 MPa (upper panel) and 1.6 to 1.7 MPa (lower panel). Lines show cumulative contributions to net ε or χ.

Averaging the temperature microstructure gives $\overline{\chi} = 9.4\times10^{-9}$ K^2 s^{-1}. The corresponding Cox number is 21, which is equivalent to $C = 7$ in previous results calculated without assuming isotropy.

Histograms of ε and χ are highly skewed to low values, even when plotted on logarithmic axes (upper panels of Fig. 6), because of instrumental noise, sections with no mixing, and internal waves. The last effect can be estimated using the Gargett et al. (1981) expression for the shear spectrum at high wavenumbers,

$$\varphi_s = (1-3)\times10^{-5}\,k^{-1} \quad [\mathrm{s}^{-2}/\mathrm{cpm}] \qquad 0.1 < k < k_c \,. \qquad (1)$$

where k_c is an undetermined upper cutoff. If the spectrum extends to $k > 2$ cpm, internal waves will be measured by the lift probes. For example, if $k_c = 10$ cpm,

$$\varepsilon = \frac{15}{2}\nu\int_{0.5}^{10}\varphi_s\,dk = (1.7-5.2)\times10^{-11}\ \mathrm{W\,kg^{-1}} \,.$$

which spans the minimum levels in Fig. 6.

Averages for the individual drops differed from the burst mean by less than $\pm50\%$ in ε and $\pm100\%$ in χ as shown in Table 1. In view of the 4-5 decades of variability in the 0.5 m values, differences between profile averages are small. Taking 10 drops in 2 hours was not necessary; 2 or 3 drops would have given a representative average.

Table 1. ε and χ averaged between 1.4 and 2.0 MPa.

Drop	$10^{10}\varepsilon$	$10^{9}\chi$
941	7.39	7.50
942	8.95	9.40
943	5.37	5.47
944	7.03	8.24
945	7.15	10.2
946	7.52	7.98
947	11.2	6.12
948	6.13	11.4
949	4.83	5.56
950	7.34	17.2
b6	6.78	9.42

5. A SUSTAINED MIXING EVENT

Examining average profiles for the burst reveals whether ε and χ are randomly distributed from drop to drop or are concentrated into mixing zones. As seen in Fig. 7, arithmetic and logarithmic averages of both variables have large changes in amplitude, indicating that mixing is not uniformly distributed in depth. Dynamic

8

Fig. 7. Values of $\overline{\varepsilon}(p)$ and $\overline{\chi}(p)$ for 10 drops in burst 6. Mixing events were found across the base of the mixed layer and in several other sections. The one between 1.6 and 1.7 MPa was in a diffusively stable section, free of intrusions.

ranges of the arithmetic means are 100:1 in ε and 1000:1 in χ. Logarithmic averaging produces a smaller dynamic range because of the greater weight given to the concentration of low-magnitude values. Changes in the averages occur over intervals of 0.1 to 0.2 M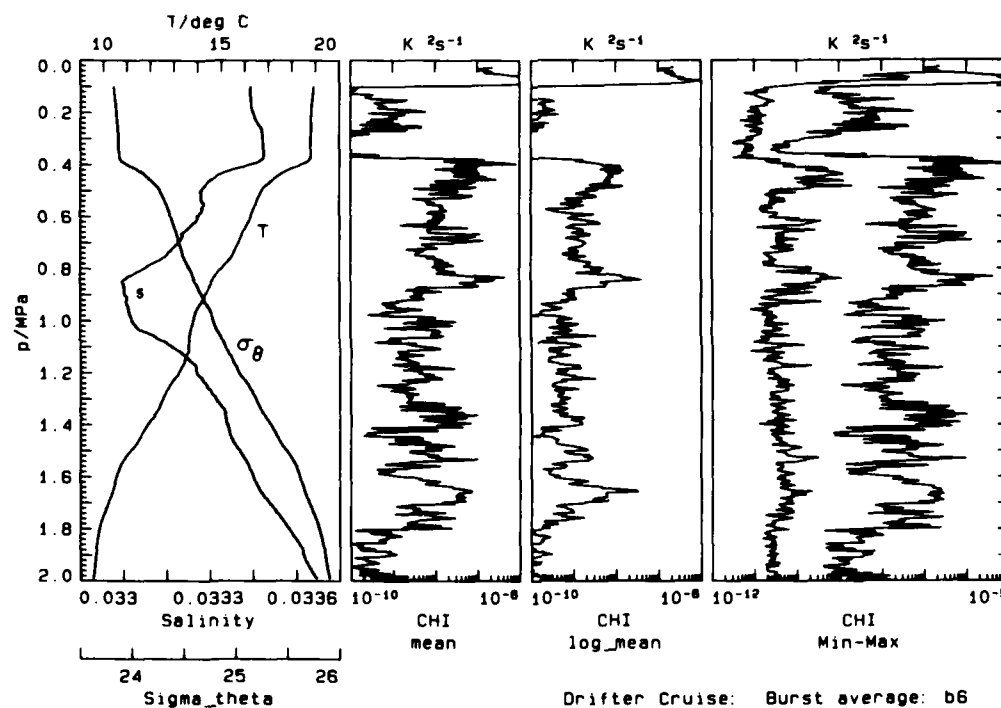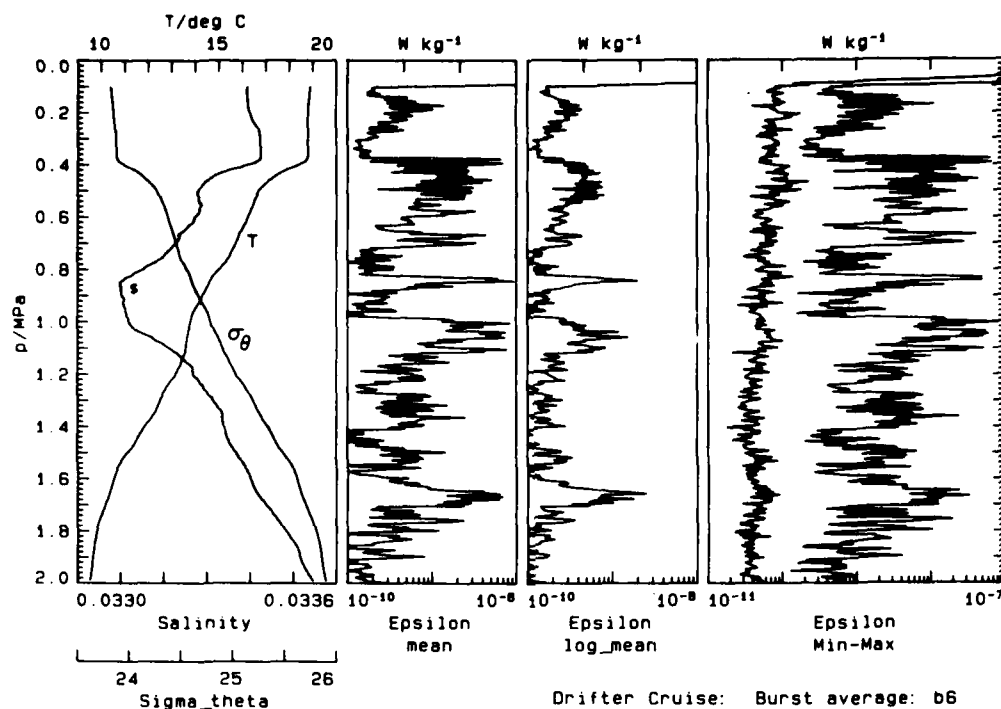Pa, showing mixing patches separated by quiet sections. The smooth profiles of minimum values (right panels in Fig. 7) demonstrate, however, that at every depth at least one profile had no detectable signal, thus illustrating intermittence, even in the active patches.

Some large amplitudes in the average profiles are due to extreme values in only one or two records--for example, the narrow peaks at 0.84 MPa, which are about only 0.1 of the maximum values at that depth. By contrast, the broader peaks between 1.6 and 1.7 MPa are 0.2 to 0.3 of the maximum levels and are due to moderately large values in most of the drops. Histograms for this section also show a general increase in the frequency of large-amplitude signals, not just a few outliers (lower panels of Fig. 6). Eight of the ten records have strong increases in ε and χ between 1.6 and 1.7 MPa (Fig. 8). The regions of strongest activity have an average thickness of 4.4 m, $\overline{\varepsilon} = 5.0 \times 10^{-9}$ W kg^{-1}, and $\overline{\chi} = 6.0 \times 10^{-8}$ K^2 s^{-1}. These are 7.4 and 6.4 times the averages across the 60 m section, respectively. Weaker mixing occurred above and below the strongest levels, making the full thickness about 8 m. Thus, a sustained mixing event took place between 1.6 and 1.7 MPa. It was the major event between 1.4 and 2.0 MPa, and contributed half of the net $\overline{\varepsilon}$ and $\overline{\chi}$ in the 60 m section.

Finestructure in the mixing zone shows a steady evolution from drop to drop. Successive profiles have many features in common (e.g., Figs. 9 and 10), but the first and last drops have completely different finestructure (Figs. 9 and 11). These changes appear to result from internal wave strain rather than from the mixing, consistent with the arguments of Desaubies and Gregg (1981), thus providing a continuously changing environment for the steady mixing.

Overlaying AMP and XCP data shows that the mixing event was close to the velocity maximum of the near-inertial jet (Fig. 12). This comparison is limited, however, by uncertainty in the XCP pressure and by the horizontal separation. XCP pressure, computed using elapsed time and the average fall rate, is estimated to be accurate to ± 0.1 MPa (T. Sanford, personal communication). Nevertheless, the close match of the two temperature records indicates that the error is only a fraction of this. Temperature changes of the mixing zone in individual AMP profiles correspond to displacements of only ± 3 m, which is a good estimate of the maximum offset of the XCP temperature from the average AMP temperature. (Elsewhere, larger disagreements are found, such as the base of the mixed layer, where large displacements due to high-frequency internal waves are expected, and 0.8-1.3 MPa, where thermohaline intrusions were common.) Across the 3 km separation between the XCP drop and the AMP track the slope of a wave having a dominant frequency 5% above the inertial frequency would produce a maximum offset less than 4 m.

If there is no error in the XCP pressure, the mixing event occurred at the velocity maximum between 1.6 and 1.7 MPa, where $Ri = 11$ is obtained from the XCP shear and the mean stratification. In this case, stronger shear must have occurred over scales smaller than the resolution of the XCP, possibly because of the focusing of energy there and a resonant interaction (Thorpe, 1973). If the XCP pressure is
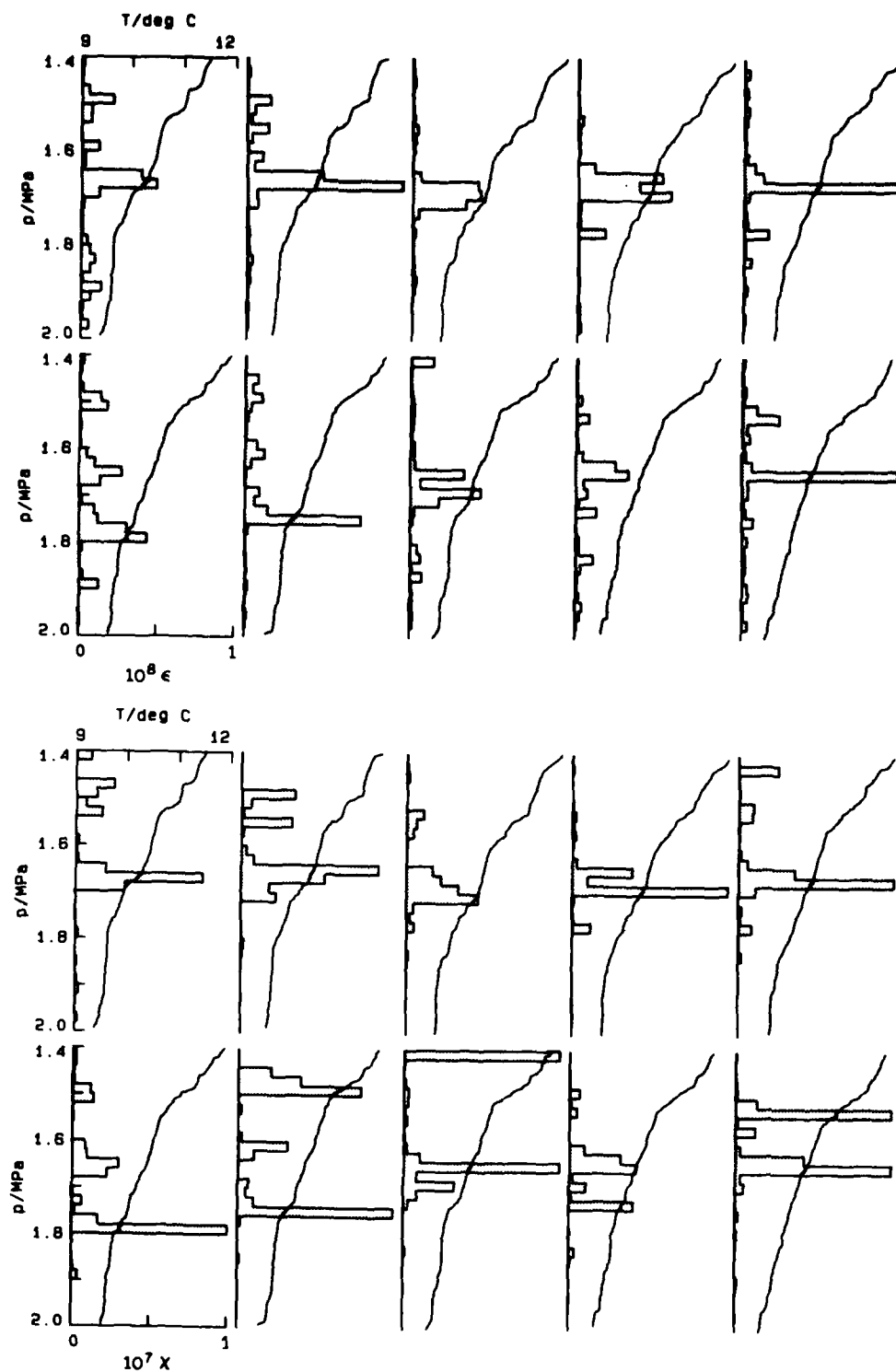
Fig. 8. High ε and χ levels occur between 1.6 and 1.7 MPa in 8 of the 10 drops. Some plots have been clipped at maximum amplitudes of 10^{-8} in ε and 10^{-9} in χ. The time sequence is drop 941, upper left of each panel, to drop 950, lower right.
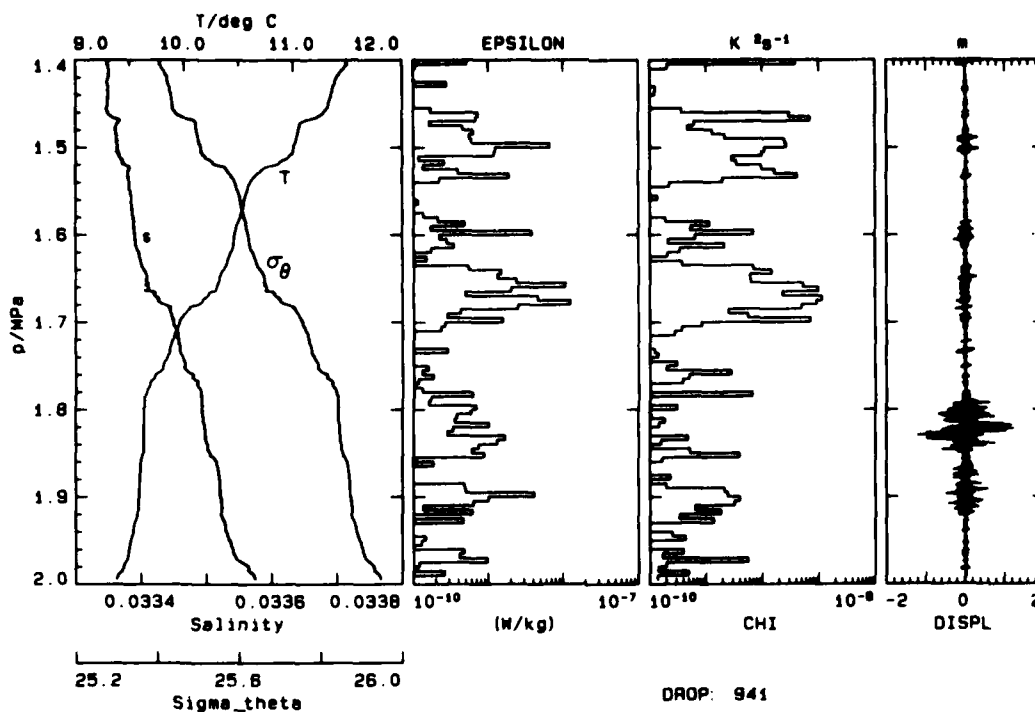
Fig. 9. Values of ε, χ, and L_T for drop 941.
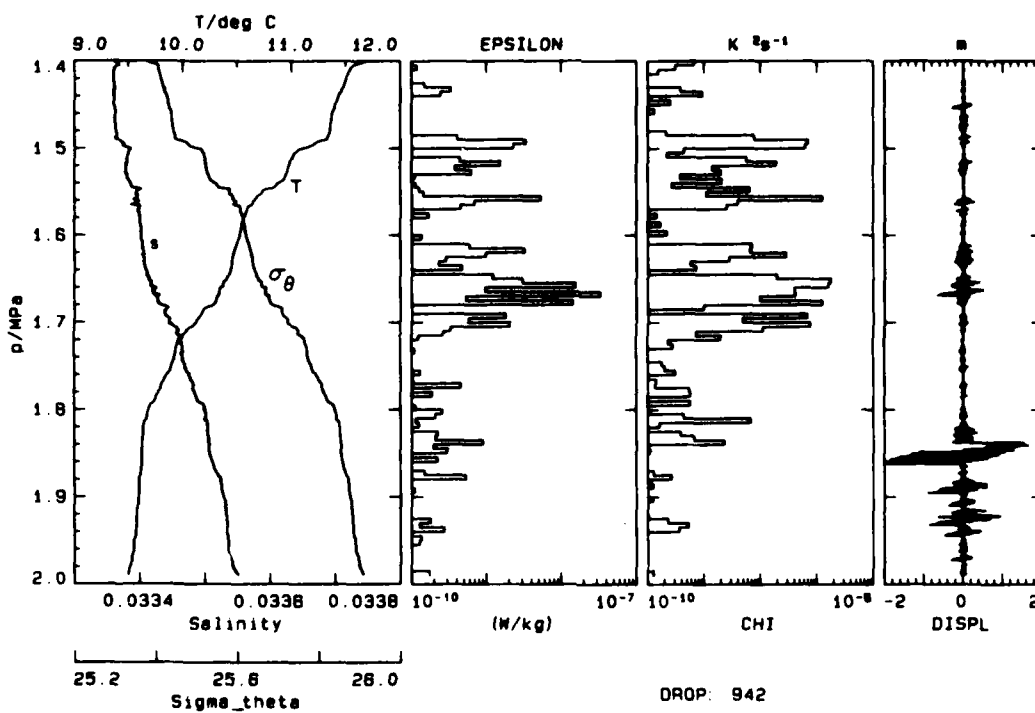
Fig. 10. Values of ε, χ, and L_T for drop 942. Note similarity of finestructure with that in Fig. 9.
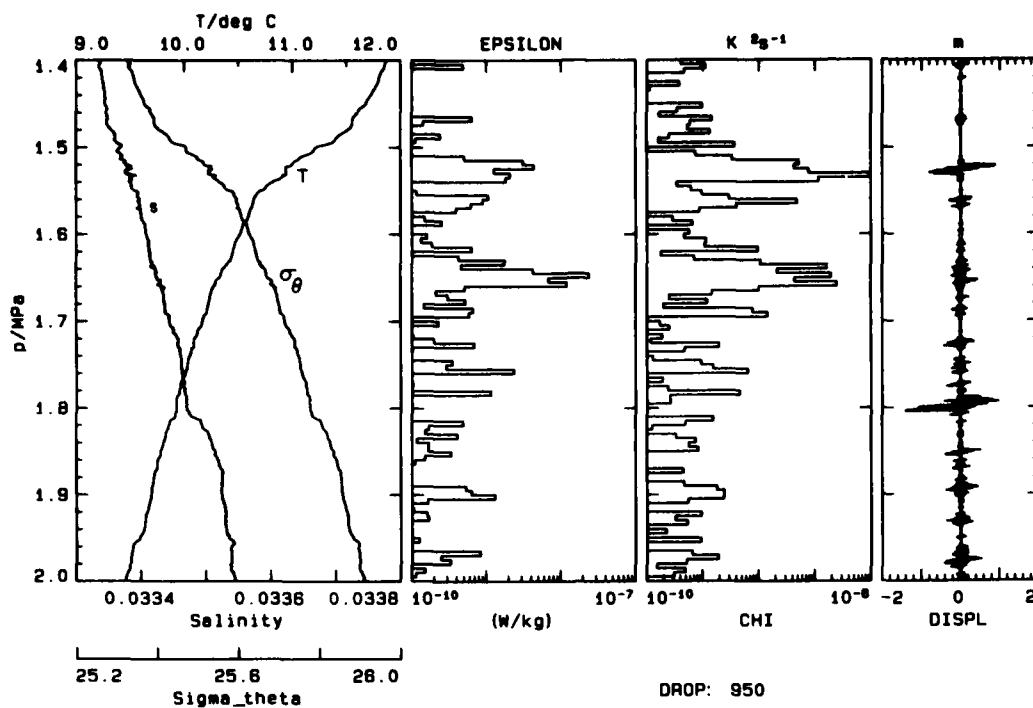
Fig. 11. Values of ε, χ, and L_T for drop 950. The finestructure is very different than in Figs. 9 & 10.
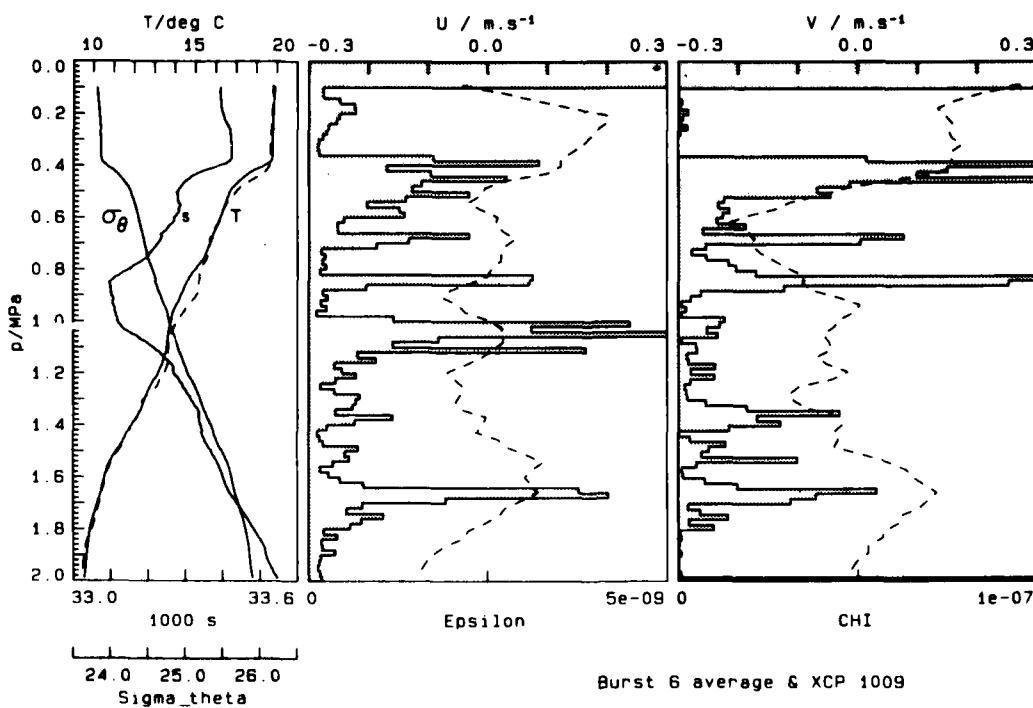
Fig. 12. Comparison of average profiles for burst 6 with XCP 1009. The XCP temperature is shown as a dashed curve in the left panel. The mixing event between 1.6 and 1.7 MPa occurs near the maximum velocity of the near-inertial feature.

wrong by 0.1 MPa, the mixing event was in a region of high large-scale shear. For example, $Ri \approx 1$ across 1.7 to 1.8 MPa. The latter case is consistent with the strong mixing found in a high-shear region of a near-inertial wave in a warm-core ring (Larson and Gregg, 1983).

Taking the peak velocity of the near-inertial feature, 0.2 m s^{-1}, and the maximum dissipation rate, 5.0×10^{-9} W kg^{-1}, gives

$$\tau = \frac{\frac{1}{2}|U|^2}{\varepsilon} = 69 \text{ days}.$$

Thus, although the dissipation rate is elevated in the near-inertial feature, the increase in kinetic energy results in a decay rate similar to that obtained with $\overline{\varepsilon}$ and the Garrett-Munk spectrum.

6. χ AS A FUNCTION OF ε

The correlation between ε and χ, evident in Figs. 7-11, is shown more clearly in the scatter plots of Fig. 13. The correlation coefficient, r, is much larger across the subset of the data containing the mixing event ($r = 0.85$) than across the full section ($r = 0.35$). The reasons for the difference have not yet been investigated, but the values averaged over 1.4-2.0 MPa are closer to instrument noise levels and the variability of $\partial T/\partial z$ is greater than across the 10 m section. In spite of the differences in scatter, both data sets give $\chi \approx 10\varepsilon$.

Oakey (1982) parameterized the correlation between ε and χ by a scaling factor, Γ, defined by

$$\Gamma = g\frac{\alpha}{2}\frac{\chi}{\varepsilon \partial \overline{T}/\partial z} , \qquad (2)$$

where his Eq. 8.5 has been evaluated in the form for full spectral isotropy. Γ corresponds to the mixing efficiency, defined as the ratio of the rate of increase of potential energy to the rate of dissipation of kinetic energy. Different lines of argument have proposed the following values: 0.33 (Lilly et al., 1974), 0.20 (Osborn, 1980), and 0.80 (Weinstock, 1981).

Lacking salinity, Oakey (1982) assumed that N was a linear function of $\partial \overline{T}/\partial z$ and obtained $\Gamma = 0.235 \pm 0.14$, using averages over 10 to 15 m from the upper 100 m in the JASIN area north of Scotland.

Using N obtained from temperature and salinity and applying Eq. 2 to the regression fits in Fig. 9 gives $\Gamma = 0.22$ and 0.21 for the 1.6 to 1.7 MPa and 1.4 to 2.0 MPa data, respectively. This corresponds to

$$C \approx 1.2 \times 10^7 \varepsilon (\partial \overline{T}/\partial z)^{-2}. \qquad (3)$$

In view of the different ways of obtaining N used in this study and in Oakey's work, the value of Γ should be viewed as tentative until observations are made with a wider variety of R_ρ. Nevertheless, these results are not significantly different from the proposals of either Lilly or Osborn, and agree with the mixing efficiencies measured in laboratory experiments by McEwan (1983), giving confirmation of a general dependence of χ on ε.

14
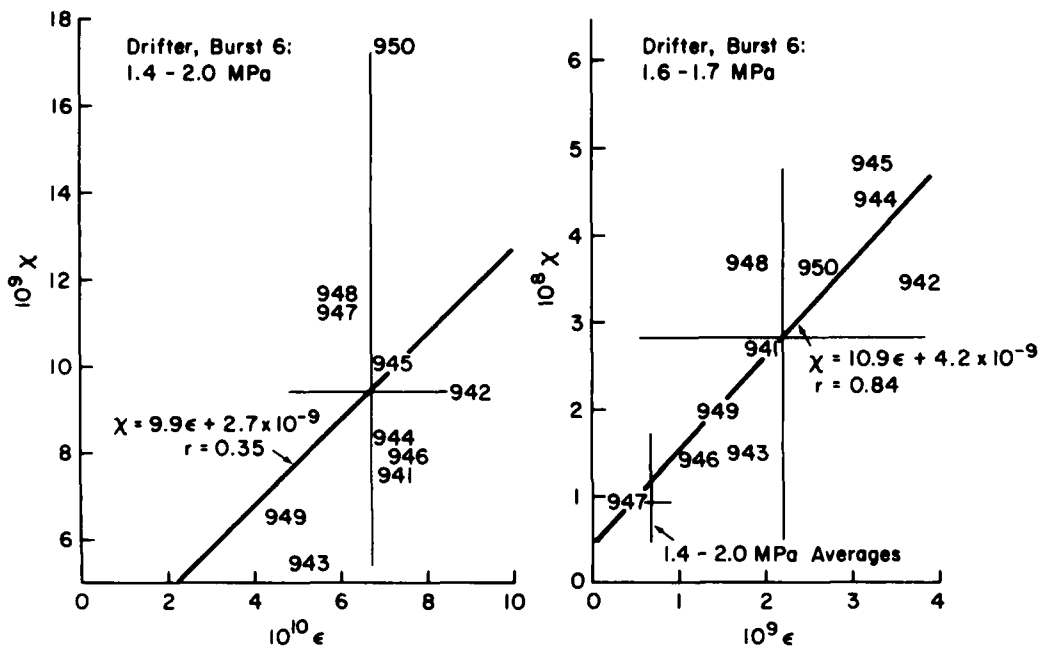
Fig. 13. Values of $\bar{\chi}$ versus $\bar{\varepsilon}$ over 1.4 to 2.0 MPa (left) and 1.6 to 1.7 MPa (right). The correlation coefficients are given by r. The crosses mark the average values, maxima, and minima for ε and χ; e.g., the horizontal lines have ordinate values equal to $\bar{\chi}$ for the ensemble and the abscissae of the end points give maximum and minimum sample values.

7. CHARACTERISTICS OF THE TURBULENCE

The relative magnitudes of inertial and buoyancy forces determine the character of turbulence in a stratified fluid. If the inertial force is stronger, the turbulence will be similar to that in homogeneous fluids; but if the buoyancy force is dominant the turbulence will be decaying and producing little or no density flux, $\overline{\rho' w'}$. Recent laboratory observations (Dickey and Mellor, 1980; Stillinger et al., 1983) provide a quantitative means for characterizing turbulence in the AMP data.

Stillinger et al. (1983) defined transition points in the evolution of a stratified turbulent wake in terms of ε and L_T, the maximum observed overturning length. The dissipation rate was used to calculate two parameters obtained by dimensional analysis: the Ozmidov scale, $L_R \equiv (\varepsilon/N^3)^{1/2}$, the length at which buoyancy and inertial forces are equal, and the Kolmogoroff scale, $L_K \equiv (\nu^3/\varepsilon)^{1/4}$, the length at which viscous and inertial forces are equal.

Active turbulence, characterized by an upward density flux, exists as long as the largest scales are unaffected by stratification and by viscosity, i.e., when

$$1.4 \, L_R \gg L_T \gg 15.4 \, L_K \ , \tag{4}$$

where the lower bound is the approximate length scale of the peak in the dissipation spectrum.

Decay begins when buoyancy affects the largest overturns, i.e., when

$$1.4 \, L_R \approx L_T \ , \tag{5}$$

and proceeds rapidly, completely suppressing the turbulence in only a fraction of a stability period, $\approx 0.15 N^{-1}$. At this point the motions are a field of random internal waves, with $\overline{w'\rho'} = 0$.

The criterion for no turbulence is that the wavenumber bandwidth goes to zero, i.e.,

$$1.4 \, L_R = 15.4 \, L_K \ , \tag{6}$$

which is equivalent to

$$\varepsilon < 24.5 \, \nu \, N^2 \equiv \varepsilon_t \ . \tag{7}$$

The change in potential energy was found to depend on the duration of overturning motion. For weaker stratifications mixing was more complete and little restratification, $\overline{\rho' w'} < 0$, was observed. In the most stable case the suppression of turbulence occurs such a short period of time after its generation that the mixing of a scalar is incomplete and restratification occurs. Because the persistence time of the turbulence, and thus the time allowed for mixing, is a function of the initial separation distance of the turbulent and buoyancy length scales, a restratification criterion can be based on the ratio L_T/L_R at the time the turbulence is initially generated. Comparison of the different runs gave an upper bound of

$$\frac{L_T}{L_R} \leq 0.3 \tag{8}$$

for complete mixing.

Although oceanic turbulence occurs within large-scale shear flows and may not evolve in the same manner as turbulence in an unsheared flow through a grid, these laboratory results provide the only criteria for evaluating activity levels. Applying the laboratory criteria is productive in focusing both oceanic and laboratory work, provided that the results are viewed as tentative until more realistic laboratory measurements are completed.

Comparisons using AMP data can be made of L_T versus $1.4 L_R$ and ε_t versus $\bar{\varepsilon}$. L_T was obtained by computing the displacements required to sort temperature into a monotonic profile, a technique first used by Thorpe (1977) on data from Loch Ness. For the displacements to be indicators of overturning scales, the temperature change due to diffusion during an overturn must be negligible, i.e., temperature is treated as a passive tracer. Also, oceanic data must be free of salt-stabilized temperature inversions; otherwise artificially large displacements will be calculated.

Only sections having dissipation rates above the measurement threshold should be used for comparing $\bar{\varepsilon}$ with ε_t. Including regions containing ε below the threshold biases $\bar{\varepsilon}$ to artificially low values. For example, between 1.4 and 2.0 MPa $\varepsilon_t = 3.0 \times 10^{-9}$ W kg^{-1}, which is about four times $\bar{\varepsilon}$. Half of the dissipation rates, however, are below the threshold. The section from 1.6 to 1.7 MPa, which has a much smaller fraction below the threshold and the same ε_t, almost satisfies the criterion with $\bar{\varepsilon} = 2.2 \times 10^{-9}$ W kg^{-1}. Because even this section contains levels below the threshold, the comparison was also done in the 4 m thick regions containing the maximum mixing rates (Table 2).

Table 2. Characteristics of turbulence in the high ε regions between 1.6 and 1.7 MPa. Pr_lb and Pr_ub are the lower and upper bounds of the pressure interval.

Drop	Pr_lb	Pr_ub	$10^2 N$	$10^9 \varepsilon$	$10^4 L_R$	$10^9 \varepsilon_t$
941	1.64	1.68	1.28	4.4	0.06	5.4
942	1.64	1.68	1.03	8.5	0.12	3.4
943	1.66	1.72	0.95	4.0	0.10	2.9
944	1.64	1.70	0.95	4.7	0.11	2.9
945	1.64	1.68	0.91	7.4	0.14	2.7
946	1.62	1.66	0.81	1.9	0.08	2.2
947	1.58	1.62	0.82	1.0	0.06	2.2
948	1.64	1.70	0.87	2.9	0.09	2.5
949	1.62	1.66	0.98	3.0	0.08	3.2
950	1.64	1.66	1.05	11.7	0.14	3.6
	1.632	1.676	0.97	5.0	0.10	3.1

Ratios of $\overline{\varepsilon}/\varepsilon_t$ vary from 3.3 to 0.45, with an average of 1.6. Thus, the Stillinger et al. criterion is met, but the separation of overturning and buoyancy length scales is so small that the mixing is inefficient. Exceptions to this exist within several well-mixed sections, up to 1 m thick, in which $\varepsilon \gg \varepsilon_t$. The most striking example was in drop 942, which contained a sequence of well-mixed layers that appear to be mixing vigorously (Fig. 14). A similar sequence was also found in drop 943. Because of the greater wavenumber bandwidth of turbulence in these layers, the mixing was more efficient than in the well-stratified sections. Thus, the turbulence is marginally active when it occurs in well-stratified profiles; even in the zone containing the highest dissipation rates, it becomes strongly active only within the embedded well-mixed layers.

Thorpe scales, L_T, are less than 0.2 m in well-stratified sections, and hence are within a factor of 2 of L_R (Table 2). Signatures that could be interpreted as billows thicker than 10 to 20 cm are missing. Values of 0.5 to 2 m are found, but only within well-mixed layers, e.g., Fig. 14. Another example of large displacements occurs between 1.814 and 1.834 MPa in drop 941 (Fig. 15), which has $\overline{\varepsilon} = 8.3\times10^{-10}$, $\overline{N} = 0.0024$, and $\varepsilon_t = 1.4\times10^{-10}$. Thus the largest Thorpe displacements not associated with intrusions occur in well-mixed sections, which had been mixing for an extended time, not in initial overturns.

Well-mixed layers, in isolation or in sequences, appear to be common only where sustained mixing has taken place. McEwan (1983) found them in a laboratory experiment with continuously forced breaking of internal waves, and Gregg and Sanford (1980) reported layers in a region of strong mixing adjacent to Bermuda, but not offshore. The time required to form a homogeneous layer, of thickness h, from a uniform initial stratification is

$$\tau = \frac{\Delta P.E.}{\text{mixing efficiency}} = \frac{(1/12)N^2h^2}{\gamma\overline{\varepsilon}} , \qquad (9)$$

where γ is the mixing efficiency. Using $\gamma=0.25$ and $h = 1$ m gives $\tau = 3$ hours, equivalent to $Nt = 108$.

In the upper ocean away from ocean boundaries, fronts, and strong quasigeostrophic flows, such as the Gulf Stream, near-inertial features are the only motions with strong shear that last long enough to form mixed layers as thick as 1 m or greater. A time history through one of these regions would show persistent mixing in which the Thorpe displacements gradually increase with time as the mixed layers form, a sequence in sharp contrast to overturning scales that reach a maximum in the initial billows and then decay rapidly.

8. GIBSON'S ALTERNATE INTERPRETATION

Gibson (1982) interpreted all observations of temperature microstructure in Gregg (1980) as buoyancy dominated remnants of patches that once contained active, inertially dominated turbulence. He then argued that the average Cox numbers were gross underestimates because the small number of profiles had sampled only the long-lived decay products and not the short-lived active structures in which most of the mixing occurred.
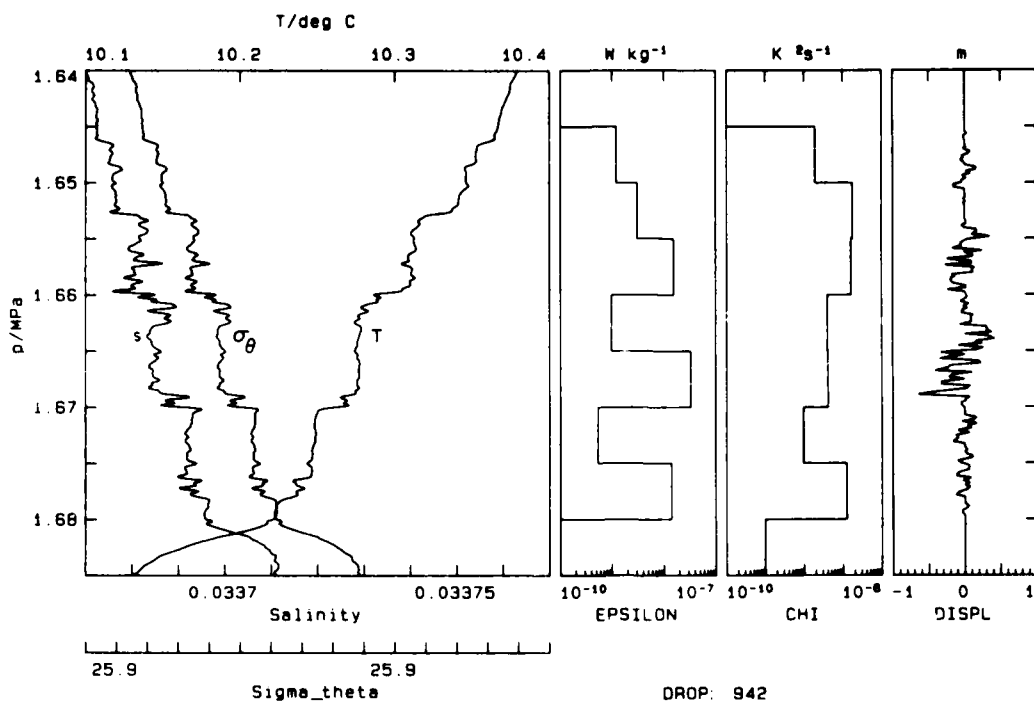
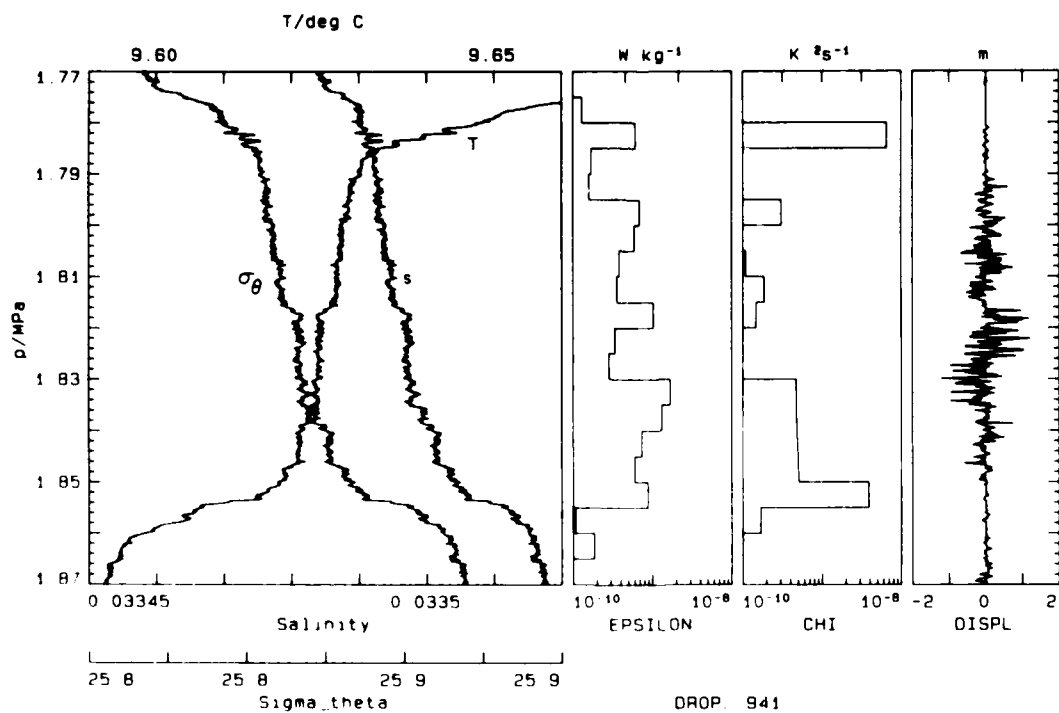Fig. 14. Sequence of well-mixed active layers in drop 942.

Fig. 15. Section of drop 941 containing the largest L_T values, which are seen to occur in a well-mixed layer.

Classification of the temperature microstructure as fossil was based on a criterion that inertially dominated turbulence can exist only when $\eta > 5.5\,N$, where η is the rate of strain. The average stratification of the 100-m-thick section was used to give $5.5\,N = 0.0275$ as the threshold for active turbulence, and η was obtained using a formula based on the separation distance of zero-crossings of temperature gradients: "The smallest zero-gradient separation distance reported by Gregg (1980) was 1.5 cm, corresponding to a rate of strain of 3.9×10^{-3} rad s^{-1}." Thus, η obtained from the data is only 1/7 of that needed for active turbulence, leading to categorization of the microstructure as fossil.

As an estimate of the initial dissipation rates, ε_0, in overturning events, Gibson assumed that L_T was preserved in the resultant mixed structures, yielding $\varepsilon_0 = 2.8\,L_T^2\,\overline{N}^3$. Applying this with $L_T = 7.5$ m and $N = 0.005$ yielded $\varepsilon_0 = 2 \times 10^{-5}$ W kg^{-1} for the dissipation rate of the initial overturn.

The crux of Gibson's interpretation is based on a misstatement; no smallest zero-crossing separation was reported by Gregg (1980) nor were any zero-crossing separations computed. Several uses were made of zero crossings, but accurate minimum separations could not have been computed because the data had been smoothed with a 1 cm cosine taper, as described in the paper. Gibson (personal communication) since stated that he is not certain how he obtained the 1.5 cm value, but believes it was by applying zero-crossing statistics to an average spectrum in Gregg (1977).

A second problem is the evaluation of $5.5\,N$. As discussed in the previous section, local values of N must be used, not bulk averages. As an example, $L_T = 1$ m is one of the largest values from Drifter in a region free of intrusions (Fig. 15). Using $\overline{N} = 0.0095$ gives $\varepsilon_0 = 2.4 \times 10^{-5}$ W kg^{-1}, which is 800 times greater than the largest 0.5 m ε value measured between 1.4 and 2.8 MPa during burst 6.

In conclusion, in addition to an unknown method of evaluating γ, Gibson's evaluation of his criterion of zero-crossing distances and his use of L_T were faulty because they were based on $\overline{N}$ over a large distance, instead of local values. Also, observation of a sustained event during the Drifter cruise is contrary to the view that these structures are decayed remnants of events that once had dissipation rates decades greater than the observed levels.

9. SUMMARY

Two hours of continuous profiling in a 60-m-thick, diffusively stable thermocline found low mixing rates: $\overline{\varepsilon} = 6.78 \times 10^{-10}$ W kg^{-1}, corresponding to a 94-day decay time for the internal wave field, and $\overline{\chi} = 9.42 \times 10^{-9}$ K^2 s^{-1}, corresponding to a Cox number of 21. As a function of $\overline{N}$, $\overline{\varepsilon}$ is well below previous data, contrary to predictions of a universal function, $\overline{\varepsilon}(\overline{N})$.

Average mixing rates in individual drops are within a factor of 2 of the burst averages, showing that only 2 or 3 drops were needed for an accurate average.

Similar patterns of mixing were found in ε and χ. The correlation was the same as observed by Oakey (1982) and agrees with predictions by Lilly et al (1974) and by Osborn (1980) that the mixing efficiency is about 25%.

Detectable mixing occurred in about half of each record, usually in 0.5-to 3-m thick patches that cannot be identified in successive profiles. These features are consistent with random internal wave breaking, as predicted by the Garrett and Munk statistical approach.

A sustained 4-m-thick mixing event produced half of the net $\bar{\varepsilon}$ and $\bar{\chi}$ in the 60-m-thick section. It persisted along the 3-km track and was at the same depth as a near-inertial internal wave, although it is uncertain whether the mixing occurred at the velocity maximum or in a high-shear zone.

Most mixing in the event consisted of overturns less than 0.2 m, consistent with the local Ozmidov scale, in an otherwise well-stratified profile. A criterion developed by Stillinger et al. (1983) shows the turbulence to be marginally active, i.e., to have a narrow wavenumber bandwidth and therefore to be inefficient at converting kinetic to potential energy. Embedded within the zone, however, are well-mixed layers, sometimes in stair-step sequences, containing strongly active turbulence and over-turns bounded only by the layer thickness.

10. HYPOTHESES ABOUT MIXING

According to the Garrett and Munk parameterization, the energy density of the internal wave field depends only on N (Garrett and Munk, 1972; Garrett, 1979; Munk, 1981), leading to mixing models in which $\bar{\varepsilon}$ and $\bar{\chi}$ also depend only on N (Gargett and Holloway, in press). In this view, instabilities occur randomly where superposition of velocities from the full internal wave spectrum produces $Ri < 1/4$. Therefore, the frequency of occurrence, duration, and length scales of shear instabilities define the statistics of mixing events; applying the mixing efficiency then gives the rate of increase of potential energy. Because the input parameters are poorly known, normally-distributed shear, constant stratification, and complete mixing are assumed.

Although the models are too primitive to incorporate specific mechanisms, based on the dye visualizations of Woods (1968), mixing events are assumed to occur as isolated Kelvin-Helmholtz instabilities on pre-existing density steps. The Kelvin-Helmholtz mechanism is a specific class of instability occurring where thin, match-ing interfaces in density and velocity separate thick, homogeneous regions. At ins-tability, a perturbation on the interface rapidly evolves into a billows, which grows until the vertical scale is too large to overturn. The billows phase lasts 10-30% of the lifetime and does little mixing. Most of the mixing occurs after collapse (Koop and Browand, 1979). Although Woods' observations, and Thorpe's (1973) application of them to the ocean, gave billows amplitudes of only 0.2 m, others have assumed that the existence of much thicker microstructure patches implied correspondingly larger billows, e.g., Gibson (1982).

Signatures in both microstructure and finestructure contradict aspects of the model of mixing outlined in the preceding paragraphs. First, very little of the mixing appears to be produced by isolated Kelvin-Helmholtz instabilities on density steps. Most mixing is found in patches 10 to 100 (or more) times as thick as the largest overturns. The nearly total absence of overturns as thick as the patches and now the evidence for sustained mixing show that most patches are not formed by a large

billows, but must occur as a mixing zone of small-scale overturns. Even within the patches, potential sites for Kelvin-Helmholtz instability are rare; most finestructure consists of ill-defined changes in the stratification rather than sharp density interfaces (Desaubies and Gregg, 1981). Second, accumulating evidence shows that strong mixing events do not occur randomly, but are at the same depths as near-inertial waves. Third, histograms of temperature difference show only a small fraction of the thermocline to be well mixed; mixing rarely goes to completion (Desaubies and Gregg, 1981). The emerging evidence can be stated as a set of testable hypotheses:

(1) Most mixing does not occur as isolated Kelvin-Helmholtz instabilities, but is formed in mixing zones containing many localized instabilities. Until simultaneous high-resolution shear and density measurements are made, the instability mechanisms will not be clear, but one possibility is the Holmboe instability, which occurs at thin density steps in a broad shear field and does not produce a billows (Koop and Browand, 1979).

(2) Mixing frequently occurs due to random superposition, but the events are brief, have short horizontal dimensions, and contain only marginally active turbulence. Hence, they produce little increase in potential energy, although they dissipate kinetic energy.

(3) Mixing zones due to near-inertial internal waves last for hours, extend horizontally for at least several kilometers, and produce a large fraction of the increase in potential energy resulting from mixing. Although the turbulence is initially only marginally active, it be omes more efficient as well-mixed layers are formed by the sustained mixing.

(4) Changes in potential energy due to mixing follow the same pattern as the distribution of near-inertial shear and thus depend on more than a universal function of N, as proposed by Gargett and Holloway (in press). Average mixing levels in the thermocline are stronger in winter under the storm track of the North Pacific than in autumn under the trade winds.

Sampling mixing is a difficult and expensive undertaking that, to produce results applicable to the general circulation, must have a carefully designed strategy. Several steps are suggested by these hypotheses:

(1) Continue simultaneous microstructure and shear measurements to establish the link between mixing and near-inertial waves on a firm statistical basis. For this purpose a resolution of 10 m, obtainable with XCP's and Doppler Acoustic Current Meters, is sufficient.

22

(2)   Take microstructure and high-resolution shear measurements fol-
lowing a near-inertial wave for a week or more to define the
mechanisms responsible for the mixing.

(3)   Obtain laboratory criteria similar to those of Stillinger et al.
(1983) in stratified shear flows. Determine the role of well-mixed
layers in the energetics.

(4)   Combine the above results to parameterize the mixing, e.g., ε, in
terms of large-scale features of the near-inertial waves.

(5)   By a combination of theory, numerical models, and measure-
ments, define the global distribution of near-inertial waves, and
apply this distribution to predict the resultant levels of mixing.
Verify by selected observations.

Work by Sanford, D'Asaro, and Kunze is establishing the climatology of near-
inertial waves. D'Asaro (in press) presents a model of the generation of near-inertial
waves by the passage of cold fronts and uses the model to simulate observations
made in the North Pacific. Kunze and Sanford (submitted) demonstrate a strong
enhancement in near-inertial energy at the subtropical front in the North Pacific,
which Kunze (in preparation) explains in terms of focusing of near-inertial energy by
geostrophic shear. Other examples of enhanced near-inertial waves have been found
in both warm-core and cold-core rings (Kunze, personal communication). Thus, the
understanding of near-inertial motions is progressing rapidly and, once the first
three steps are completed, will provide a framework to use in evaluating their global
importance as mixing agents.

ACKNOWLEDGMENTS

REFERENCES

D'Asaro, E.A., 1984:   Wind forced internal waves in the North Pacific and Sargasso
Sea. J. Phys. Oceanogr. (in press).

Desaubies, Y.J.F., and M.C. Gregg, 1981: Reversible and irreversible finestructure.
J. Phys. Oceanogr., Vol. 11, pp. 541-556.

Dickey, T.D., and G. L. Mellor, 1980: Decaying turbulence in neutral and stratified
fluids. J. Fluid Mech., Vol. 99, pp. 13-31 .

Gargett, A.E., P.J. Hendricks, T.B. Sanford, T.R. Osborn, and A.J. Williams III, 1981: "A composite spectrum of vertical shear in the upper ocean," J. Phys. Oceanogr., Vol. 11, pp. 1258-1271.

Gargett, A.E., and G. Holloway, 1984: "Dissipation and diffusion by internal wave breaking," J. Marine Res. (in press).

Gargett, A.E., and T.R. Osborn, 1981: "Small-scale shear measurements during the Fine and Microstructure Experiment (FAME)," J. Geophys. Res., Vol. 86, pp. 1929-1944.

Garrett, C.J.R., 1979: "Mixing in the ocean interior," Dyn. Atmos. Oceans, Vol. 3, pp. 239-265.

Garrett, C.J.R., and W.H. Munk, 1972: "Space-time scales of internal waves," Geophys. Fluid Mech., Vol. 11, 225-264.

Gibson, C.H., 1982: "Alternative interpretations for microstructure patches in the thermocline," J. Phys. Oceanogr., Vol. 12, pp. 374-383.

Gregg, M. C., 1977: "Variations in the intensity of small-scale mixing in the main thermocline," J. Phys. Oceanogr., Vol. 7, pp. 436-454.

Gregg, M.C., 1980: "Microstructure patches in the thermocline," J. Phys. Oceanogr., Vol. 10, pp. 915-943.

Gregg, M.C., T.B. Meagher, A.M. Pederson, and E.A. Aagaard, 1978: "Low noise temperature microstructure measurements with thermistors, Deep-Sea Res., Vol. 25, pp. 843-856.

Gregg, M C., W.E. Nodland, E.E. Aagaard, and D.H. Hirt, 1982: "Use of a fiber-optic cable with a free-fall microstructure profiler," J. Phys. Oceanogr., Vol. 10, pp. 260-265. Marine Technology Soc. Oceans '82: Conference Record, Sept. 20-22, 1982.

Gregg, M.C., and T.B. Sanford, 1980: "Signatures of mixing from the Bermuda Slope, the Sargasso Sea and the Gulf Stream," J. Phys. Oceanogr., Vol. 10, pp. 105-127.

Koop, C.G., and F.K. Browand, 1979: "Instability and turbulence in a stratified fluid with shear," J. Fluid Mech., Vol. 93, pp. 135-159.

Kunze, E., "Near-inertial propagation in geostrophic shear," in preparation.

Kunze, E., and T.B. Sanford, 1984: "Observations of near-inertial waves in a front," J. Phys. Oceanogr. (submitted).

24

Larson, N.G., and M.C. Gregg, 1983: "Turbulent dissipation and shear in thermohaline intrusions," Nature, Vol. 306, pp. 26-32.

Leaman, K.D. and T.B. Sanford, 1975: "Vertical energy propagation of inertial waves: A vector spectral analysis of velocity profiles," J. Geophys. Res., Vol. 80, pp. 1975-1978.

Lilly, D.K., D.E. Waco, and S.I. Adelfang, 1974: "Stratospheric mixing estimated from high-altitude turbulence measurements," J. Appl. Meteor., Vol. 13, pp. 488-493.

Lueck, R.G., W.R. Crawford, and T.R. Osborn, 1983: "Turbulent dissipation over the continental slope off Vancouver Island," J. Phys. Oceanogr., Vol. 13, pp. 1809-1818.

McEwan, A.D., 1983: "The kinematics of stratified mixing through internal wavebreaking," J. Fluid Mech., Vol. 128, pp. 47-57.

Munk, W., 1981: "Internal waves and small scale processes.," Evolution of Physical Oceanography, Scientific Surveys in Honor of Henry Stommel, C. Wunsch, Ed., The MIT Press, 264-291.

Oakey, N.S., 1982: "Determination of the rate of dissipation of turbulent energy from simultaneous temperature and velocity shear microstructure measurements," J. Phys. Oceanogr., Vol. 12, pp. 256-271.

Osborn, T. R., 1974: "Vertical profiling of velocity microstructure," J. Phys. Oceanogr., Vol. 4, pp. 109-115.

Osborn, T.R., 1980: "Estimates of the local rate of vertical diffusion from dissipation measurements," J. Phys. Oceanogr., Vol. 10, pp. 83-89.

Stillinger, D.C., K.N. Helland, and C.W. Van Atta, 1983: "Experiments on the transition of homogeneous turbulence to internal waves in a stratified fluid," J. Fluid Mech., Vol. 131, pp. 91-122.

Thorpe, S.A., 1973: "Turbulence in stably stratified fluids: A review of laboratory experiments," Boundary-Layer Meteor., Vol. 5, pp. 95-120.

Thorpe, S.A., 1977: "Turbulence and mixing in a Scottish loch," Phil. Trans. Roy. Soc. London, Vol. 286, pp. 125-181.

Weinstock, J., 1981: "Energy dissipation rates of turbulence in the stable free atmosphere," J. Atmos. Sci., Vol. 38, pp. 880-883.

Woods, J.D., 1968: "Wave-induced shear instability in the summer thermocline," J. Fluid Mech., Vol. 32, pp. 791-800.

OCEANIC SHEAR SPECTRA FROM A SUBMARINE

Thomas R. Osborn

Rolf G. Lueck

U.S. Naval Postgraduate School
Monterey, California 93943

ABSTRACT

The research submarine Dolphin has been used to measure the horizontal variation of $\partial w/\partial x$ and $\partial v/\partial x$ over scales ranging from 5m to 0.01m. The data show that stratification suppresses the low wavenumber portion of the spectrum of the vertical velocity shear relative to the horizontal velocity component. The scale for the buoyancy effect is $l_b = 2\pi(\varepsilon/N^3)^{1/2}$. The temperature spectra peak at a lower wavenumber than the shear spectra. A possible explanation for this difference of the temperature spectra from the Batchelor (1959) prediction is that the temperature gradient variance is dominated by anisotropic features associated with the fine structure, the edges of the patch, and the large scale structures that generate the patch.

INTRODUCTION

The stratification of the ocean limits the vertical extent of mixing by turbulence of a given intensity. Vertical profiles of turbulent velocity fluctuations in the ocean have revealed patches of turbulence up to 45m thick (Osborn, 1978) but these regions were not overturning from top to bottom. Temperature restratification calculations (Thorpe 1977, Dillon 1982) show the overturning scales to be limited to a meter or less in the stratified parts of lakes and oceans.

Direct measurements of the three-dimensional turbulent fluctuations became possible with the instrumentation of the Pisces submersible by Gargett (1982), who used that vehicle to measure the downstream variation of the three perpendicular velocity components. The effects of stratification on the turbulent flow was examined by Gargett et al. (1984) as a function of a ratio called I and defined as,

$$I = l_b/l_s \qquad (1)$$

where the buoyancy scale, l_b, is defined as,

$$l_b = 2\pi(\epsilon/N^3)^{1/2} \qquad \qquad (2)$$

and the Kolmogorov scale, l_s, is defined as,

$$l_s = 2\pi(\nu^3/\epsilon)^{1/4}. \qquad \qquad (3)$$

The data analyzed by Gargett et al. were collected in a breaking internal wave train adjacent to the sill in a British Columbia fjord. The turbulent intensity varied over a wide range so that the approach to isotropy could be studied as the scale ratio, I, decreased from 3000 to 50. The effect of stratification was found to be a suppression of the low wavenumber portion cross-stream velocity components below the level consistent with the downstream velocity component and the isotropic relationship. The geometry of the flow indicated that the turbulent production occurred in the downstream component.

In this paper we report on the preliminary analysis of some measurements in the ocean adjacent to San Diego California. The submarine Dolphin was outfitted with velocity sensors to resolve the two lateral components of the velocity. We examine the relationship between the vertical and horizontal lateral velocity as a function of downstream wavenumber to look for the effects of stratification on the turbulence. In this region the stratification was substantial ($N \approx 8$cph) and the turbulence intensity not large enough to push the ratio I above 30, substantially smaller than the values studied by Gargett et al.

INSTRUMENTATION

The instrumentation and operation of the Dolphin submarine for turbulence measurements is described in detail by Osborn and Lueck(1984a,b). We will briefly outline the instrumentation so the reader can understand the nature of the data to be presented. The axis system is right-handed with the x axis aligned with the centerline of the submarine and positive towards the bow, the y axis athwartships, and the z axis vertical and positive in the upward direction. The velocity components are (u,v,w) corresponding to the (x,y,z) directions.

The submarine is fitted with a tripod above the bow on which the sensors are mounted (figure 1). At the top of the tripod are two airfoil probes to measure the vertical, w, and the lateral, v, velocity components. These signal are differentiated immediately by the electronics so that the recorded data are $\partial w/\partial t$ and $\partial v/\partial t$. The spatial derivatives are calculated by using the mean speed and Taylor's hypothesis. A thermistor is mounted next to the airfoil probes. This signal is used for temperature and differentiated to give $\partial\theta/\partial t$ which can also be converted to a spatial derivative with Taylor's hypothesis. These sensors on the upper package measure the small-scale temperature and velocity fluctuations down to dissipation scales. Three perpendicular accelerometers are mounted at the back end of the turbulence package. These sensors monitor the vibration of the frame as well as the lower frequency motion of the boat. All the data from the turbulence package
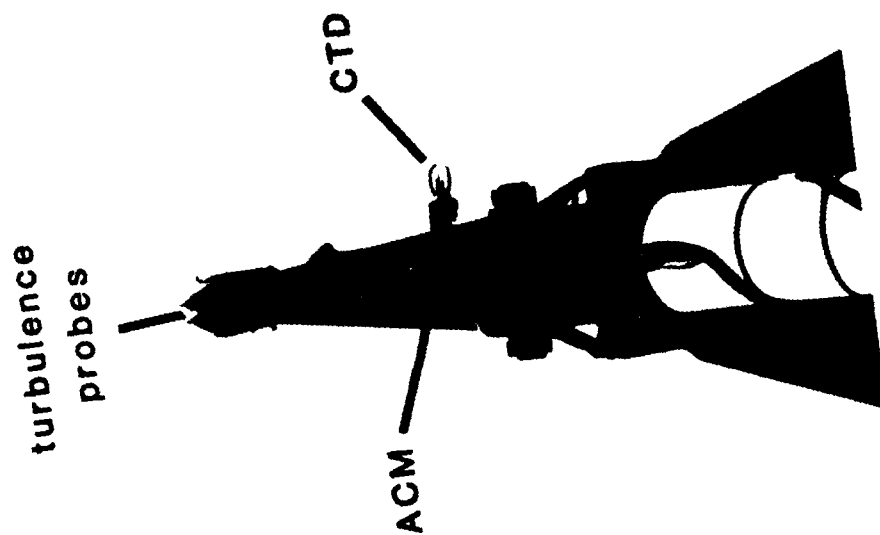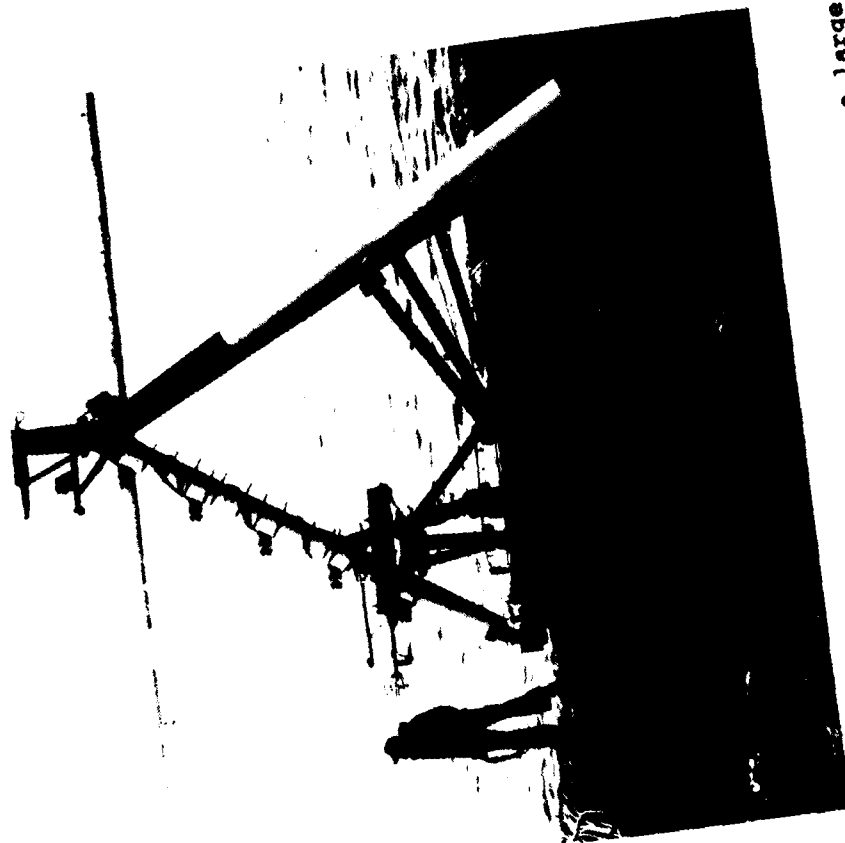
Fig. 1. The USS Dolphin has a large frame mounted on the bow to support the turbulence probes and the sensors for the mean field measurements. The acoustic current meter (ACM) is mounted 0.56m below the axis of the turbulence package.

An acoustic current meter (hereafter called ACM) and a CTD are located
0.56m below the turbulence probes. The equipment, produced by Neil
Brown Instrument Systems, was used to measure the large scale parameters
of the water column and the submarine's speed. The sampling interval for
all of this data is 0.038 sec. The acoustic current meter has a path
length of 0.1m for each component. The vertical velocity, w, and the
lateral horizontal velocity, v, are each sampled individually. The third
acoustic path is inclined at 45° to the vertical axis, the horizontal
axis, and the direction of travel. From this third acoustic path the
forward speed of the submarine can be calculated by removing the
contributions from the other two components. The design of the head is
constrained by the need to keep each acoustic path from being in the wake
of any of the transducers. Hence, the downstream speed of the submarine
cannot be measured with a single pair of transducers. One benefit of the
design is that the two cross-stream velocities are each measured by a
single acoustic path. The calibration values we use for the acoustic
current meter are the nominal values from the factory. Some tow tank work
with the system suggests they are accurate to 5% (Tochko, personal
communication).

The CTD system consists of the 0.03m conductivity cell, a platinum
thermometer and a fast thermistor. The three sensors are recorded
separately. We use the fast thermistor (first correcting for the
electronics with a third order polynomial) for the salinity calculations
as well as the spectra calculations of the CTD temperature.

MEASUREMENTS AND DISCUSSION

The submarine follows a predetermined pattern for each dive that is
determined by the objectives of the dive. The pattern is often modified
as we watch the data on chart recorders. The track for April 22, 1982 is
shown in figure 2. This dive was designed to study the turbulence and
salt-finger signatures associated with the salinity minimum about 40m
depth in the water adjacent to San Diego, California. The dive commenced
at 1357 local time and consisted of two circuits around a rectangle while
the depth was varied on an irregular basis to profile up and down through
the various features of interest.

The salinity and temperature data for five portions of the dive are shown
in figure 3 for the 30-to 50-decibar pressure interval. The intervals are
marked on the ship track in figure 2. The situation is very complicated
with the salinity minimum changing signature and depth quite frequently.
Looking at the T-S diagrams, we see a progression of the minimum towards
lower salinity and warmer temperature. This progression continues
through the rest of the temperature and salinity data, with the
salinity finally dropping below 33.36°/oo. The change in the nature of
salinity minimum in both time and space is probably due to advection.
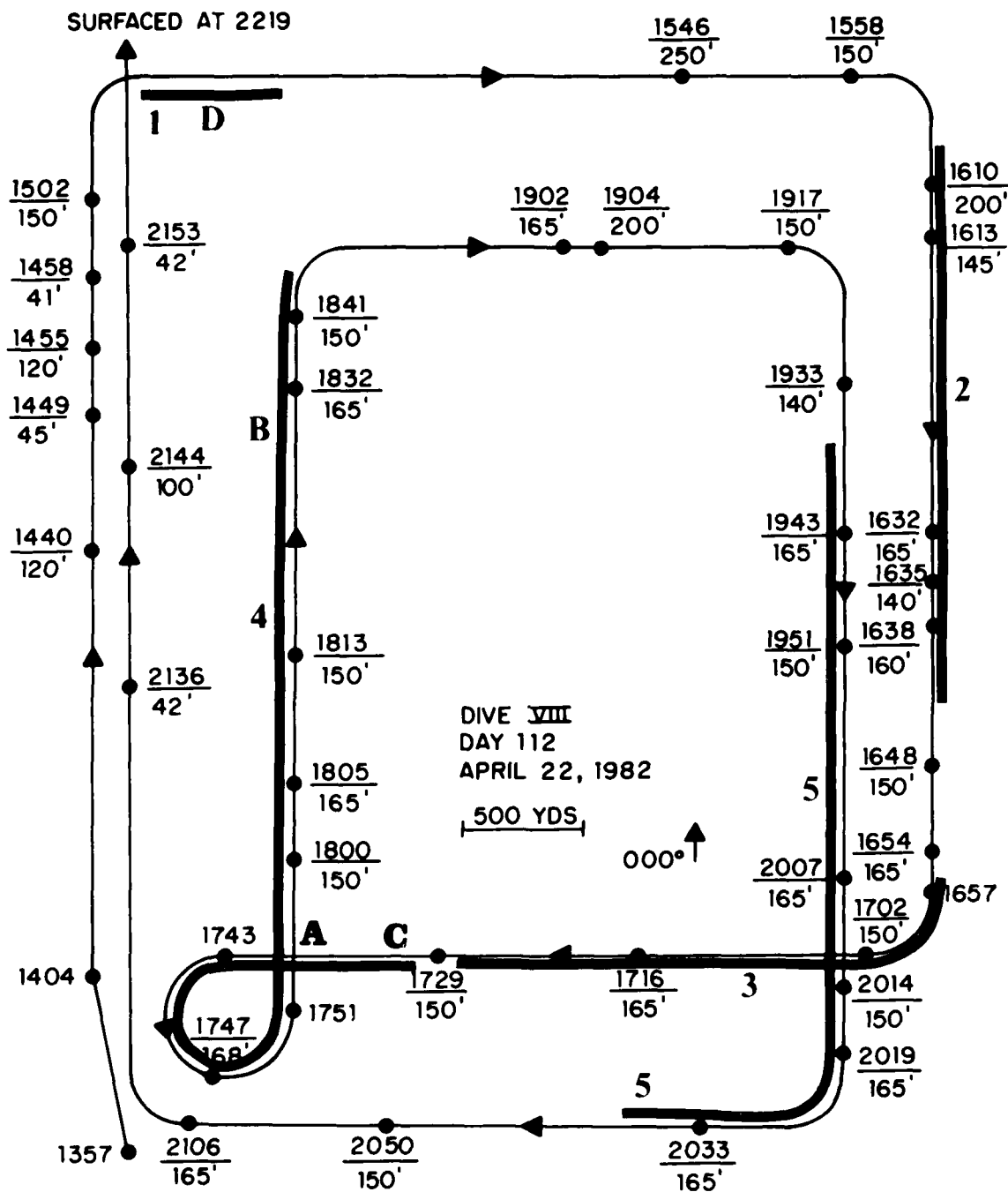
Fig. 2. The ship track is reconstructed from the logbook of the Dolphin for heading and the acoustic current meter for speed. The times are correct as indicated but the depths are requested value (orders to the coxswain) rather than the actual values at that moment. The time intervals corresponding to the temperature and salinity data of figure 3 are delineated with the heavy lines numbered 1 through 5. Locations of the turbulence patches are indicated by the letters A through D.

30
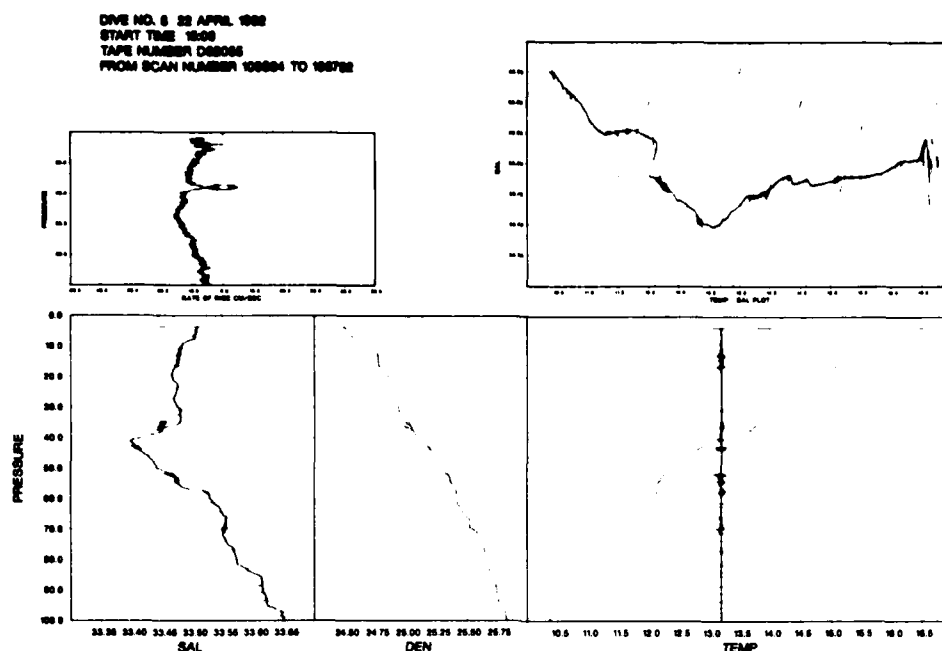
Fig. 3a. The CTD data from the transect to 100 decibars starting at 1502 shows the surface salinity maximum, the minimum about 40 decibars, and the thermal stratification that extends to the surface. The 30 to 50 decibar portion of this record is reproduced in figure 3b. The sloping lines in the temperature-salinity plot are the lines of constant density.
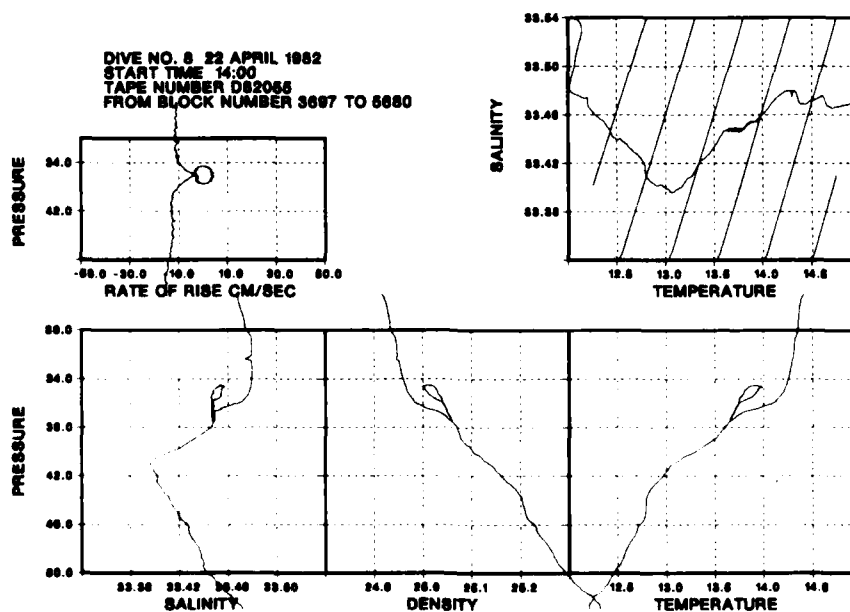
Fig. 3b. The CTD data from the first pass through the salinity minimum, corresponding to region 1 on figure 2, shows a broad trough on the temperature-salinity plot. The temperature decreases monotonically.

DIVE NO. 8 22 APRIL 1982
START TIME 14:00
TAPE NUMBER D82055
FROM BLOCK NUMBER 5661 TO 9176

PRESSURE

34.0

42.0

-50.0 -30.0 -10.0 10.0 30.0 50.0
RATE OF RISE CM/SEC

SALINITY

33.54
33.50
33.46
33.42
33.38

12.5 13.0 13.5 14.0 14.5
TEMPERATURE

PRESSURE

30.0
34.0
38.0
42.0
46.0
50.0

33.38 33.42 33.46 33.50
SALINITY

24.9 25.0 25.1 25.2
DENSITY

12.5 13.0 13.5 14.0 14.5
TEMPERATURE
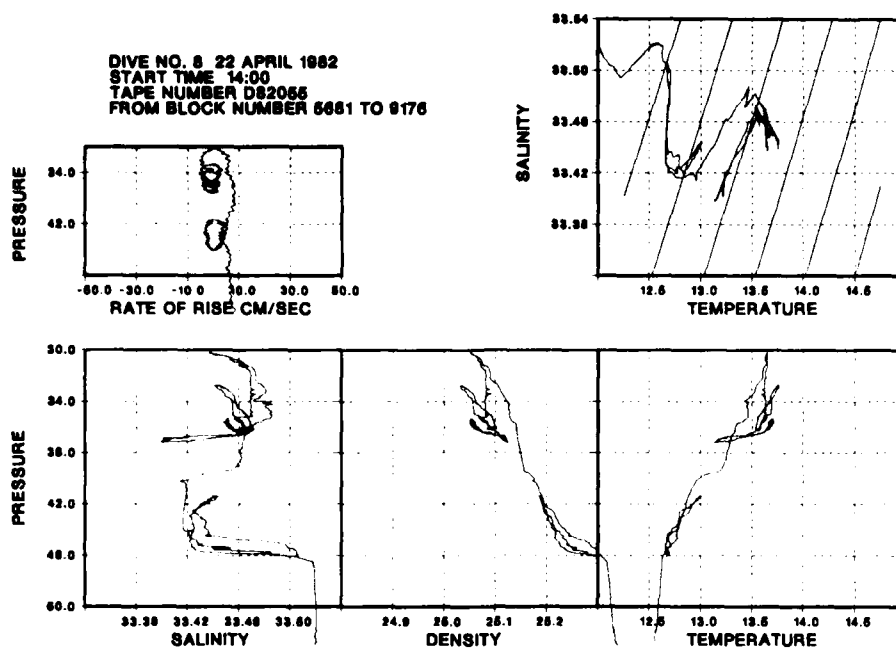
Fig. 3c. This CTD data contains several depth cycles along the segment
of the path labelled 2 in figure 2. The first excursions through the
salinity minimum find it saltier than in figure 3b. After those depth
cycles the T-S relation jumps to a line suggesting a fresher and warmer
intrusion.

DIVE NO. 8 22 APRIL 1982
START TIME 14:00
TAPE NUMBER D82055
FROM BLOCK NUMBER 10185 TO 11848

PRESSURE

34.0

42.0

-50.0 -30.0 -10.0 10.0 30.0 50.0
RATE OF RISE CM/SEC

SALINITY

33.54
33.50
33.46
33.42
33.38

12.5 13.0 13.5 14.0 14.5
TEMPERATURE

PRESSURE

30.0
34.0
38.0
42.0
46.0
50.0

33.38 33.42 33.46 33.50
SALINITY

24.9 25.0 25.1 25.2
DENSITY

12.5 13.0 13.5 14.0 14.5
TEMPERATURE
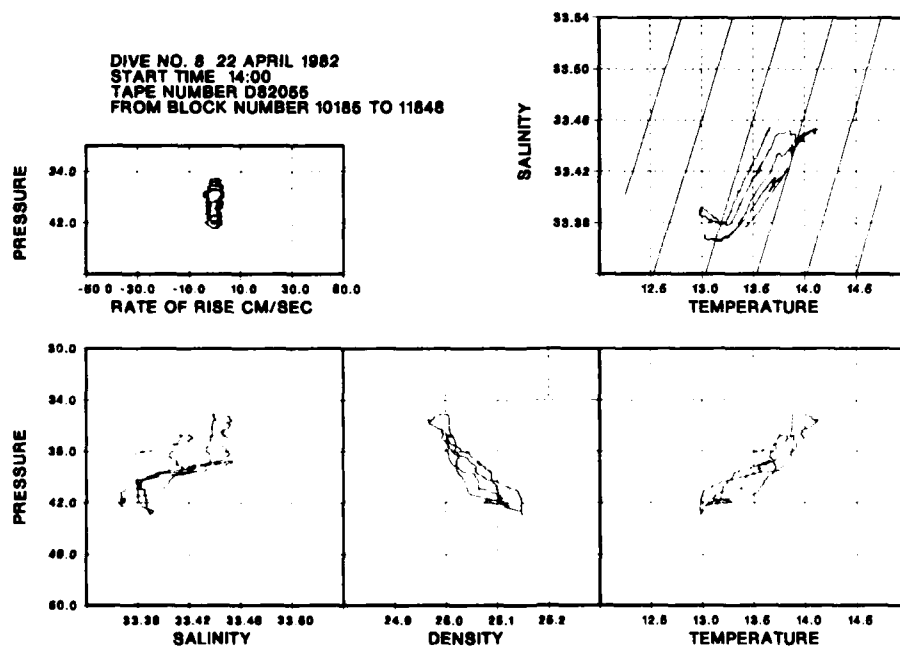
Fig. 3d. This data corresponds to region 3 in figure 2. The salinity
minimum is again fresher and warmer than the previous region. Sometimes
we get more than one pass through the same small water mass and sometimes
not.

32
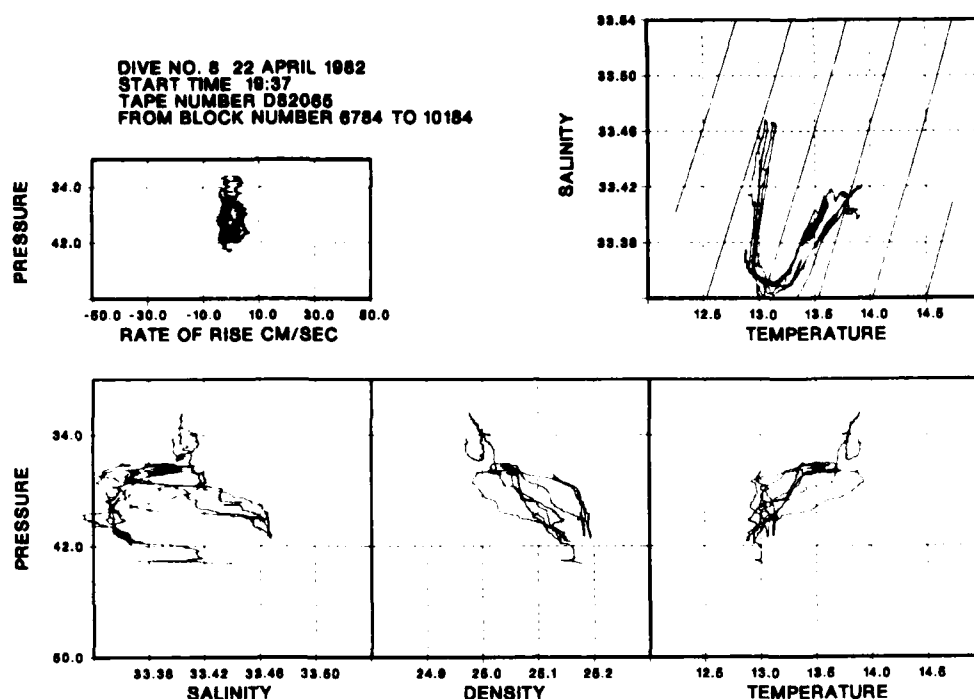
Fig. 3e. This data set finishes within 1000yds of the data forming
figure 3b, but we see little similarity in the signature of the salinity
minimum. This data is from region 4 on figure 2.
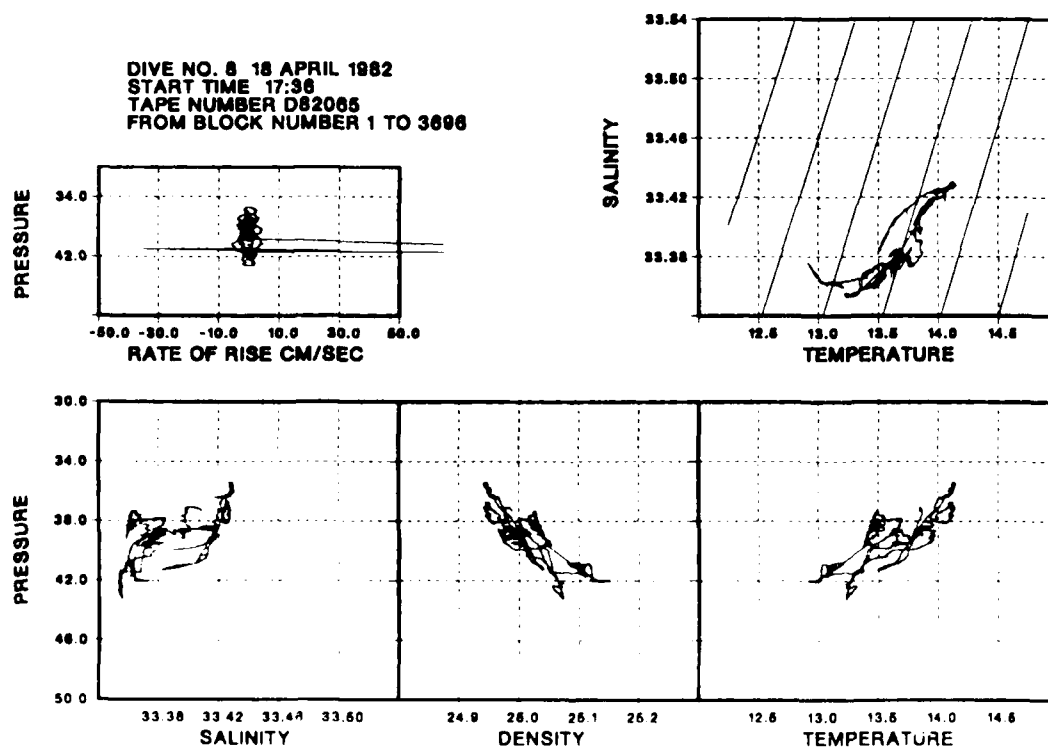
Fig. 3f. The data from region 5 on figure 2 shows the salinity minimum
to be more strongly developed than it was 3 hours earlier. The CTD data
from this dive show the salinity minimum to be changing in both time and
space.

During some of the depth cycles we encountered continuous turbulent
patches that we sampled for several minutes at a time. Two of these
occurrences have been selected to study the effects of stratification on
the turbulent velocity fluctuations. The time series of the turbulence
data are shown in figure 4. The turbulent patches, labelled A and B,
were selected for their intensity (they are among the strongest signals
in the time series) and because the depth excursion was limited. Patch C
was chosen to show the noise level of the velocity shear circuits. The
temperature and salinity data corresponding to the two turbulent regions
are shown in figure 5.

The long continuous patches were desirable since the ACM and turbulent
sensors are not coincident in space. Also, the spectra that we show to
compare the ACM to the airfoil probes are overlapping in time but do not
cover exactly the same time interval. The ACM spectra for region C
covers a longer time period than the airfoil probe spectra while the
airfoil spectra are longer for patch B. The problem arises because there
are two recording systems, digitizing at different rates, and we do our
spectra with a FFT algorithm that requires the number of data points be
a power of 2. The objective was to find relatively homogeneous regions
so that the spectra could be compared in spite of slight spatial and
temporal misalignment.

To calculate the spectra from the low frequency data of the ACM and CTD
we remove the mean from a block of 4096, apply a full cosine taper, fast
Fourier transform, multiply by f^2, and then band average in a geometric
progression. There are no corrections applied for the response of the
thermistor or the spatial averaging of the ACM. The turbulence spectra
are calculated slightly differently; we remove the mean from blocks of
8192 points, cosine taper, transform, correct for thermistor response,
and then average spectral estimates from adjacent data blocks. Some of
the turbulent spectra are band averaged and some are not, depending on
the resolution and stability desired. In all cases we correct for the
loss of variance of the cosine taper by multiplying the individual
estimates by 8/3. Since the ACM and CTD data are recorded on a different
data system from the turbulence data and the sensors are displaced 0.56m
vertically, we are not comparing data from exactly the same place and
time. We have aligned and selected the data as well as possible to
minimize these effects. The spectra are plotted in terms of power per
hertz against frequency in hertz, both on logarithmic scales. We chose
frequency rather than wavenumber because we are more accustomed to
analyzing the data in that framework and many of the limitations on the
data are due to processes that occur at fixed frequencies, vibration and
ship motion, rather than at fixed wavelengths.

The band averaging of the spectra is done in a geometric fashion. The
first four points are individual estimates, the next two points represent
the average of two estimates, the next two represent four point averages,
the next two points are eight point averages and so on. The appropriate
frequencies for each spectral estimate are calculated by averaging the
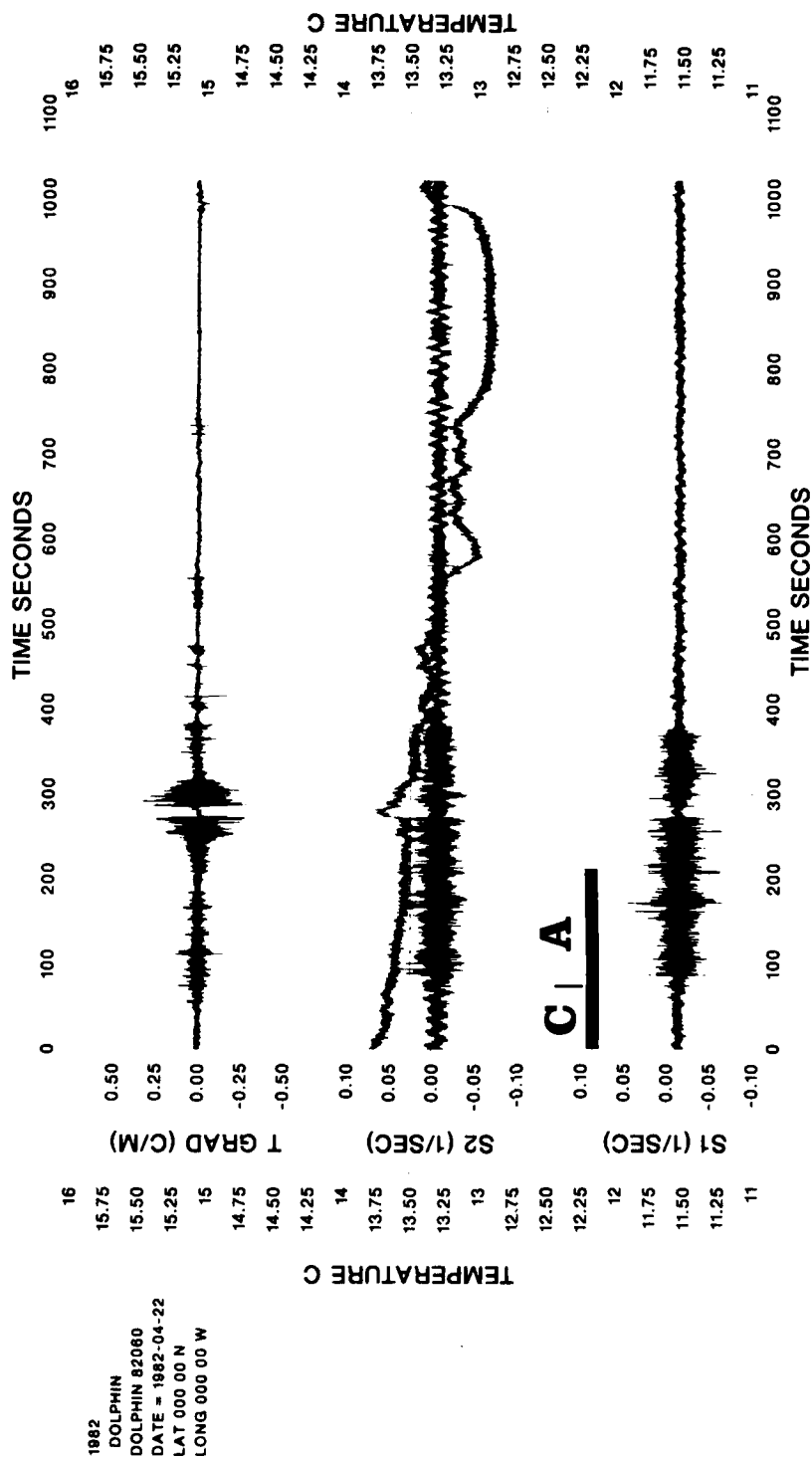
Fig. 4a. The time series for the turbulent shears and temperature gradient for the turbulent patches marked A and C in figure 2. S1 is ∂w/∂x and S2 is ∂v/∂x. The roll of the submarine is visible on channel S2.
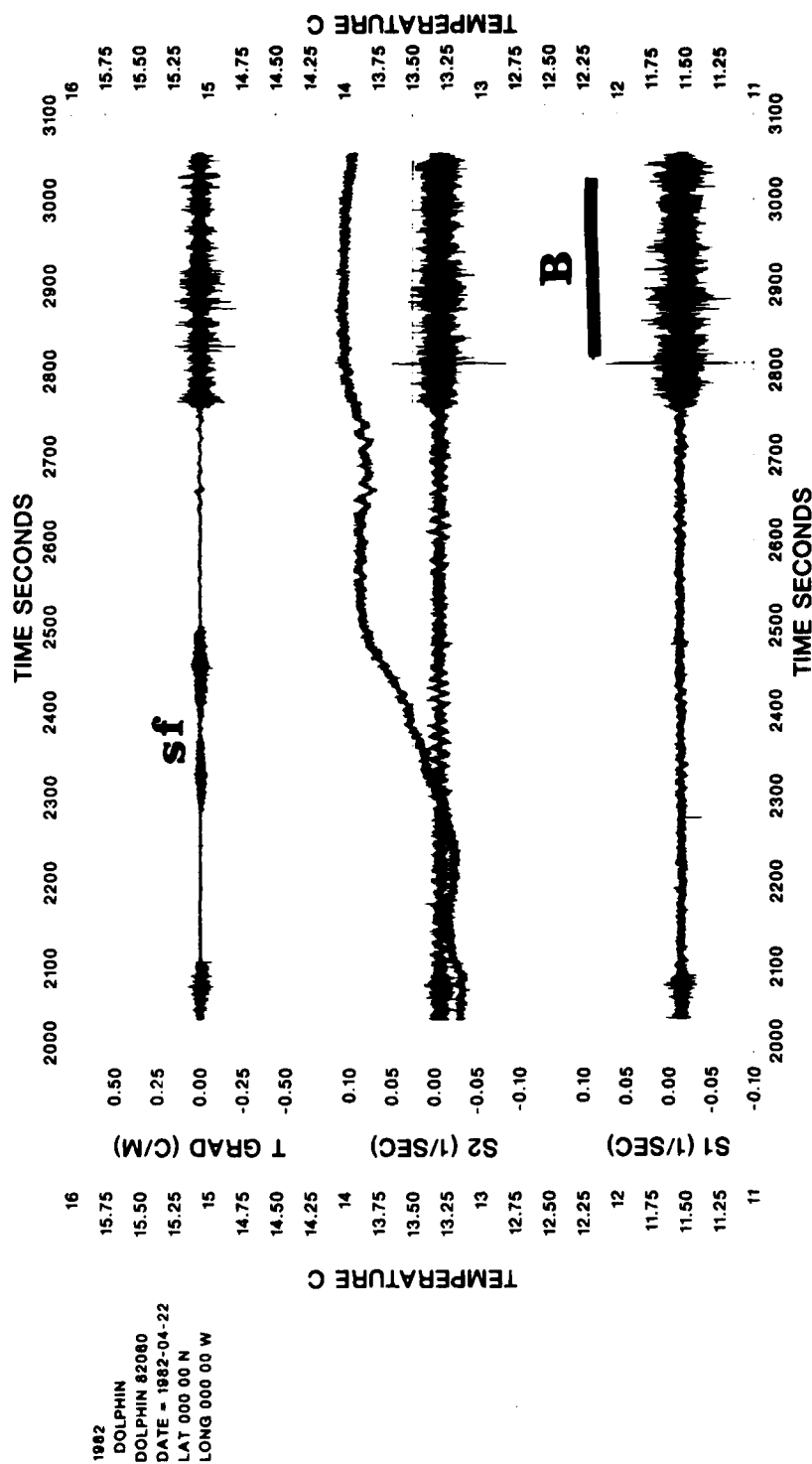
Fig. 4b. The time series for the turbulent patch labelled B. The temperature gradient data shows a patch of salt fingers (labelled sf) that can be compared with the figure 3a of Gargett and Schmitt(1982).

DIVE NO. 8 22 APRIL 1982
START TIME 17:33
TAPE NUMBER D82065
FROM BLOCK NUMBER 1 TO 700

A & C
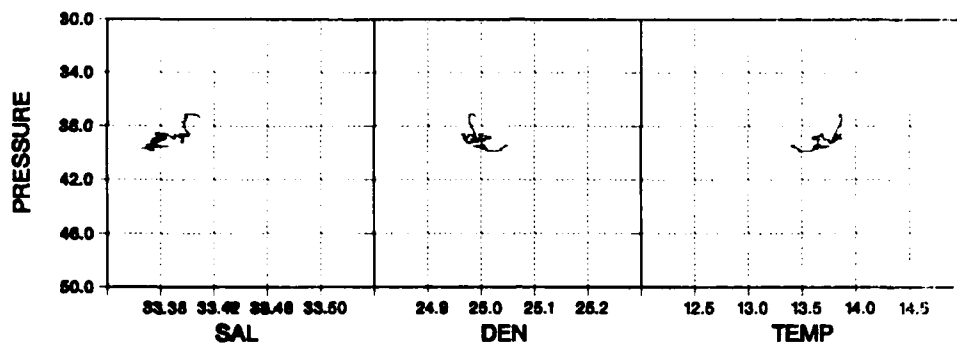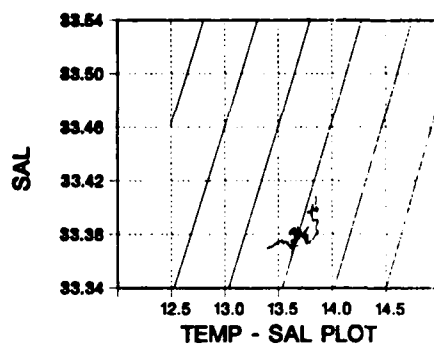
DIVE NO. 8 22 APRIL 1982
START TIME 18:24
TAPE NUMBER D82065
FROM BLOCK NUMBER 2665 TO 2998

B
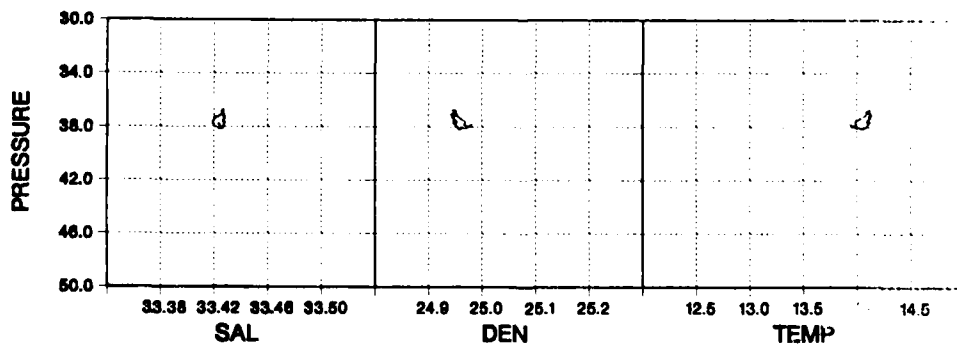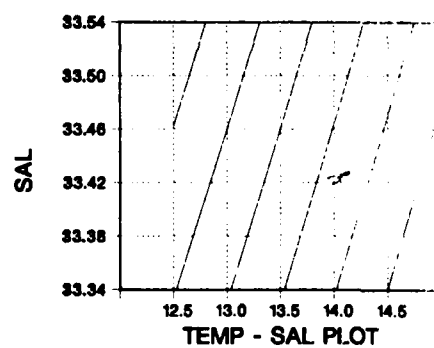
Fig. 5. The temperature and salinity data corresponding to the turbulent patches A and B as well as the relatively quiet region C. The depth variation is limited to 1.5m during these time periods.

frequencies with the same algorithm. The ACM spectra and the turbulence spectra that are not band averaged are plotted as horizontal lines across the appropriate frequency interval, and the band averaged turbulent spectra are plotted as points.

The data from region C shows the noise level of the airfoil probes (figure 6c). The spectral peaks above 30Hz are due to the vibrations of the framework. Comparison with the airfoil probe data from regions A and B, shown in figures 6a and 6b, reveals that the variance of the turbulent velocity shear signals occurs in the frequency range from 0.2Hz to 50Hz. The system was designed to separate the vibrations from the dissipation signal based on operating speeds from 1.0m/s to 1.5m/s. For the data shown in this paper the speed ranges from 1.1 to 1.2m/s and we use a value of 1.15m/s to convert the frequency scale to a wavenumber scale.

The spectra of the ACM (figure 7) cover a much lower range of frequencies that the airfoil probes. There is a strong peak in the spectra at 0.1Hz associated with the rolling of the submarine. This contamination of the velocity signal sets the low frequency limit on the validity of the ACM data as a measure of oceanic variability. We will return to this subject after the comparison of the airfoil probes with the ACM.

Many spectra of the data were calculated to compare the airfoil probes with the acoustic current meter. The results were, to us, surprisingly favorable. The essence of the comparison is shown in Figure 8 where the spectra from the Neil Brown temperature and velocity channels are compared to the spectra of the data from the turbulence package for the three regions. In the frequency range where the two systems overlap, individual spectral estimates agree within a factor of 2 and the overall agreement is considerably better. The airfoil probe spectra track the ACM spectra down to their lowest frequency bin at 0.0625Hz where the contamination from the boat motion is quite obvious. The airfoil probes resolve the complete band of shear from the scales of the ship motion to the dissipation scale. The favorable comparison is a strong test of the calibration of the ACM, since the ACM shear spectrum is independent of its calibration and the airfoil probe shear spectrum depends on the 4th power of the mean speed as measured by the ACM.

The shear measurements from the Dolphin appear to be viable measures of oceanic variability down to frequencies of 0.25Hz corresponding to scales of almost 5m horizontally. This scale is substantially smaller than the submarine and we presumably would not be limited at such a small scale if the probes were not mounted so far above the center of roll of the vessel. Spectra of the accelerometers in the turbulence package (figure 9) show the low frequency peak in both components. Using the simple idea of a rolling ship to model the low frequency accelerations one calculates the contamination of the $\partial v/\partial x$ spectrum as:

$$a_r^2(f)/(U^2*(g/(2\pi f)^2*d + 1)^2) \qquad (4)$$

where $a_r^2(f)$ is the spectral level of the roll-sensitive accelerometer

38
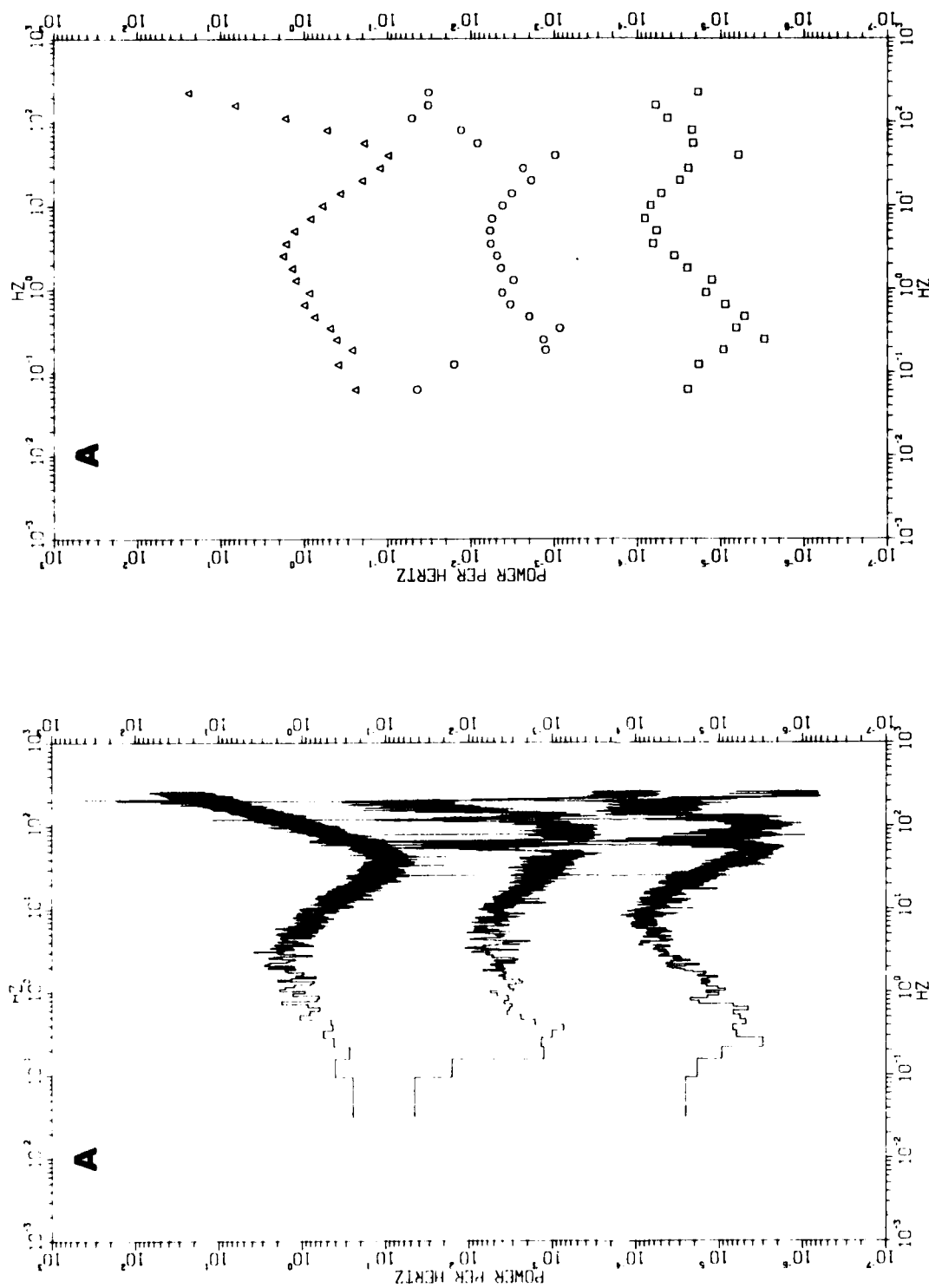
Fig. 6a. The spectra of the turbulent temperature gradient and velocity shear. The spectra are ∂w/∂x at the bottom, ∂v/∂x•100 in the middle, both in units of sec⁻²/Hz, and ∂T/∂x•10⁴ in units of °C/m. The left-hand spectrum of each set has not been band averaged while the right-hand spectrum is the same data band averaged in a geometric progression. Figure 6a is made from 13 sets of 4096 data points. The rising tail on the temperature gradient spectrum above 40Hz is due to system noise as are the peaks in the shear spectra starting at 50Hz.
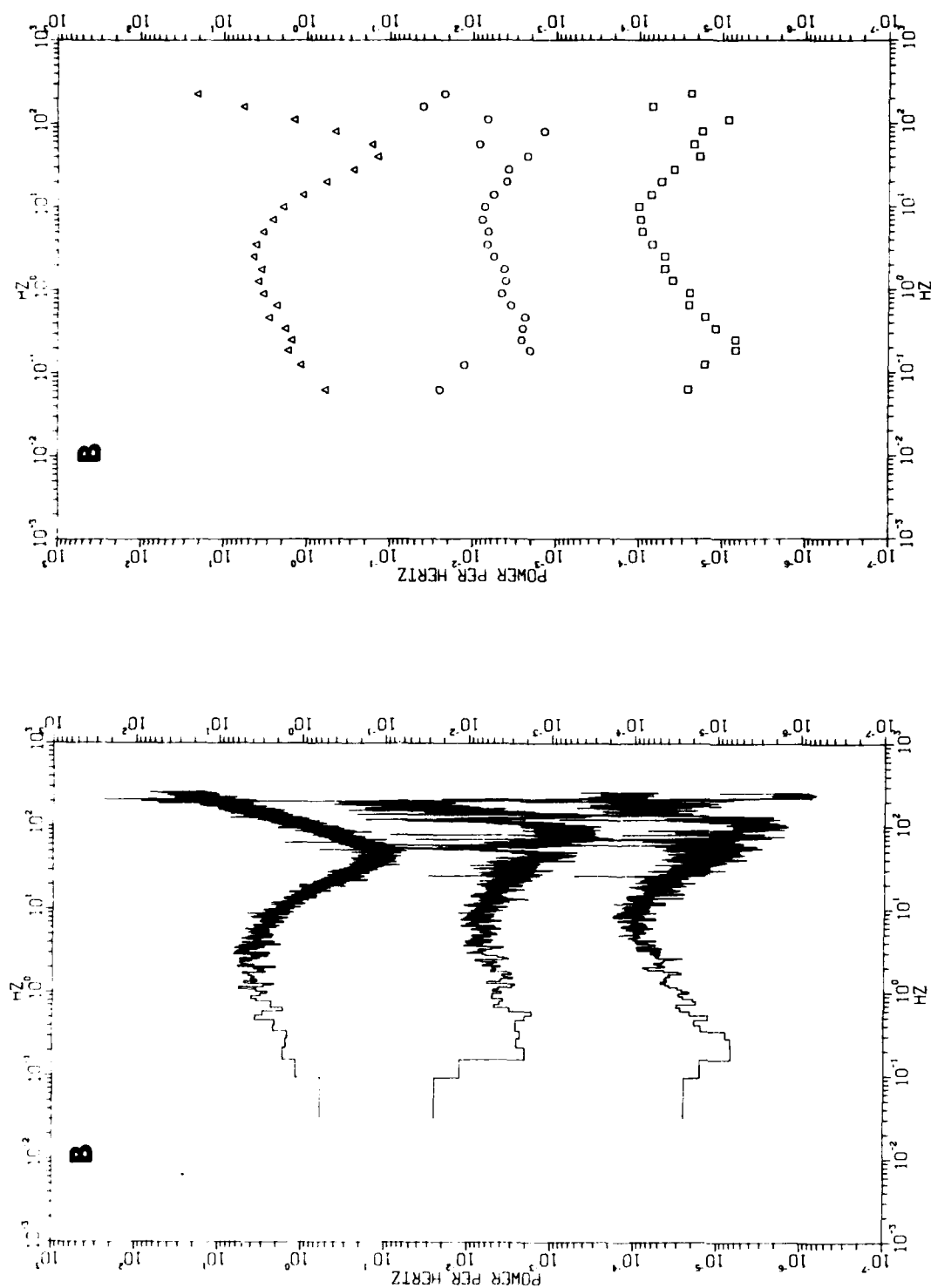
Fig. 6b. The spectra of the turbulent temperature gradient and velocity shear. The spectra are ∂w/∂x at the bottom, ∂v/∂x*100 in the middle, both in units of sec⁻²/Hz, and ∂T/∂x*10⁴ in units of °C/m. The left-hand spectrum of each set has not been band averaged while the right-hand spectrum is the same data band averaged in a geometric progression. Figure 6b is made from 10 sets of 4096 points.
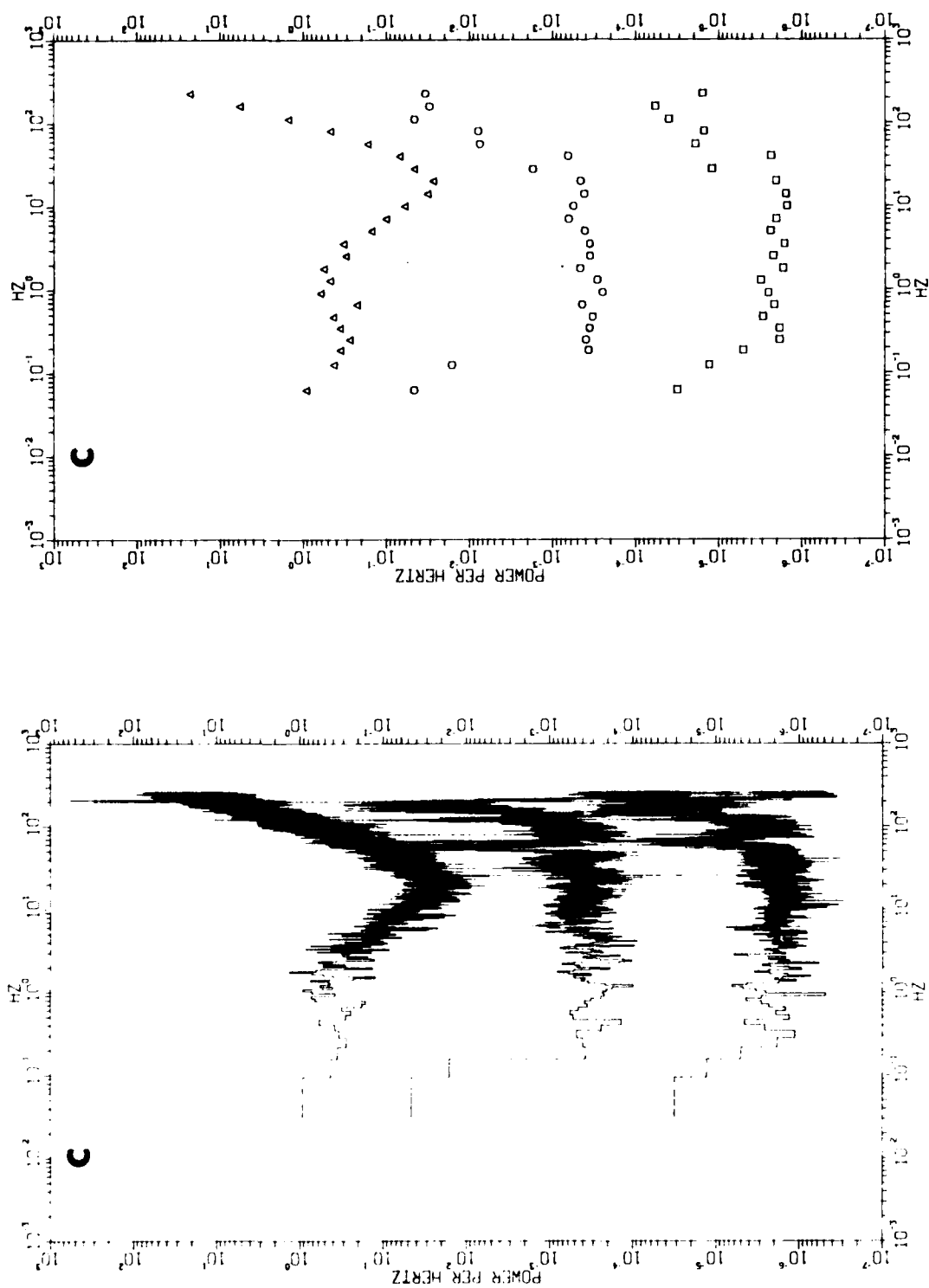
Fig. 6c. The spectra of the turbulent temperature gradient and velocity shear. The spectra are ∂w/∂x at the bottom, ∂v/∂x·100 in the middle, both in units of sec⁻²/Hz, and ∂T/∂x·10⁴ in units of °C/m. The left-hand spectrum of each set has not been band averaged while the right-hand spectrum is the same data band averaged in a geometric progression. Figure 6c is made from 4 sets of 4096 points.
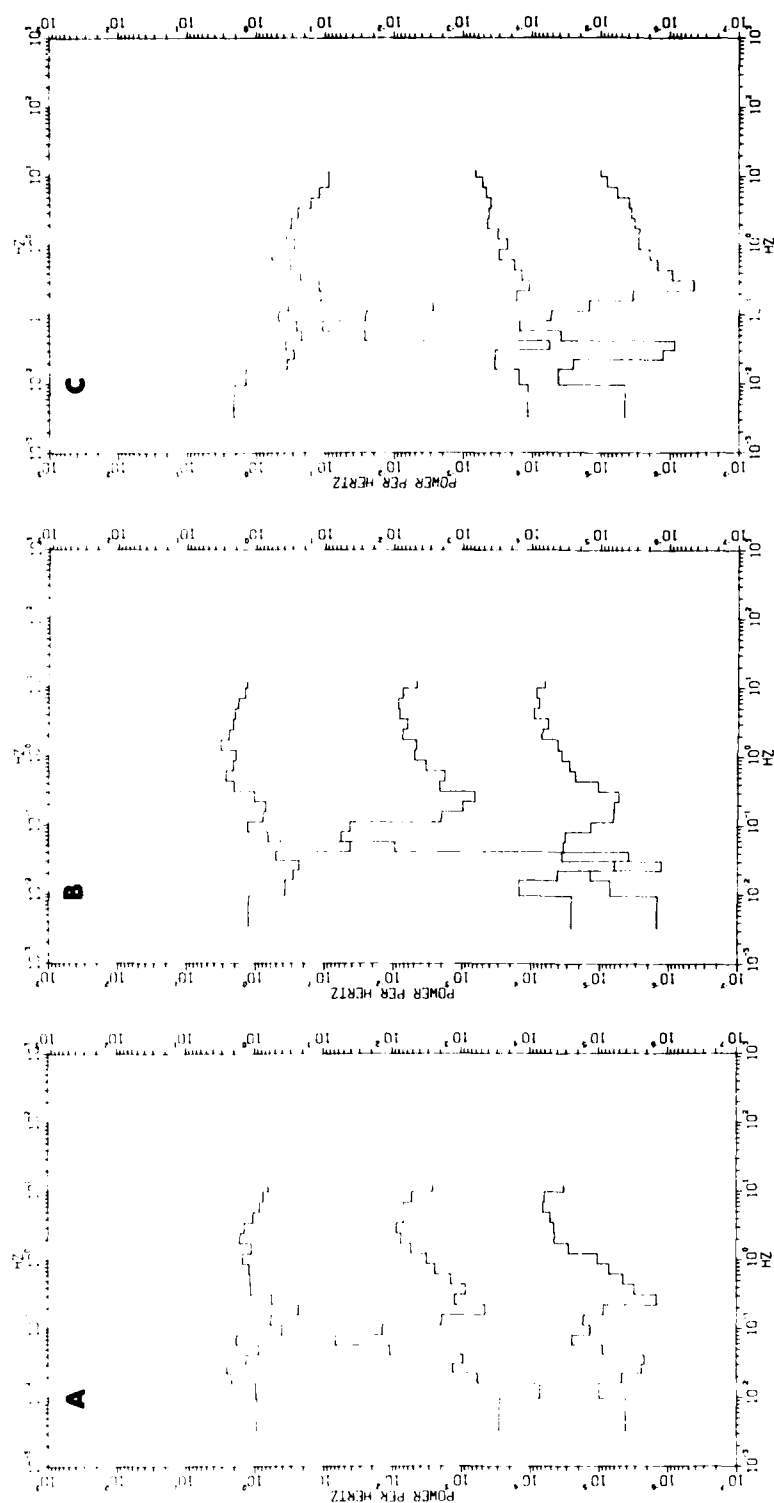
Fig. 7. The velocity shear and temperature gradient spectra from the acoustic current meter and CTD fast thermistor that correspond to the turbulent spectra of figure 6. The velocity shears and temperature gradient are plotted in the same order in the same units and with the same multiplicative factors as in figure 6.
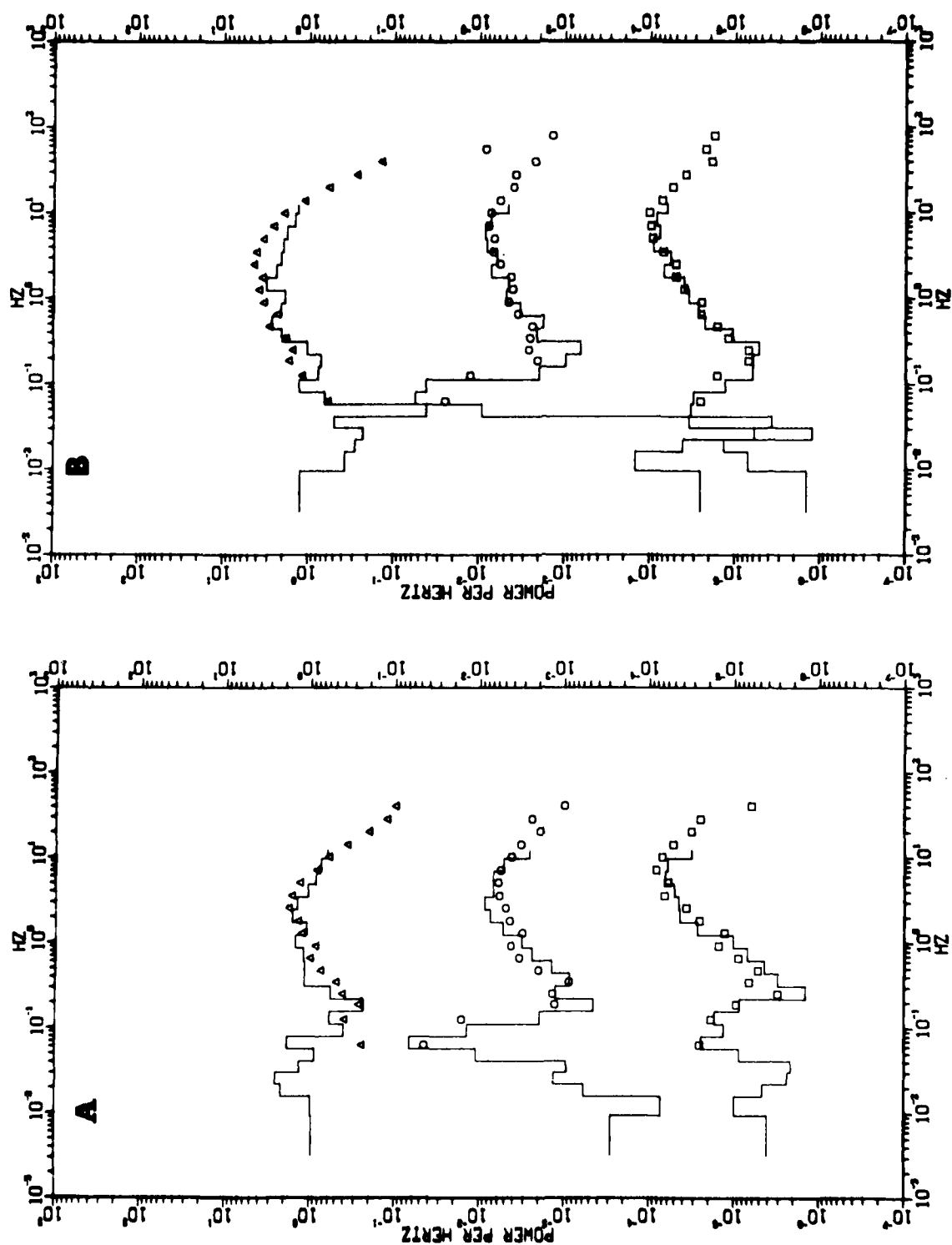
Fig. 8.

Fig. 8.
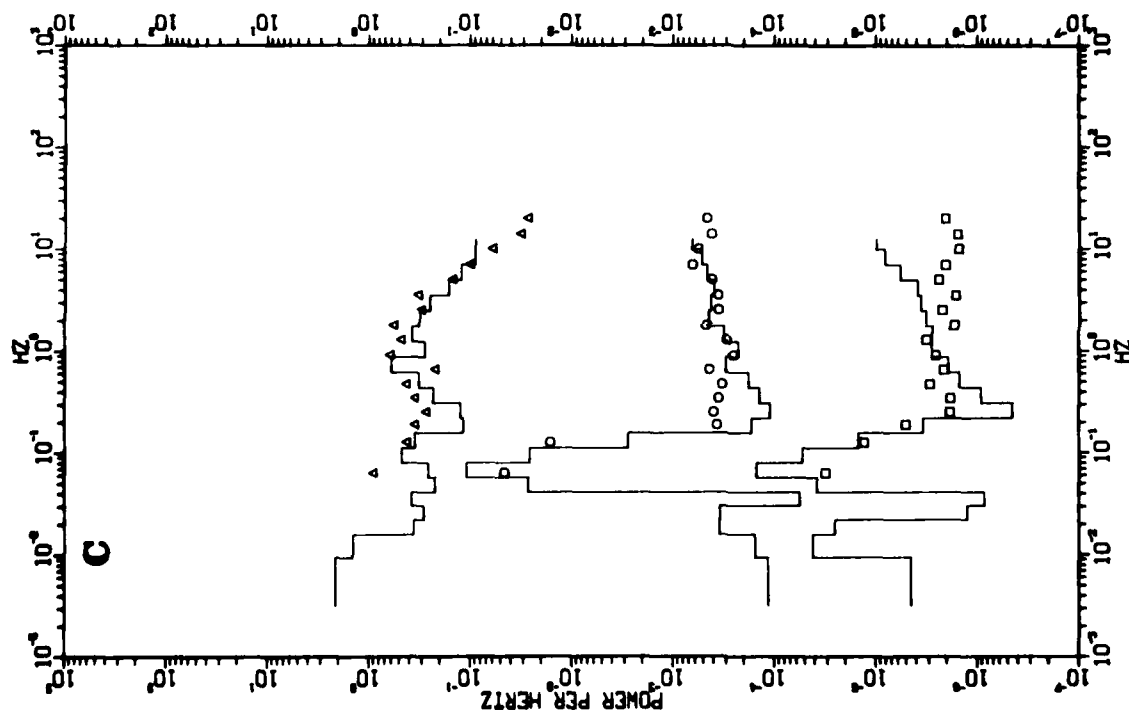
Fig. 8. The band averaged spectra from the turbulence package that are shown in figure 6 have been superimposed on the shear spectra and temperature gradient spectra from the NBIS instrumentation shown in figure 7. The agreement of the shear spectra in the turbulent patches A and B is quite good. As explained in the text, this comparison is a strong test of the calibrations of both measurements.
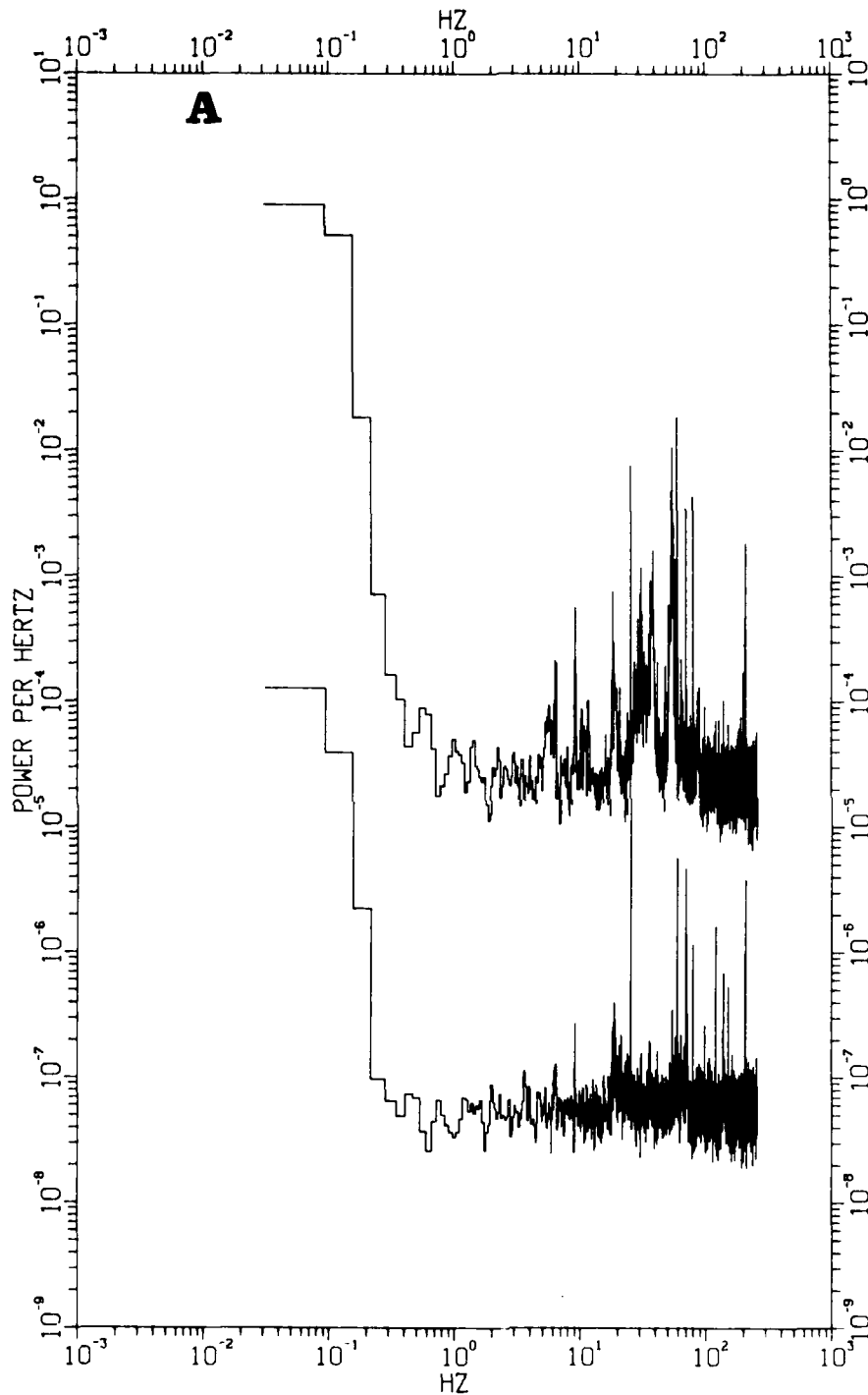
Fig. 9. The spectra of the vertical and lateral acceleration as
measured by the accelerometers located in the turbulence package show the
low frequency motion associated with the roll of the vessel. These
spectra correspond to the turbulent spectra for patch A. The lower trace
is the vertical acceleration in units of $(m/s^2)^2/Hz$, the upper trace is
the lateral acceleration in the same units but multiplied by a factor of
100.

signal at frequency f, U is the mean speed of the submarine, g the acceleration of gravity, and d the vertical distance from the center of rotation to the axis of the velocity probes. When value of 6m is used for d, this model scales the lowest frequency part of the roll accelerometer to levels comparable with the level of the $\partial v/\partial x$ spectrum in figure 6a.

The contamination of the vertical shear spectrum is just:

$$a_z^2(f)/U^2. \qquad (5)$$

Again the acceleration accounts for most of the energy at the lowest frequencies. It is unfortunate that the low frequency is limited by the boat roll. This problem arises because the probes are mounted so far above the center of roll. Perhaps the contamination can be reduced in the future by careful shiphandling, trimming of the vessel, and limitation of personnel movements during sampling periods.

A calculation of the potential flow field around the hull has been performed by Loeser and Chapman (1979) with further analysis by Osborn and Lueck(1984b) to estimate the effect of the mean flow on the turbulent velocity fluctuations. The analysis shows a 4.5% stretching of a line element aligned with the y-axis and a 5.5% compression of line elements aligned with the z-axis. Using the analysis of Hunt(1973) for fluctuations that are small scale with respect to the submarine, one would expect the effect on the vorticity or shear to be the same as the effect on a parallel line element. Thus we expect the $\partial w/\partial x$ spectra to be 9% high and the $\partial v/\partial x$ spectra to be 11% low. These effects are consistent with the observed differences between the two channels. The spectra of velocity shear from regions A and B have been plotted in figure 10 with the two orthogonal channels superimposed on each other, corrected for the flow distortion, and trimmed to remove the values dominated by noise and boat motion. The vertical channel still gives a 12% higher value of ϵ which is well within the uncertainty of the calibration of the velocity probes. This comparison is independent of uncertainty in the submarine speed and is also aided because the probes were selected to be very close to each other in sensitivity.

The airfoil probe shear measurements can be used to examine the effects of stratification on the turbulent velocity fluctuations. Gargett et al compared downstream, u, velocity spectra to vertical, w, velocity spectra to show that the effect of stratification is a suppression of the large scale (low frequency) vertical velocity fluctuations. The appropriate scale parameter is the buoyancy scale, l_b defined as:

$$l_b=2\pi(\epsilon/N^3)^{1/4} \qquad (6)$$

where ϵ is the dissipation rate and N is the buoyancy frequency.
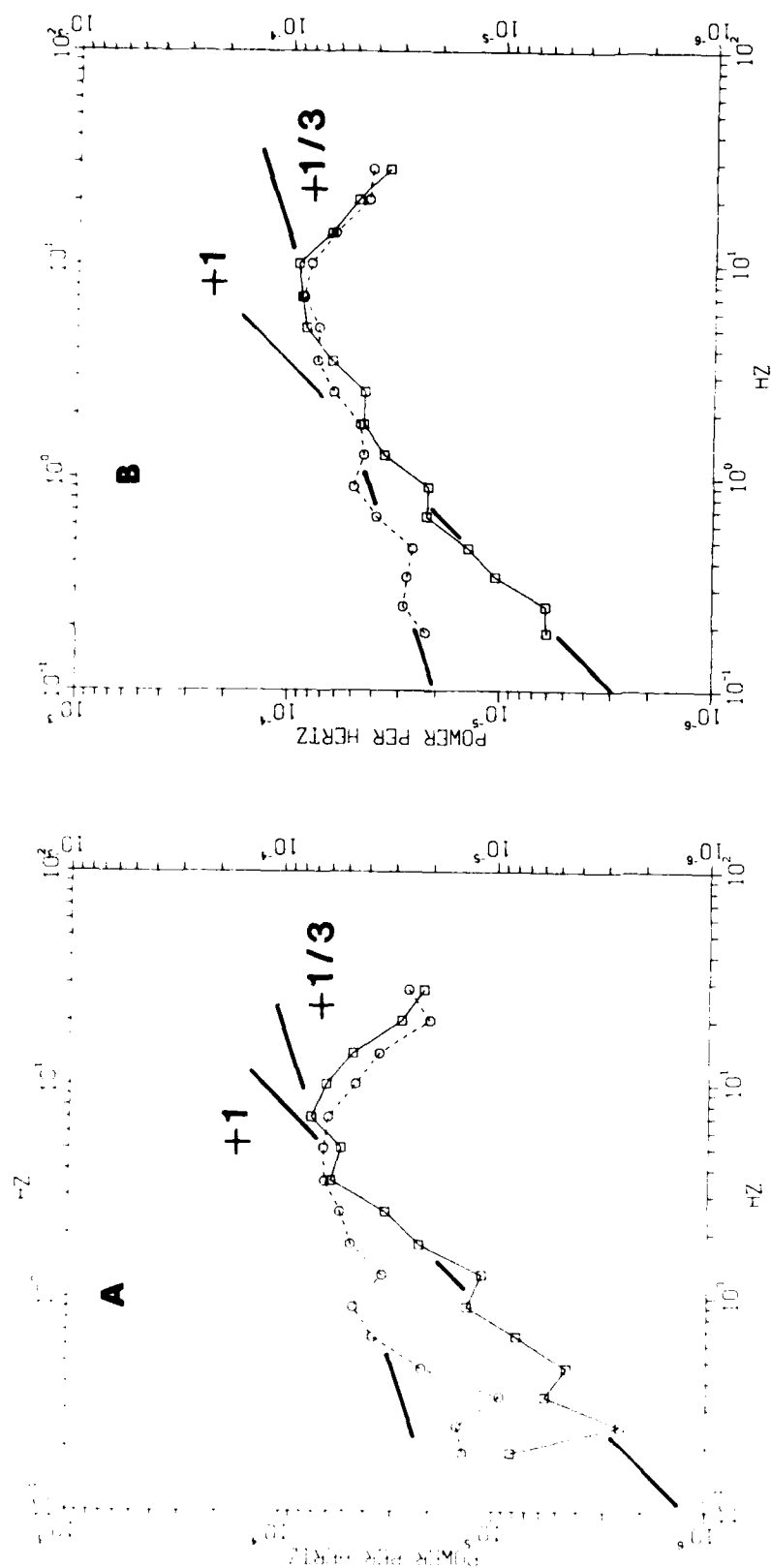
Fig. 10. The band averaged turbulent shear spectra for patches A and B are plotted after being corrected for the potential flow distortion, and trimmed to remove the portions that are dominated by body motion or vibration. A line of +1 slope has been fitted by eye to the $\partial w/\partial x$ spectra (open squares) and a line of +1/3 slope fitted to the $\partial v/\partial x$ spectra (open circles). The effect of stratification on the turbulence is seen to be a suppression at low wavenumber (frequency) of the vertical velocity relative to the lateral velocity. The effect of stratification is stronger in region A, extending almost to the peak of the dissipation spectrum.

The rolloff of the vertical shear at low frequencies is quite apparent in figure 10 (the two lowest frequency spectral estimates have been removed since they are contaminated by ship motion and are not germane to this discussion). The slope of the horizontal velocity shear is +1/3 when the slope of the vertical shear has increased to +1. These slopes are consistent with the effects seen by Gargett et al. Table 1 gives values for ϵ, N, l_b and I for the two patches. The values of I are substantially lower than those studied by Gargett et al. because the dissipations are relatively low and the stratification pretty high. There are not any really large values of I available to us in this data set. These data do not show the surpression of the lateral velocity component observed by Gargett et al. For their work the mean shear was aligned with the downstream direction, we cannot presume that situation occurred here. There is probably production of turbulent kinetic energy in the cross-stream component.

TABLE 1: Numerical values of the salient parameters for the three patches

	A	B	C
ϵ [cm^2/s^3]	$1.3 \cdot 10^{-4}$	$2.2 \cdot 10^{-4}$	$2.1 \cdot 10^{-6}$
N [cph]	8.9	7.4	8.9
l_b [m]	0.36	0.58	0.05
l_s [m]	0.023	0.022	0.06
I	16	26	n.a.

Another interesting aspect of the data can be seen by comparing the temperature gradient spectra with the velocity shear spectra. In the averaged spectra we see that the peak in the temperature gradient is at a lower frequency (and hence wavenumber) than the peak in the velocity shear spectra. This result is contrary to the Batchelor (1959) explanation of the behavior of a passive scalar in homogeneous isotropic turbulence. Two simple explanations are possible. First, our thermistor may have suffered contamination and not have had the frequency response that we assumed of being 3dB down in response at 22Hz. Second, the spectrum of temperature gradient fluctuations may be dominated by the anisotropic features associated with the fine structure, the large scale structures that formed or maintain the patch, and the entrainment processes at the edge of the patch.

48
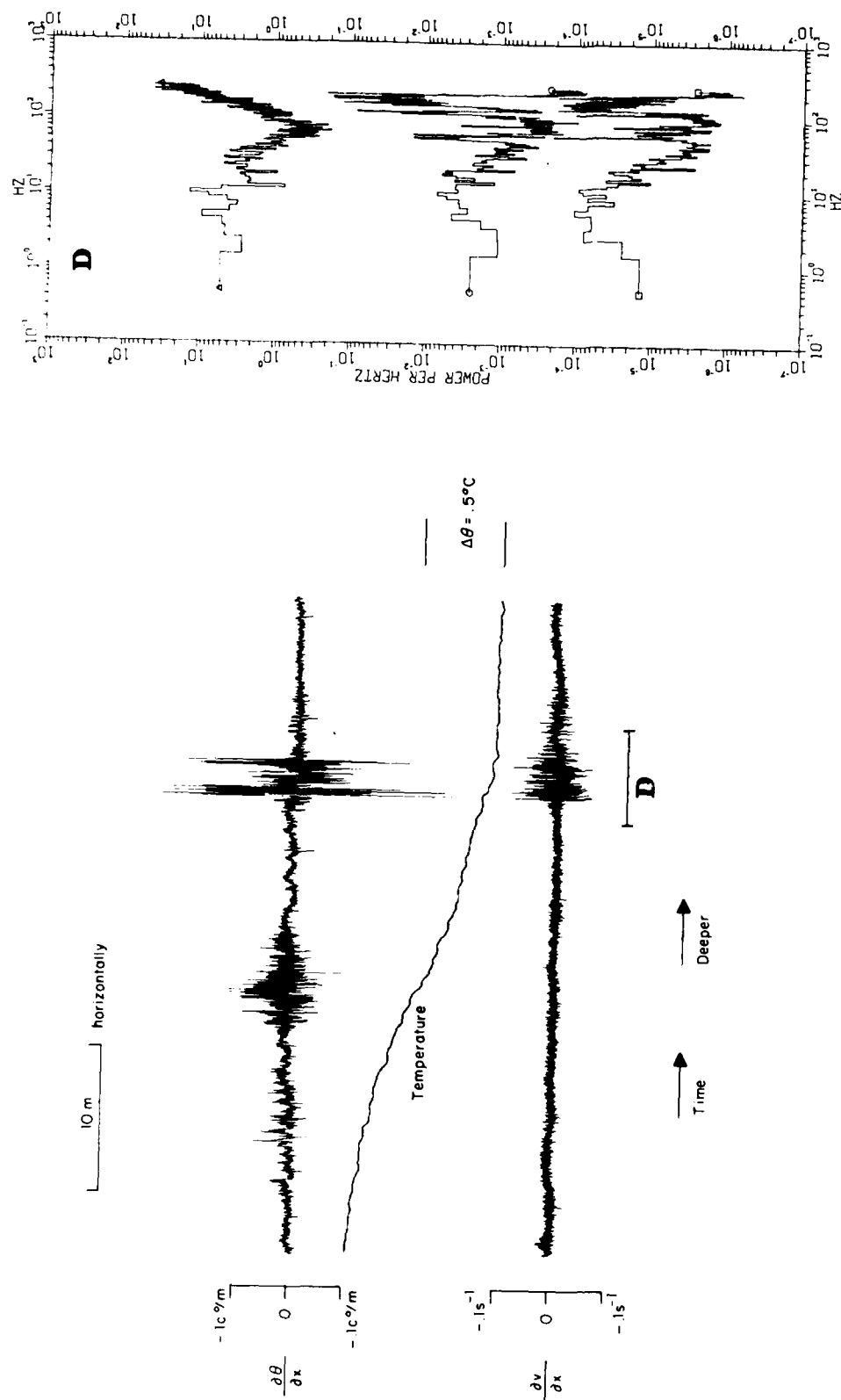
Fig. 11. This data shows salt fingers above a turbulent patch at the location marked by D in figure 2. The spectra at the right cover the turbulent patch. The temperature gradient spectrum has a peak around 30Hz which is above the peak of the shear spectra and is probably related to the turbulent straining of the temperature fluctuations as described by Batchelor(1959). There is as much variance in the low frequency portion of the spectrum (10Hz and below) as above 10Hz up to 60Hz where the electronic noise starts to dominate the spectrum.

Examination of other data from the same day (figure 11) shows a peak in
the temperature gradient above the peak in the velocity shear spectra.
This spectra also shows considerable low frequency (low wavenumber)
energy in the temperature gradient. In fact, the variance of the
temperature gradient below 10Hz (corresponding to 0.12m for this specific
piece of data) is comparable to the variance above 10Hz and below 60.0Hz
where the spectrum starts to rise due to noise. Dillon and Caldwell
(1980) modelled the vertical temperature gradient spectrum as a composite
of the turbulent Batchelor type spectrum and a finestructure spectrum.
We are possibly seeing a similar composite spectrum with the
finestructure contribution dominating.

CONCLUSIONS

1) There is excellent agreement between the velocity shear measurements
by the airfoil probes and the Neil Brown Instrument Systems' acoustic
current meter over a wide range of scales, from 0.05Hz to greater than
5Hz. The low frequency limit of usefulness for both systems is set by
the boat motion (roll frequency of 0.01Hz). The upper limit is set by
the sampling volume of the systems as long as there is sufficient signal
so they are not limited by their noise levels.

2) The effect of stratification is a suppression of the vertical
velocity fluctuations with the appropriate scaling parameter being l_b as
detailed by Gargett et al.

3) The vertical and lateral shear channels give comparable estimates of
the shear variance within experimental uncertainties when appropriate
corrections are made for the distortion of the potential flow around the
hull of the submarine, even for values of I as low as 16.

4) The temperature gradient spectra are peaking at wavenumbers below the
peak of the shear spectra, possibly due to effects related to the
anisotropy of the temperature field on the scale of the patch.

ACKNOWLEDGEMENTS

50

REFERENCES

Batchelor, G. K. 1959; Small-scale variation of convected quantities like temperature in a turbulent liquid, part 1. Journal of Fluid Mechanics, 5, 113-133.

Dillon, T.M., 1982; Vertical overturns: a comparison of Thorpe and Ozmidov scales, Journal of Geophysical Research, 87(C12), 9601-9613.

Dillon, T.M., and D.R. Caldwell, 1980; The Batchelor spectrum and dissipation in the upper ocean, Journal of Geophysical Research, 85(C4), 1910-1916.

Gargett,A.E., 1982; Turbulence measurements from a submersible, Deep Sea Research, 29(9a), 1141-1158.

Gargett, A.E., T.R. Osborn, and P.W. Nasmyth, 1984; The approach to isotropy in stratified turbulence, in press Journal of Fluid Mechanics.

Gargett,A.E., and R.W. Schmitt 1982; Observations of salt fingers in the central waters of the eastern North Pacific, Journal of Geophysical Research, 87(C10), 8017-8029.

Hunt, J.C.R., 1973; A theory of turbulent flow round two-dimensional bluff bodies, Journal of Fluid Mechanics, 61(4), 625-705.

Loeser, D.J., and R.G. Chapman, 1979: Flow perturbations introduced by the Dolphin. Science Applications Inc. Report 052-79-848-LJ 37pp.

Osborn, T.R., 1978; Energy dissipation adjacent to an island. Journal of Geophysical Research, 83(C6), 2939-2957.

Osborn, T.R., and R.G. Lueck, 1984a; Turbulence measurements from a submarine, submitted to Journal of Physical Oceanography

Osborn,T.R. and R.G. Lueck, 1984b; Turbulence and hydrographic measurements from the USS Dolphin (AGSS 555), manuscript report U.S. Naval Postgraduate School in preparation

Thorpe, S.M. 1977; Turbulence and mixing in a Scottish Loch, Philosophical Transactions of the Royal Society of London, Series A 286, 125-181.

TOWED OBSERVATIONS OF INTERNAL WAVES AND PATCHES OF FINE-SCALE ACTIVITY

J.P. Dugan

Marine Technology Division
Naval Research Laboratory, Washington, District of Columbia, 20375

ABSTRACT

Ocean temperature structure as measured with towed instruments consists of overlapping scales of internal waves, patches of small-scale activity, and layered fine structure. Observations with a vertical array of sensors are exhibited, and rudimentary analyses of the data are presented. The small-scale patches exhibit large levels of variability, have log normal statistics, have ratios of horizontal to vertical sizes near N/f, and consist of more than one species.

INTRODUCTION

Measurements of small-scale fluctuations in the ocean are undertaken because the observations are necessary for unravelling the physics of the processes which are occurring. Both the actual dissipation processes and the mechanisms by which energy gets to the scales on which it is dissipated are important. As an example of their importance, these small-scale processes result in vertical mixing and thus dictate mass fluxes which affect even the largest existing scale, the general circulation.

These measurements have been made only with tremendous advances in the technology. Observations of fluctuations smaller than the grossest scale in the ocean became available on a regular basis for the first time with the discovery of the mechanical bathythermograph because one had a continuous profile of the temperature. Actually, this instrument gave the temperature along an arc as it was deployed or recovered but, because it registered pressure along one axis of the slide (and the ocean conveniently cooperated with a high anisotropy between horizontal and vertical scales), the data were considered to yield a vertical profile. The advent of the tethered CTD gave better data and, in addition, some salinity information. The more recent free fall profilers are of course highly refined and yield extremely high-

quality data, but they generally have continued to be one-dimensional in nature. There have been a number of notable cases in which some two-dimensional information has been obtained by yo-yoing a towed or free fall instrument (eg. Gargett,1975; Gregg,1980; Cairns,1980). Unfortunately, the full details of the two-dimensional structure have eluded observation, primarily because of technical difficulties in constructing appropriate instruments. A significant contribution to this difficulty has been the large mismatch between horizontal and vertical scales. (On the other hand, this difference in scales has contributed strongly to the appropriate interpretation of the tow-yo observations mentioned above.) As an example of the technical problems, it is extremely difficult to tow an instrument platform in a straight enough horizontal line to prevent contamination of the data by swell-induced modulations of the tow depth (eg. Dugan et al., 1980). These problems have been alleviated somewhat in the last few years, and it has been possible to obtain valid measurements in the horizontal dimension.

This communication is intended to exhibit the horizontal domain and, especially, the horizontal-vertical one. The general nature of the observations and some elementary statistics are described. The details of the measurement system are given in Morris et al.(1983) and initial conclusions on oceanographic implications are given in Dugan et al.(1984).

DATA

The two-dimensional data have been acquired with a vertical array of thermistors which is towed at a speed of about 250 cm/sec. Fig. 1 is a sample of the data; it shows temperature plotted over a distance of 5 km. Each line is the temperature registered by a particular sensor. The sensors are separated by about 50 cm in the vertical, so the distance between lines is a direct function of the local vertical temperature gradient. The vertical depth range of the data is from the surface to about 90 m. The dark line at the top is caused by a number of sensors which register nearly the same temperature in the mixed layer. Just below this, the sharp step at the bottom of the mixed layer is indicated by the large average separation between lines. The lines gradually get closer together as the temperature gradient gets smaller with increasing depth as the 18° water is approached (this was in the Sargasso Sea). The real interesting features in this plot, though, are the wiggles on the lines. The dark, linear regions are layers which are nearly isothermal in the vertical. It is interesting to note that these layers migrate in temperature along the plot. They also change their depths as, on the average, one often sees a change in the particular sensors in a given layer. A second obvious feature in this plot is the vertically coherent internal waves. These are first mode waves which are trapped in this seasonal thermocline. The final feature which is of interest here is the appearance of
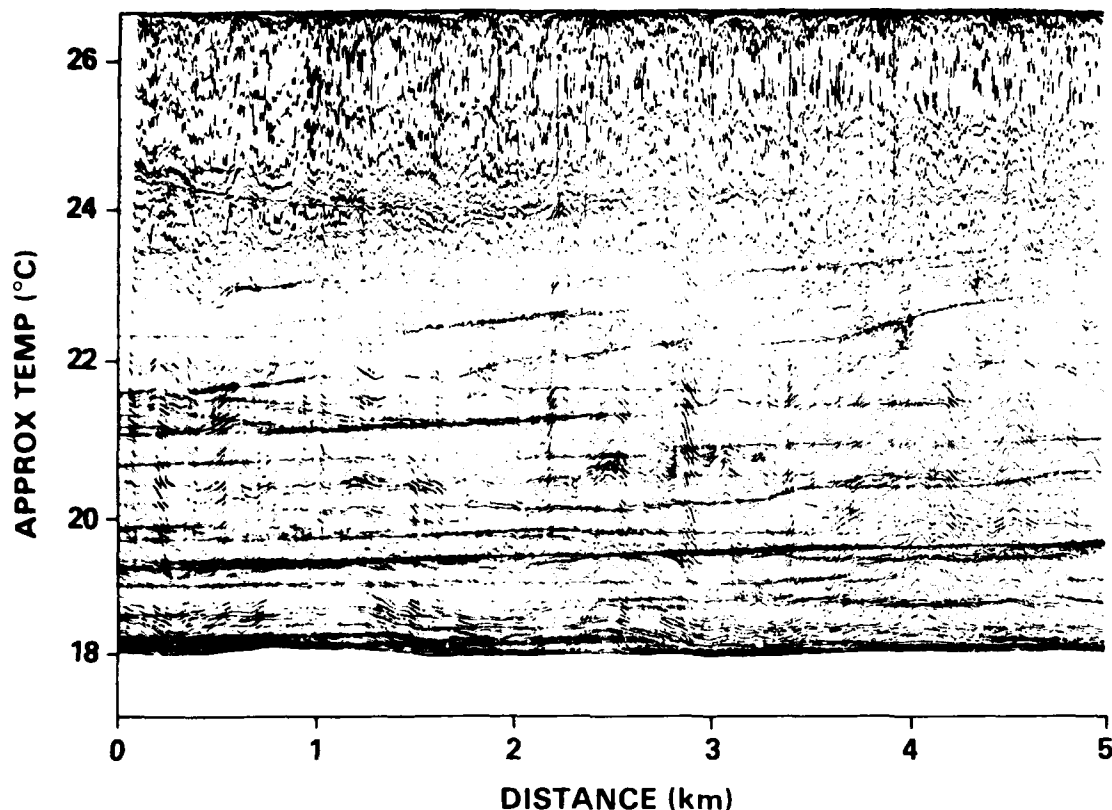
Fig. 1.   Plot of temperature from towed vertical array of sensors.

small regions of short wavelength activity. They are evident
under close scrutiny but they are not too obvious in this figure
because the total variance is dominated by the longer scales.

   Figure 2 exhibits the same data as in Figure 1, but in this
case the display is a raster plot of the vertical temperature
gradient. The origin of each line is the zero value of the gradient,
and this is located at the depth of each sensor; the gradient is
estimated by centered differences. Regions of small gradient are
seen as relatively straight lines, while the high gradient steps
(like the bottom of the surface mixed layer) cause overlapping
lines, and therefore the darker strips. These steps are easily
traced from sensor to sensor as the long internal waves modulate
their depths. In addition, it is clear that the layers are modulated
in depth by the waves.

   Figure 3 again is a temperature plot but this time it exhibits
data from a small aperture array which has much better vertical
resolution. In this case, the widely separated traces are the half-
meter resolution array, and the group of closely spaced lines are
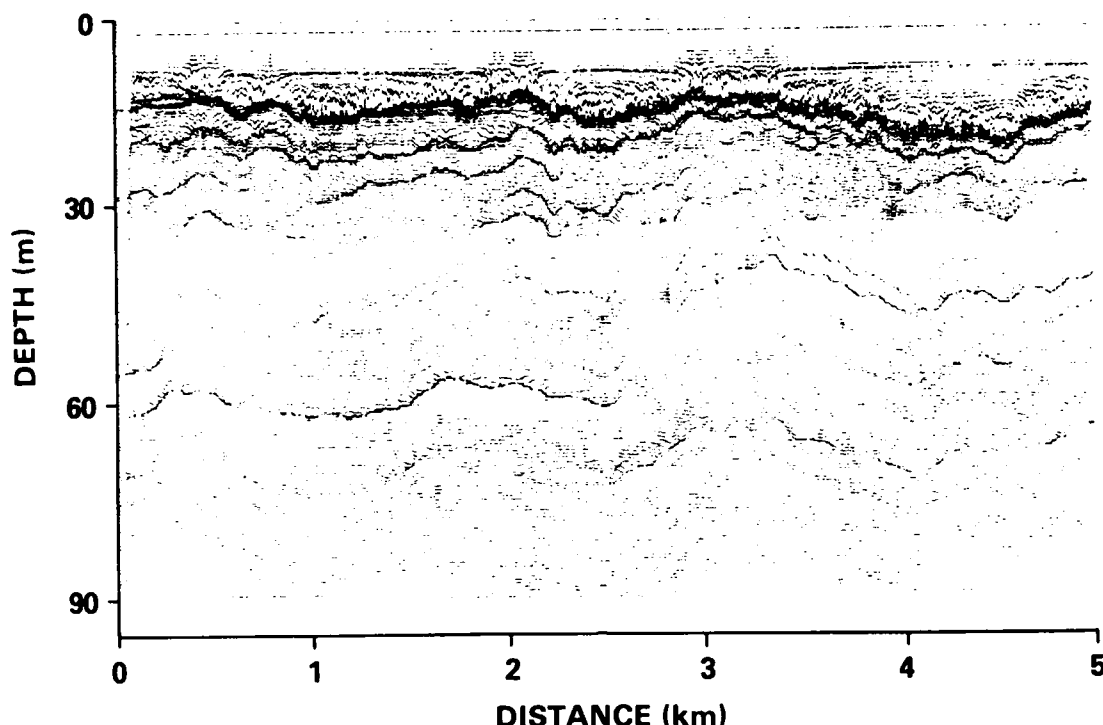
Fig. 2. Raster plot of vertical temperature gradient from towed vertical array of sensors.

from the high vertical resolution sensors which are spaced 6 cm apart and embedded in the larger array. As may be seen, the temperature signals from this array are quite coherent except toward the right-hand side. There clearly is a patch of high energy in small wavelengths which is several hundred meters long and only several meters high. Even at 6-cm spacing, the temperature fluctuations are not fully resolved by this array.

SPECTRAL ANALYSIS

Sample horizontal spectra of the temperature fluctuations are shown in Figure 4. They span the scales from about 1 to 700 m and, on scales longer than about 25 m, they are quite similar and exhibit steep slopes. On smaller scales, the slopes flatten out considerably and the level varies significantly, with the higher ones occurring intermittently. Figure 5 exhibits spectra which have been ensemble averaged over a number of temperature sensors on a 140-km tow. There are 4 such spectra obtained over different tracks but in the same general area, and they are quite similar in level and shape. They exhibit slopes near -2 for scales longer than several hundred meters, they steepen to about -3 in the band from several hundred meters to about 25 m, and they flatten out to about -2 on
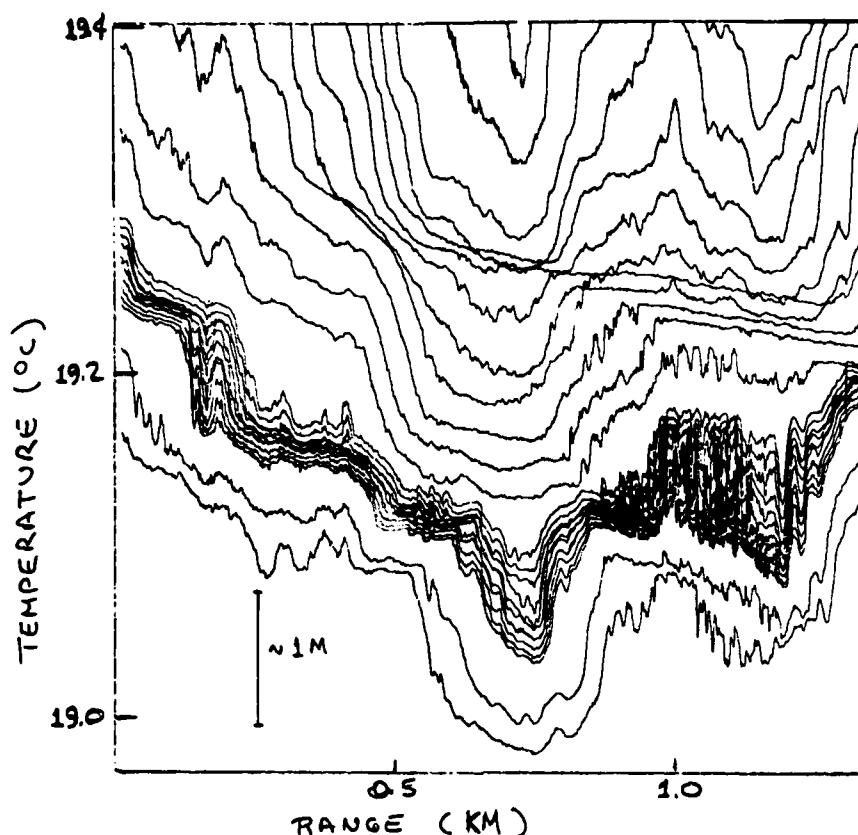
Fig. 3.   Plot of temperature from a high vertical resolution array
          of sensors.

the shorter scales. Except for a scale factor of about 20 or 30,
these three bands are similar to bands identified in vertical spectra
(eg. Gregg,1977). That is, the longest band has been called the internal
wave band, the middle one the band of decaying waves and fine structure,
and the shortest one the band of microstructure. This nomenclature
continues to make some sense. The longest band looks wavelike, and
200 m is about the length of the shortest waves which are coherent
across the seasonal layer. The intermediate scale has some shorter
wavelike events, but it is dominated by (nearly) horizontally coherent
layers which are wafted around by the waves. The resulting spectral
slope is steeper than -2, presumably because the steps are not sharp.
The shortest scale is made up of intermittent regions of high fluctua-
tion levels and, although they appear to be similar to dissipation or
mixing events, we are reluctant to label them microstructure because
the sensors do not actually resolve the scales over which dissipation
occurs. We have no explanation as to why the average spectra are
nearly -2 in slope.

56
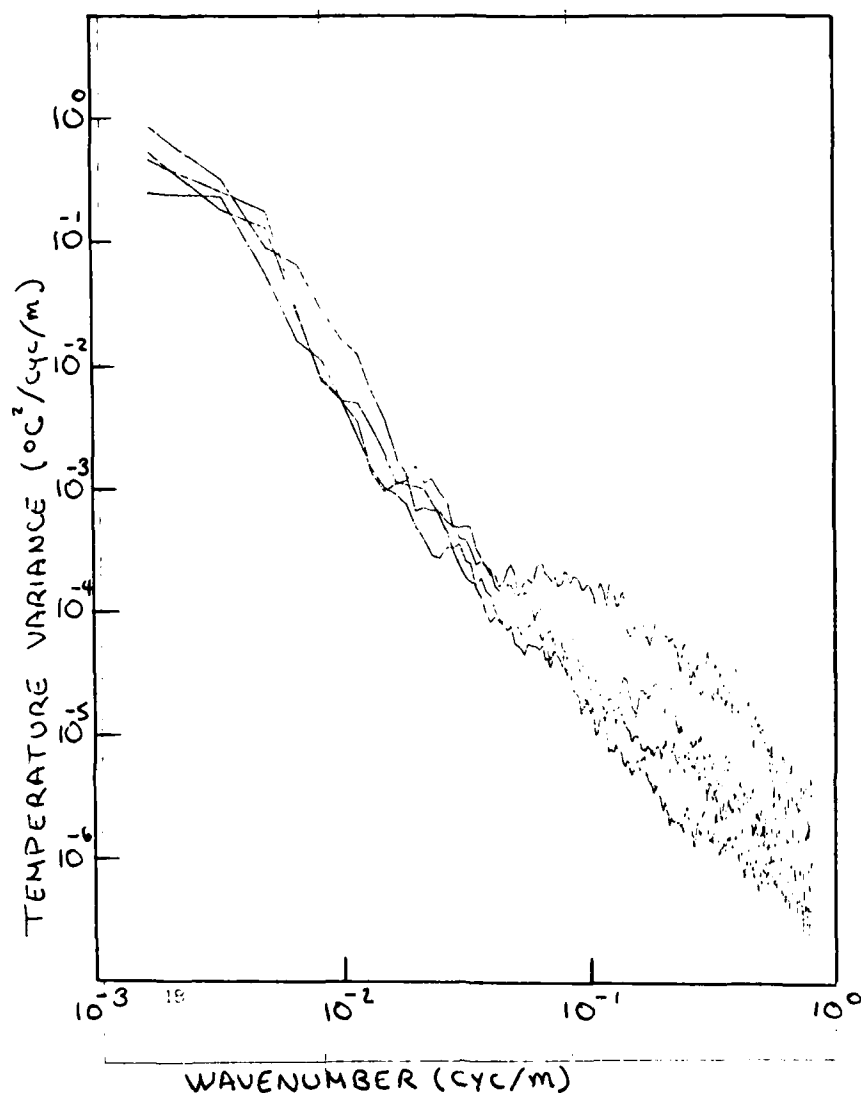
Fig. 4. Sample horizontal temperature spectra from towed sensors.

Actually, the variations in spectral level are as interesting as
the mean. Figure 6 is the ratio of the rms divided by the mean of
the spectral estimates. For normally distributed Fourier amplitudes
this statistic would be unity. It clearly approaches this for the
longest scales, but departs significantly from unity on scales less
than about 25 m. The magnitude provides a quantitative estimate of
the intermittence which occurs on these shorter scales.

We also have had occasion to measure scalar fluctuation levels
on smaller wavelengths. This has been done by using a towed con-
ductivity sensor and, although biological fouling is a major source
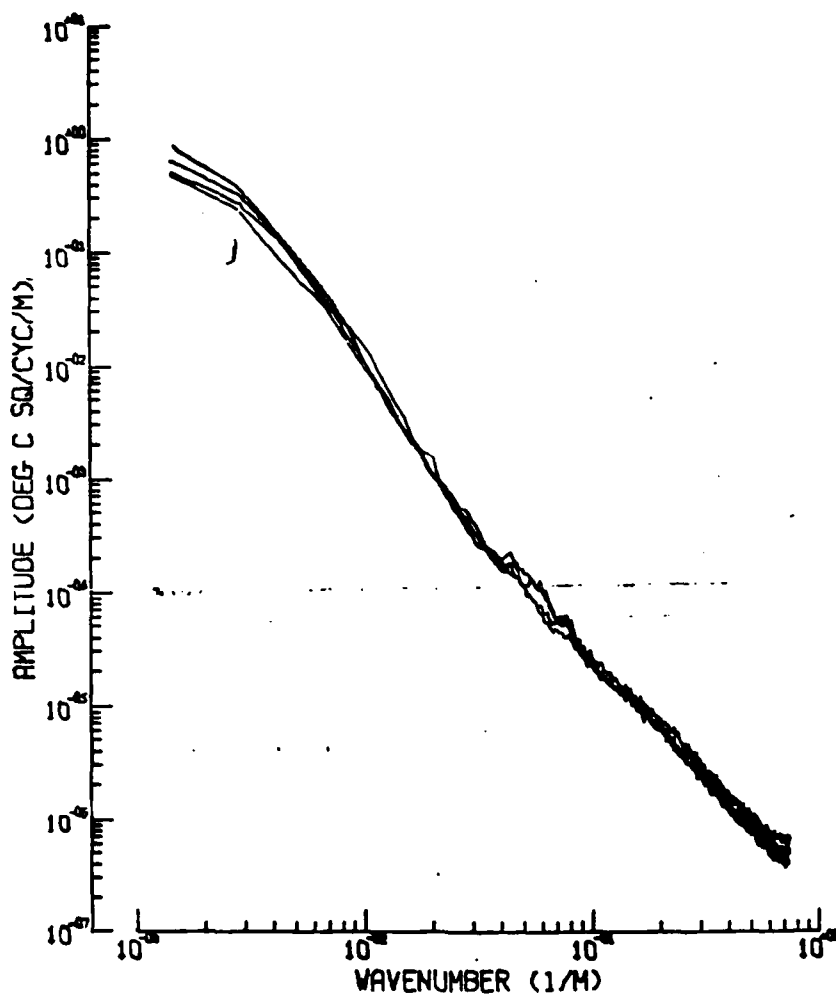
Fig. 5.   Mean horizontal displacement spectra from four 140-km tows.

of difficulty (eg. Okawa and Dugan,1984), preliminary results are
available. This has extended the bandwidth of the measurements to
about 1 cm and (no surprise) the fluctuations on this very small
scale are intermittent just as on the somewhat longer scale. We
are not prepared to review these results in great detail yet, but we
have constructed a composite spectrum which covers a wide range of
scales. Figure 7 is the composite spectrum; the amplitude has been
normalized by using estimates of potential energy, and the bandwidth
is from 1 cm to 2000 km. The potential energy is estimated by
$N^2\zeta^2$ where N is an estimate of the local buoyancy frequency and
ζ is an estimate of the vertical fluid displacement. (Estimates of
displacements are quite good on long scales, they are questionable on
scales down to tens of meters, and they are practically useless on
the smaller scales. We have studied several types of displacement
estimators and the results are interesting, but that is another
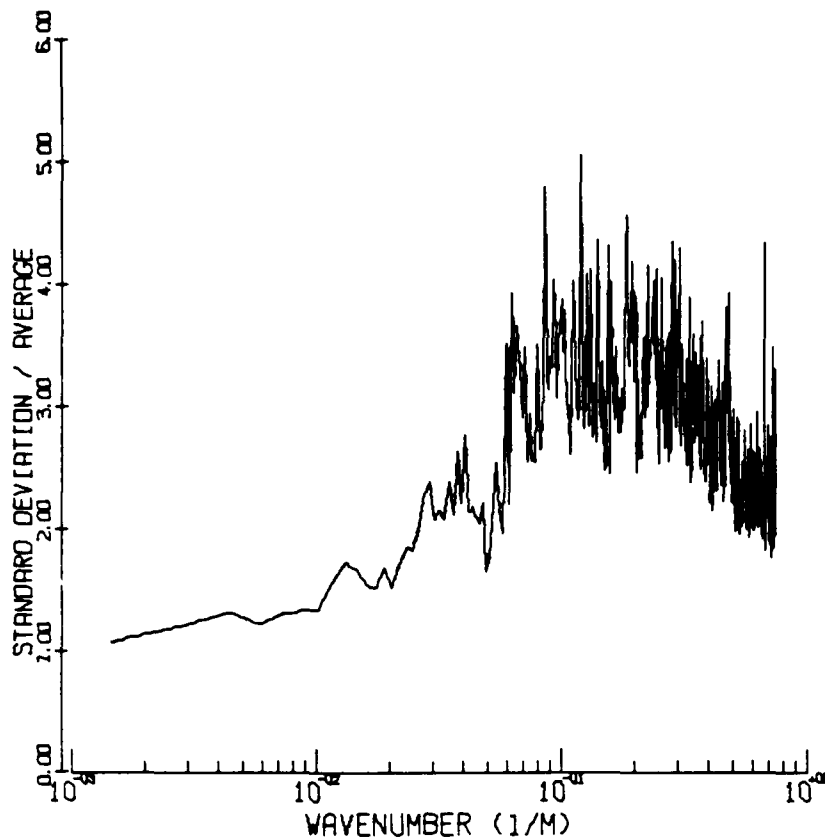
Fig. 6.   Ratio of rms to mean value of spectral estimates for a
140-km tow.

story.) The data sources for Figure 7 are varied, but all data for
scales less than several hundreds of meters are from either our towed
temperature or conductivity sensors. The wide range of levels which
occurs at any one wavelength is due to actual differences in energy
level seen in the data at that wavelength. Clearly, there are
level changes of about a decade on the mesoscale which are due to
the presence or absence of mesoscale features in the data. The
band from 50 km down to about 25 m shows much less variability in
level, and the shorter band exhibits very large changes in level.
These latter changes in level correlate with the presence or
absence of the intermittent small scale patches. A -2 line is
drawn through the data for your amusement. It is not a bad estimate
of the wavenumber distribution of energy over these many decades,
although the deviations from it clearly are significant. There are
local "excesses" in energy at all times near 1 km, and on the
meso- and micro-scales in the the presence of significant features.

The two-dimensional nature of the towed thermistor array data
is shown in Figure 8. This is the towed vertical coherence, and
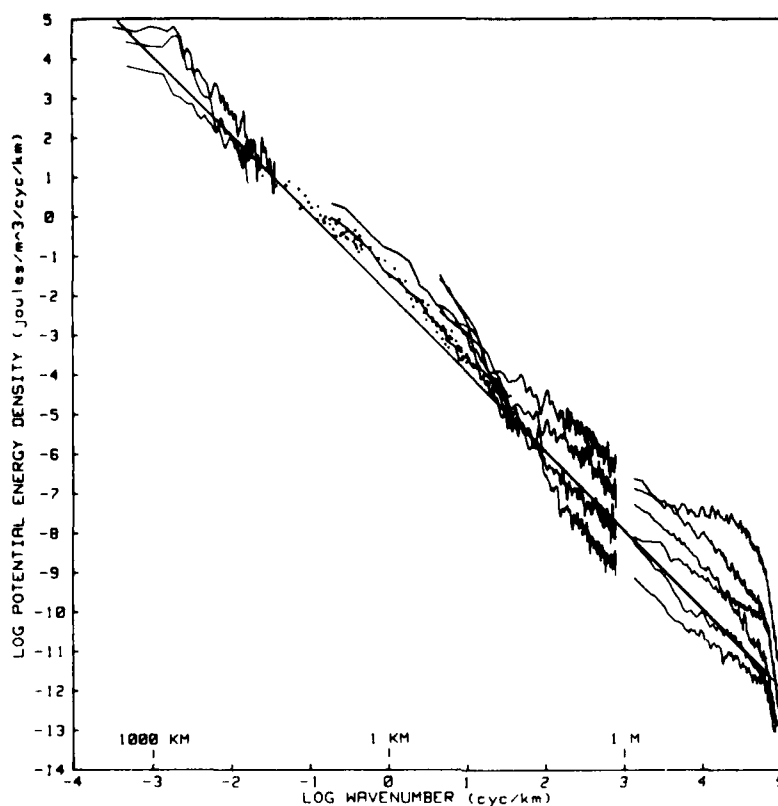
Fig. 7.   Composite plot of horizontal distribution of potential energy.

estimates have been calculated for sensor spacing from 6 cm to 50 m.
The black dots are the half-squared coherence level and the two
solid lines represent the 0.3 and 0.7 levels. Thus, the top right
of the diagram represents low coherence and the bottom left repre-
sents high coherence. Previous results are indicated and, although
no buoyancy frequency scaling has been applied to the data, the
agreement is quite good. (Note that some of the previous results
were for half-amplitude level or 0.25-squared coherence level.)
The diagonal on the plot from top left to bottom right represents a
horizontal to vertical scale ratio of 100:1, and this ratio is a
reasonable approximation of the half-squared coherence level for
the longer scales. This ratio changes at about 25 m or so and, at
the shortest scale resolved, the ratio is decreased to about 20:1.
Thus, even though this is an average estimator which does not
account for the differences between patches or their surroundings,
the shorter scales are more isotropic than the longer ones.

PATCH STATISTICS

     The temperature cross sections obtained with the array con-
tain more information on the two-dimensional structure than
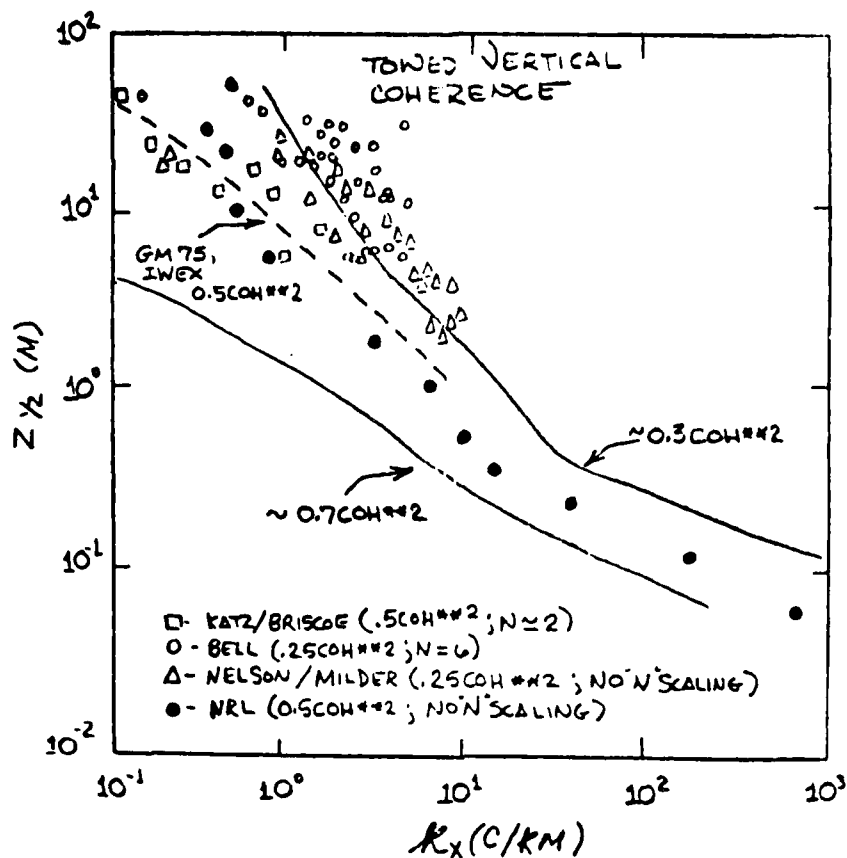
Fig. 8. Towed vertical coherence calculated from vertical array data.

exhibited above. This is due to the red nature of the spectra, which causes the smaller scale fluctuations to be overwhelmed by the more energetic fluctuations on longer scales. In this section, we will exhibit the structure of the small scale patches. In order to do this, the data are high-pass filtered in the horizontal to remove the longer wavelength fluctuations. The cutoff wavelength is chosen to be 10 m, and the rms level of the residual fluctuations is calculated in 50-m windows for each sensor. Histograms of the rms level reveal that the distribution is skewed. If the temperature fluctuations were normally distributed, these distributions should be Rayleigh. They have too long a tail, and taking the logarithm of the level shows it to be approximately log normally distributed (Figure 9). This is rather interesting because it provides an estimator for infrequent though energetic events. On the other hand, it provides no new physical insight.

Figure 10 is a 30-m-high by 5-km-long section of ocean in which the rms levels have been contoured. Actually, the levels have been normalized by the mean level on each sensor, so the first contour level (set at 1.3) encloses regions having a level 30% above the
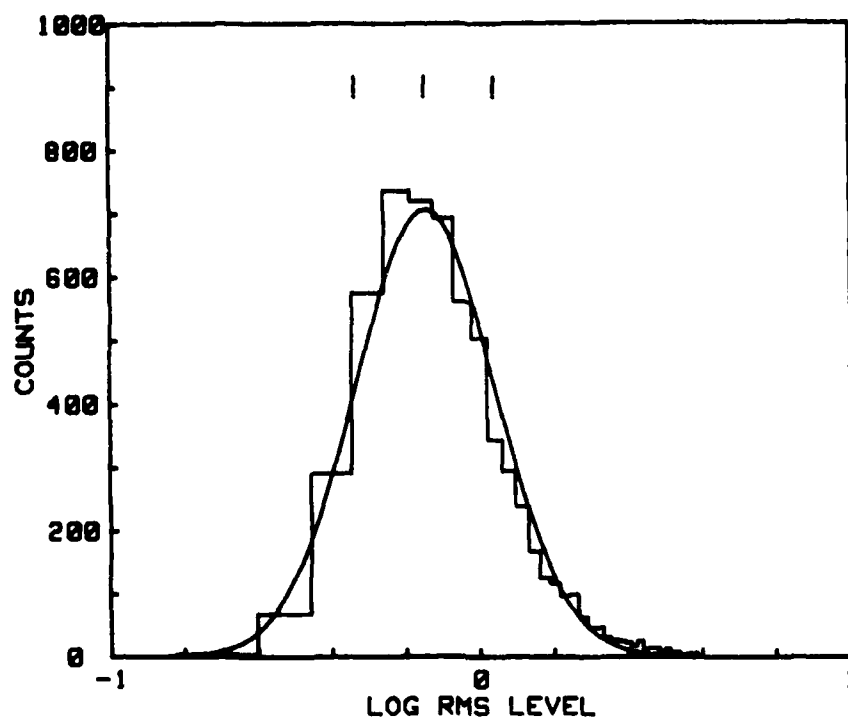
Fig. 9.   Histogram of log rms temperature fluctuations on small
          horizontal scales.
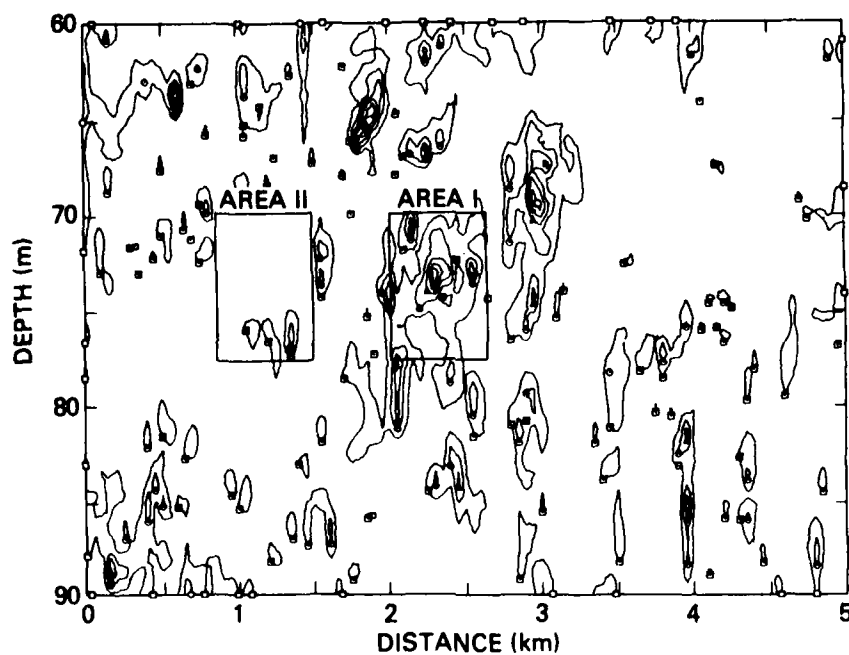
Fig. 10.   Contours of rms activity in temperature section.

62
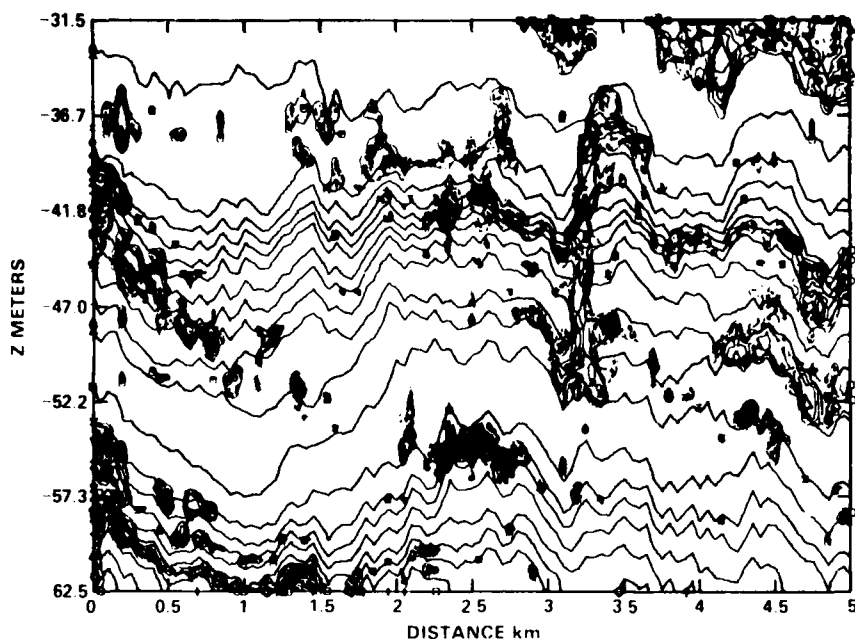
Fig. 11. Another example of contours of rms activity in temperature
          section. In this case, rms level is on grey scale, and
          lines represent isotherms.

mean. The second contour is 130% above the mean and so on. This
plot is nteresting because it shows that the energetic regions are
in fact clustered in "patches". Some statistics of these patches
have been accumulated, and it seems that they come in all sizes and
shapes, with some tendency to have a ratio of length to height of
about 100:1. For what it is worth, the ratio of buoyancy to
inertial frequencies in this vicinity also was nearly 100:1. The
region of Area I in Figure 10 was less stratified than the surround-
ings but the region of the large patch above and to the right of
this exhibited nothing obviously different from the remainder of the
section.

     Figure 11 is another cross section, but in this case, the con-
tour levels have been grey scaled and have been superimposed on the
local isotherms. This plot is interesting because it seems to exhibit
two different types of features. On the lower left and middle right,
the patches more or less align with the isotherms. On the other
hand, the 15-m-high patch just to the right of the middle crosses
over a number of isotherms. To understand these differences, it is
necessary to have other information in addition to the temperature
field.

CONCLUSIONS

Towed scalar data and simple statistics have been exhibited.
Towed spectra are similar in form to vertical spectra, and exam-
ination of the two-dimensional data leads to the identification of
three bands; ie, internal waves, finestructure, and microstructure.
The shortest band, although termed micro, exhibits intermittence in
the form of patches which have elevated spectra out to wavelengths
of about 20 m. Using displacement scaling, and specifically
potential energy scaling, the fluctuation levels on the small scale
blend in very nicely with longer scale internal waves and the meso-
scale. The small scales exhibit log normal statistics and the patch
widths tend to be the order of 100 times the heights.

This effort discussed here clearly has been one of quantifying
the temperature variability. The more interesting questions about
the processes responsible for these features and the anatomy of
particular ones are just now being asked of the data. To make sig-
nificant progress, though, it is clear that other parameters such as
the local density ratio and Richardson number are necessary pieces of
information, and future experiments should include these additional
measurements.

ACKNOWLEDGMENT

This presentation synopsizes the work of many of my colleagues
at NRL. A number of people have been responsible for build-
ing and maintaining the systems used to acquire the data and Bill
Morris, Benn Okawa, and Arnim Schuetz have in addition been
productive in processing it. My many thanks to them.

REFERENCES

Cairns, J.L., 1980: Variability in the Gulf of Cadiz: internal
waves and globs. J. Phys. Oceanogr. 10, 579-595.

Dugan, J.P., W.D. Morris, B.S. Okawa, E.E. Rudd, and B.W. Stalcup,
1980: Motion stabilization for towed oceanographic sensors.
Marine Technology '80, Wash. D.C., Oct 1980; proceedings,
529-534.

Dugan, J.P., B.S. Okawa, and W.D. Morris, 1984: Horizontal
distribution of potential energy in the ocean (submitted).

Gargett, A.E., 1975: Horizontal coherence of oceanic temperature
structure. Deep-Sea Res. 22, 767-776.

Gregg, M.C., 1977: Variations in intensity of small-scale mixing
in the main thermocline. J. Phys. Oceanogr. 7, 436-454.

Gregg, M.C., 1980: The three-dimensional mapping of a small
thermocline intrusion. J. Phys. Oceanogr. 10, 1468-1492.

64

Morris, W.D., J.P. Dugan, B.S. Okawa, C.W. Martz, and E.E. Rudd,
    1983: Towed thermistor system for marine research. IEEE Symp.
    on Oceanogr. Data Systems, Woods Hole, Oct 1983; Proceedings,
    147-153.

Okawa, B.S. and J.P. Dugan, 1984: Contamination of conductivity
    measurements by waterborne particles. Ocean Engng. (in press).

THE TRANSITION FROM KELVIN-HELMHOLTZ INSTABILITY TO TURBULENCE

By S.A. Thorpe

Institute of Oceanographic Sciences,
Brook Road, Wormley, Godalming, Surrey, GU8 5UB, UK

ABSTRACT

Using existing laboratory data and criteria proposed by Gibson (1982),
we find that Kelvin-Helmholtz billows observed in the ocean and in
lakes should lead to motions which are actively turbulent. Recent
laboratory experiments have revealed organised secondary structures in
developed billows. The side walls of the apparatus are, however,
significant generators of small scale motions or turbulence, and their
importance in the estimates of energy partition by K-H billows should
be reviewed.

1. INTRODUCTION

Of all the areas of fluid dynamics which related directly to processes
in the ocean, arguably the most exciting, important, and poorly
understood are those related to the onset of turbulence. I have in
mind particularly those phenomena which occur during transition and
which produce organised patterns of motion or density some of which
seem to survive and appear as large coherent structures in turbulent
flows. These are notoriously difficult to identify from measurements
at discrete points or from single profiles (Brown and Roshko, 1974).

Except for the first transition or bifurcation, of a steady parallel,
stably stratified, shear flow due to Kelvin-Helmholtz (K-H)
instability, the conditions and manner in which this flow becomes

turbulent are at present unknown*. Vortex pairing, the amalgamation of neighbouring billows in pairs, occurs at sufficiently low values of the Richardson number which characterises the flow in which the billows grow (Koop and Browand, 1978) but does not lead to motion in the horizontal direction normal to the mean flow. In their description of the generation and onset of three-dimensional motions, existing reports of laboratory experiments are vague, inadequate and even, as we shall see, misleading. They produce no definite evidence of the nature of secondary instabilities within the structure of K-H billows, although it is within the billows that "turbulent" small-scale structures first seem to appear at a stage when static instability favouring convective motions has been reached.

Recent numerical studies of K-H billows by Klaassen and Peltier (1984), however, indicate that secondary instabilities do indeed result from gravitatioinal instability within the spiral structure of the billows, and take the form of convective rolls aligned with the mean flow.

We have made further laboratory experiments which are reported in section 3, but before describing these it is pertinent to review the observations of K-H billows and to consider the conditions in which they may lead to turbulence.

2. K-H BILLOWS IN OCEANS AND LAKES

The existence of K-H billows in the ocean was established by Woods (1968), direct observations of dye layers being made by divers. Mean temperature profiles were measured using thermistors and pellets of dye were used to measure velocities. The shear leading to instability was induced by internal waves. Woods and Wiley (1972) claimed that billow turbulence is the principal mechanism for vertical mixing in the ocean, although doubts have since been cast on this claim (e.g. Gregg, 1980). The apparent absence of evidence of active turbulence in microstructure profiles (Gibson, 1982) is a connected problem to which we shall return. Observations of K-H billows have also been made in Loch Ness in much the same parameter regime as that in the ocean. Measurements were made by arrays of thermistors and a profiling current meter. The bravest and most ambitous attempts to make equivalent measurements in the ocean were those of Eriksen (1978). These demonstrated that periods when the gradient Richardson

---

* We should not be too surprised! Thermal convection between parallel plates and Couette flow between circular cylinders have been far more thoroughly studied and, after more than 50 years, are still not fully understood and continue to be active areas of research.

number, Ri, is less than $1/4$ are rare, although inversions in temperature are sometimes found to be associated with their occurrence. The experiments, however, failed to resolve adequately either the mean shear (observations limited to differences over 7m in the vertical) or temperature field (observations every 40s at 1m spacing) and did not provide positive identification of any K-H billows. Gregg (1980) has reported signatures in vertical profiles of temperature microstructure resembling those which might be produced by billows, but simultaneous information about the development of the billows in time is lacking.

Figure 1 shows the parameters of K-H billows for those observations which have sufficient information to define them. The value J is the minimum gradient Richardson number at the onset of instability, and Re is the Reynolds number;

$$J = \frac{g\Delta h}{u^2} \quad \text{and} \quad Re = \frac{uh}{v} \tag{1}$$

where 2u is the difference in speed across the interface (or 'sheet' in Woods terminology) of thickness 2h on which the billows are growing. The other symbols represent the fractional density difference (Δ), the acceleration due to gravity (g), and the kinematic viscosity (v). We have had to make some assumptions to determine these values, the most doubtful being that the maximum slope of the billows is related to J according to laboratory observations (Thorpe, 1973; fig. 3). It is interesting that the Reynolds numbers are not very high and that the Richardson numbers are not far below that at which instability might first occur $(J=1/4)$. The data set is however a very limited one, being biased towards those events which could be adequately resolved by the observational techniques or recognised by the observers, and may not be typical. In particular, none is at great depth and all occur on 'sheets'. Secondary instabilities in the billows themselves have not been identified, although temperature records there show the presence of rapid (or small-scale) fluctuations (e.g. Thorpe, 1978a; fig. 2a).

Is the motion produced by these billows likely to be turbulent? If we adopt the criteria proposed by Gibson (1982) based on laboratory measurements by Stillinger et al. (1983), the ratio of the Ozmidov length $(\epsilon^{1/2}/N^{3}/2)$ to the Kolmogorov scale $(v^{3}/\epsilon)^{1/4}$ must exceed 11.0, or

$$\frac{\epsilon}{N^2 v} > 24.5 \tag{2}$$
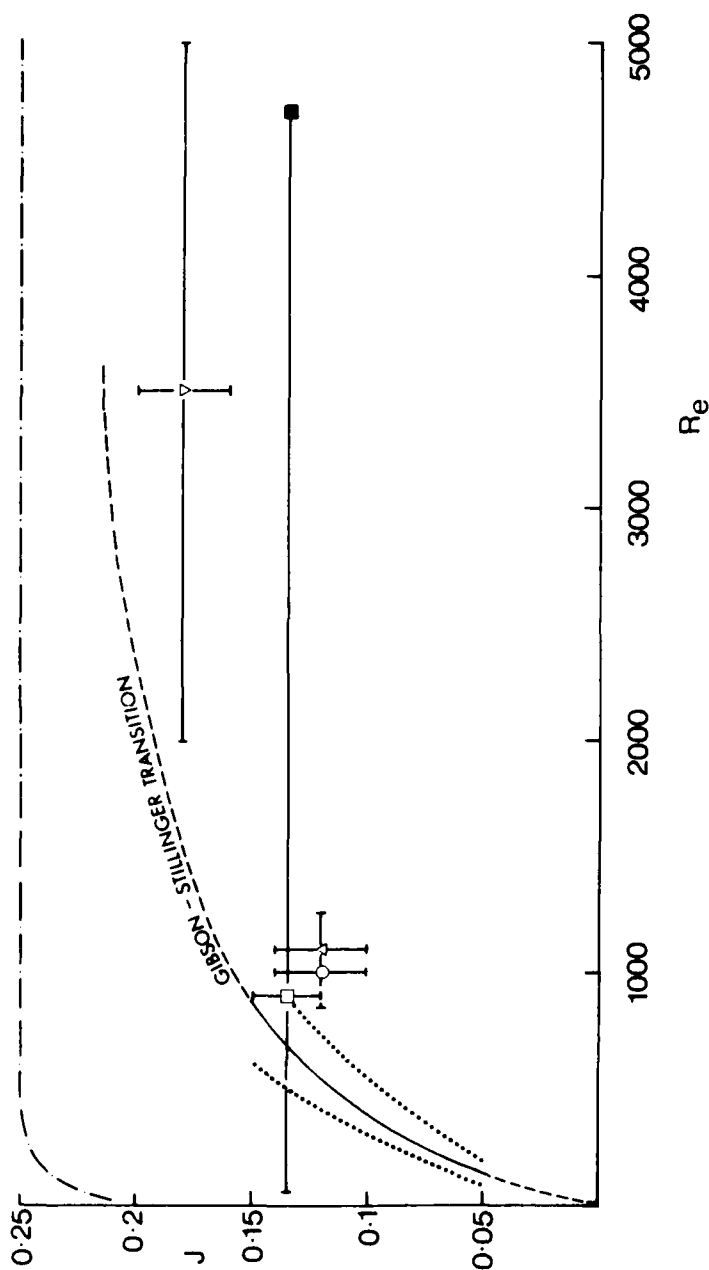
Fig. 1. Estimated values of parameters (Re vs. J) of billows occurring in Loch Ness and the ocean. □ marks 'typical' billows reported by Woods (1968) in the Mediterranean seasonal thermocline. The horizontal and vertical lines indicate the range over which billows are observed and the uncertainty in the estimated value of J. The black square marks an 'exceptionally large billow'. O, △ and ▽ mark billows in Loch Ness reported by Thorpe and Hall (1974), Thorpe et al. (1977), and Thorpe (1978a), respectively. The bars represent the uncertainty in the estimated values. The wavelengths of the observed billows are □ : 0.75m; ■ : 2.5m; O : 3m; △ : 2.7m; ▽ : 26.5m. The curve labelled 'Gibson-Stillinger transition' is that given by equality in equation 5, the dashed parts being beyond the range of its (empirical) validity. The dotted lines represent errors derived from the uncertainty in equation (3). Motion derived from billows in a flow with (Re,J) to the right of the curve are turbulent. The curve marked with dots and dashes marks the stability boundary for infinitesimal disturbances for a flow with hyperbolic tangent profiles of velocity and density.

Now the energy dissipated by K-H billows was estimated empirically from laboratory experiments by Thorpe (1973). The billows collapsed to form a state of quasi-parallel laminar flow in a time $\tau=12u/g\Delta$ with a mean loss of energy per unit horizontal area of

$$E = \frac{\rho_o u^4}{g\Delta}(0.25-J\pm0.025) \qquad (3)$$

in $0.045 < J < 0.15$; the standard deviation is given. The rate of loss of energy per unit mass is thus

$$\bar{\epsilon} = \frac{E}{H\tau\rho_o} \qquad (4)$$

where H is the thickness of the layer in which fine-scale motions occur, which is given by $N^2=2g\Delta/H$. Combining (2) (3) and (4) and using (1), we conclude that active turbulence should be produced provided that

$$Re > \frac{588\ J}{(0.25-J\pm0.025)} \qquad (5)$$

This is shown in figure 1. Turbulence can be expected at points below the curve. The majority of the observed billows appear to satisfy (5) although only marginally, and according to the criterion, the motion should therefore be turbulent for some part of the transition.

The weakest points in this argument lie in the uncertainty of the points in the (Re,J) plane and in the assumptions leading to (2) and (3). Is the value of the constant in (2) appropriate? It is determined in laboratory experiments in conditions of overall Richardson number which do not extend to those at which K-H billows occur. The observations in section 3 cast doubt on the validity of (3).

We are thus left

   (a) needing more observations in the ocean to define the nature (evolution, structure, intermittency and local flow conditions) of microstructure of whatever form

and   (b) needing more information about transition and turbulence in stratified shear flows.

The latter is probably best studied in the laboratory, and is the subject of section 3.

3. LABORATORY EXPERIMENTS

A full account of the experiments has been prepared for publication
(Thorpe, 1984) and only a brief description is given here.
Experiments were made in a tilting tube (see Thorpe, 1973) of internal
dimensions 10.2cm high, 30.5cm wide, and 5.48m in length. The width is
greater than in earlier tubes, and the top and bottom are perspex so
that the evolution of the billows can be viewed from above or below
using shadowgraph (see sketch in figure 2). Experiments were made
using brine (Prandtl number, $Pr=800$) and covered the range
$300 < Re < 1500$, $0.06 < J < 0.34$.
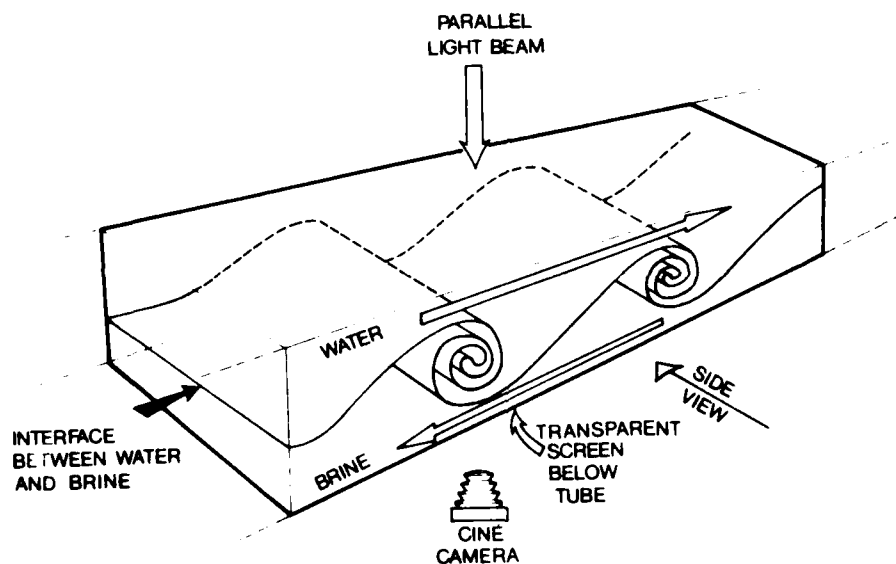
Fig. 2.   Sketch of the geometry of billows in the laboratory tube.
The shadowgraphs (fig. 3) are produced by shining a parallel beam of
light downwards through the tank onto a screen which is photographed
from below using a ciné camera.

Figure 3(a and b) are photographs from a cine film showing plan-view
shadowgraphs of two billows. The photographs show only the central
part of the tube and span only part of its full width. Regions of
unresolved fine-structure created by the presence of the tube walls
are seen at positions marked A. A view of the billows through the
side walls of the tube at this stage gives a false impression that the
whole of the billow is turbulent. The growth of secondaries in the
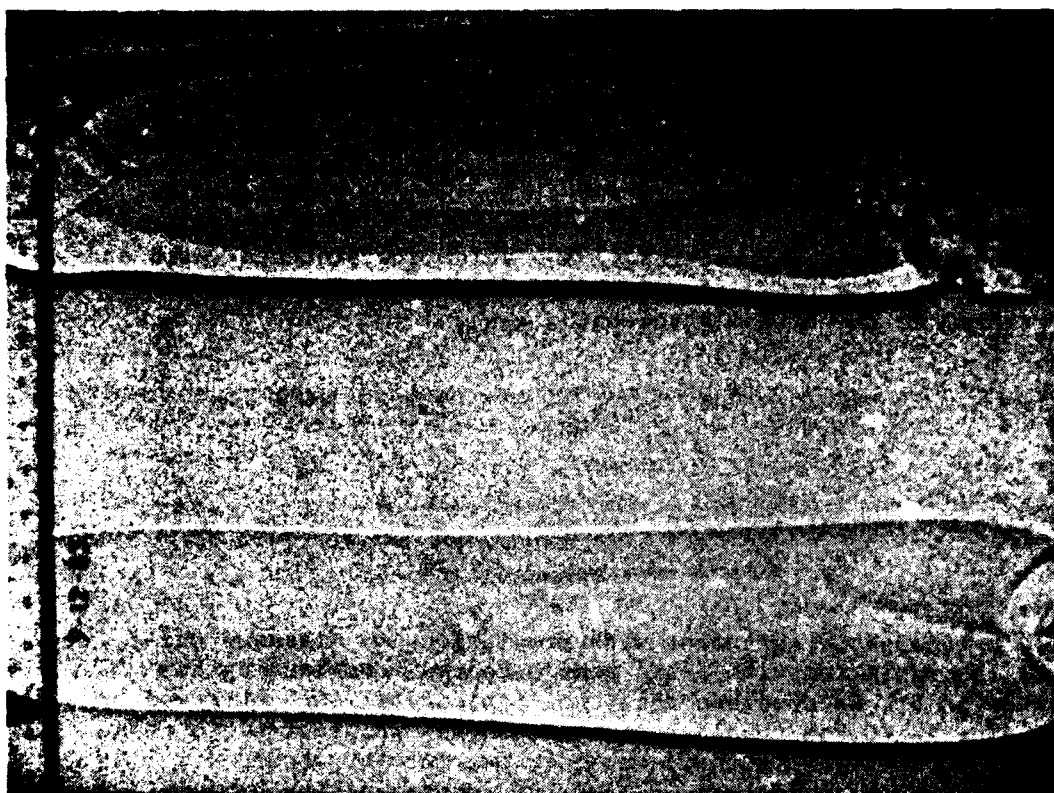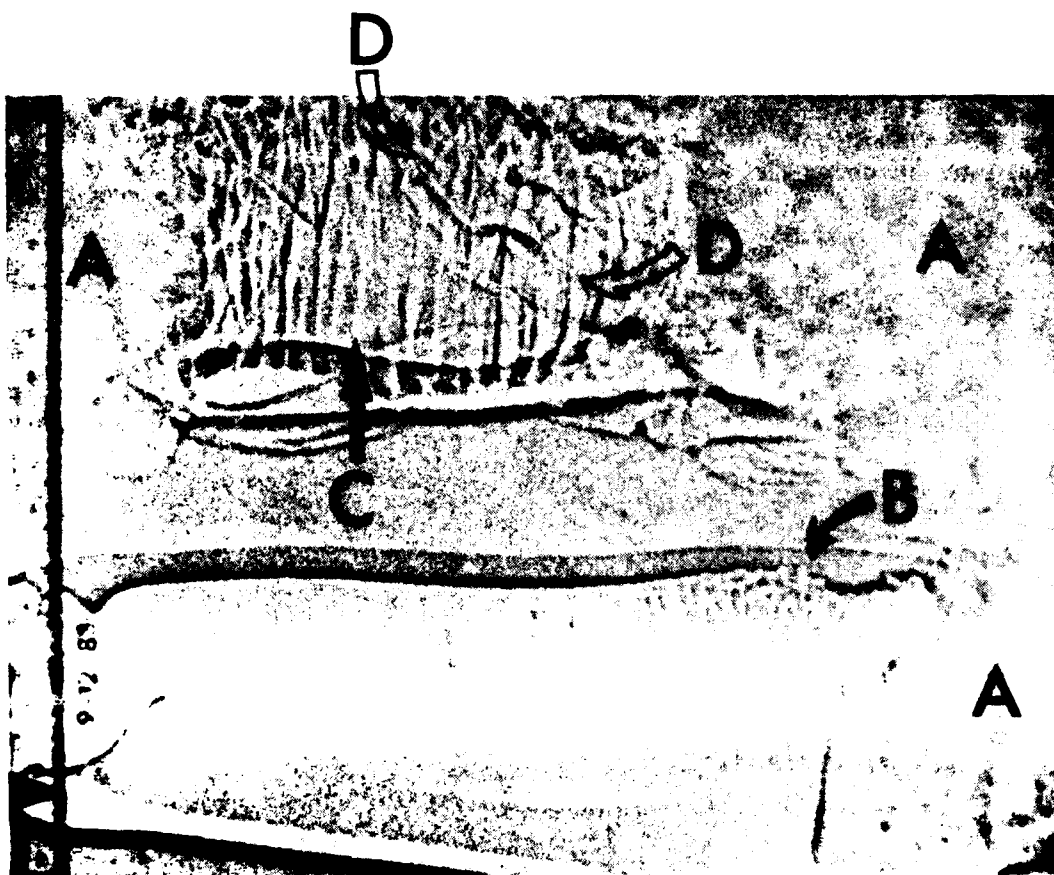
Fig. 3. Shadowgraphs showing two billows at Re=1160, J=0.18. The time between the two photographs (a) and (b) is 0.68s, approximately 0.7 T, where T is the stability period.

billows is visible at points marked B. These appear first at the
nearly vertical edges of the billows (i.e. at A and D in the sketch of
figure 4) well after the flow first becomes statically unstable, and
spread across the billows to form the predominently two-dimensional
pattern at C, figure 3. This pattern resembles the convective rolls
predicted by Klaassen and Peltier (1984), which are sketched (at B and
C) in figure 4. The ratio of twice their width, λ_c (the wavelength
of the rolls) to the billow wavelength, λ_{KH},

$$r = \lambda_c / \lambda_{KH} \qquad (6)$$

varies with Re approximately as

$$r = 28.4 \ (Re-100)^{-0.92} \qquad (7)$$

This is in reasonable agreement with predictions by Klaassen and
Peltier. No variation with J has been detected. Neglecting the
difference in Pr, we conclude that the 'typical billows' observed by
Woods having $\lambda_{KH}=0.75m$ should develop secondary rolls of width about
2 cm. The secondaries in the laboratory persist for about one
stability period, a time scale comparable to that of the billows
themselves before they are sheared and amalgamate.

Other secondary structures can also be seen (e.g. that at D-D in
figure 3b). Because of the turbulence generated at the side walls and
by other instabilities in which neighbouring billows interact with
each other, we have not as yet been able to follow the development of
the roll-like secondary structures though their full cycle.
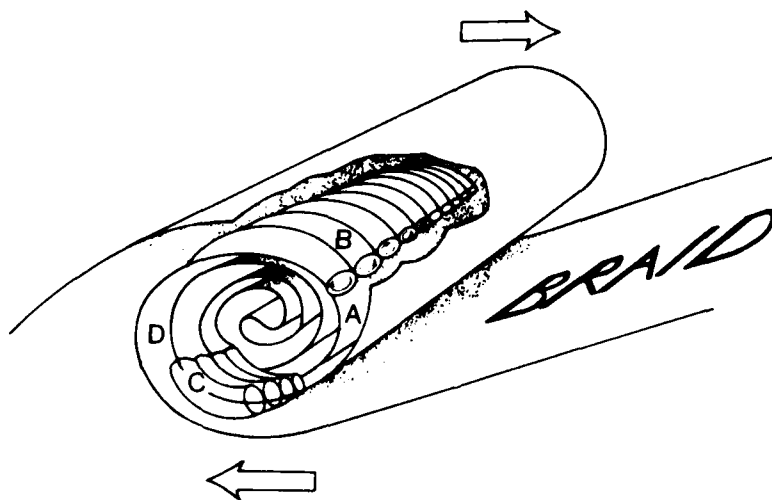
Fig. 4.   Sketch showing convective rolls (at B and C) in a K-H
billow.   The arrows mark the direction of the relative flow and
circulation in the rolls.

4. CONCLUSIONS

    (i)   Earlier observers (Thorpe, 1973; Koop and Browand, 1979)
            may have erroneously interpreted the occurrence of
            small-scale structures caused by the side walls of their
            apparatus as the onset of billow-generated turbulence.

    (ii)   Side wall-generated turbulence may effect the energy
            balance (equation 3) and the return to laminar flow in a
            way not presently known. In particular if, as seems
            likely, equation 3 overestimates the energy dissipated by
            the billows (that is if a significant amount of energy is
            dissipated in well-generated turbulence), the factor 588
            appearing in (5) will be increased and the
            Gibson-Stillinger transition curve in figure 1 will be
            shifted downwards. The observed billows would then be less
            likely to generate turbulent motion in the sense proposed
            by Gibson. Earlier estimates of the fraction of kinetic
            energy transferred to potential energy by billow turbulence
            should be treated with caution.

    (iii)   Secondary instabilities have a form and scale, and occur
            during the evolution of the billows at a time, in general
            accordance with the predictions of Klaassen and Peltier, in
            spite of a difference in Pr. (The numerical studies were
            at Pr=1, laboratory at Pr=800).

    (iv)   The lifetime of secondaries is about one stability period.
            The transition to turbulence is thus not a fast or
            explosive event, but is slow.

    (v)   The occurrence of secondary structures with scales similar
            to those of salt fingers (and similarly aligned in a mean
            flow; Linden,1974) should be taken into account when
            interpreting horizontal tows of microstructure sensors.

    (vi)   The billows and secondaries contain points at which the
            density gradient is zero. It has been suggested that the
            presence of such zero gradient points is evidence of
            isotropic turbulence, past or present (Gibson, 1982).
            However, the motion is not turbulent and has not been
            turbulent, it is not isotropic, and the microstructure is
            not fossil turbulence. The interpretation of features in
            microstructure records as fossils shoud be revised, and the
            classification of microstructure as active turbulence or
            fossil turbulence needs to be extended to include
            transitional features which may, or perhaps may not, lead
            to active turbulence.

74

Organised patterns of convective instability are likely to occur as
secondary stages of transition to turbulence in other phenomena,
notably in internal wave breaking in shear flows (Thorpe, 1978b,c, and
1981), and these deserve more study.

REFERENCES

Brown, G.L. and A. Roshko 1974: On density effects and large
    structure in turbulent mixing layers. J. Fluid Mech. 64,
    775-816.

Eriksen, C.C., 1978: Measurements and models of fine structure,
    internal gravity waves, and wave breaking in the deep ocean.
    J. Geophys. Res. 83(C6), 2989-3009.

Gibson, C.H., 1982: Alternative interpretations for microstructure
    patches in the thermocline. J. Phys. Oceanog. 12, 374-383.

Gregg, M.C., 1980: Microstructure patches in the thermocline. J.
    Phys. Oceanogr. 10, 915-943.

Klaassen, G.P. and W.R. Peltier, 1984: The onset of turbulence in
    finite amplitude Kelvin-Helmholtz billows (submitted for
    publication, 1983).

Koop, C.G. and F.K. Browand, 1978: Instability and turbulence in a
    stratified shear flow with shear. J. Fluid Mech., 93, 135-159.

Linden, P.F., 1974: Salt fingers in a steady shear flow. Geophys.
    Fluid Dyn. 6, 1-27.

Stillinger, D.C., K.N. Helland. and C.N. Van Atta, 1983: Experiments
    on the transition of homogeneous turbulence to internal waves in
    a stratified fluid. J. Fluid Mech. 131, 91-122.

Thorpe, S.A., 1973: Experiments on instability and turbulence in a
    stratified shear flow. J. Fluid Mech. 61, 731-751.

Thorpe, S.A., 1978a: The near-surface ocean mixing layer in stable
    heating conditions. J. Geophys. Res. 83(C6), 2875-2885.

Thorpe, S.A., 1978b: On the shape and breaking of finite amplitude
    internal gravity waves in a shear flow. J. Fluid Mech. 85,
    7-31.

Thorpe, S.A., 1978c: On internal gravity waves in an accelerating
    shear flow. J. Fluid Mech. 88, 623-639.

Thorpe, S.A., 1981: An experimental study of critical layers. J.
    Fluid Mech. 103, 321-344.

Thorpe, S.A., 1984: Laboratory observations of secondary structures
    in Kelvin-Helmholtz billows (prepared for submission).

76

Thorpe, S.A. and A.J. Hall, 1974: Evidence of Kelvin-Helmholtz billows in Loch Ness. *Limnology and Oceanography* 19, 973-976.

Thorpe, S.A., A.J. Hall, C. Taylor and J. Allen, 1977: Billows in Loch Ness. *Deep Sea Res.* 24, 371-379.

Woods, J.D., 1968: Wave induced shear instablity in the summer thermocline. *J. Fluid Mech.* 32, 791-800.

Woods, J.D. and R.L. Wiley, 1972: Billow turbulent and ocean microstructure. *Deep-Sea Res.* 19, 87-121.

INTERNAL WAVES AND MIXING IN THE OCEAN: OBSERVATIONS AND SPECULATIONS

Ann E. Gargett

Institute of Ocean Sciences, Patricia Bay
P.O. Box 6000
Sidney, B.C., Canada   V8L 4B2

ABSTRACT

This paper offers a personal view of the observational basis for our limited understanding of connections between internal waves and diapycnal mixing. Emphasis is on specific areas where observations and/or theory will most advance such understanding.

1. INTRODUCTION

Advances in velocity measurements over the last decade have begun to reveal something of the boundary between those fluctuating velocities which are dominantly wavelike, ie. which propagate and are effectively non-dissipative, and those non-propagating, highly dissipative motions which may more properly be considered turbulence. It has become clear that in the stratified interior of the ocean, disruption of density surfaces and generation of turbulence is sporadic in both space and time and, moreover, occurs at vertical scales not very much larger than those scales at which energy is dissipated. The first characteristic has implications for the amount of data necessary for meaningful "average" turbulent quantities, while the second implies that the connection between internal waves and turbulence is an intimate one. In dealing with the boundary between waves and turbulence in the stratified ocean, we cannot take refuge in either linear internal wave theory or classical high Reynolds number turbulence theory. Stratified flow experiments in the laboratory may provide some guidance but frequently fail to achieve features which are significant in the oceanic case (e.g. appropriate values of Re, sporadic nature of breaking events, etc.). Thus it appears that we must work with oceanic data, however limited, and examine each type of measurement for clues to the nature of the wave/turbulence boundary. In the first part of this paper (Sec. 2) I will summarize some information of relevance to this region, emphasizing features which are of particular importance to subsequent discussion of a simple (-minded?) model which attempts to use part of

this information to predict the rest (Sec. 3). The excitement of such
a model lies in further predictions of various features which could be
tested by observation. Sec. 4 is a discussion of significant questions
raised by our present level of (mis-) understanding.

2. OBSERVATIONS OF RELEVANCE TO THE RELATIONSHIP BETWEEN INTERNAL WAVES AND TURBULENCE.

2.1 Vertical gradient spectra

The first observations of relevance to the wave/turbulence boundary
were those of Gregg (1977), who presented spectra ψ_s of vertical
temperature gradients over wavenumbers corresponding to scales from
hundreds of meters down to the centimeter range at which gradients are
erased by molecular effects. The ψ_s spectra varied approximately as k^0
at the lowest wavenumbers, change to k^{-1} above a wavenumber $k_0 \simeq 0.1$ cpm,
then rose again in microstructure "bumps" at dissipation scales. While
WKB scaling with N collapsed the k^0 and k^{-1} ranges, suggestive of
wave-induced gradients, it normalized neither the height of the
microscale "bump" nor the wavenumber at the minimum formed between this
"bump" and the k^{-1} range.

Because the velocity field contains the dynamics of flows, further
advances became possible when Gargett et al. (1981) presented similar
spectra ϕ_s of vertical shear of horizontal velocity, patched together
(with success that surprised the authors as much as anyone) from measure-
ments taken nearly simultaneously by three instruments. The
characteristics of these velocity gradient (shear) spectra were
amazingly similar to the temperature gradient spectra - a range of $\phi_s \sim$
k^0 between wavenumbers of ~ 0.01 cpm and $k_0 \simeq 0.1$ cpm, followed by a
roll-off as $\phi_s \sim k^{-1}$ to a shear spectral minimum beyond which rose
microscale "bumps" of varying heights. Over the limited range of
$N(\sim 1-3$ cph) sampled, WKB normalization was necessary to collapse the
low wavenumber k^0 range to a 'universal' level but was again
unsuccessful at high wavenumber normalization.

Further progress was possible because the high wavenumber shear
measurement allowed calculation of ϵ, the kinetic energy dissipation
rate (per unit mass), a turbulence parameter of fundamental importance
in determining overturning scale in a stratified fluid. Using arguments
dating back to Dougherty (1961) (and perhaps farther), Gargett et al.
demonstrated (Fig. 1) that the region of the shear spectral minimum,
dividing the high wavenumber dissipation range from lower wavenumbers,
was collapsed to "universal" values by scaling with buoyancy wavenumber

$$k_b \equiv \left(\frac{N^3}{\epsilon}\right)^{\frac{1}{2}} = \frac{2\pi}{\ell_b} \tag{1}$$

and an associated buoyancy velocity scale

$$u_b \equiv \left(\frac{\varepsilon}{N}\right)^{\frac{1}{2}} \tag{2}$$

(from which comes the scale of $\phi_b = (\varepsilon N)^{\frac{1}{2}}$ for shear spectral density used in Fig. 1). Although based at that time on very limited data, the relevance of the scales k_b and u_b has since been confirmed by more extensive measurements (Gargett, Osborn, and Nasmyth, 1984).
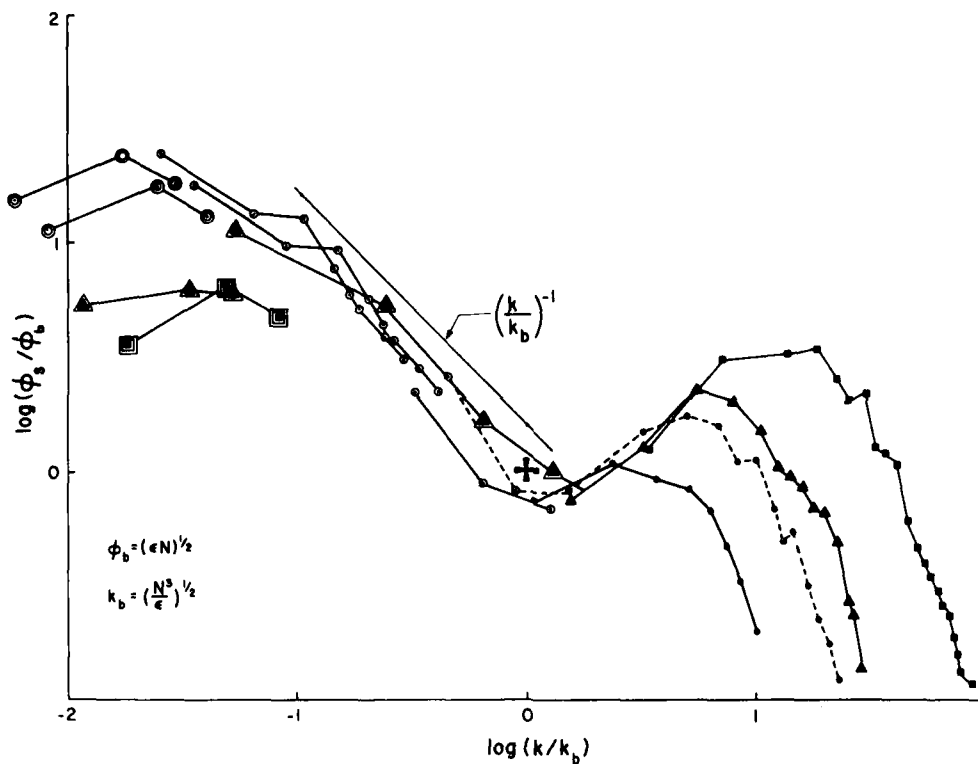
Fig. 1: Spectral densities of vertical shear of horizontal velocity, composited from measurements of three profilers, are here scaled by the buoyant turbulence scales $k_b \equiv (N^3/\varepsilon)^{\frac{1}{2}}$ and $\phi_b = (u_b^2 \, k_b)$ where $u_b \equiv (\varepsilon/N)^{\frac{1}{2}}$. Note that this scaling does not produce universal levels at the lowest wavenumbers (where internal wave motions scale only with N) or at the highest wavenumbers (where turbulence dissipation scales only with ε and molecular visocity ν), but does produce a universal shear spectral minimum near $\phi_s = \phi_b$, $k = k_b$.

A very significant result can now be deduced using only (i) the observed k^0 and k^{-1} spectral _shapes_ (not levels) below $k = k_b$ and (ii) the fact that the high wavenumber end of the k^{-1} range occurs at

(ϕ_b, k_b). Defining a scale-dependent Richardson function

$$Ri(\hat{k}) \equiv \frac{N^2}{\displaystyle\int_0^{\hat{k}} \phi_S(k)\,dk} \tag{3}$$

as the ratio of the mean square buoyancy frequency to the mean square shear resident in wavenumbers up to $\hat{k}$, these observational features alone imply that $Ri(k_o) = 1$, i.e. that the wavenumber k_o of the break-in-slope between k^0 and k^{-1} ranges of the shear spectrum is characterized by a near-unity Richardson function (Fig. 2). When in addition (iii) the level of the observed k^0 range WKB-scales with N, as suggested by the observations, the fact that $Ri(k_o) = 1$ implies that k_o must be a constant dimensional wavenumber, i.e. does not WKB-scale with N (Fig. 2).
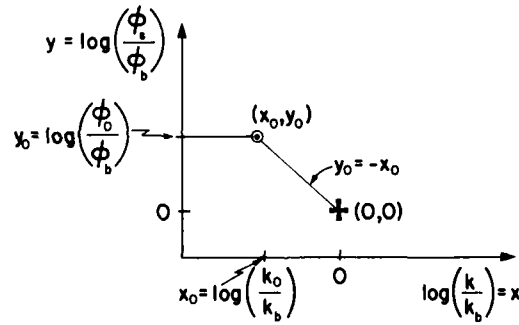
$$Ri(k_o) = \frac{N^2}{\displaystyle\int_0^{k_o} \phi_s\, dk} \simeq \frac{N^2}{\phi_o k_o}$$

$$Ri(k_o) = \frac{N^2}{\phi_o k_o} \times \frac{k_b}{k_b} = \left(\frac{N^2}{k_b}\right)\frac{k_b}{\phi_o k_o} = \frac{\phi_b}{\phi_o}\frac{k_b}{k_o} = \left(\frac{\phi_o}{\phi_b}\frac{k_o}{k_b}\right)^{-1} = 10^{-(y_o + x_o)} = 1$$

$$Ri(k_o) = \frac{N^2}{\phi_o k_o} = 1 \longleftrightarrow k_o = \text{constant } \underline{\text{dimensional}} \text{ wavenumber}$$

Fig. 2: Existence of a shear spectral minimum near $\phi_s = \phi_b$, $k = k_b$, coupled with the observed behaviour of the shear spectrum as a function of wavenumbers $k < k_b$, implies that the internal wave field maintains a near-constant Richardson-function $Ri(k_o) \sim O(1)$ at $k_o \sim O(0.1$ cpm).

The first conclusion, that Ri(k_O) $\sim$ 1, is an intuitively attractive one - it means that the internal wave field maintains its mean-square shear close enough to critical levels that increases would quickly lead to increased probability of "breaking", with rapid and irreversible transfer of excess energy to dissipation scales. Moreover, it is consistent with a condition in which the interaction time of non-resonant components ("turbulence" or "strongly nonlinear" waves?) becomes comparable to the (wave) period of resonant components ("weak" waves?) of a velocity field (Gargett et al., 1981). Further observational support for this criterion comes from E. D'Asaro (pers. comm., 1984) who calculates an average Richardson number of $\sim$ 2.5 using differences of horizontal velocity over 10 m: since a first-difference operator underestimates the mean-square shear used in eq. (3), this result seems in reasonable agreement with the prediction. The second prediction, that $k_O \simeq 0.1$ cpm independent of N, adds to the (observational) assumptions associated with Ri (k_O) $\sim$ 1 only our rather firmly established notion that low vertical wavenumbers behave (hence scale) as internal waves: despite this, it seems less intuitive. It has been interesting to find that both Evans (1982) and Toole and Hayes (1984) have obtained further evidence of a high wavenumber shear spectral cut-off at 0.1 cpm. However, neither measurement resolved the shear spectral minimum nor dissipation scales and, as well, the equatorial spectra appeared to fall as $\sim k^{-2}$ instead of k^{-1} above 0.1 cpm. It is not clear whether the simple arguments given above are inapplicable to internal waves in the relatively strong directional mean flows characteristic of equatorial regions or whether the k^{-1} slope is not a universal characteristic. The constancy of the spectral shape in the k^{-1} range and of the wavenumber k_O are important features to check in future observations.

2.2 Distribution of dissipation quantities

Other observations relevant to the connections between waves and turbulence are measurements of the rates of dissipation of potential energy (related to density or temperature) and of kinetic energy associated with the microscales of each field. Since Osborn and Cox (1972) first measured and interpreted temperature microscales, many people have contributed to the growing body of oceanic measurements of χ, the temperature variance dissipation rate. For our purpose, however, the most useful data set remains that of Gregg (1977), who measured χ values down to 1200-m depth on three cruises to the same mid-ocean site. Averages of one-dimensional Cox number Cx (usuallly associated with χ via the Osborn-Cox model) over two depth ranges show a distinct increase with depth (triangles in Fig. 3).

Routine measurement of velocity microscales, hence ε , became possible when Osborn and Siddon (1975) pioneered use of airfoil probes in the ocean. To date, much of the growing body of ε measurements comes from Osborn and his co-workers (Osborn, 1978; Crawford, and Osborn, 1979; Gargett and Osborn, 1981; Leuck, Crawford and Osborn, 1983; Moum, 1984). Cruise-averaged values of ε from a number of different sites and oceans are plotted in Fig. 4 as a function of averaged Väisälä frequency $\bar{N}$. As a

$$C_x \equiv \frac{\overline{(\partial T'/\partial z)^2}}{(\partial \overline{T}/\partial z)^2}$$
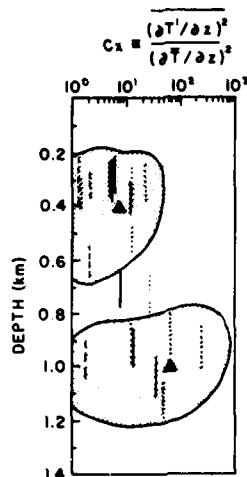
Fig. 3: Ensemble-averaged values of the one-dimensional Cox number Cx measured by Gregg (1977) in the course of three cruises to 28N, 155W.
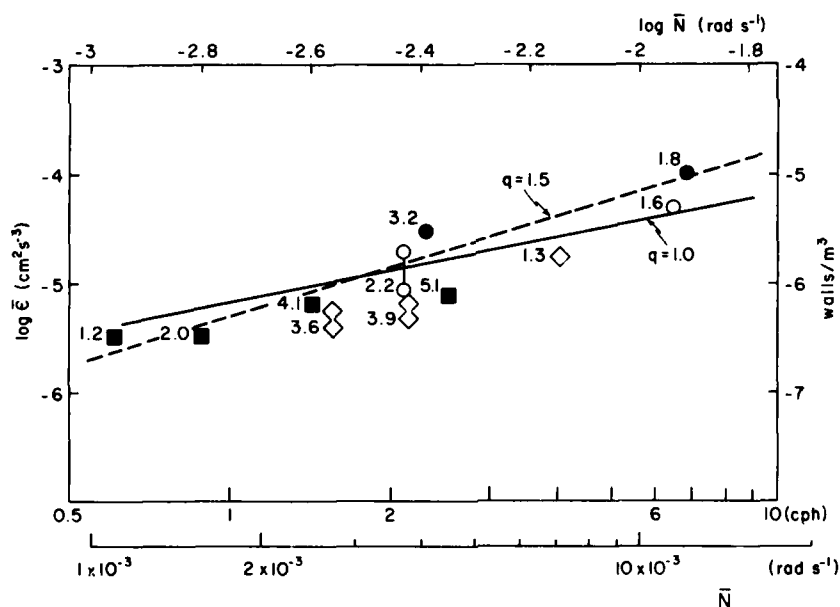
Fig. 4: Ensemble-averaged values of $\overline{\varepsilon}$, the rate of kinetic energy dissipation per unit mass, as a function of average Väisälä frequency $\overline{N}$. Data are from a variety of sources and locations: Gargett and Osborn (1981) from the Sargasso Sea near (dark circles) and far (open circles) from the island of Bermuda; Lueck, Crawford, and Osborn (1983) from the eastern boundary region of the North Pacific (triangles); Moum (1984) from the western North Pacific (squares). Straight lines are fits (by eye) to the form $\overline{\varepsilon} \propto \overline{N}^q$ for q = 1.0 and 1.5.

first order approximation, these varied measurements are described by a
relation of the form

$$\overline{\varepsilon} = a_o \, N^q$$

where $1 < q < 1.5$ and a_o (dependent upon choice of q) is approximately
constant (to the same factor (~ 2) generally understood to denote
constancy with respect to internal wave scalings). The evolution of this
diagram, as future data sets become available, will affect the evolution
of models, such as the one discussed in the following section, which
attempt to describe mechanisms by which such a connection may arise between
a turbulence quantity such as ε and the wave quantity N.

3. A SIMPLE MODEL

In recent work (Gargett and Holloway, 1984), Greg Holloway and I
tried to incorporate observed features of the oceanic shear spectrum
(Sec. 2.1) into a model which would predict observed relationships
between microscale and wave-scale parameters (Sec. 2.2). Our aim in
this has been to start the debate, rather than to have the last word;
nevertheless, we do feel that certain features of this model differ
from conventional ones in ways which, while subtle, are of considerable
importance to an appropriate description of the oceanic wave/turbulence
regime and must be taken seriously. Most radical is the decision that,
on the basis of the observed vertical wavenumber spectrum of horizontal
velocity (obtained by dividing the shear spectrum by k^2), there is no
basis for the normal Reynolds decomposition of the <u>velocity</u> field into
mean and turbulent parts. Relinquishing this assumption leads one onto
unfamiliar ground; we proceed from a time-averaged kinetic energy
equation <u>without</u> the Reynolds decomposition by assuming steady-state and
negligible contribution by either the pressure-velocity correlation or
the horizontal stress/shear terms. Finally, we assume that dissipative
("tubulent") processes are characterized by a small flux Richardson
number

$$R_f \equiv \frac{-g\rho_o^{-1} \, \overline{\rho w}}{\left(\overline{u_i w \, \frac{\partial u_i}{\partial z}}\right)} \ll 1,$$

defined in a way which differs from the more normal definition involving
$\overline{u_i w} \, \partial \overline{U}_i / \partial z$ in the denominator. With these assumptions, the steady-state
energy equation reduces to

$$-\left(\overline{u_i w \, \frac{\partial u_i}{\partial z}}\right) = \frac{\varepsilon}{1-R_f} \simeq \varepsilon \quad . \tag{4}$$

Formally expressing the triple correlation as a triple correlation coefficient T_1 times the square root of the product of the variances, we rewrite eq. 4 as

$$T_1 \left[\overline{u_i^2} \; \overline{w^2} \; \overline{\left(\frac{\partial u_i}{\partial z}\right)^2} \right]^{\frac{1}{2}} \simeq \varepsilon \; . \tag{5}$$

We now appeal to observations. The observed <u>velocity</u> spectrum is dominated by low wavenumbers which scale as internal waves. Thus the velocity variances in eq. (5) are those of the internal wave field, and we may consider two limiting cases.

<u>Type 1 (narr w-band case):</u> waves of a single frequency scale as $\overline{u_i^2} \sim N$ and $\overline{w^2} \sim N^{-1}$ (Phillips, 1977).

<u>Type 2 (broad-band case):</u> if frequency bandwidth as well as velocity magnitude varies with N as the GM79 model spectrum (Munk, 1981), then $\overline{u_i^2} \sim N$ and $\overline{w^2} \sim N^0 \sim$ constant.

We finally add the observation that $Ri(k_o) \sim 1$: if shears leading to turbulence generation and transfer of energy to (near-by) dissipation scales are due to those motions (at scales $z \gtrsim 10$ m) which scale as internal waves, then $\overline{\left(\frac{\partial u_i}{\partial z}\right)^2} \sim N^2$. Using these relations in eq. (5), one obtains

Type 1: $\quad \varepsilon \sim N^{+1}$

Type 2: $\quad \varepsilon \sim N^{+1.5}$,

the range which provides a reasonable description of the N-dependence of observations in Fig. 4.

Similar treatment of the available potential energy equation leads to the conclusion that

Type 1: $\quad \chi \sim N^{+3}$ and $Cx \sim N^{-1}$

Type 2: $\quad \chi \sim N^{+3.5}$ and $Cx \sim N^{-0.5}$,

a reasonable description of the data in Fig. 3. However, it also raises some doubt as to the validity of the calculation of diapycnal eddy diffusivity K_ρ by the Osborn-Cox model for such a system. An alternate estimate of K_ρ (independent of the Osborn-Cox assumptions) is obtained from the present theory if it is assumed that, in addition to being small, R_f is approximately constant (see Gargett and Holloway, 1984, for supporting evidence). Then

$$K_\rho = \frac{R_f}{1-R_f} \; \frac{\varepsilon}{N^2}$$

and

Type 1: $\quad K_\rho \sim N^{-1}$

Type 2: $\quad K_\rho \sim N^{-0.5}$.

It has proven both entertaining and informative to discover how sensitive various aspects of large-scale ocean circulation may be to very subtle variation of K_ρ with N, such as that suggested by the above results (Gargett, 1984). The direction of meridional flow in the interior of the classical Stommel-Arons thermohaline circulation is <u>reversed</u> when a constant K_ρ is replaced by $K_\rho \sim N^{-1}$. Such sensitivity was foreseen by Stommel and Arons (1960), who remarked that, although they had been able to show that the dynamics of the flow was insensitive to horizontal diffusivity up to values thought reasonable for the ocean interior, the same could not be claimed for the vertical diffusivity, and that they used a constant K_ρ only for lack of any better idea. It is amusing to find that attention to the smallest scales of variance in the ocean may have such large-scale repercussions.

4. DISCUSSION

While the fore-going makes an appealing construction, one must recognize its weaknesses, for these will be places where further observational information will most affect the next generation of theory. A major weakness is the implicit assumption that the triple correlation coefficient T_1 in eq. (5) is independent of N. We argued that T_1 couldn't depend upon N because there was no other frequency (time) scale available to make the correlation coefficient dimensionless. But of course one <u>could</u> notice that f is another frequency scale of relevance to internal waves – so the assumption is that T_1 doesn't vary as some function of N/f. This appears to require that variances involved in the transition between waves and turbulence are those of waves which don't feel the earth's rotation, and this of course is an argument about the <u>time scales</u> of the waves involved in "breaking". This question and the associated one of the average time between breaking events at a fixed location are of fundamental importance to any theory attempting to quantify the mixing caused by internal waves (Desaubies and Smith, 1982; Garrett and Munk, 1972). Rob Pinkel's velocity spectra (Pinkel, 1984; see also this volume) from the upper ocean show waves of inertial frequency dominating low vertical wavenumbers: however, the high-wave-number roll-off of inertial waves is <u>much</u> steeper than that of waves near the Väisälä frequency, so the latter may come to dominate the vertical wavenumber spectrum by $k_0 \sim 0.1$ cpm. This suggestion is also present (extended through the full depth of the ocean) in velocity profile results of Tom Sanford (pers. comm., 1983). Thus it appears possible that the waves involved in 'breaking' are dominantly of near-Väisälä periods, hence that T_1 is independent of f and consequently independent of N.

This tentative conclusion does not necessarily conflict with the discovery by Mike Gregg and Eric D'Asaro (this volume) of a long-lived patch of strong dissipation associated with an inertial jet, since the observed connection may not necessarily imply that the energy being dissipated is that of the inertial wave – the inertial wave may provide only the locale for a critical-layer mechanism involving waves of higher

frequency. However, a very important aspect of this observation lies in the extended lifetime of the dissipative _patch_ relative to both Väisälä and inertial periods. The suggestion that dissipation patch lifetimes may greatly exceed the longest internal wave periods (which in turn exceed "turbulent" time scales) is reminiscent of repeated observations of vertical dissipation patch scales which considerably exceed vertical overturning scales. If L is the vertical extent of a patch of continuous dissipation and $\ell_o \sim \ell_b/3 \sim 2(\varepsilon/N^3)^{1/2}$ is the appropriate overturning scale (as suggested by Gargett, Osborn, and Nasmyth, 1984), oceanic measurements frequently exhibit $\ell_o \ll L$. Both characteristics seem to indicate the importance of internal wave _groups_ in setting time and space scales of the largest dissipation patches, even though turbulent scales within these patches are set by local values of N and of ε, the rate at which energy is being supply to dissipation scales. Perhaps it is the dynamics of the internal wave field which determines turbulence scales (through ε), but kinematics which determine patch scales.

Returning to the problem of parameterizing the averaged effects of large numbers of turbulent events, note that if on average $\bar{\varepsilon} \propto N$, as suggested by the observations of Fig. 4, then

$$\bar{\ell}_o \propto \bar{\ell}_b \propto \left(\frac{\bar{\varepsilon}}{N^3}\right)^{1/2} \propto N^{-1} ,$$

i.e. the _average_ overturning scale varies inversely with N. Using $\bar{\ell}_o \sim H$ in the expression

$$K_\rho \sim H^2 T_e^{-1} \sim N^{-2} T_e^{-1}$$

due to Garrett and Munk (1972), we see the importance of T_e, the time scale between mixing events at a given location, to the N-scaling of K_ρ. Surveying some possible candidates, if $T_e \sim (\text{constant}, (Nf)^{-1/2}, N^{-1})$ then $K_\rho \sim (N^{-2}, N^{-1.5}, N^{-1})$, various inverse power laws. These are quite different from the results of Chris Garrett (this volume), who used the Gargett et al. spectrum to infer that H should be independent of N, hence (again depending upon T_e) K_ρ should vary as a zero or positive power of N. The difference between his result and mine lies, I think, in the endpoint chosen for the "wave" shear integral. Chris chooses $k_o = 0.1$ cpm (his k_o) independent of N, while I choose $k \sim (N^3/\varepsilon)^{1/2}$ and further allow for evidence that the wave field sets _averaged_ $\bar{\varepsilon}$ such that $\bar{\varepsilon} \propto N$.

As anyone who has experienced a severe storm at sea knows, the boundary between waves and turbulence can prove an uncomfortable place to be. Attempts to measure this area in the interior of the ocean are just beginning, and the initial framework provided to fit observations may soon be swept away by new observations: in the meantime, it provides direction for these observations. I think the most significant advances will come from measurements of time scales of dissipation events, observations of $\bar{\varepsilon}$ and/or χ in the deep ocean, and careful comparison of oceanic measurements with results of relevant laboratory experiments.

REFERENCES

CRAWFORD, W.R. and T.R. OSBORN (1979): Microstructure measurements in the Atlantic Equatorial Undercurrent during GATE. Deep-Sea Res., GATE Suppl. II to Vol. 26, 285-308.

DESAUBIES, Y.F. and W.K. SMITH (1982): Statistics of Richardson number and of instability in oceanic internal waves. J. Phys. Oceanogr., 12, 1245-1259.

DOUGHERTY, J.P. (1961): The anisotropy of turbulence at the meteor level. J. Atmos. and Terr. Phys., 21, 210-213.

EVANS, D.L. (1982): Observations of small-scale shear and density structure in the ocean. Deep-Sea Res., 29 (5A), 581-595.

GARGETT, A.E. (1984): Vertical eddy diffusivity in the ocean interior. J. Mar. Res., 42 (2).

GARGETT, A.E., P.J. HENDRICKS, T.B. SANFORD, T.R. OSBORN and A.J. WILLIAMS III (1981): A composite spectrum of vertical shear in the upper ocean. J. Phys. Oceanogr., 11 (9), 1258- 1271.

GARGETT, A.E. and G. HOLLOWAY (1984): Dissipation and diffusion by internal wave breaking. J. Mar. Res., 42 (1).

GARGETT, A.E. and T.R. OSBORN (1981): Small-scale shear measurements during the Fine and Microstructure Experiment (FAME). J. Geophys. Res., 86, 1929-1944.

GARGETT, A.E., T.R. OSBORN and P.W. NASMYTH (1984): Local isotropy and the decay of turbulence in a stratified fluid. J. Fluid Mech., 144, 231-280.

GREGG, M.C. (1977): Variations in the intensity of small-scale mixing in the main thermocline. J. Phys. Oceanogr., 7, 436-454.

GARRETT, C. J. and W. MUNK (1972): Oceanic mixing by breaking internal waves. Deep-Sea Res., 19, 823-832.

LUECK, R.G., W.R. CRAWFORD and T.R. OSBORN (1983): Turbulent dissipation over the continental slope off Vancouver Island. J. Phys. Oceanogr., 13, 1809-1818.

MOUM, J.N. (1984): Measurements of velocity microstructure in the central equatorial and western Pacific Ocean. PhD Thesis, Dept. of Oceanography, Univ. of British Columbia, Vancouver, B.C., Canada.

MUNK, W. (1981): Internal Waves and Small-Scale Processes. In The Evolution of Phys. Oceanography: Scientific Papers in Honour of Henry Stommel. B.A. Warren and C. Wunsch ed., MıT Press, 1981. 264-291.

OSBORN, T.R. (1978): Measurements of energy dissipation adjacent to an island. J. Geophys. Res., 83, 2939-2957.

OSBORN, T.R. and C.S. COX (1972): Oceanic fine structure. Geophys. Fluid Dyn., 3, 321-345.

OSBORN, T.R. and T.E. SIDDON (1975): Oceanic shear measurements using the airfoil probe. Proc. of the Third Biennial Symp. on Turbulence in Liquids, Dept. of Engineering, Univ. of Missouri, Rolla.

PHILLIPS, O.M. (1977): The Dynamics of the Upper Ocean, Second Edition. Cambridge Univ. Press, 336 pp.

PINKEL, R. (1984): Doppler sonar observations of internal waves: the wavenumber frequency spectrum. pre-print.

STOMMEL, H. and A.B. ARONS (1960): On the abyssal circulation of the world ocean - II. An idealized model of the circulation pattern and amplitude in oceanic basins. Deep-Sea Res., 6, 217-233.

TOOLE, J.M. and S.P. HAYES (1984): Fine scale velocity-density characteristics and Richardson number statistics of the eastern equatorial Pacific, pre-print.

RICHARDSON NUMBER APPROACH TO INTERNAL WAVE INSTABILITY IN THE OCEAN AND STRATOSPHERE

Y. Desaubies

Woods Hole Oceanographic Institution, Woods Hole, Massachusetts 02543

ABSTRACT

Further evidence is presented showing that the internal wave fields in the ocean and atmosphere are such that the Richardson number $\overline{Ri} = \langle n^2 \rangle / \langle (du/dz)^2 \rangle$, constructed on the variances of buoyancy frequency and velocity shear, is of order one. We argue in favor of shear instability as an instability mechanism. We compare high-resolution temperature and velocity data from the stratosphere (Barat,1983) with a gravity wave spectral model of VanZandt (1982) and find the agreement to be quite good. This indicates that gravity waves are an important source of fluctuations in the atmosphere, as they are in the ocean.

INTRODUCTION

A statistical model describing fluctuations in Richardson number and the mixing resulting from shear instability was presented by Desaubies and Smith (1982). Only a brief summary of the model and the results is given here. In a field of internal waves all quantities of physical interest, such as the buoyancy frequency, n, and the shear, s, fluctuate erratically and must be considered random variables. Thus the Richardson number, $Ri = n^2/s^2$, is also a random variable whose value will occasionally fall below the critical value $Ri_c = 0.25$. Here n is the instantaneous of the buoyancy frequency; it is assumed that n^2 is a normal random variable with mean $\langle n^2 \rangle = N^2$ and normalized variance

$$\frac{\langle n^4 \rangle - N^4}{N^4} \cong \lambda^2 \ .$$

Similarly the shear

$$s = [(\partial_z u)^2 + (\partial_z v)^2]^{1/2}$$

where $\partial_z u$ and $\partial_z v$ are normal random variables with zero mean and
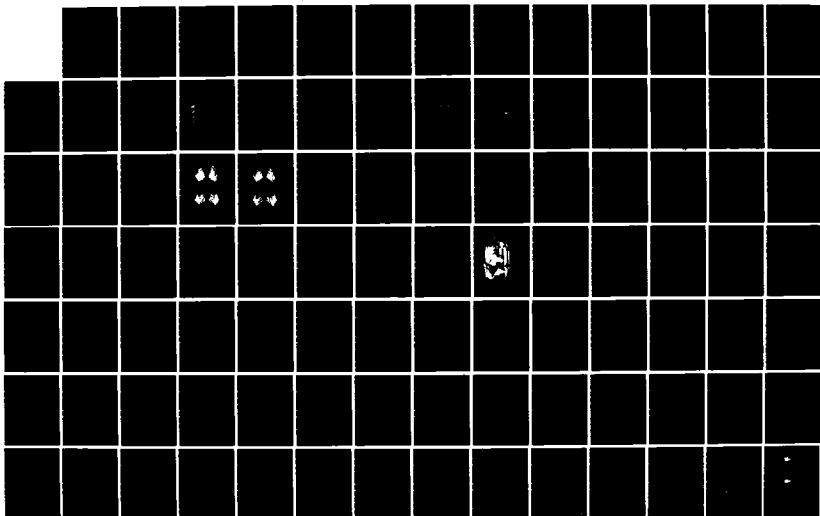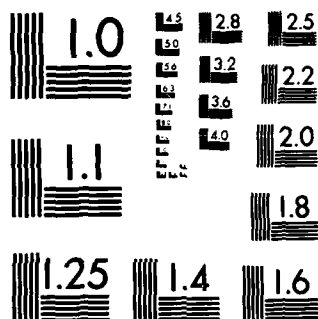
MICROCOPY RESOLUTION TEST CHART

NATIONAL BUREAU OF STANDARDS-1963-A

variance $\langle(\partial_z u)^2\rangle = \langle(\partial_z v)^2 = \sigma^2$. Within the framework of a slightly modified Garrett and Munk spectrum, D.S. find

$$\lambda^2 = Z^2 \beta_* \beta_c \quad , \quad S^2 \equiv \langle s^2 \rangle = 3N^2 Z^2 \beta_* \beta_c = 3N^2 \lambda^2 \qquad (1)$$

where Z = r.m.s. vertical displacement, β_* = vertical wave number bandwidth, $\beta_c \simeq (2\pi/10)m^{-1} \simeq 0.6\ m^{-1}$ = vertical wave number cutoff. It is useful to introduce a Richardson number

$$\bar{Ri} \equiv \frac{N^2}{S^2} = \frac{1}{3\lambda^2} \qquad (2)$$

which __is not__ the expected value $\langle Ri \rangle$.

With these assumptions D.S. derive the probability density function of Ri, which is found to be in excellent agreement with observed histograms from a variety of sources. The fits require $\lambda \simeq 0.56$ corresponding to $Ri \simeq 1$ which appear to be "universal constants" of the internal wave field.

A simplified mixing model is then constructed as follows: consider the depth statistics of Ri and assume that when over some depth interval Ri < 0.25, perfect mixing occurs instantly, corresponding to an increase of potential energy, a vertical buoyancy flux, and a loss of kinetic energy from the wave field. Results from numerical simulations and calculations from a stochastic differential equation formalism led to the following conclusions: the "predicted" value of the eddy diffusivity for buoyancy are comparable to those deduced from finestructure measurements; significant events (i.e. those contributing to the mixing) are rare (only a few percents of the profiles) and small (at most 1 or 2 m) although a larger fraction of the profiles (about 10 percent) shows many small-scale, nonenergetic events; the dissipation rate is extremely sensitive to the value of λ (or Ri). The latter observation suggested an interpretation of saturation: if the energy in the internal wave field increases, the λ increases and dissipation increases dramatically; conversely if E and λ decrease the dissipation is effectively turned off. Chris Garrett argued that this was not necessarily so: since $\lambda = Z^2 \beta_* \beta_c$ (and $Z^2 \sim E$) it is possible that if E increases, β_c might decrease correspondingly (lower wave number cutoff, larger scale instability) in such a way that λ does not necessarily increase in proportion to E. Only observation could resolve this argument: do lower (higher) energy levels correspond to higher (lower) cutoff β_c?

Despite several obvious shortcomings of the model, we believe it confirmed the importance of shear instability and Richardson number statistics in the study of internal wave dissipation. Further evidence for this can be obtained by considering a rather different system, the atmosphere.

Internal waves in the atmosphere

There has recently been renewed interest in the study of internal waves (gravity waves) in the atmosphere (Fritts et al., 1984); for our purposes the atmosphere constitutes an analogous system to the ocean or can be viewed as a different realization, albeit with rather different parameters. VanZandt (1982) has proposed an empirical spectrum describing gravity waves in the atmosphere. Proceeding very much like Garrett and Munk (1972, 1975), he considered wavenumber and frequency spectra of horizontal velocity and fitted them with the various projections of a single power spectrum.

There has been some criticism of VanZandt's approach (see Lilly's contributions in these proceedings) by those who advocate two-dimensional turbulence; they point out some apparent inadequacies of the model: the absence of proper scaling with the changing density of the atmosphere; the incorporation in the model of data from rather different regions—troposphere, tropopause, and stratosphere; the less than perfect fit with some of the data. The question whether atmospheric mesoscale variablity should be interpreted as two-dimensional turbulence or gravity waves (or a mix of both), and whether there is a universal spectrum can be answered only by further observational and theoretical evidence. We present here a preliminary analysis of stratospheric data from Barat (1983), that seems to fit nicely with the Van Zandt model for gravity waves (hereafter referred to as the VZ spectrum).

The VZ spectrum

The model can be written

$$P_Q(\omega, \beta) = R'Q^2 \frac{1.4}{\beta_*(1 + \beta/\beta_*)^{2.4}} f^{2/3} \omega^{-5/3} \tag{3}$$

where

$$Q^2 = \frac{\omega^2 - f^2}{n} \qquad \text{if the spectrum of w is considered}$$

$$= \frac{n}{2} \frac{\omega^2 + f^2}{\omega^2} \qquad \text{if the spectrum of u is considered} \quad .$$

u is one component of horizontal velocity; w is vertical velocity, the form of Q being derived from the linearized internal wave equations. The constants are $R' \simeq 5.81 \ 10^3 (m/s)^2 (cps)^{-1}$ and $\beta\star = tn$, $t \simeq 7.43 \times 10^{-2} (s/m)$; n and f are buoyancy and inertial frequency, respectively. The spectra are such that

$$\int_f^n d\omega \int_0^\infty d\beta \ P_u(\omega,\beta) = <U>^2 \tag{4}$$

$$\int_f^n d\omega \int_0^\infty d\beta \ P_W(\omega,\beta) = <W^2> \quad . \tag{5}$$

For the stratosphere at midlatitude, $f = 1.64 \ 10^{-5} cps$; $n = 3.18 \ 10^{-3} cps$; we find

$$<U^2> = 17.3(m/s)^2 = (4.16 \ m/s)^2 \quad . \tag{6}$$

The Richardson number statistics depends on the strain and shear variance (1). We have

$$\lambda^2 \equiv <(\partial_z \eta)^2> = \int_f^n d\omega \int_0^{\beta_c} d\beta \left(\frac{\beta}{\omega}\right)^2 P_W(\omega,\beta)$$

$$\tag{7}$$

$$\simeq \frac{21}{8} \frac{R'}{n} \beta_\star^2 (\beta_c/\beta_\star)^{3/5}$$

where the high wavenumber cutoff β_c has been introduced to prevent divergence of the integral. Similarly, for the shear:

$$S^2 = 2<(\partial_z u)^2> = 2 \int_f^n d\omega \int_0^{\beta_c} d\beta (2\pi\beta)^2 P_u(\omega,\beta)$$

$$\tag{8}$$

$$= \frac{35}{8} nR'(2\pi)^2 \beta_\star^2 (\beta_c/\beta_\star)^{3/5} = \frac{5}{3} (2\pi n)^2 \lambda^2 \quad .$$

It follows that (see (2))

$$\bar{R}i = \frac{(2\pi n)^2}{S^2} = \frac{3}{5\lambda^2} \quad . \tag{9}$$

Comparison of Barat's data with the VZ model

Barat reports on high-resolution observations of temperature and velocity shear profiles in the stratosphere. The instrumentation consists of temperature sensors and ionic anemometers attached to a drifting balloon (fig. 1); as the balloon is advected by the wind, the anemometers measure the relative wind, i.e. the shear over 150 and 100 m. The whole system can be controlled to rise or descend at about 0.3 to 0.5 m/s. Figure 2 shows the track along which the data to be discussed here were taken.

The shear measurements reported by Barat are computed as finite differences

$$S_\delta^2 = \delta^{-2}[(u(z + \delta) - u(z))^2 + (v(z + \delta) - v(z))^2] \quad . \tag{10}$$

Taking averages over a vertical profile the following values are reported:

$$\langle S_{50} \rangle = 2.55 \times 10^{-2} s^{-1} \; , \; \langle S_{50}^2 \rangle^{1/2} = 2.72 \times 10^{-2} s^{-1}$$

$$\tag{11}$$

$$\langle S_{150} \rangle = 1.8 \times 10^{-2} s^{-1} \; , \; \langle S_{150}^2 \rangle^{1/2} = 1.931 \; 10^{-2} s^{-1} \quad .$$

We shall assume later that u and v are normal random variables; it follows from (10) that S^2 has an exponential probability density function, with the property

$$\langle S^{2n} \rangle = \langle S^2 \rangle^n \, \Gamma(n + 1) \quad . \tag{12}$$

For n = 1/2 we predict

$$\langle S^2 \rangle^{1/2} / \langle S \rangle = 2/\sqrt{\pi} = 1.128 \quad .$$

From the data (11) we find

94
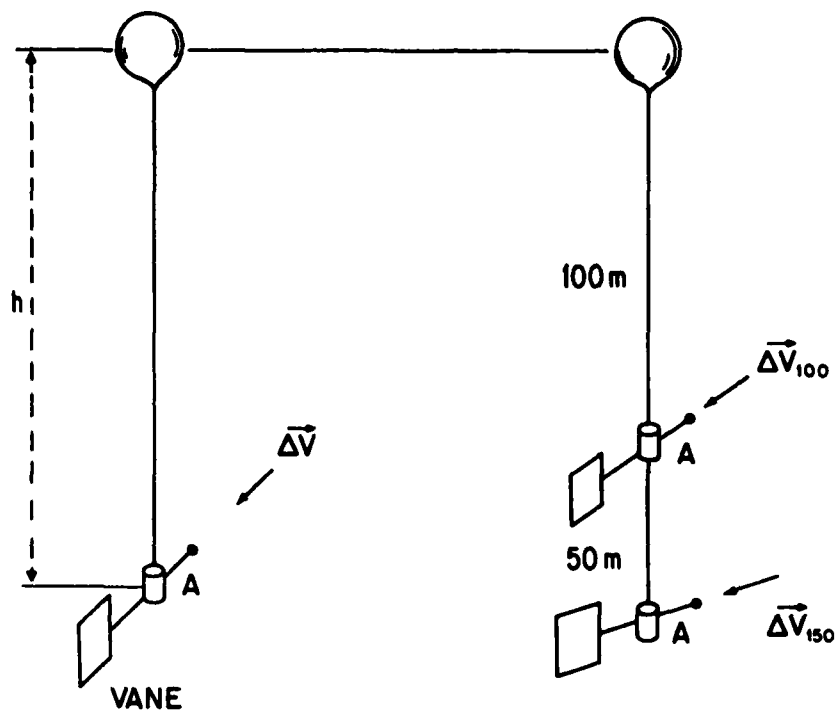
Figure 1.   The instrumented balloon used for stratospheric measurements
             (from Barat,1983).
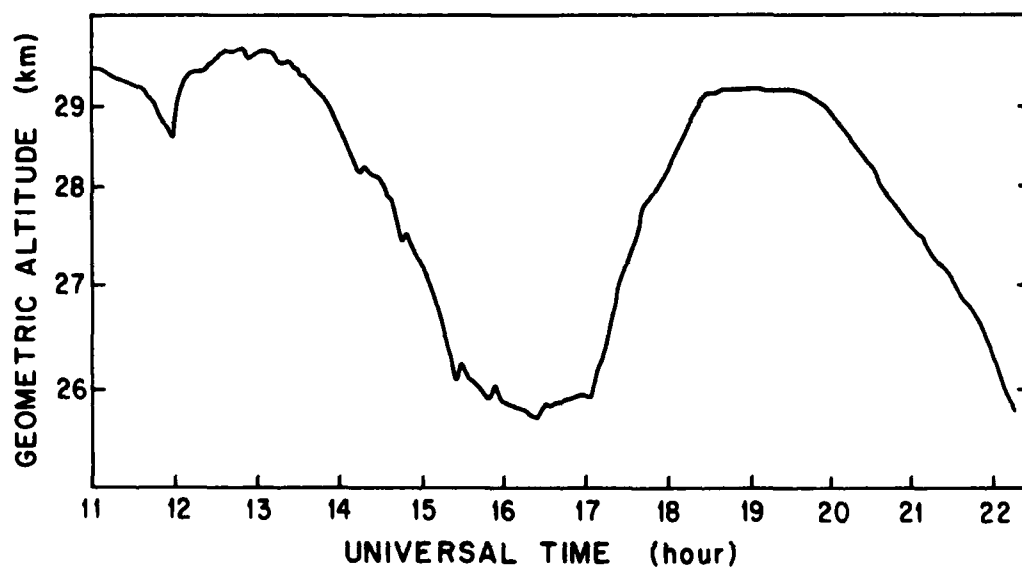
Figure 2.   Track of the instrumented balloon (from Barat,1983).

$$\langle S_{50}^2 \rangle^{1/2} / \langle S_{50} \rangle = 1.067$$

$$\langle S_{150}^2 \rangle^{1/2} / \langle S_{150} \rangle = 1.073$$

suggesting, but not proving, a nearly normal distribution for the components u and v. In (10) we can write

$$\langle (u(z + \delta) - u(z))^2 \rangle = 2\langle U^2 \rangle [1 - \rho(\delta)] \qquad (13)$$

where

$$\rho(\delta) = \langle U^2 \rangle^{-1} \langle u(z + \delta)u(z) \rangle \qquad (14)$$

is the velocity correlation function and $\langle U^2 \rangle$ the variance of one velocity component. Assuming that for small separation

$$\rho(\delta) \simeq 1 - (\delta/l_0)^n \qquad (15)$$

we get

$$\langle S_\delta^2 \rangle = \frac{4\langle U^2 \rangle}{l_0^n} \delta^{n-2} \quad . \qquad (16)$$

Combining (11) and (16):

$$\langle S_{150}^2 \rangle / \langle S_{50}^2 \rangle = (\frac{150}{50})^{n-2} = 3^{n-2} = 0.5$$

whence n = 1.38. But an expansion of the form (15) for the correlation function corresponds to a power law dependence at high vertical wavenumber

$$P_u(\beta) \sim \beta^{-(n+1)} = \beta^{-2.38}$$

to be compared to VanZandt's model $\beta^{-2.4}$. Thus, with this limited information we have confirmed the spectral shape at high wavenumber.

With the information given here we cannot deduce $\langle U^2 \rangle$ and l_0 independently, but we find from (16) and (11)

$$\langle U^2 \rangle / l_0^{\ n} = 2.08 \ 10^{-3} \qquad (U \text{ in m/s, } l_0 \text{ in m}) \tag{17}$$

If we identify in VZ model the correlation length with the inverse bandwidth:

$$l_0 = (2\pi B_*)^{-1} = 674 \text{ m}$$

the model predicts (6)

$$\frac{\langle U^2 \rangle}{l_0^{\ n}} = 2.16 \ 10^{-3}$$

in excellent agreement with the observed value (17).

Up to this point we have not said anything about gravity waves; all we have shown is that the velocity fluctuations observed by Barat in the stratosphere over France agree (spectral slope, bandwidth, and level) with the VZ model. A convincing argument for internal waves can be made by considering temperature fluctuations and their relation to the velocity field, in particular through the Richardson number.

Richardson number fluctuations

We cannot estimate apriori the required parameters λ^2 and S^2, because we have no indication on the value of the wavenumber B_c. But Barat and Sidi (private communication) have calculated

λ^2 directly by computing the variance of temperature gradient profiles: they find $\lambda = 0.58$, which is very nearly identical to the ocean value. Fig. 3 shows a comparison of observed histogram of Ri and the model of Desaubies and Smith. Here it has been assumed that, as in the ocean, the shear variance is related to the strain variance by $(2\pi n)^2 \lambda^2 / S^2 = 1/3$. However, we have seen in (9) that $(2\pi n)^2 \lambda^2 / S^2 = 3/5$; the origin of this discrepancy (by a factor of 2) is not clear and requires further investigation.

With the observed value of λ, we find from (9)

$$\overline{Ri} = 1.78 \quad ,$$

a value about twice that of the ocean, but still of order one.
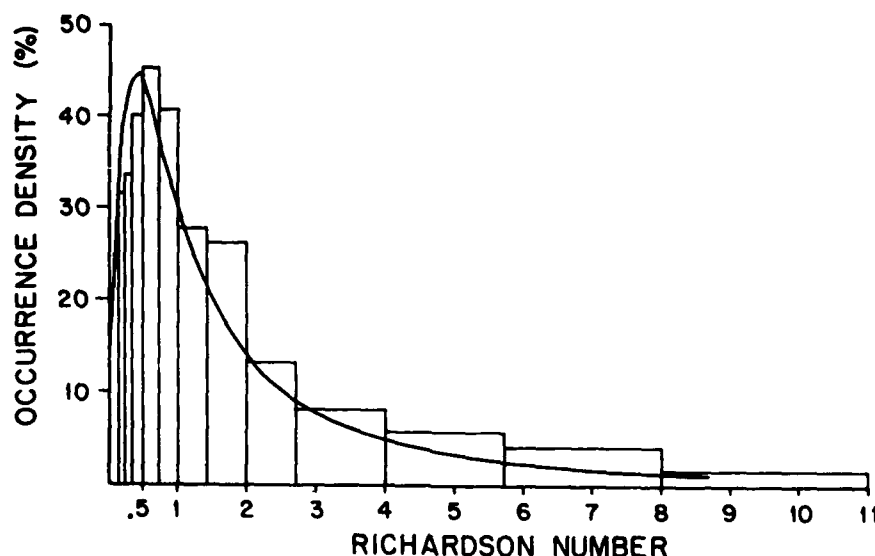
Figure 3. Comparison of observed (Barat,1983) Richardson number statistics with model by Desaubies and Smith (1982). Best fit is obtained for λ = 0.58.

Conclusions

We have confirmed the importance and universality of the parameter $\lambda \simeq 0.56$ for the ocean and atmosphere. This parameter can be viewed alternatively as the normalized variance of temperature (or density) gradient fluctuations or as a measure of nonlinearity. As a measure of gradient fluctuations it indicates that those distortions are important and cannot be neglected in an instability/mixing model; it is also clear that nonlinear effects are important. The parameter $Ri = N^2/S^2$ is found to be of order 1 for both ocean and atmosphere, in agreement with a suggestion by Munk (1981), with data presented by d'Asaro in this workshop (if allowance is made for measurements over a finite interval of 10 m), with results of numerical simulations by Holloway (these proceedings) who finds instability to occur at $Ri \simeq O(1)$, and with nonlinear instability analysis by Abarbanel (see Abarbanel et al.,1984).

Comparisons of stratospheric data of Barat with the VZ gravity wave model are found to be in general agreement, providing evidence in favour of gravity waves as the cause of the observed fluctuations. However, further analysis of the data is underway (in particular, spectral analysis of the small-scale fluctuations) to

reach more definite conclusions. It is likely that in the light of new data further refinements of the model will be required, as has been the case with the G.M. model.

REFERENCES

Abarbanel, H.D.I., Helm, Marsden and Ratin, 1984: Richardson number criterion for the nonlinear stability of stratified flow. In press.

Barat, J., 1983: The fine structure of the stratospheric flow revealed by differential sounding. J. Geophys. Res., 88, 5219-5228.

Desaubies, Y. and W.K. Smith, 1982: Statistics of Richardson Number and of instability in oceanic internal waves. J. Phys. Oceanogr., 12, 1245-1259.

Fritts, D.C., Geller, Balsley, Chanin, Hirota, Holton, Kato, Lindzen, Schoeberl, Vincent, Woodman, 1984: Research status and recommendations from the Alaska Workshop on Gravity Waves and Turbulence in the middle atmosphere. Bull. Amer. Met. Soc., 65, 149-159.

Garrett, C. and W.H. Munk, 1972: Space-time scales of internal waves. Geophys. Fl. Dyn., 3, 225-264.

Garrett, C. and W.H. Munk, 1975: Space-time scales of internal waves: a progress report, J. Geophys. Res., 80, 291-297.

Munk, W.H., 1981: Internal waves and small scale processes, in Evolution of Physical Oceanography, Ed.: B.A. Warren and C. Wunsch, MIT Press.

VanZandt, T.E., 1982: A universal spectrum of buoyancy waves in the atmosphere, Geophys. Res. Lett., 9, 575-578.

RECENT OBSERVATIONS OF NEAR-INERTIAL FREQUENCY INTERNAL WAVES

Eric A. D'Asaro

Applied Physics Laboratory, University of Washington
1013 N.E. 40th Street, Seattle, Washington 98105

ABSTRACT

Recent measurements of near-inertial frequency internal waves in the upper kilometer of the ocean using expendable velocity profilers (XCP) have revealed several new features. The near-inertial internal wave spectrum, measured in the Sargasso Sea in late summer, is highly asymmetric: the downward-going waves are not only more energetic than the upward-going waves, but also have a frequency closer to the inertial frequency and therefore travel with a slower vertical group velocity. The net downward energy flux roughly matches the average summer input of energy to surface inertial motions as measured from a nearby NDBC buoy. Other measurements made before and after a strong storm in the eastern North Pacific indicate near-inertial waves that are generated in a manner consistent with linear models. Measurements made in the subtropical front and in Gulf Stream rings show a strong modulation of the inertial wave energy by these mesoscale features. A ray tracing model predicts the major observed features. The shear field measured at a 10-m separation appears to be the sum of a background shear field, proportional to the local buoyancy frequency, and an inertial frequency shear field, which varies in space and time. The near-inertial internal wave field seen in these data is far from universal and shows many deterministic features related to its sources and sinks.

INTRODUCTION

Direct velocity measurements in the open ocean invariably show a spectral peak near the local inertial frequency. This peak typically contains at least half the total energy in the internal wave frequency band. The canonical internal wave spectra (Garrett and Munk, 1979) do not accurately model observations of the near-inertial frequency band. Unlike higher frequency internal waves, near-inertial waves are typically highly intermittent (Webster, 1968), dominantly downward propagating (Leaman and Sanford, 1975), and do not scale with the local buoyancy frequency (Fu, 1981). Inertial motions in the surface mixed layer appear to contain a large component that is forced by the local wind (Pollard and Millard, 1970), which suggests that wind forcing is a major source of deep ocean inertial motions.

Recent studies of near-inertial motions by T. Sanford and E. D'Asaro have concentrated on measuring the spatial structure of near-inertial motions, especially in potential source and sink regions. Typically, a given area is surveyed using expendable electromagnetic current profilers (XCP's), which

measure velocity and temperature to a depth of 900 m, supplemented by CTD and other measurements. The XCP's are particularly suited for measuring the spatial structure of near-inertial motions, since the typical horizontal scales of these motions can be sampled in a time less than their period from a ship under way. The inertial motions are usually sufficiently strong that only a small amount of additional temporal or spatial filtering is necessary to separate them from the geostrophic and high-frequency internal wave motions. Several of these recent studies are described below.

VERTICAL ENERGY FLUX OF NEAR-INERTIAL WAVES

The vertical and horizontal fluxes of energy are an important characteristic of the internal wave field. Waves near the inertial frequency are not vertically symmetric and may therefore carry a significant energy flux. For a spectrum of waves characterized by frequency σ and vertical and horizontal wavenumbers β and α, the vertical energy flux F_z can be evaluated from the product of the energy density E and the vertical group velocity G_z integrated over all of the waves.

$$F_z = \int E(\beta,\sigma)G_z \, d\beta \, d\sigma \tag{1a}$$

or

$$F_z = \int E(\beta,\alpha)G_z \, d\beta \, d\alpha \,. \tag{1b}$$

where the group velocity is given by

$$G_z = -\frac{\sigma^2 - f^2}{\sigma\beta} \tag{2a}$$

or

$$G_z = -\frac{N^2\alpha^2}{\sigma\beta^3} \tag{2b}$$

for a WKB-stretched ocean with reference buoyancy frequency N (Leaman, 1976). The hydrostatic dispersion relation

$$\sigma^2 - f^2 = \frac{N^2\alpha^2}{\beta^2} \tag{3}$$

is used in converting between (2a) and (2b). If (1a) and (2a) are used, as would be done using a time series of velocity profiles, σ must be measured with sufficiently high resolution to resolve the group velocity near f. Typically, the inertial peak is within 10% of f (Fu, 1981) so that the time series must be at least several months long to estimate $\sigma^2 - f^2$, and therefore G_z, accurately. The computed energy flux will be an average over the time series and thus may not resolve shorter variations in the wave field due to individual forcing events. Alternatively, a spatial survey of velocity profiles can be used to compute $E(\alpha,\beta)$. F_z is then computed employing (1b) and (2b). This can be done rapidly, and is therefore better suited for the investigation of transient or spatially inhomogeneous features.

D'Asaro and Perkins (1984) have computed the frequency spectrum and vertical energy flux of near-inertial internal waves using this second approach. A survey of XCP profiles (Fig. 1) taken during late summer in the Sargasso Sea was used to compute the correlation function of velocity
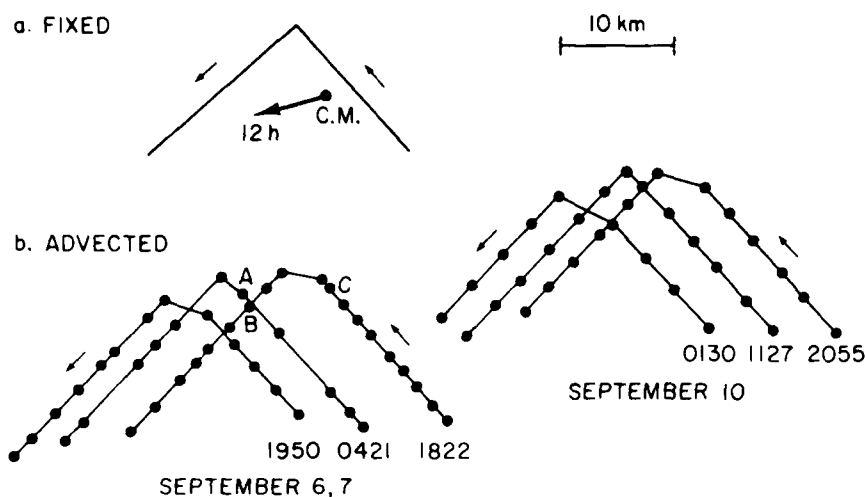
Fig. 1. A survey of XCP profiles. a) The L-shaped pattern was
repeated six times in the direction shown. Dot indicates a
current meter mooring; arrow indicates the average 12-
hour displacement of water past the mooring. b) The XCP
survey in "advected" coordinates, i.e., with respect to the
water. Dots indicate individual profiles.

$C(r^*,0)$, $r^*=\beta\Delta rf/N$ as a function of horizontal separation Δr for two vertical
wavenumber bands with central wavenumber β (Fig. 2a,b). The correlation
functions were inverted to form a horizontal wavenumber spectrum, or
equivalently a frequency spectrum (Figs. 2c,3c) with very high resolution
near the inertial frequency. Both the upward- and downward-going waves are
resolved.

The computed spectrum is profoundly asymmetric in the vertical at fre-
quencies below $2f$. The downward-going waves are more energetic and of
lower frequency. They carry a vertical energy flux of 0.26±0.11 mW/m² with
an average group velocity of 0.08 cm/s. The upward-going waves are less
energetic, but of higher frequency. They carry a smaller vertical energy flux
of 0.14±0.5 mW/m² at a larger average group velocity of 0.23 cm/s. The net
energy flux is downward and of magnitude 0.12±0.12 mW/m², roughly in
agreement with the less precise estimates of Leaman (1976) in the same
area. These features agree qualitatively with estimates of $E(\beta,\sigma)$ made from a
single mooring deployed for 1 month at the same location. The downward
energy flux roughly balances the average energy put into mixed layer inertial
motions by the wind during the summer months. A value of 0.18 mW/m² was
computed using wind data from an NDBC data buoy 360 km northwest of the
experimental site (Hamilton, 1980) and the model of Pollard and Millard
(1970). This adds additional weight to the longstanding hypothesis that the
downward energy flux in the near-inertial wave field is due to the generation
of waves by wind stress fluctuations.
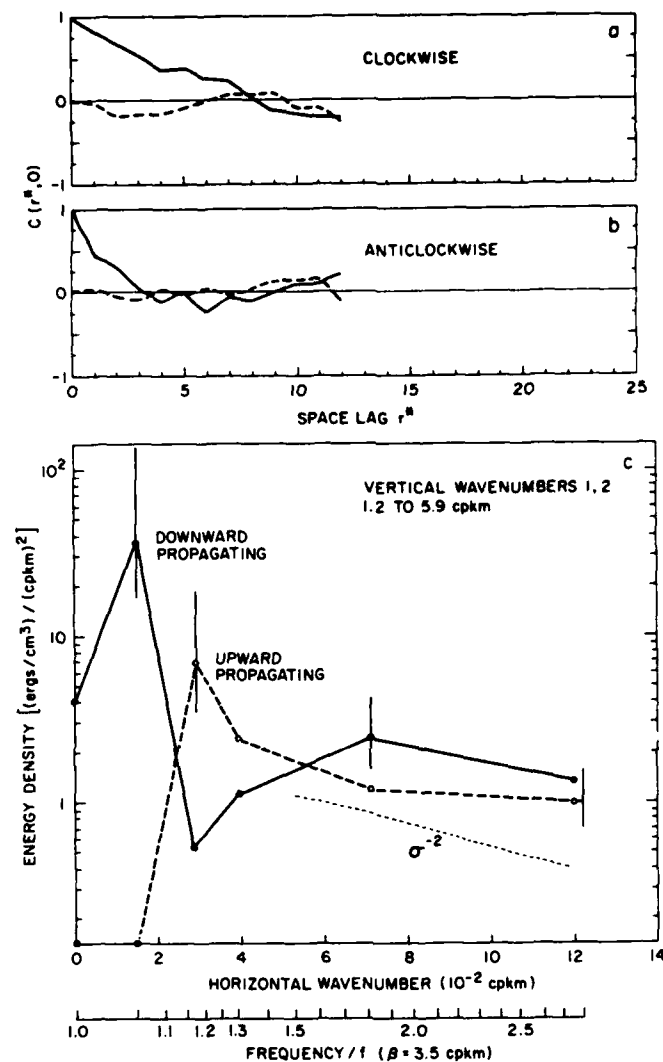
Fig. 2. a) Real (solid) and imaginary (dashed) part of inertial velocity coherence function for wavenumber band 1.2 to 5.9 cpkm computed from the XCP survey shown in Fig. 1. For ideal data the imaginary part should be identically zero. Clockwise rotating component with depth component is shown here. This corresponds to downward-propagating waves. b) Same as a), but for anticlockwise, or upward-propagating, component. c) Energy spectrum computed from the real part of the coherence functions. This can be interpreted as either a horizontal wavenumber magnitude spectrum (upper axis) or an energy preserving frequency spectrum (lower axis). The light dashed line shows a frequency^{-2} spectrum in these coordinates.
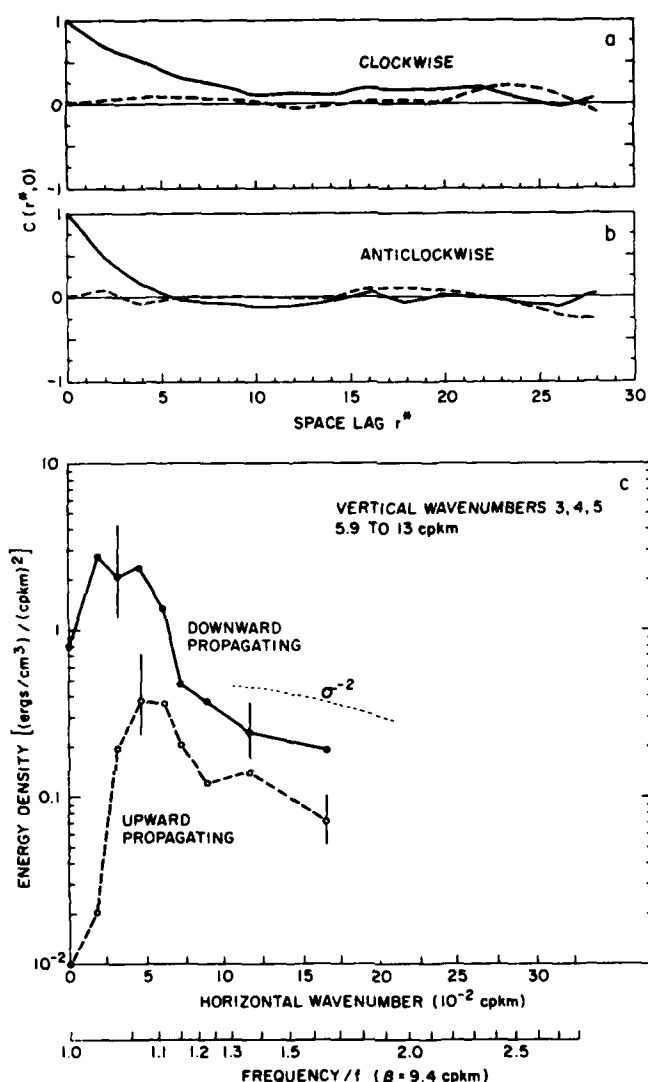
Fig. 3. Same as Fig. 2, but for wavenumber
band 5.9 to 13 cpkm.

STORM FORCED NEAR-INERTIAL WAVES

In the past few years, a number of theoretical studies have investigated
the generation of near-inertial waves by storms, especially hurricanes (Price,
1983; Greatbatch,1983; Gill, 1984). They predict that near-inertial energy ini-
tially concentrated in the mixed layer will propagate downward by linear
internal wave dynamics, exciting near-inertial waves in the upper thermo-
cline with vertical scales comparable to the thermocline thickness and hor-
izontal scales set by the storm size and translation speed. For typical
storms, significant energy should be observed in the thermocline within a few
inertial periods of the storm's passage.

104
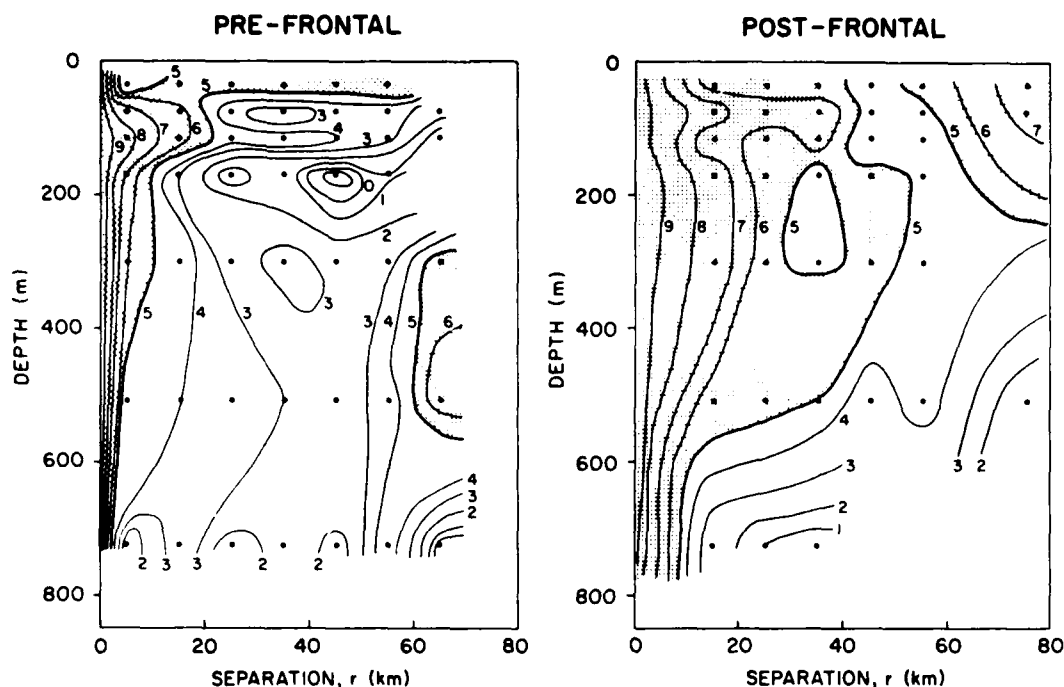
Fig. 4. Contours of the real part of the inertial velocity coherence function as a function of depth and horizontal separation for profiles taken before and after the passage of a strong cold front during STREX. Data points are indicated by dots. Only data points with a 95% confidence level below 0.5 are plotted. Regions with a coherence greater than 0.5 are shaded. Contours are labeled with 10 x actual value.

Observations taken during STREX in the Northeast Pacific in November 1980 confirm these predictions (D'Asaro, 1984). In that experiment, spatial surveys using XCP's were taken before and after the passage of a strong cold front. The horizontal correlation function of inertial velocity was then computed for both surveys (Fig. 4). The inertial motions have a larger horizontal scale after the storm's passage than before. If the cold front is two-dimensional and advects over the experimental area without changing, the horizontal scale of the waves generated by the storm is set by the translation speed of the storm. Based on our estimate of the translation speed from a meteorological buoy and the NOAA ship Oceanographer, the storm-generated waves should have a horizontal scale of about 60 km, which is consistent with the correlation function in the upper few hundred meters computed after the storm. This suggests that near-inertial internal waves were generated by this storm.

A direct comparison of observed and simulated near-inertial waves can also be made. It is assumed that the storm directly forces inertial motions in the mixed layer. These then linearly propagate into the thermocline. If we assume a two-dimensional storm with the translation speed observed during STREX, the linear internal wave equations can be solved to yield the sequence of simulated inertial velocity profiles shown in Fig. 5. The inertial motions
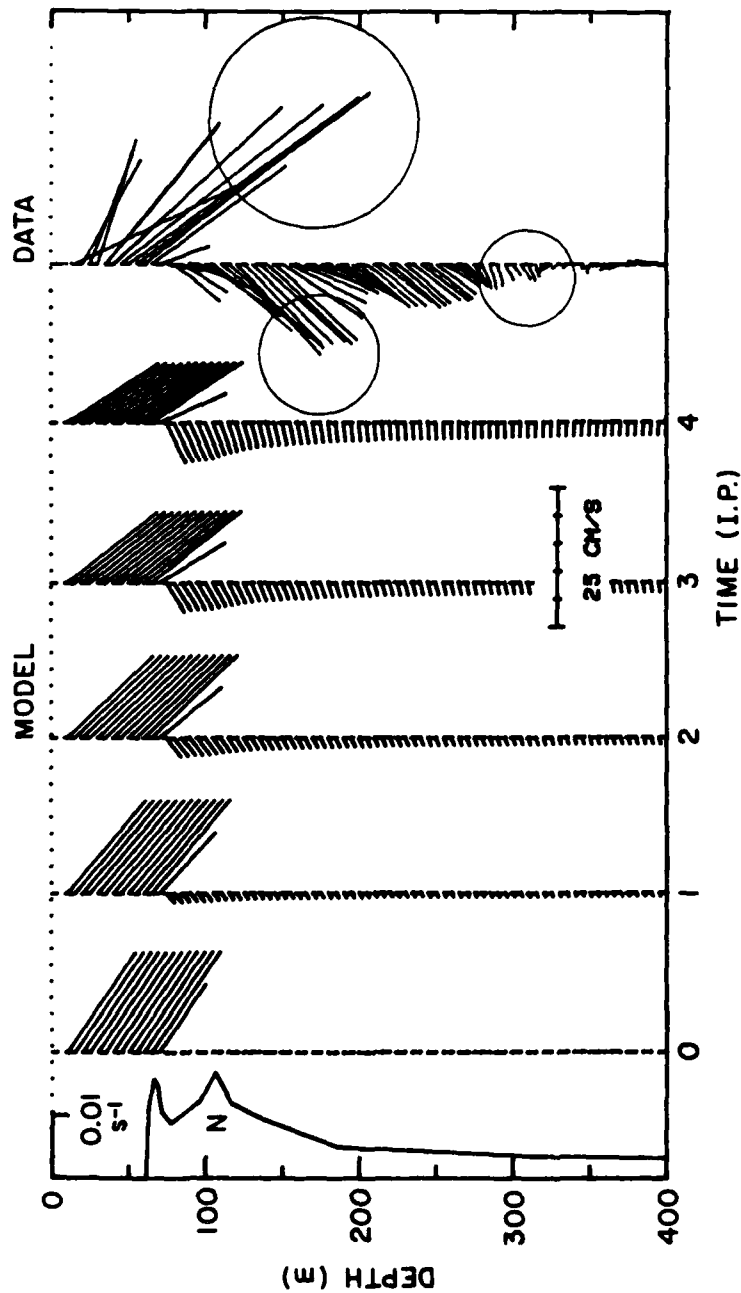
Fig. 5. Simulated and measured inertial currents generated by the STREX cold front. The linear internal wave equations are solved as an initial value problem with the N profile shown on the left. The amplitude of the initial slab-like inertial velocity profile, plotted at t = 0, is estimated from wind data. The model solutions are shown at the start of each inertial period. The actual response of the ocean is estimated from the difference between the pre-storm and post-storm average inertial velocity profiles as shown on the right with 77% confidence circles. This should be compared with the simulated profiles at t = 3 or 4 inertial periods.

actually generated by the storm are estimated as the difference between the average pre-storm and post-storm inertial velocity profiles (right-most profile, Fig. 5). These should be directly comparable to the simulated profiles at t = 3 or 4 inertial periods.

Clear similarities between the model and the data are apparent. The direction and magnitude of the model currents are comparable to measured currents. The relative magnitudes of the mixed layer currents and the currents below the mixed layer are roughly the same as those predicted by the model. The currents below the mixed layer are roughly 90° clockwise of those in the mixed layer, as predicted by the model. Several significant differences between the data and the model results are apparent. The measured currents decay to nearly zero by a depth of 400 m, in contrast to the simulated currents, which decay much more slowly. The model currents are significantly smaller than those computed using the data. The model simulations show the relative angle between the mixed layer currents and the upper thermocline currents to be somewhat larger than 90°. The data show an angle somewhat less than 90°. These differences appear to be within the measurement error as indicated by the 77% confidence circles.

In summary, the model simulations agree qualitatively with the data. The quality of the data is sufficiently poor that the observed differences are as likely due to statistical noise as to physical differences between the model and the ocean. The limited agreement does suggest, however, that a linear internal wave model may be useful in describing the evolution of storm forced inertial motions in the upper ocean. Clearly, better data, both of the oceanic inertial motions and of the atmospheric forcing, are needed.

INTERACTION OF NEAR-INERTIAL MOTIONS WITH SMALLER SCALES-- RICHARDSON NUMBERS

Shear instability induced by internal waves is commonly assumed to play a major role in ocean mixing. A key parameter in this process is the Richardson number, $Ri = N^2/S^2$, for local buoyancy frequency N and shear S. Locally in space and time, it is perhaps reasonable to assume that mixing will occur whenever $Ri < 0.25$. The average amount of mixing should depend, however, on some average Richardson number, in a manner that is presently unknown. Desaubies and Smith (1982) assume Gaussian statistics and a constant spectral shape for the internal wave field and find that the average mixing rate is a strong function of an average Richardson number $Ro = <N^2>/<S^2>$, the ratio of average squared buoyancy frequency to average squared shear.

Profiles of N^2, S^2 and Ro, computed over 10 m, are shown in Fig. 6 for the pre-storm STREX data. Below 200 m, Ro is nearly constant with a value of about 2.5. Above 50 m, Ro is much less than 1, as would be expected within the mixed layer. Ro falls below its deep water value above about 75 m, indicating enhanced mixing 10-20 m below the bottom of the mixed layer. The inertial frequency shear S_I is large in this same region, suggesting that the reduced value of Ro is due to the additional inertial shear. If Ro is computed using only the noninertial shear, i.e., $R_H = N^2/(S^2 - S_I^2)$, R_H does not fall significantly below its deep water value until the base of the mixed layer is reached. The same pattern is evident at a secondary peak in the inertial shear at about 150 m and in the post-storm data (Fig. 7). The variations in
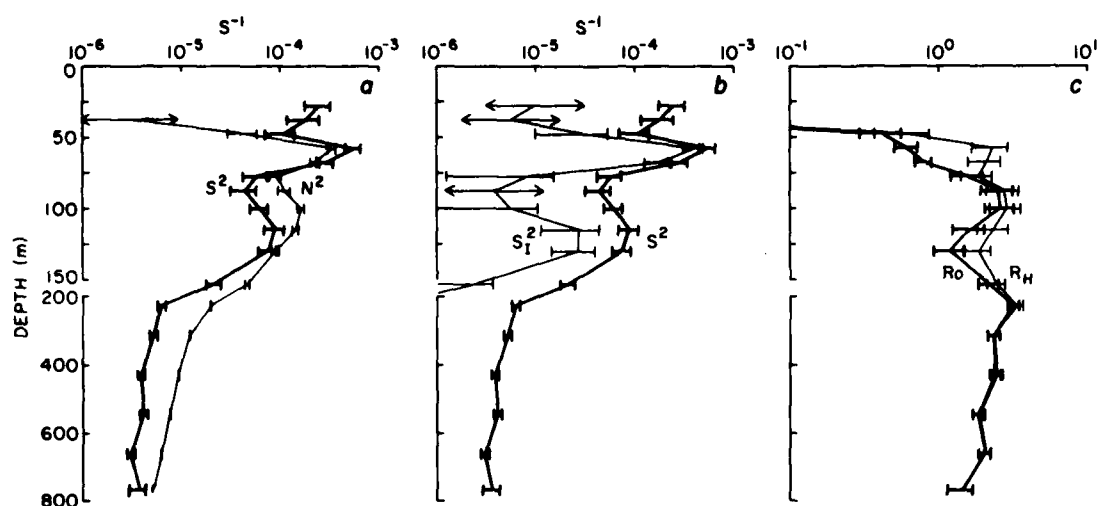
Fig. 6. STREX Richardson number profiles for pre-storm data. a) Average buoyancy frequency squared (N^2, light line) and average squared shear (S^2, heavy line). b) Inertial shear S_I squared (light line) and S^2 (heavy line). c) "Average" Richardson numbers $Ro = N^2/S^2$ (heavy line) and $R_H = N^2/(S^2 - S_I^2)$. Error bars represent 95% confidence limits; arrows indicate very large errors. Profiles have been shifted in depth so that maximum of N is at 60 m for each profile; depths are therefore not absolute to better than 10 m. Also note the split depth scale.
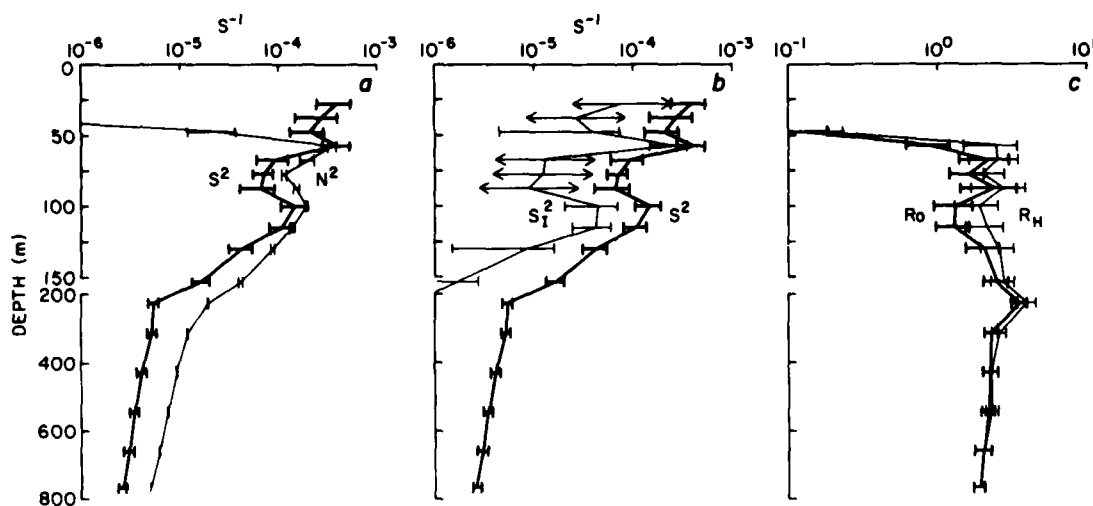
Fig. 7. STREX Richardson number profiles for post-storm data.

108

Ro are almost entirely due to variations in S_I, the inertial part of the shear. These data are consistent with a model in which the oceanic shear field is the sum of a steady component, characterized by a value of $Ro \approx 2.5$, and a variable inertial frequency component. If the rate of turbulent mixing is indeed governed by Ro, this implies a background mixing rate due to noninertial shear, and a variable mixing rate that depends on the inertial shear.

INTERACTION WITH GEOSTROPHIC FLOWS

Recent measurements of near-inertial waves in fronts and eddies have revealed significant correlations between the waves' energy level and location
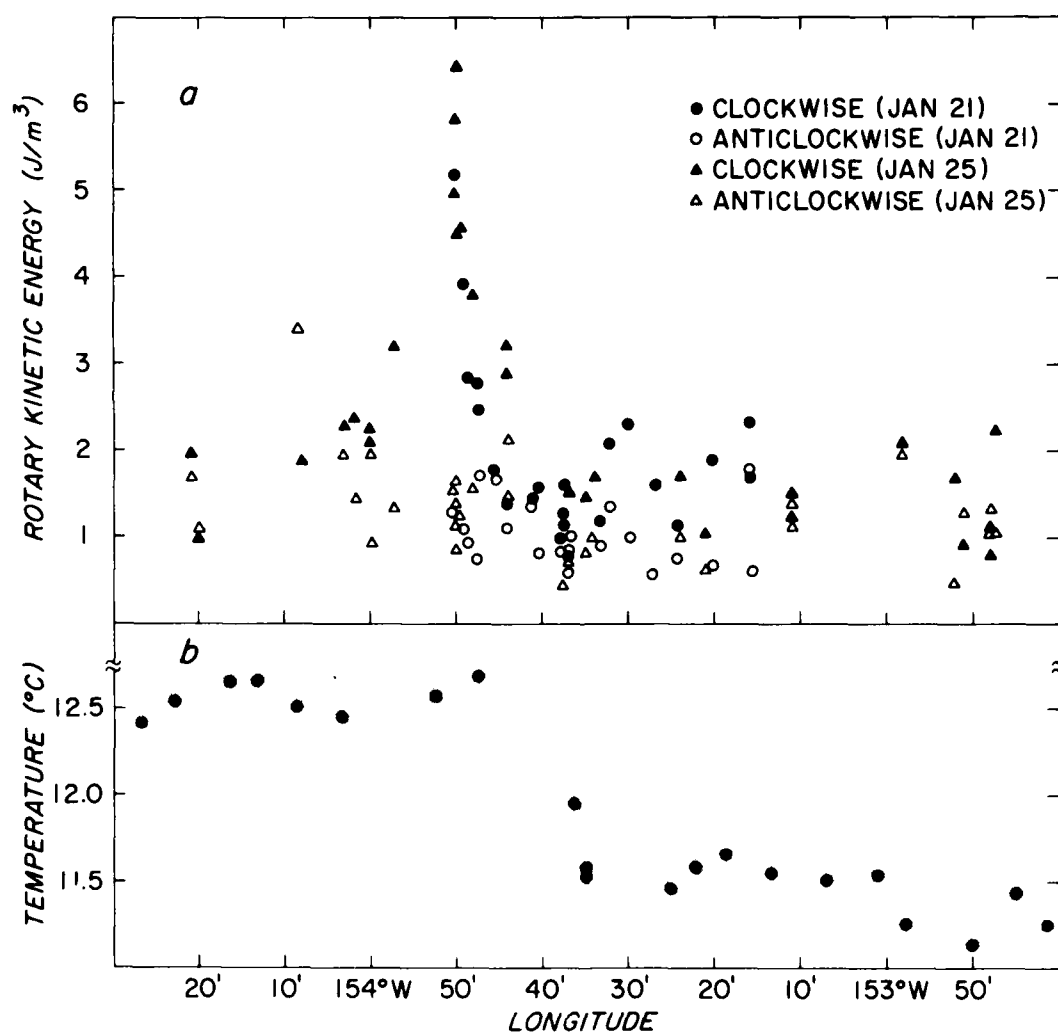
Fig. 8. a) Near-inertial energy in the subtropical front as a function of position perpendicular to the front. Dark symbols denote the velocity component rotating clockwise with depth (downward propagating); light symbols denote the velocity component rotating anticlockwise with depth. b) The average temperature from 180 m to 300 m (from Kunze and Sanford, 1984).

in the geostrophic flow. Kunze and Sanford (1984) measured the energy density of downward- and upward-propagating near-inertial waves in the subtropical front. A strong peak in downward-propagating energy was found on the warm edge of the front (Fig. 8). They offer the following explanation: Away from the front, free internal waves can exist with frequencies as low as f. In a geostrophic flow they exist down to a frequency $f + \zeta/2$, where ζ is the geostrophic relative vorticity. On the warm edge of the front, ζ is negative and the waves can exist at a frequency lower than f. A free wave generated in the negative vorticity region, or scattered into it by nonlinear processes, cannot propagate out because its frequency is too low. This is seen in ray tracing calculations (Fig. 9). Waves generated in the negative vorticity region
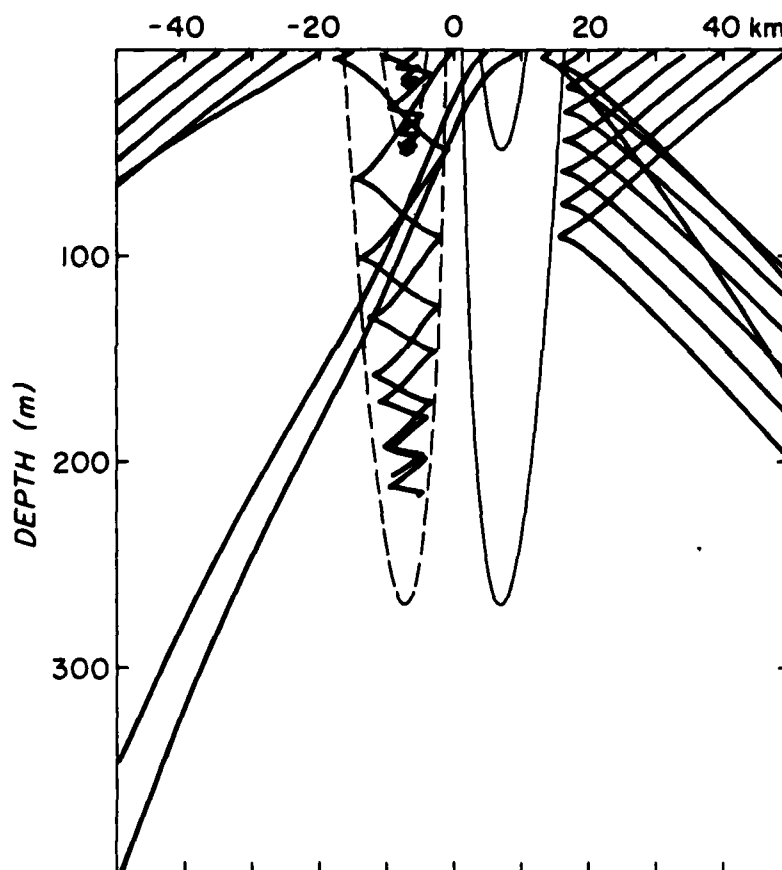
Fig. 9. Paths of internal wave rays in a two-dimensional geostrophic jet similar to the subtropical front. Rays start at the surface and terminate as they approach a critical layer. Rays propagate at right angles to the front. Contours of relative vorticity are shown, dashed for negative. Notice that waves generated within the negative vorticity region are trapped (from Kunze and Sanford, 1984).

110

that attempt to propagate horizontally are reflected at horizontal turning points. As these waves propagate downward their vertical wavelength decreases and their energy density increases, until they encounter a critical layer where their energy is presumably dissipated by turbulent processes. These theoretical considerations predict a concentration of inertial wave energy in regions of negative ζ, and a corresponding increase in turbulent kinetic energy dissipation.
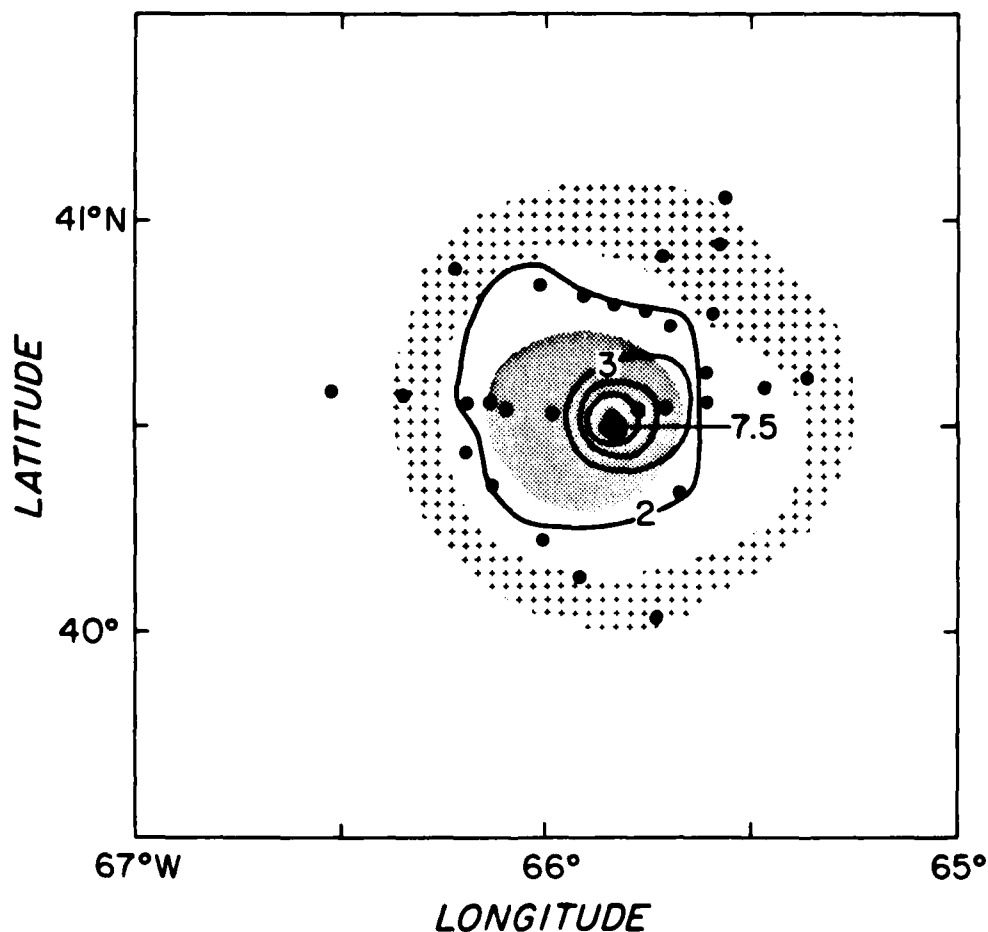
Fig. 10. Internal wave energy density in a warm core Gulf Stream ring. Dots show XCP stations. Contours of the clockwise (downward propagating) kinetic energy from approximately 400 m to 800 m are plotted. Darker shading indicates regions of negative relative vorticity; lighter shading indicates regions of positive relative vorticity; unshaded areas indicate uncertainty as to the sign of the relative vorticity. Internal wave energy has been separated from geostrophic velocity by removing a quadratic fit from each velocity profile (E. Kunze and T. Sanford, personal communication).

Measurements made in several warm core rings confirm these predictions (E. Kunze and T. Sanford, personal communication). The center of a warm core ring is a region of negative ζ. As predicted, it is also a region of high inertial wave energy (Fig. 10). Measurements of turbulent kinetic energy dissipation in a similar ring show a maximum at the depth predicted by ray calculations. Correspondingly, the center of a cold core ring should be a region of low inertial wave energy. Recent measurements also confirm this prediction.

These results show a strong interaction between near-inertial internal waves and the geostrophic flow field. This provides a mechanism by which the geostrophic flow can intensify the inertial wave field at certain locations. Coupled with the Richardson number results just discussed, these results suggest that the rate of small-scale mixing is related to the mesoscale eddy field. It may therefore be possible to parameterize the mixing rate in terms of mesoscale quantities.

CONCLUSION

During the 1970's internal wave research concentrated on describing the universal aspects of internal waves, expressed in the statistical language of the universal internal wave spectrum. These recent studies of internal waves near the inertial frequency highlight the deterministic and space-time aspects of the internal wave field. Significant deterministic signals clearly exist. The energy level and spectral characteristics of the near-inertial waves vary. The studies described here show that at least some of this variation is clearly attributable to the sources (wind, mean flow) and sinks (critical layers) of the wave field. Ultimately, a hybrid picture of the internal wave field is likely: In source and sink regions, the deterministic signals will be dominant; here, the wave field will reflect the local environment. Away from these regions, the stochastic nature of the internal wave field will be dominant; here, the wave field will reflect the integrated effect of many sources and sinks, modified by the propagation of the waves. However, as pointed out by Wunsch (1973) over a decade ago, the physics of internal waves will be clearest in the source and sink regions; it is here that additional measurements will be most useful.

REFERENCES

D'Asaro, E. A., 1984: Wind forced internal waves in the North Pacific and Sargasso Sea, J. Phys. Oceanogr., in press.

D'Asaro, E. A., and H. T. Perkins, 1984: A near-inertial internal wave spectrum for the Sargasso Sea in late summer, J. Phys. Oceanogr., in press.

Desaubies, Y., and W. K. Smith, 1982: Statistics of Richardson number and instability in oceanic internal waves, J. Phys. Oceanogr. 12(11), 1245-1259.

Fu, L. L., 1981: Observations and models of inertial waves in the deep ocean, Rev. Geophys. and Space Phys. 1a(1), 141-197.

112

Garrett, C. J. R. and W. Munk, 1979: Internal waves in the ocean, Ann. Rev. Fluid Mech., 11, 339-369.

Gill, A., 1984: On the behavior of internal waves in the wakes of storms, J. Phys. Oceanogr., submitted.

Greatbatch, R. J., 1983: On the response of the ocean to a moving storm: The non-linear dynamics, J. Phys. Oceanogr., 13(3), 357-367.

Hamilton, G.D., 1980: NOAA Data Buoy Office programs. Bull. Am. Met. Soc., 61, 1012-1017.

Kunze, E., and T. B. Sanford, 1984: Observations of near inertial waves in a front, J. Phys. Oceanogr., in press.

Leaman, K. D., and T. B. Sanford, 1975: Vertical energy propagation of inertial waves: a vector spectral analysis of velocity profiles, J. Geophys. Res., 80(15), 1975-1978.

Leaman, K. D., 1976: Observations on the vertical polarization and energy flux of near-inertial waves, J. Phys. Oceanogr., 6(6), 894-908.

Pollard, R. T., and R. C. Millard, 1970: Comparison between observed and simulated wind generated inertial oscillations, Deep-Sea Res., 17, 813-821.

Price, J. F., 1983: Internal wave wake of a moving storm. Part 1: Scales, energy budget and observations, J. Phys. Oceanogr., 13(6), 949-965.

Webster, F., 1968: Observations of inertial-period motions in the deep sea, Rev. Geophys., 6, 473-490.

Wunsch C., 1975: Deep ocean internal waves: what do we really know? J. Geophys. Res., 80(3), 339-343.

THE WAVENUMBER FREQUENCY SPECTRUM OF THE INTERNAL WAVEFIELD

R. Pinkel

University of California, San Diego Marine Physical Laboratory of the Scripps
Institution of Oceanography, La Jolla, California 92093

ABSTRACT

In May 1980 an eighteen-day sequence of velocity profiles of the top 600 m of the sea was
collected off the coast of Southern California. The measurements were obtained using a
pair of Doppler sonars mounted on the Research Platform FLIP. From these data,
estimates of the wavenumber-frequency spectrum of the oceanic internal wavefield are
obtained. The spectra are characterized by a series of ridges, which occur at near-inertial
and tidal frequencies as well as higher harmonics and sums of these fundamentals. The
ridges run parallel to the wavenumber axis. There is a pronounced near-inertial spectral
peak. The near-inertial motions are dominated by a few identifiable wave groups. There is
a net downward energy propagation in the near-inertial frequency band. The wavenumber
dependence of the spectrum is decidedly asymmetric in this region. Surprisingly, the
asymmetry extends to five times the inertial frequency, making much of the so-called
continuum asymmetric. A high wavenumber cut-off at approximately 60-m vertical
wavelength extends from the inertial frequency to approximately 8 cycles per day. The
changing form of the wavenumber dependence of the spectrum with frequency frustrates
any simple attempt to assign a scale wavenumber bandwidth to the spectrum.

INTRODUCTION

Internal waves are found throughout the ocean interior. They are properly described by a
four-dimensional wavenumber-frequency spectrum, $E(\bar{k}, \omega)$. To resolve this spectrum a
set of measurements dense in both spatial and temporal separations is necessary.
Measurements such as these are difficult to obtain. At Scripps, Doppler sonar technology
was developed for this purpose. A sonar provides an estimate of the component of oceanic
(scatterer) velocity parallel to the sonar beam as a function of range. Maximum ranges of
order 1 km can be achieved, with 20-m range resolution (Pinkel, 1981).

In May of 1980 four such sonars were mounted on the research platform FLIP and
operated for an 18-day period in the deep sea approximately 400 km west of San Diego.

114

Two of the sonars, pointed 45° downward and at right angles to each other, obtained slanting profiles of the velocity field to a depth of 600 m. These repeated profiles can be Fourier transformed in both time and depth to provide an estimate of the slant-wavenumber frequency spectrum, $E(k, \omega)$. At frequencies low compared to the local Väisäla frequency, N, this spectrum is related to the vertical wavenumber spectrum of horizontal velocity by a multiplicative constant. These spectral estimate is resolved in sufficient detail that interesting observations can be made without the assistance of a specific spectral model.

This paper discusses the wavenumber-frequency spectra estimated from the downward slanting sonar data. It is an abstracted version of a more lengthy work (Pinkel, 1984), presenting material covered orally at the Conference. A companion paper (Pinkel, 1983) describes these data in the depth-time and depth-frequency domain. The experiment is reviewed briefly in the next section. The method of spectral analysis is then described and the wavenumber frequency spectra are presented.

MEASUREMENTS

The observations were made during an 18-day period in May 1980 as FLIP drifted southward in the California Current. Measurements commenced at approximately 30°50'N, 124°0'W and concluded at 28°40'N, 124°0'W, approximately 100 km to the south. During this period FLIP's azimuthal orientation was regulated by a thruster system linked by a standard auto-pilot to the ship's gyrocompass. This enabled azimuthal stability in the orientation of the sonar beams. Heading stability was maintained to ± 3° for the majority of the observing period. Excursions up to ± 30° occurred occasionally, during squalls or major wind shifts.

Equipment on board FLIP included a profiling current meter system (Weller, 1984) a profiling CTD (Pinkel, 1975), the sonar system, and a number of environmental sensors.

The downward-slanting Doppler sonars were mounted at a depth of 38 m and operated at frequencies of 70 and 75 kHz. During the course of the experiment the 70-kHz sonar was nominally directed toward 235° true, while the 75-kHz sonar pointed toward 145° T. Accurate slant velocity estimates were achieved over the depth range of 80 to 600 m. Maximum range was limited by electronic noise in the sonar receive system. A more complete description of the experiment is presented in Pinkel, 1983.

The response of the sonar measurements to the internal wavefield is complicated by the geometric properties of the instruments, which only measure the component of velocity parallel to the beam, and by those of the wavefield (Pinkel, 1981). If the downward slant angle of the sonar beam is steep compared to the slope of the internal wave rays, a vertical profile of the wavefield is effectively achieved. Since internal wave ray slopes depend on wave frequency, and steepen with increasing frequency, only the lower-frequency waves sensed by a fixed sonar have this simple interpretation. Given the 45° downward angle of the sonar beams used in 1980, effective vertical profiles are achieved for motions of frequency $\omega \ll N/\sqrt{2}$. For simplicity in interpretation, only frequencies below this value are considered in the present analysis.

To illustrate the nature of the data set, a series of hourly averaged profiles of slant velocity is presented in Fig. 1 for the first week of the cruise. Flat spots in the figure correspond to intervals when the sonar was not operating. Dominant contributors to the velocity field are near-inertial motions. Smaller scale higher frequency motions are also present, although more difficult to track in the confused near-inertial sea. Much of the irregularity of Fig. 1 disappears when the data are plotted differently. Figures 3 and 4 of Pinkel (1983) present these identical data in the form of color contour maps of velocity and shear. In these representations considerable structure can be seen in the near-inertial motions.

SPECTRAL ANALYSIS

The acoustic data were divided into two segments, corresponding to observation intervals of 4-11 May and 12-23 May. During the first observing interval, pulses of 32-ms duration were transmitted. These resulted in a range resolution of 24 m and a depth resolution of 17 m. (Subsequent averaging in range degraded this nominal resolution, however). Average velocity profiles were formed at five-minute intervals. During the second observing period, 40-ms pulses were transmitted, corresponding to range and depth resolution of 30 m and 21.4 m, respectively. Average profiles were formed at 5.6-minute intervals.

The velocity data series were first differenced in time, and the series means were removed. Gaps in the time records were zero filled. The time series were then multipled by a triangular data window and digitally Fourier transformed. Complex "depth series" were obtained in 1200 frequency bands, at frequency increments of 0.1 cpd, for both data collection intervals.

An attempt was made to reduce the effects of refraction due to depth variations in Väisäla frequency, using the now-standard technique of WKB stretching. The velocity Fourier coefficients were weighted by the factor:

$$WT = C_1/(N^2(z)-\omega^2)^{1/4}$$

where the constant C_1 was chosen such that the integral WT^2 over the depth range to be Fourier transformed was equal to unity. Similarly the depth was stretched such that:

$$dz_s = dz \,^*C_2 \, (N^2 \, (z)-\omega^2)^{1/2}$$

The constant C_2 was chosen such that the total vertical aperture of the array was the same whether in stretched or unstretched units.

In each frequency band, the complex depth series was WKB weighted and first differenced in depth. The complex depth mean was then removed and the series was multiplied by a triangle window. Note that the data are not equally spaced in "stretched depth" as they originally were in actual depth. A (slow) digital Fourier was again employed to implement the Riemann Sum:

$$A(\omega,k) = \sum_{z=z_o}^{z_{max}} WDO(z) \, A(\omega,z_s) \, e^{ikz_s} \, dz_s$$

116

The maximum depth, z_{max}, was adjusted frequency by frequency such that only depths where $\omega < N(z_{max})$ were transformed. Typically forty-five depths were included in the vertical transform. Fourier coefficients were produced at 1/1500-cpm increments in wavenumber.
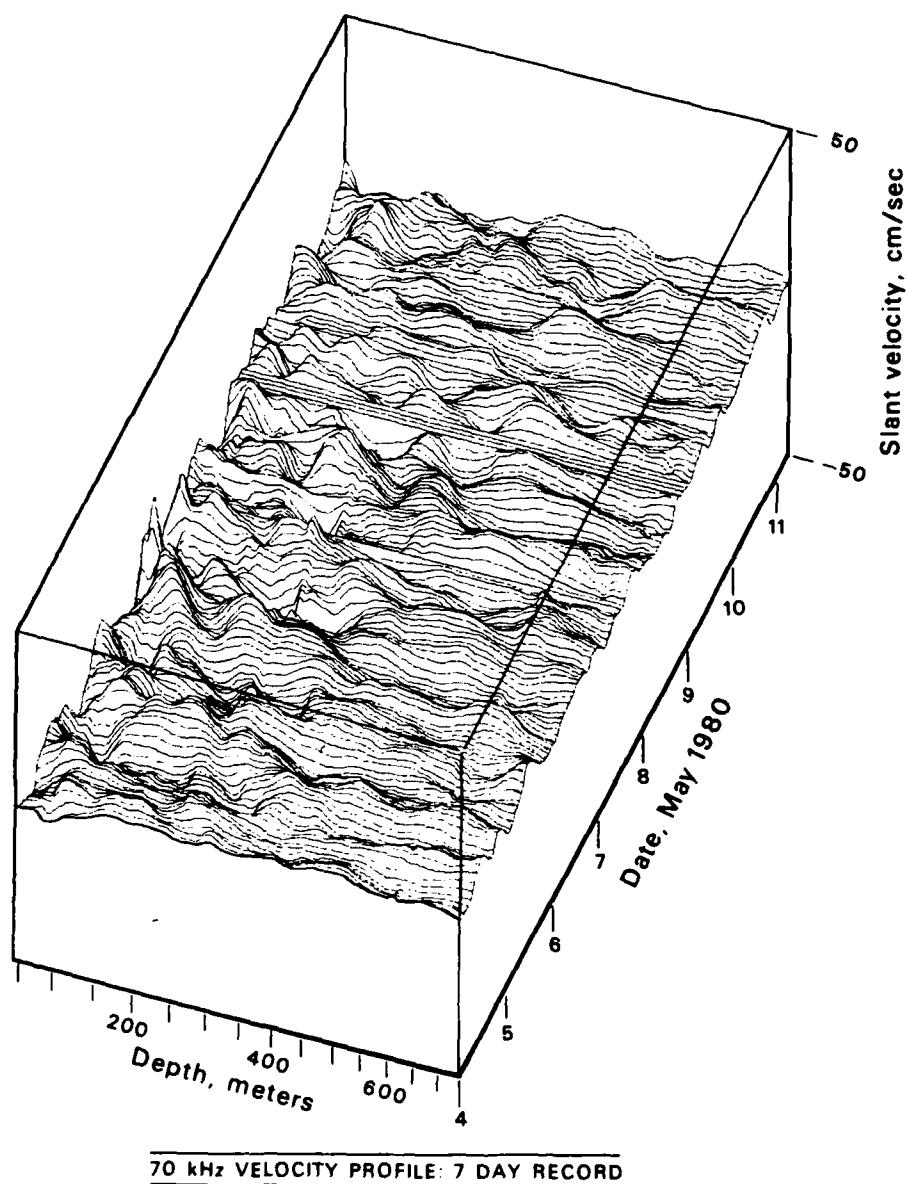

70 kHz VELOCITY PROFILE: 7 DAY RECORD

Fig. 1. A one-week series of hourly averaged velocity profiles obtained from the 70 kHz sonar. The depth scale and the velocity magnitudes have been Väisäla stretched. Near-inertial waves dominate the field of motions. Flat spots in this deformed surface record correspond to periods when the sonar was not operating.

An analytical model of the local Väisäla profile was used in the WKB stretching.

$$N(z) = N_0 e^{-bz}$$

$$N_0 = 6cph$$

$$b = 1\ km^{-1}$$

Other models of the Väisäla profile were tried, as well as the actual, measured profile. The resulting spectral estimates proved quite insensitive to the particular form of the Väisäla profile used and to the details of the stretching.

The complex Fourier coefficients were squared, averaged, recolored, and normalized to produce the various (two-sided) spectral estimates. Data from both observing intervals were averaged together to improve the statistical precision of the estimates. Separate wavenumber frequency spectra have been estimated using data from each of the slant sonars. Discussion in the text is confined to the 70 and 75 kHz wavenumber frequency spectra. The implications of these measurements are presented in greater detail in Pinkel, 1984.

Given the short duration of the experiment the spectra represent an essentially deterministic description of the specific low-frequency (near-inertial) wave groups which passed under FLIP during the cruise. At high frequencies, the statistical significance of the spectral estimates becomes large. In principle, these high-frequency spectral estimates should be representative of the typical oceanic wavefield. However, the high-frequency waves might well be modified by the specific low-frequency background through which they propagate. In this event, the conceptual link between "global representativeness" and "degrees of freedom" is not valid.

The spectra $E(k, \omega)$ are presented in three different formats in this paper:

1. Spectral Cross Sections

The spectrum $E(k, \omega)$ is plotted vs. k for a set of fixed frequencies. Statistical stability is achieved by averaging in frequency.

2. Logarithmically Averaged Two-Dimensional Spectra

The squared Fourier coefficients are averaged over bins in both frequency and wavenumber. The averaging interval increases logarithmically with both ω and k. The resulting spectral estimates have 4 degrees of freedom in the lowest ω-k bands and several hundred degrees of freedom at large ω, k. Again, the spectral estimates can be viewed as snapshot quantifications of the low frequency-low wavenumber motions which happened to occur under FLIP during the experiment. At high frequency and wavenumber the "statistical significance" of the estimates is greater, in principle.

3. Frequency-Smoothed Logarithmically Averaged Spectra

One of the striking features of the logarithmically averaged spectra is a series of ridges which run parallel to the wavenumber axis at fixed frequencies. The ridges are sufficiently

strong to obscure much of the underlying form of the spectrum in the frequency band between the semi-diurnal tide and 1 cph. In order to compare the oceanic spectral estimates with the Garrett Munk model spectrum, which did not anticipate these ridges, additional smoothing in frequency is necessary. The frequency smoothing enables a clear look at the resulting continuum (i.e., the spectrum which is forced to appear continuous by the smoothing process).

Deformed surface plots of the 70 and 75 kHz spectral estimates are presented in Figs. 2 and 3. Contour maps of the frequency smoothed log-log averaged data are presented in Figs. 4 and 5. Spectral cross-sections are presented in Fig. 6. A discussion of various aspects of these spectra is given next.

DISCUSSION: SPECTRAL ESTIMATES

The Wavenumber Frequency Spectrum

Deformed surface plots of the log-log averaged spectra from the 70 kHz sonar and 75 kHz sonar are presented in the top halves of Figures 2 and 3. The spectra are essentially red in frequency for frequencies greater than inertial. They are also red in wavenumber except near the inertial frequency, where a broad band of wavenumbers is energetic. The total integrated variance of the spectra is 19.7 cm^2/sec^2 for the 70 kHz spectrum of downward propagating energy (henceforth referred to as a downward spectrum), 15.9 cm^2/sec^2 for the spectrum of upward energy propagation (upward spectrum), 18.7 cm^2/sec^2 for the 75 kHz downward spectrum, and 13.8 cm^2/sec^2 for the 75 kHz upward spectrum. These variance estimates are underestimates of the total wavefield variance. They represent the contribution due to motions of vertical wavelength 600 m and less. Longer wavelengths contribute variance to the zero wavenumber band of the spectrum, which is not plotted. Since FLIP drifted freely during this experiment, only motions which vary significantly over the vertical aperture of the array can be distinguished from the signal of FLIP's drift. As the navigation was not sufficiently precise to remove the drift signal, the zero wavenumber band has been neglected. The spectra drop into the noise at high frequency and high wavenumber. The observed level implies an integrated noise variance of $\sim$ 2 cm^2/sec^2, assuming a white noise spectrum.

Spectral Ridges

The deformed surface plots of the spectra are dominated by a series of ridges, which run parallel to the wavenumber axis at several frequencies. The lowest frequency ridge corresponds to near-inertial motion. A broad band of near-inertial wavenumbers is energetic. Higher frequency ridges correspond to the baroclinic tide and what might be harmonics of the tidal and inertial frequencies (Pinkel, 1983). The fact that these possible harmonics stand out at low wavenumber, but not at high indicates a steeper spectral slope (in wavenumber) for these ridges than for the regions between the ridges. The vertical coherence of the wavefield, which is related to the wavenumber bandwidth of the spectrum, should correspondingly be greater for the ridges than between them. This is seen in Pinkel, 1983.

Fig. 2. Wavenumber frequency spectral estimates obtained from the 70 kHz sonar (direction 235°). The upper spectrum has been logarithmically averaged in both wavenumber and frequency. The lower spectrum has been additionally smoothed in frequency to supress the series of ridges which parallel the wavenumber axis. At low frequencies, a high wavenumber cut-off is seen at slant wavenumber of order k_z = 0.01 cpm.

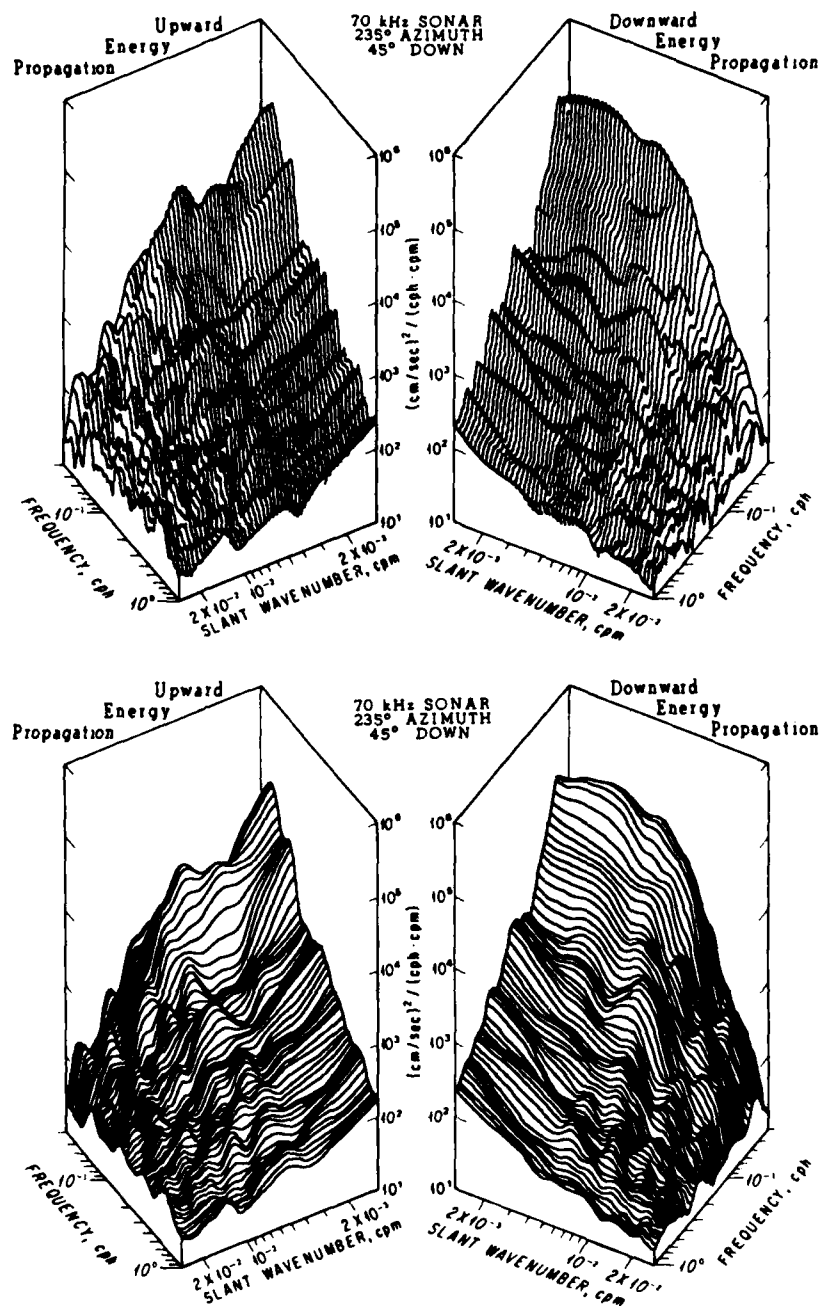Fig. 3. Wavenumber frequency spectral estimates obtained from the 75 kHz sonar (direction 145°). The upper spectrum has been logarithmically averaged in both wavenumber and frequency. The lower spectrum has been additionally smoothed in frequency, to supress the series of ridges which parallel the wavenumber axis. At low frequencies, a high wavenumber cut-off is seen at slant wavenumber of order kz = 0.0l cpm.
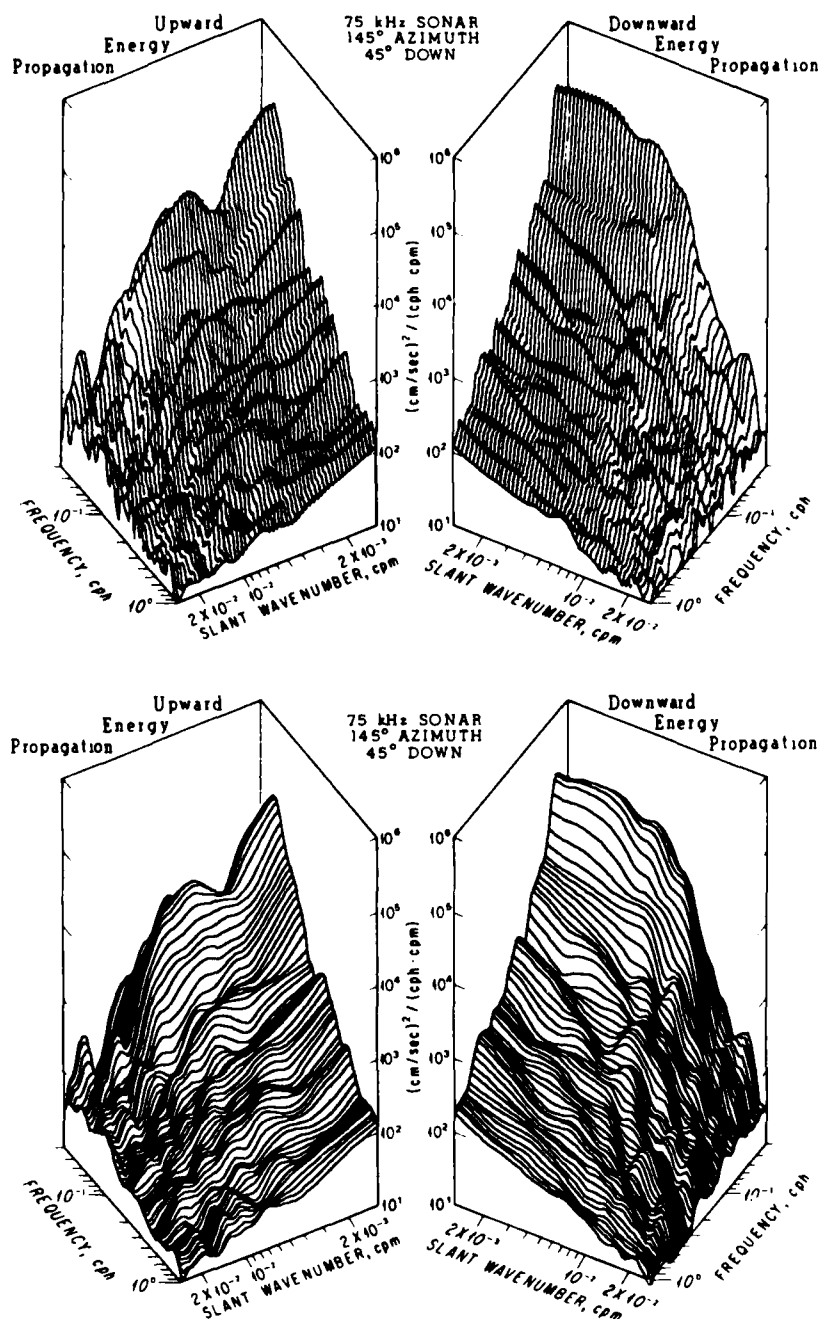
In part, the regularity of these ridges is due to the poor resolution of the spectrum at low wavenumber. The log-log averaging process obscures the fact that independent estimates of the spectrum are much more widely spaced (on a log-log plot such as this) at low frequency and wavenumber than at high. Nevertheless, there is no corresponding set of ridges paralleling the frequency axis, an artifact of log averaging in frequency. The point is that the irregularities in these spectra are not symmetric with respect to the ω-k axes. This symmetry would be expected if the irregularities were strictly due to statistical imprecision in the spectral estimates.

Spectral Shoulder

The ridges make it difficult to visualize the underlying form of the spectrum. To see this form, the log-log averaged portraits were further smoothed in frequency, forcing the spectrum to appear continuous. The frequency-smoothed log-log averaged spectra are displayed in Figs. 2 and 3 (lower) as deformed surface plots, and in Figs. 4 and 5 (upper) as contour maps. The interesting feature which emerges from the smoothing is a distinct change in the slope of the spectrum with wavenumber. This occurs at a slant wavelength of approximately 100 m. The change is frequently preceded by an irregularity in the spectrum reminiscent of the pre cut-off peak which is found in frequency spectra of internal waves just prior to the Väisäla cut off. This wavenumber pre cut-off spectral shoulder extends continuously from the inertial frequency band up to 0.5 cycles per hour, with little change in wavenumber. The slope of the spectrum with wavenumber is very steep in the region of the cut-off, exceeding k^{-5} in some instances.

The spectral shoulder and high-wavenumber cut-off were first seen in temperature profiling data also taken from FLIP (Pinkel, 1975, Figs. 16-18). They would appear to be a ubiquitous feature of the spectrum and a strong clue to the physics of the wavefield.

Separability

Garrett and Munk hypothesized that the wavenumber dependence of the spectrum does not change with frequency, except for perhaps a scale factor. This hypothesis can be investigated by plotting cross sections of the spectrum with wavenumber at a set of fixed frequencies. A set of cross sections is presented in Fig. 6 for the 70 and 75 kHz spectra. Cross sections are given at octave increments with center frequencies of 1,2,4,8,16,32, and 64 cpd. The averaging bandwidth about these center frequencies is increased with increasing center frequency. Note that at 64 cpd, these data can no longer be thought of as vertical profiles of horizontal velocity. Nevertheless, no dramatic change in spectral form is seen.

It is interesting that differences in these cross sections are more pronounced between upward and downward propagation direction than between azimuthal directions. In the near-inertial cross sections, motions with downward energy propagation are energetic over a wide range of wavenumbers, with maximum energy density at slant wavelengths of 500 m. Energy levels are uniformly greater for the downward propagating than for upward
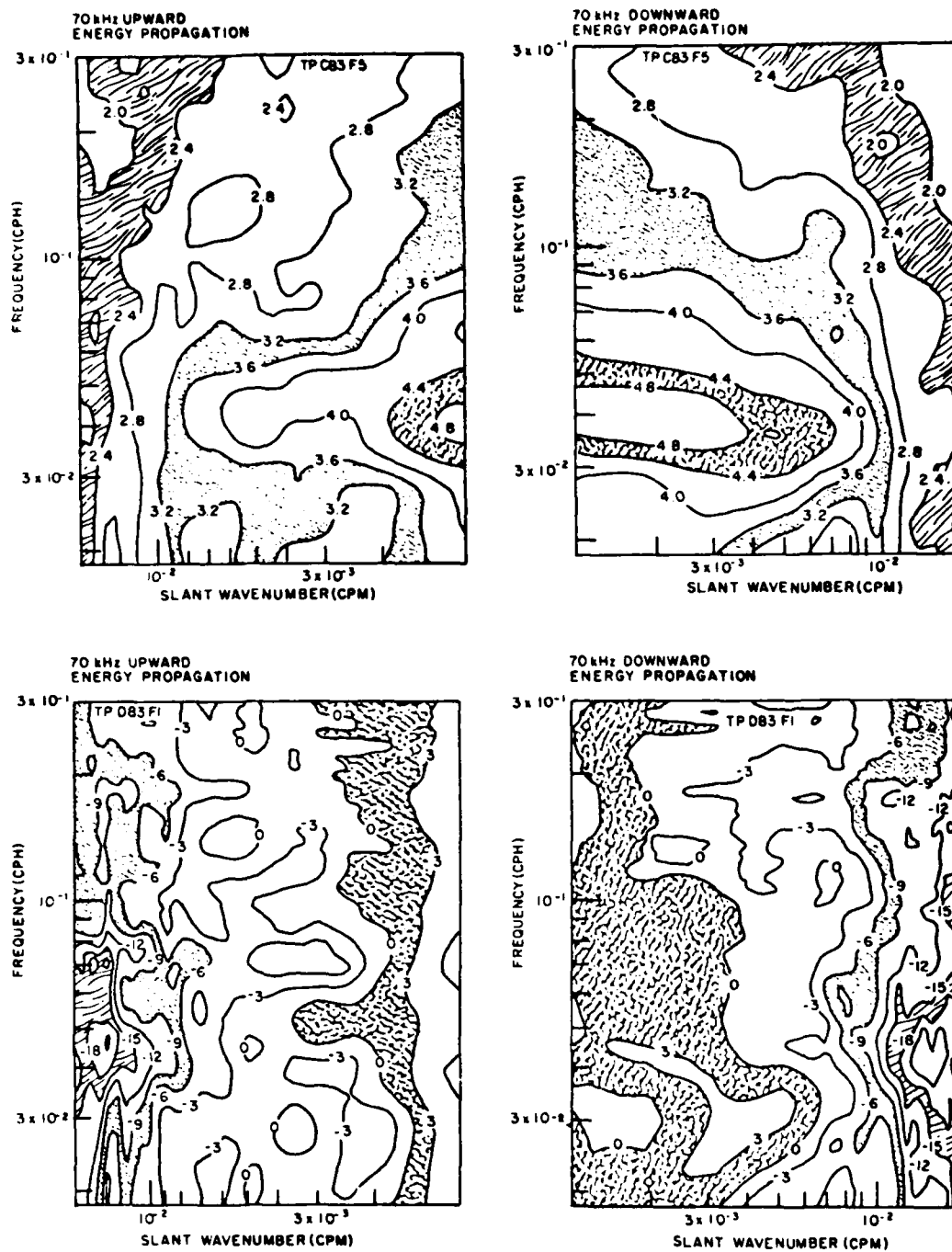
Fig. 4. Contour map of the frequency-smoothed log averaged spectral estimates from the 70 kHz sonar (top). This spectrum is presented as a deformed surface plot in Fig. 2 (bottom). A contour map of the dimensionless 70 kHz spectrum normalized such that

$$\frac{1}{k_{max}} \int_0^{k_{max}} E(k,\omega)dk = 1$$

for all ω (bottom). This enables comparison of the wavenumber dependence of the spectrum at different frequencies. For the upward spectrum, contour lines run parallel to the frequency axis, except near the inertial frequency. This is not the case with the downward spectrum. The highest contours diverge from the frequency axis with decreasing frequency, suggesting a wavenumber "bandwidth" which grows with decreasing frequency.
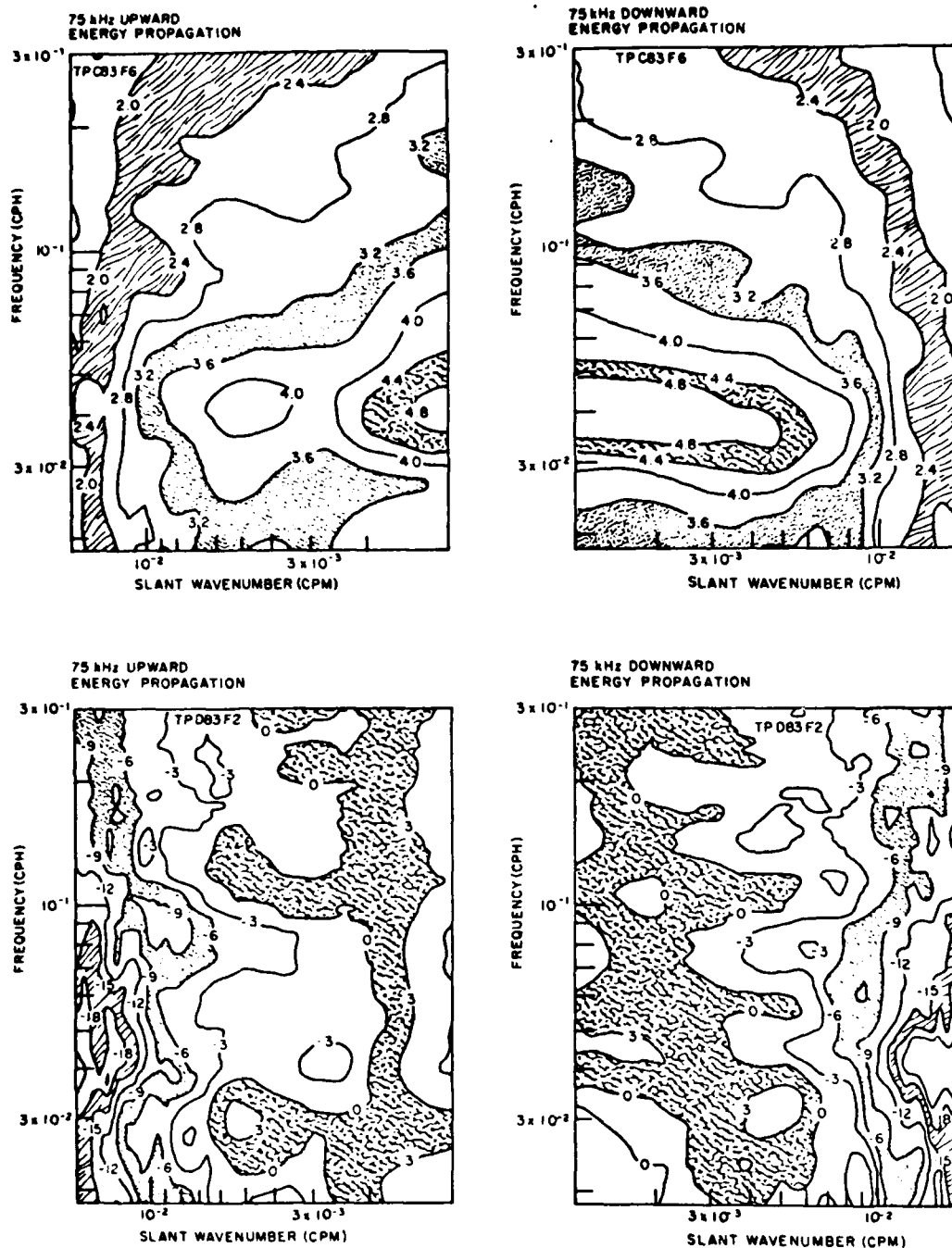
Fig. 5. Contour map of the frequency-smoothed log averaged spectral estimate from the 75 kHz sonar (top). This spectrum is presented as a deformed surface plot in Fig. 3 (bottom). A contour map of the dimensionless 75 kHz spectrum, normalized such that

$$\frac{1}{k_{max}} \int_0^{k_{max}} E(k,\omega)dk = 1$$ for all ω (bottom). This enables comparison of the wavenumber dependence of the spectrum at different frequencies. For the upward spectrum, contour lines run parallel to the frequency axis, except near the inertial frequency. This is not the case with the downward spectrum. The highest contours diverge from the frequency axis with decreasing frequency, suggesting a wavenumber "bandwidth" which grows with decreasing frequency.

124
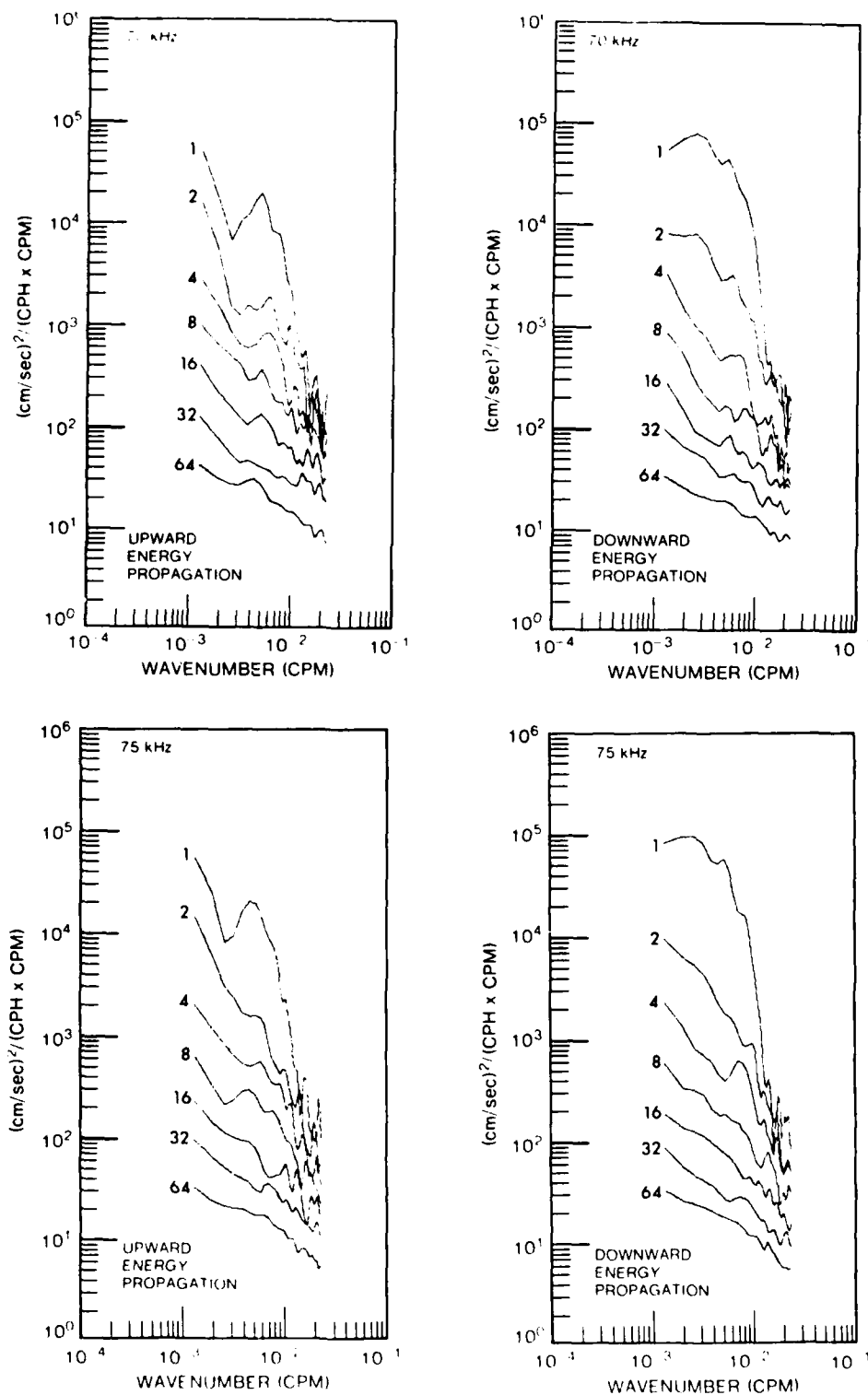
Fig. 6. Cross sections of the 70 and 75 kHz wavenumber frequency spectra. Sections are taken at frequencies of 1, 2, 4, 8, 16, 32 and 64 cpd. Averaging across frequency is done to improve the statistical stability of the sections. The spectral estimates are formed at 20, 36, 68, 132, 260 and 516 degrees of freedom.

propagating motions. The upward spectra decay quickly from a low wavenumber maximum and exhibit a pronounced secondary peak at slant wavelengths of 200 m. Traces of this peak are seen at the same wavenumber in the higher frequency cross sections, forming the pre cut-off spectral shoulder. The near-inertial cross sections sensed by the different sonars are nearly identical. This is expected, however, as these near-inertial motions are almost circular when viewed from above. Estimates of near-inertial velocity variance should not be sensitive to the azimuthal direction of measurement.

The two cycle per day cross section is dominated by the baroclinic tide. At low wavenumber the upward propagating motions are more energetic by a factor of two. However, the situation reverses at higher wavenumber, with downward propagating motions becoming more energetic. This crossover is more apparent in the 70 kHz spectrum than in the 75 kHz spectrum.

At higher frequencies the vertical asymmetry is reduced, although there are significant differences up to 16 cpd, particularly in the 70 kHz data. Upward energy propagation tends to exceed downward. The spectral shoulder, prominent in the spectrum of upward energy propagation at low frequency, becomes less distinct at high frequency. The wavenumber slope of the spectrum decreases with increasing frequency, approaching k^{-1} at 64 cpd. The high wavenumber-high frequency levels are significantly influenced by noise in the sonar measurements. The k^{-1} slope must eventually steepen in order that the shear variance be finite.

Bandwidth

It is not clear that one is justified in parameterizing the changes in these cross sections with frequency with some single variable, *bandwidth*. Indeed, for the upward spectra, the cross sections appear remarkably similar, except for a progressive change in mean spectral *slope*. Nevertheless, the notion of gross spectral bandwidth is useful. It is worthwhile to introduce a definition of bandwidth which is appropriate, given the changing form of the spectrum. A simple approach is to remove the frequency dependence of the spectrum, calculating a normalized, dimensionless, spectrum

$$\hat{E}(k,\omega)=E(k,\omega)/E(\omega)$$

$$whereE(\omega)=\frac{1}{k_{max}}\int_0^{k_{max}}E(k,\omega)dk$$

Frequency smoothed log-log averaged contour maps of the normalized spectra are presented in Figs. 4, 5 lower. The maps are contoured in db relative to unity, with a 3 db contour interval. The individual contour lines can be taken as separate measures of the spectral bandwidth. There is a clear difference in the gross form of these frequency normalized spectra. The upward spectra have contours generally parallel to the frequency axis. There is a significant widening of the contours at the inertial frequency, corresponding to an increase in short wavelength upward propagating motions. Curiously, the inertial bandwidth maximum falls below the local inertial frequency. The energy spectra themselves (Fig. 4-5-top) show the energy peak at the inertial frequency. The downward spectra also show the broadest bandwidth at and below the inertial frequency. However, if

126

one traces the 0 db contour line, the "bandwidth" is seen to decrease gradually with frequency, up to frequencies of .4 cph. While the internal wave spectrum has been known to be asymmetric in the near-inertial frequency band (Leaman and Sanford, 1975), this is the first clear indication that the asymmetry extends to much higher frequency. It is interesting that the upward and downward energy levels are not greatly different, yet the gross form of the corresponding spectra are. Note that the lower value contour lines do not parallel the 0 db line. This is in part a consequence of the normalization procedure, which forces the noise level of the high-frequency regions of the spectrum to appear larger than at low frequency. In spite of these effects, the vertical asymmetry in spectral form is striking.

SUMMARY AND CONCLUSIONS

During an eighteen-day period in May 1980, while FLIP drifted southward in the California Current, oceanic velocity data were obtained in the top 600 m of the sea using a pair of Doppler sonars. These data were used to estimate the slant wavenumber-frequency spectrum of the motions observed. The spectral estimates, at low frequency, represent an accurate description of the particular wave groups which passed under FLIP during the course of the experiment. At higher frequency, the statistical confidence of the spectral estimates is much greater. However, to the extent that the high-frequency motions are influenced by the lower frequency "background" through which they propagate, standard measures of statistical precision do not necessarily imply representativeness.

The spectral estimates are basically red in both frequency and wavenumber. Near inertial peaks dominate the spectra. The spectrum of downward-going near-inertial motions is both more energetic and broader in wavenumber bandwidth than that of upward motions. This asymmetry is seen to extend to frequencies nearly five times inertial. The excess downward energy is associated with a clockwise (viewed from above) sense of rotation.

Over this frequency region both upward and downward spectra appear to have high wavenumber cut-off at a vertical scale of 60 m. Spectral slopes in the cut-off region approach k^{-5}. The cut-off is much less visible at frequencies above 8 cycles per day. As a consequence of this changing spectral form with frequency, the major contribution to the shear on vertical scales less than 60 m is from high frequency motions. In contrast, the Garrett-Munk model indicates that near-inertial motions dominate the shear field at all vertical scales.

With minimal smoothing, the spectral estimates display prominent ridges which run parallel to the wavenumber axis. The ridges might be harmonics of the inertial and tidal fundamental peaks. That the spectrum is so irregular is of relevance to modelers who are attempting to estimate wave-wave interaction rates for the wavefield. Holloway (1982) has emphasized that the number of wave groups in any one volume of the sea, available for interaction, is fewer than the smooth "process spectrum" of the wavefield would indicate. The average interaction resulting from many realizations of the instantaneous wavefield can be different than the net interaction predicted from the averaged wavefield spectrum.

If the ridges are indeed forced harmonics of the tide, there are additional dynamic implications. Olbers and Pomphrey (1981) have argued that scattering of the barotropic tide from the sea floor can be at most a negligible source of energy for the internal

wavefield. Their argument is based on the fact that the weak resonant non-linear transfer rates from the baroclinic tidal band to other regions of the internal wave spectrum are very slow. Energy can not leak out of the tidal band at an adequate rate to source the wavefield. However, if forced non-resonar. interactions are occurring, tidal energy can be transferred to higher frequencies at a much greater rate. At high frequencies, even the weak resonant transfer rates become large. It would be interesting to repeat the "spectral bump" experiments of McComas and Müller (1981) from a different perspective. Rather than estimating the decay time of a perturbation on an otherwise smooth spectrum, one might calculate the energy flux needed to maintain a "spectral bump", steady state. This would provide the beginning of a theoretical perspective to these observations.

128

References

Garrett, C. J. R., and W. H. Munk, 1972. Space-time scales of internal waves. *Geophys. Fluid Dyn., 2*, 225-264.

Garrett, C. J. R., and W. H.Munk, 1975. Space-time scales of internal waves, a progress report. *J. Geophys. Res., 80*, 291-297.

Garrett, C. J. R., and W. H. Munk, 1979. Internal waves in the ocean. *Ann. Rev. Fluid Mech., 11*, 339-369.

Holloway, G., 1982. On interaction time scales of oceanic internal waves. *J. Phys. Oceanogr., 12*, 293-296.

Leaman, K. D., and T. B. Sanford, 1975. Vertical energy propagation of internal waves: a vector spectral analysis of velocity profiles. *J. Geophys. Res., 80*, 1975-1978.

McComas, C. H., and P. Müller, 1981. Time scales of interaction among oceanic internal waves. *J. Phys. Oceanogr., 11*, 139-147.

Müller, P., D. J. Olbers, and J. Willebrand, 1978. The IWEX spectrum. *J. Geophys. Res., 83*, 479-500.

Olbers, D. J., and N. Pomphrey, 1981. Disqualifying two candidates for the energy balance of oceanic internal waves. *J. Phys. Oceanogr., 11*, 1423-1425.

Pinkel, R., 1975. Upper ocean internal wave observations from FLIP. *J. Geophys. Res., 80*, 3892-3910.

Pinkel, R., 1981. On the use of Doppler sonar for internal wave measurements. *Deep-Sea Res., 28A*, 269-289.

Pinkel, R., 1983. Doppler sonar observations of internal waves: wavefield structure. *J. Phys. Oceanog., 13*,.

Weller, R. A., 1984. Near inertial motions observed in and below the mixed layer. *J. Phys. Oceanog.*, in press.

THE MONTHLY VARIABILITY OF UPPER-OCEAN INTERNAL WAVE ENERGY:
A PROGRESS REPORT ON THE CORRESPONDENCE WITH WIND STRESS

Melbourne G. Briscoe

Woods Hole Oceanographic Institution
Woods Hole, Massachusetts 02543

ABSTRACT

High-frequency kinetic energy from near-surface current meter moorings is
examined to test for seasonal and geographical patterns of variability.
In the North Atlantic the monthly average wind stress is compared to the
monthly average internal wave energy and a significant, positive
correlation is found. On average, a 1-dPa change in the monthly wind
stress causes a 220 - microJ/kg high-frequency kinetic energy change, 2 to 3
months later. As a tentative explanation, the long time lag together with
the spatial patterns of the kinetic energy suggest mesoscale eddy
generation by the wind, followed by internal wave generation by the eddies.

INTRODUCTION

We previously examined the high-frequency (0.1 to 4.0 cph) horizontal
kinetic energy from the Long-Term Upper Ocean Study (LOTUS) at 34N, 70W in
the deep water of the Sargasso Sea, and found an unexpected and surprising
seasonal variation (Briscoe and Weller, 1984). The observation was
clearest at depths of 200-300 m; shallower the seasonal variation was
obscured by shorter-term events, and deeper the signal began to decay,
although remnants were still visible at 1000 m.

Figures 1 and 2 give the principal high-frequency results from that study:
Figure 1 shows the record-mean depth profiles of high-frequency (solid
circles) and near-inertial energy (open circles; inertial frequency plus
and minus 15 percent). The records are 9 to 11 months long. Figure 2
displays, for selected depths, the time-varying (8-day running averages of

---

NOTE: This manuscript is an early, partial draft of a full paper to be
submitted for later publication in a reviewed journal.

HORIZONTAL KINETIC ENERGY $[cm^2 s^{-2} = erg\, gm^{-1} = 10^{-4} J kg^{-1}]$
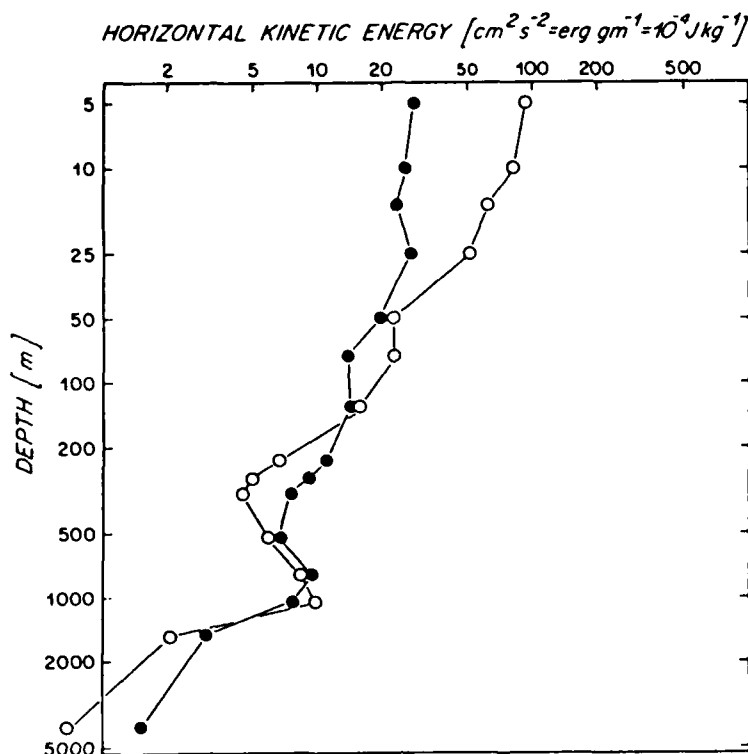
Fig. 1.   Near-inertial band (open circles; local f ± 15 percent) and
    high-frequency band (solid circles; periods shorter than 24 hours, less
    the near-inertial band energy) horizontal kinetic energy (annual
    average) versus depth from the first year of LOTUS (Briscoe and Weller,
    1984).

a sharp band-pass filter) high-frequency energy. At 300-500 m the energy
is clearly seen as least in the summer, most in the winter, and the pattern
seems delayed with increasing depth. We were unable to relate the energy
variations to any seasonal trends in the eddy kinetic energy, nor could we
account for them by the seasonally changing stratification. Figure 3 shows
the mean and standard deviation of Brunt-Väisälä frequency at the LOTUS
site, based on 10 CTD stations over a 3-year period. Even as shallow as
200 m the standard deviation is only 38 percent, which is not nearly enough
to account for the observed energy variation of a factor of 8 at 300 m, and
even more at some other depths. Also, the stratification is greatest in the
summer, which should increase the horizontal kinetic energy, not decrease
it as observed.

We have selected the 0.1-4 cph band (or 0.1-2 cph, depending on the data
set) as a diagnostic for the energy of the internal wave field, to which we
should add inertial motions and internal tides to obtain the complete
picture of variability. Any variability seen in these high-frequency
results is therefore probably an underestimate of the total variability.
Based on the numerous weak and not-so-weak nonlinear interaction theories

HIGH-FREQUENCY ENERGY
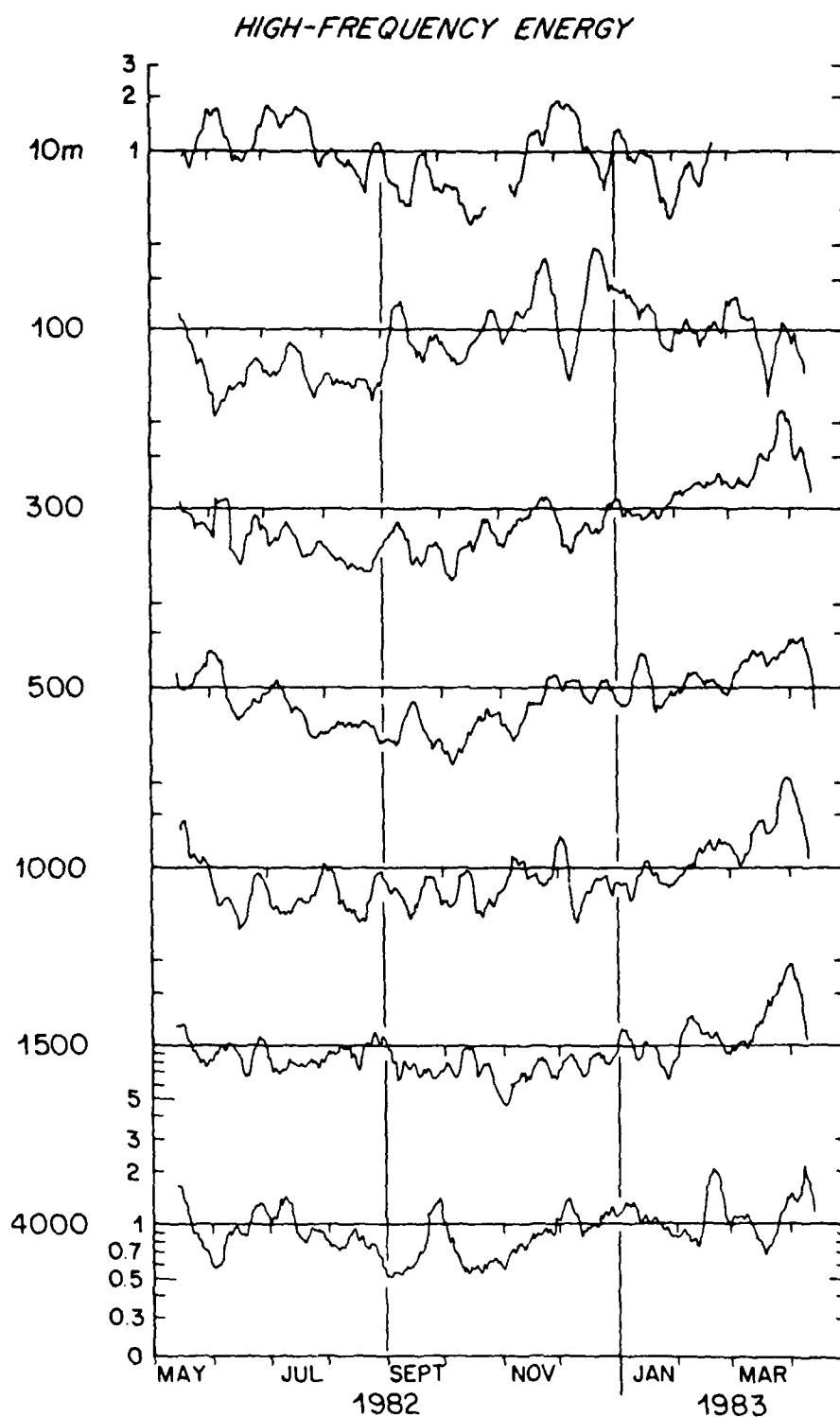
Fig. 2.   High-frequency (0.1-4 cph) horizontal kinetic energy versus
time, for selected depths from LOTUS (Briscoe and Weller, 1984). The
plots are smoothed with an 8-day running average, and each depth is
normalized by the annual average energy at that depth. The vertical
scale for each plot is logarithmic; the spacing between horizontal base
lines is one decade.

132
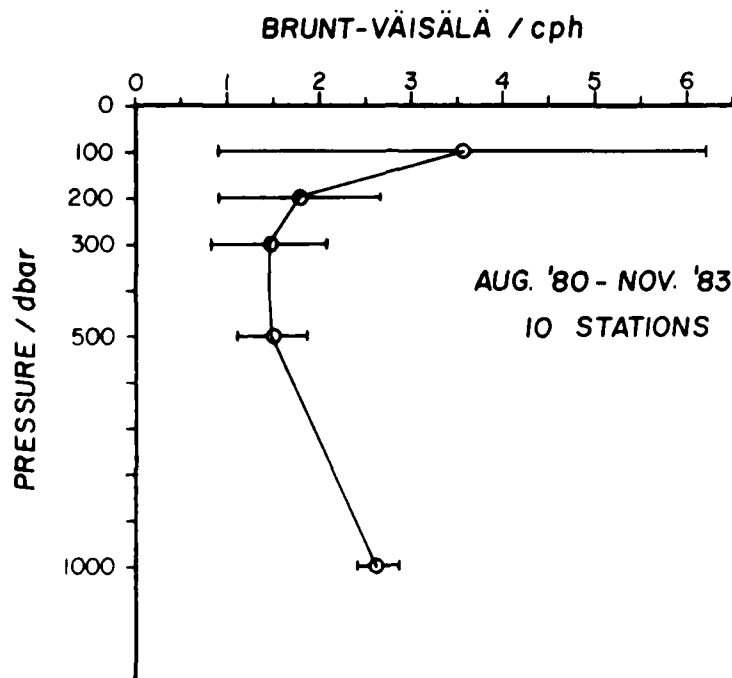
BRUNT-VÄISÄLÄ / cph

Fig. 3.   Brunt-Väisälä frequency mean and ± 1 standard deviation for the
    LOTUS site over a 39-month period, at selected depths.

(Müller and McComas, 1981; Henyey, 1984; Olbers, 1983) we expect that this
high-frequency band tends to stay in equilibrium with the rest of the
spectrum. That is, given the dynamics that shape the spectrum and force it
to maintain a nearly constant shape, we use the high-frequency band to
assess the changing level of the spectrum. Our goal is to interpret the
variations of the high-frequency energy in terms of possible energy sources
and sinks for the spectrum.

DATA SETS FOR ANALYSIS

Current Meter and Hydrographic Data

Wunsch (1976) and Wunsch and Webb (1979) have previously searched for
variations and patterns in internal wave energy. However, they only
considered measurements from deeper than 1000 m or immediately above the
bottom from some shelf and slope sites. The focus here, motivated by the
LOTUS observation of a seasc.... variation at a few hundred meters depth, is
the 100-300 m depth regime. Because of the interest in the seasonal time
scale and in order to maintain confidence in the statistics, only data
series at least a month long will be examined. Horizontal kinetic energy
is a robust estimator of the internal wave energy because, unlike
temperature measurements, only the point data are necessary (no vertical
gradients are needed). Finally, only data from subsurface moorings were

used to eliminate questions of contamination by mooring motion.
Consequently, when the Woods Hole and NODC archives were searched, only 54
data sets could be found; most of these were in the North Atlantic, with
the others being in the Indian Ocean and the western Pacific Ocean.
Of the 54 data sets, only a few could be considered independent. For
example, some of the internal wave experiments had several instruments in
the 100-300 m depth range, and some of the array experiments had several
moorings within a few tens of kilometers of each other. A harsh pruning of
the data yielded 17 independent sets, from only 13 different sites because
of four sites with two years (not necessarily consecutive) of data. The 17
data sets are tabulated in Table 1; the depth range is 114-306 m, the time
period 1974-1983. The first 13 of the 17 data sets are from the North
Atlantic.

The Levitus (1982) atlas of hydrographic data provided the Brunt-Väisälä
frequency for the 17 data sets. Only the annual average frequency at 250 m
depth was used to scale the kinetic energies; our LOTUS results suggested
that we were looking for a signal much larger than contained in small
variations with depth or time of the Brunt-Väisälä frequency. Figure 4
shows the 9 sites in the North Atlantic, comprising data sets 1-13 of Table
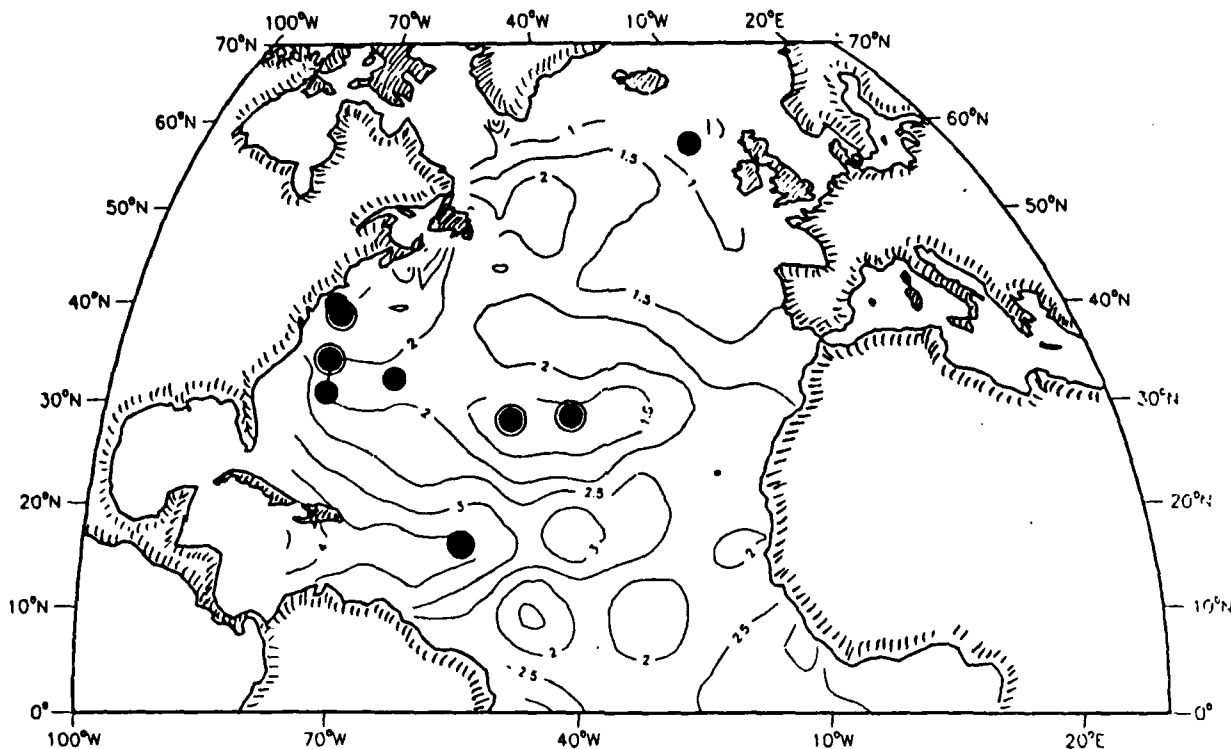
Fig. 4.   North Atlantic chart showing location of data sets 1-13 listed
   in Table 1, plotted on a contour map of Brunt-Väisälä frequency (cph) at
   250 m from Levitus (1982) using Sgouros and Keffer (1983). The circled
   circles represent two non-similtaneous experiments at the same site. The
   mid-Atlantic ridge runs between the two double circles in the central
   Atlantic.

Table 1. Mooring Data

DATA SET (1)	MOORING ID (1)	DATA DEPTH (m)	WATER DEPTH (m)	MONTHS DURATION	STARTING MO/YEAR	LAT	LONG	B-V FREQ (cph) (2)	EXPERIMENT	NOTES
1	5172	193	2647	11	01/1974	39.2N	70.0W	2.51	SITE D	(3)
2	5231	181	2504	7	05/1974	39.4N	70.0W	2.51	SITE D	(3)
3	5531	306	4353	8	05/1975	31.8N	64.4W	1.78	BERMUDA	(3)
4	5871	145	496	5	02/1976	39.9N	71.1W	2.63	SHELF-SLOPE	(3)
5	6291	203	4954	10	07/1977	28.0N	48.1W	1.95	CLUSTER A	(3)
6	6231	128	4251	10	07/1977	27.4N	41.1W	2.18	CLUSTER B	(3)
7	0791	172	5500	10	06/1977	16.7N	54.3W	3.55	CLUSTER C	(3)
8	6481	178	4881	15	06/1978	27.9N	48.7W	1.95	CLUSTER A	
9	6491	216	4268	15	06/1978	27.4N	41.1W	2.18	CLUSTER B	
10	6401	245	5355	13	05/1978	31.0N	69.5W	1.86	LDE	
11	65118	200	1558	1	08/1978	59.0N	12.5W	0.79	JASIN	(3)
12	6933	114	5370	6	06/1980	34.0N	70.0W	1.86	LOTUS	
13	7664	228	5368	10	06/1982	34.0N	70.0W	1.86	LOTUS	(3)
14	5971	201	5072	5	07/1976	0.0N	52.3E	3.93	INDEX	(3)
15	6561	200	5065	12	04/1979	0.0N	50.0E	3.51	INDEX	(3)
16	7011	250	5278	9	08/1980	32.5N	151.5E	2.63	WESTPAC	(3)
17	7211	265	5756	11	06/1981	32.5N	151.5E	2.63	WESTPAC	(3)

NOTES:
1. First 3 digits are mooring number; next digits are instrument number.
2. From Levitus (1982) annual average at 250-m depth.
3. Part of an array; multiple moorings and/or depths available for analysis.

134

1 (circled points are double data sets), overlaid on a contour plot of buoyancy frequency (Sgouros and Keffer, 1983) at 250 m. The range of variation is 3.55 cph for the near-Caribbean site (Polymode Cluster C) to 0.79 cph for the far northern site (JASIN).

Kinetic Energy Time Series

Figures 5a and 5b show the monthly-average, high-frequency, horizontal kinetic energies for each of the 17 data sets in the world sample; 5a (top) is without any normalization by the Brunt-Väisälä frequency, and 5b is with each energy value divided by the Levitus 250-m frequency and multiplied by 3 cph as a scaling value. The solid line drawn in each Figure connects the average of all the data sets for each month. A March energy maximum and a broad July minimum are visible, slightly enhanced in the Figure 5b normalized version. The ratio of maximum to minimum of the solid line in Figure 5b is about a factor of 2. Note that we are looking at monthly average values of the specific energy of a high-frequency spectral band that has for ten years been thought to have a single, constant, universal value (Garrett and Munk, 1972; Munk, 1981; Briscoe, 1983) of about 330 microJ/kg at mid-latitudes for a Brunt-Väisälä frequency of 3 cph. Instead, the monthly values at a given site vary (in the normalized data) as much as a factor of 5.6, the values from site to site for a given month vary as much as 11 (October), and the maximum to minimum values regardless of month vary by almost 13.

Figures 6a and 6b show the same information as Figures 5a and 5b but only for the North Atlantic, at the locations given in Figure 4; the March maximum of the average curve is a little lower and a little broader. As in Figures 5, even the envelope of the sample points shows the winter increase and summer decrease. The overall variability is less: within a data set, within a month, and within the entire North Atlantic (normalized) sample the ratio of maximum to minimum values is 5.6, 6.4, and 7.1, respectively.

No latitudinal scaling (Munk, 1981) has been used in Figures 5 or 6 because the idea has not really been tested. For the North Atlantic data that are concentrated upon in the rest of this paper, the latitudes vary from 16 to 59 degrees north; hence latitudinal scaling would decrease the 16N energies by 55 percent and increase the 59N values by 71 percent, relative to 30N values. The latitudinal scaling only affects the relative energy between data sets whereas we concentrate on seasonal variations within each set.

Wind Stress

Hellerman and Rosenstein (1983) have produced a tape of world wind stress based on 106 years of ship observations; monthly values of the East and North stress components in 2-degree squares are available. Figure 7a is a world chart of the stress magnitude, and Figure 7b gives zonal averages
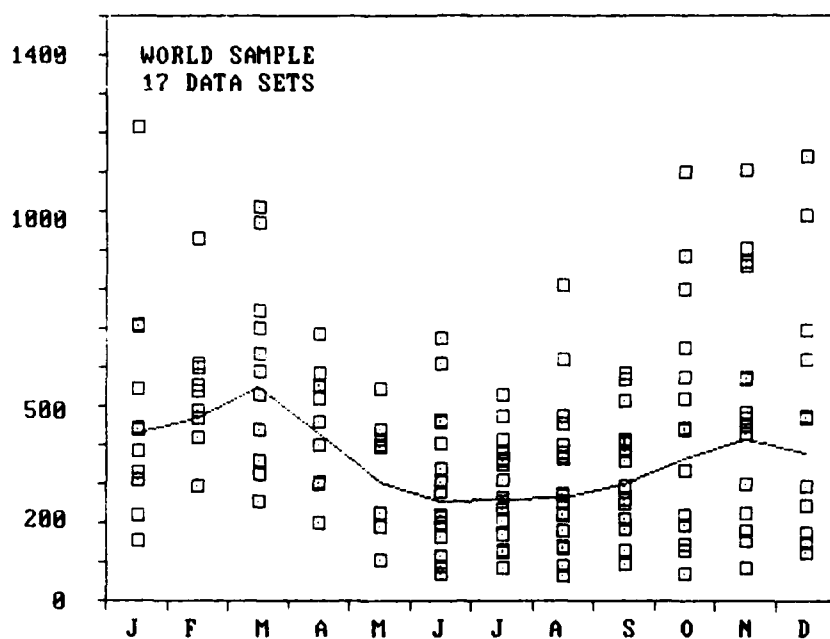
Fig. 5a.   Monthly high-frequency (0.1-2 cph) horizontal kinetic energy
from the 17 data sets in Table 1. The energy units are microJ/kg, or
100 times the traditional units of cm^2/s^2 (= erg/gm = 10^{-4} J/kg). The
solid line connects the average value for each month.
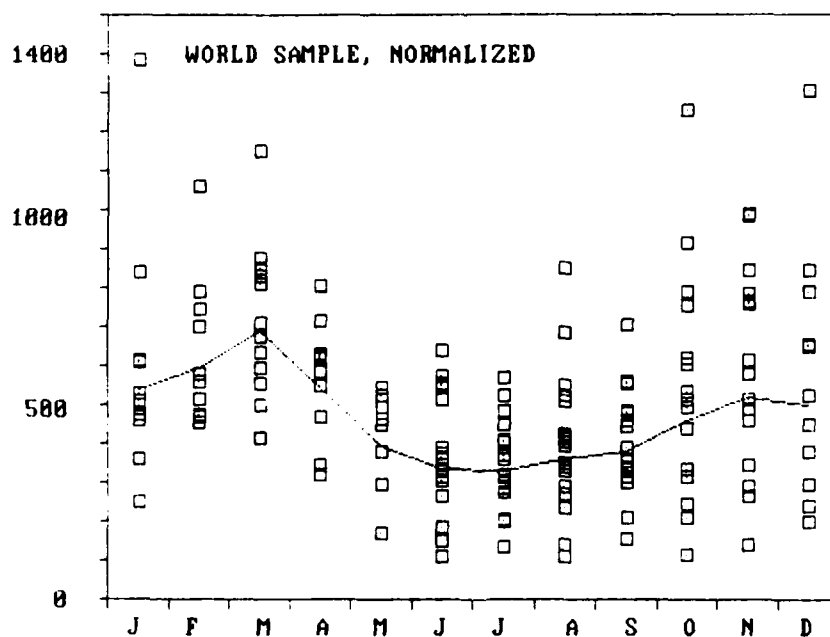
Fig. 5b.   The same as Figure 5a, but the energies for each data set have
been multiplied by 3 cph and divided by the Brunt-Väisälä value listed
in Table 1.
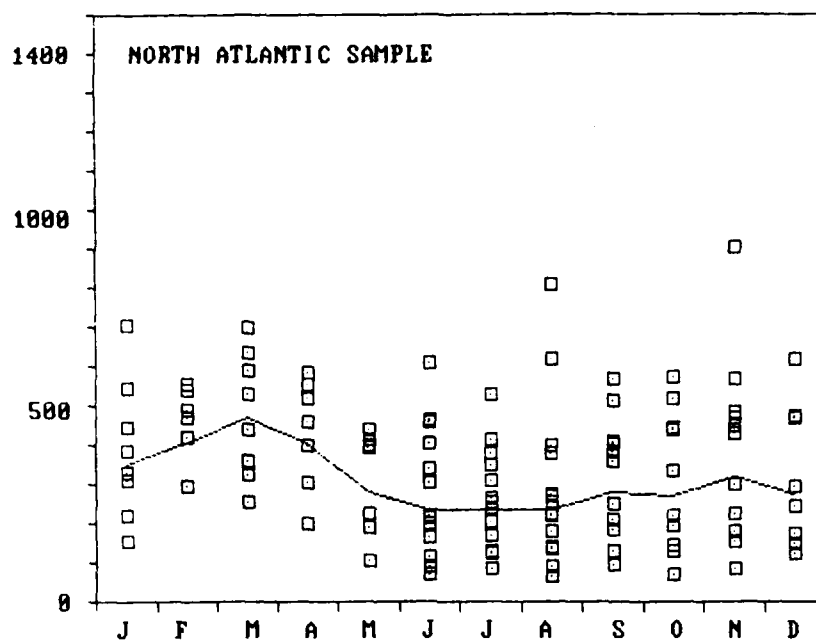
Fig. 6a.   The same as Figure 5a, but for the North Atlantic data only.
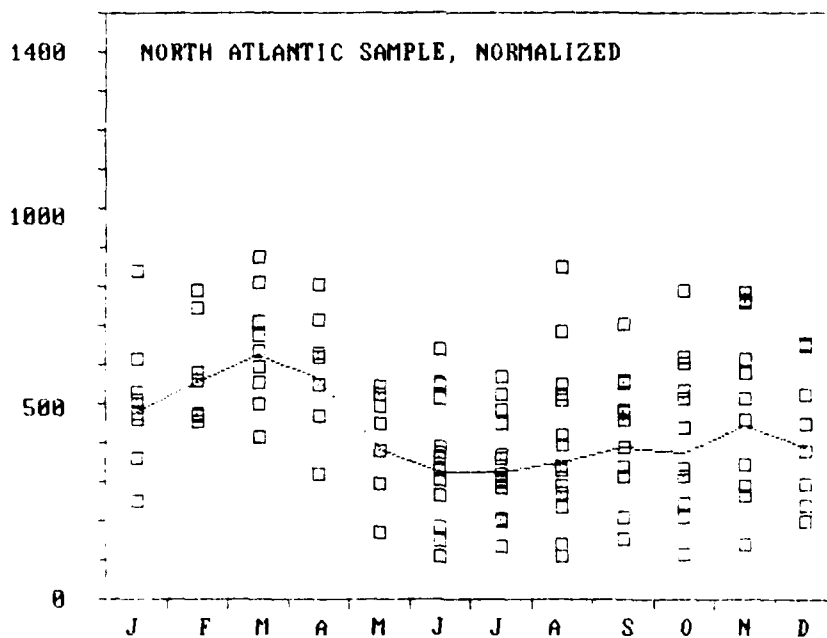
Fig. 6b.   The same as Figure 5b, but for the North Atlantic data only.

138

Fig. 7a.   Annual wind stress magnitude based on Hellerman and Rosenstein (1983). The values plotted are calculated from 2-degree square monthly averages of the wind stress components. The stress units are 10^{-1} Pascal (= dPa), which are numerically equal to dyne/cm^2.
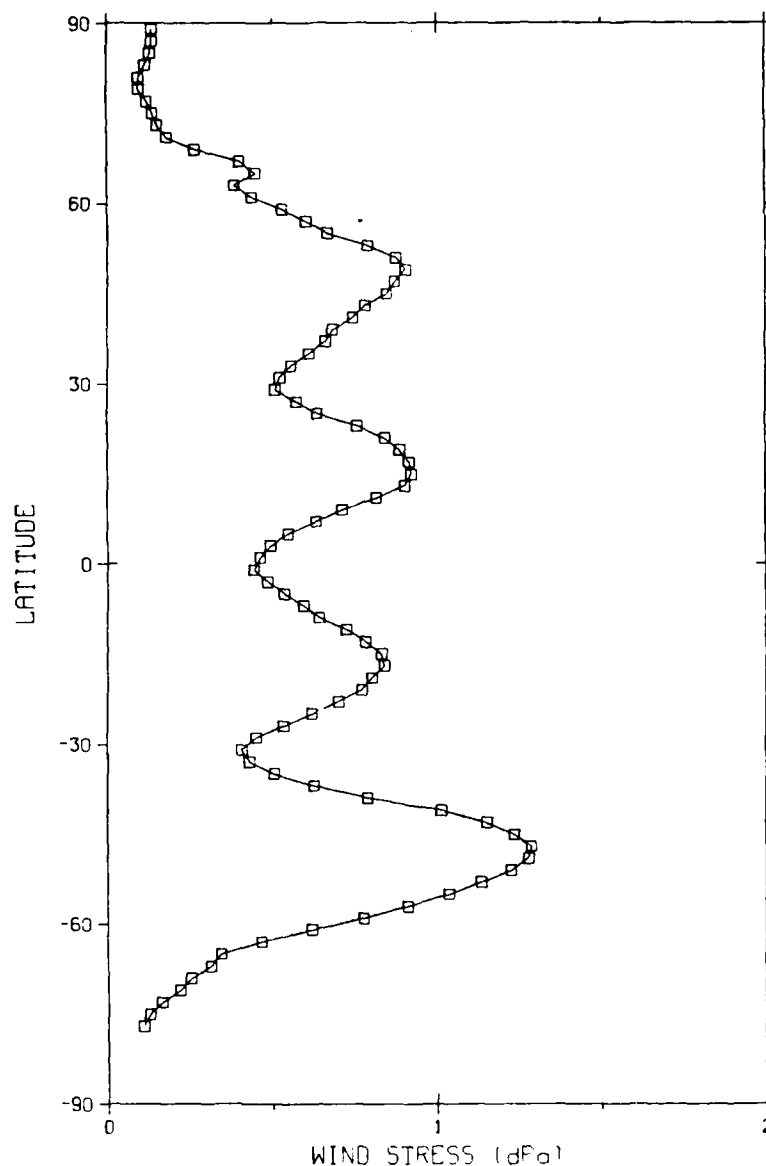
Fig. 7b.   Zonal average of the data shown in Figure 7a, excluding values
over land.

over the ocean. The monthly variation of wind stress in the North Atlantic
at the sites shown in Figure 4 (the nearest 2-degree square was selected)
is shown in Figure 8; the summer minimum and winter maximum shows clearly
in the average curve as well as in the envelope of the data points.

The least variable wind at the sites examined is in the Polymode Cluster B
area in the central Atlantic east of the mid-Atlantic ridge. The most
variable site is the northern JASIN location, but only one month of mooring
data is available from there; the next most variable location is Site D
just south of Cape Cod.

140
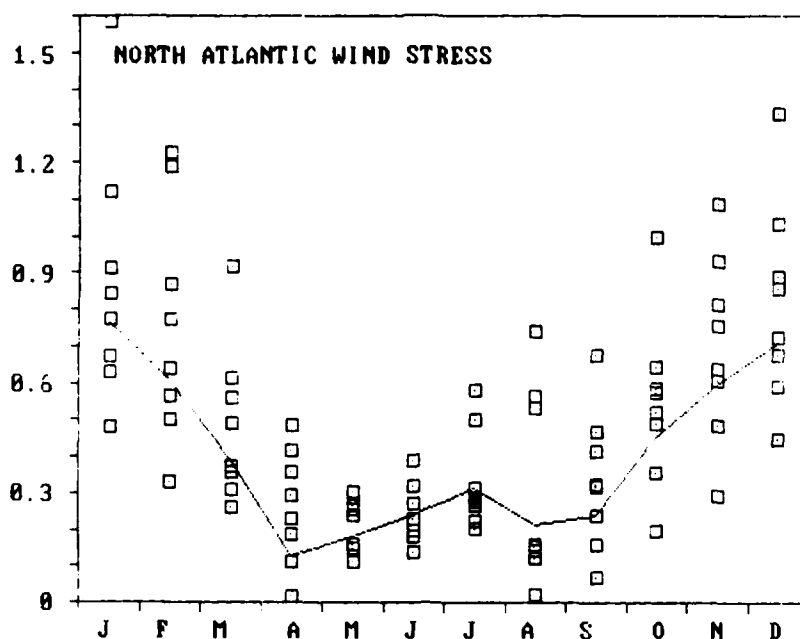
Fig. 8.   Monthly wind stress at the North Atlantic sites (Figure 4).

The month of maximum wind is January for all the North Atlantic sites except the JASIN location in the far north, which is February. The month of minimum wind is April or May except for August at the Bermuda and JASIN sites; Bermuda has a secondary minimum in May.

COMPARISON OF WIND STRESS AND INTERNAL WAVE ENERGY

If the level of internal wave energy at any given location is related to the wind stress in the vicinity of that location, then Figure 7b suggests there might be an energy minimum around 30N corresponding to the stress minimum between the trades and the westerlies. Figure 9 plots the available North Atlantic high-frequency internal wave kinetic energy (full record averages) versus latitude. The four points constituting the minimum near 32N are from the Local Dynamics Experiment, Bermuda, and two different years of LOTUS. The 59N point is a single August value from JASIN.

Direct comparison of the wind stress and wave energy requires some information on what time and space averaging is appropriate: should the local wind from the 2-degree square around the mooring be used, or perhaps from the surrounding 10-degree square, in accordance with the suggestion (Garrett, 1979) that the internal wave field has an implicit 1000 km averaging scale due to horizontal propagation and diffusion balanced by slow dissipation? There is also the question of time-averaging: if all the mooring data sets covered a full 12 months, then annual averages of wind stress could be compared with annual averages of internal wave energy. But
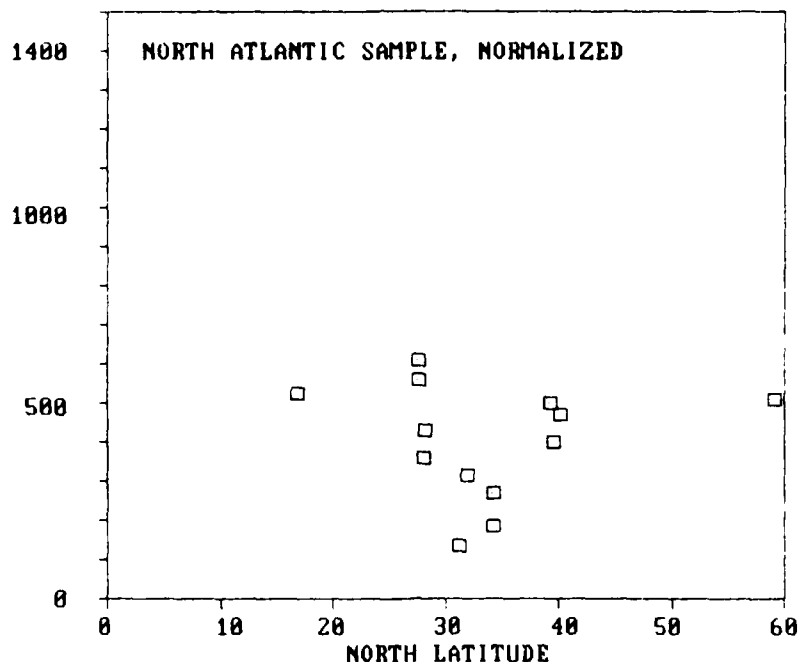
Fig. 9.   North Atlantic high-frequency horizontal kinetic energy
(averaged over the length of each record) plotted versus latitude. The
energy values have been WKB-normalized as in Figures 5b and 6b.

when the internal wave energy is just averaged over, say, 6 months, should
the same 6 months be used for the wind stress average, or perhaps an
earlier 6-month period to account for a time delay in the energy arriving
at depth and at high frequencies? Some sense of the relevant physics is
required.

Time Delays and Energy-input Mechanisms

There are at least 6 ways that the wind can put energy into the high-
frequency internal wave field; they are listed below in a sequence
corresponding approximately to an increasing delay between the wind and the
internal waves.

o   Direct generation of high-frequency internal waves by wind
    stress or pressure (e.g., Käse and Clark, 1978). The mechanism
    operates essentially instantaneously but is inefficient in
    producing waves at depth. Near-surface high-frequency waves
    must propagate to depth at vertical group velocities that are
    O(1) km/day, so less than a day is required to get energy
    to 200 m.
o   Nearby generation of a surface wave field that nonlinearly
    interacts to produce internal waves of high frequency (Olbers
    and Herterich, 1979; Olbers, 1983). The theoretical time to

produce the internal waves can be as short as (for favorable conditions) 10^5 seconds; 10^6 seconds is O(10) days.

o   Nearby generation of near-inertial waves (Weller, 1982) that propagate to depth and deliver their energy to the high frequencies by nonlinear interactions. The vertical propagation is slow, of O(10) days to get to 200 m, and there are no good estimates available for the transfer to high frequencies.

o   Direct generation (very inefficient) of lower frequency waves that pass their energy to the high frequencies by nonlinear interactions (e.g., Müller and McComas, 1981). The lower frequencies have vertical group velocities of O(10) m/day, so can only get the energy to depth slowly. The transfer to high frequencies takes at least a few wave periods to as many as hundreds, say O(10) days. The total time to get energy to 200 m is O(1) month.

o   Distant generation of an internal wave field that slowly diffuses to other locations (Garrett and Munk, 1979). An estimate of the diffusion rate is 10 km/day (Garrett and Munk, 1979; Olbers, 1983), so with the assumed slow dissipation (O(100) days) of the internal wave field, energy hot spots can spread 1000 km. One could then see O(100) day delays between distant wind events and local internal wave energy changes, but the mechanism also implies considerable spatial uniformity in the energy levels.

o   Atmospheric generation of mesoscale eddies (Müller and Frankignoul, 1981) and an energy flux from the eddy field to the internal wave field (Brown and Owens, 1982). Theory suggests that the eddy growth lags the wind growth by O(3) months, and that the energy flux to the internal wave field is O(10) days.

Although the time delay estimates given above are mostly tentative, they indicate that delays of a few hours to three or more months are possible, depending on the operative physics. However, our use of monthly average internal wave energy and wind stress precludes examination of the shorter time lags. If we find a zero-lag correspondence (i.e., data from the same month for both variables) between stress and kinetic energy, any of the first four mentioned processes could be responsible. A lag of 1 to a few months suggests one of the latter two processes, with the longer lags and any spatial inhomogeneity in the internal wave energy suggesting the process involving mesoscale eddies.

Lagged Correlations

Scatterplots of monthly values of high-frequency kinetic energy versus wind stress at the same site were made for various time lags (energy lagging stress); Figure 10a gives the result for a 2-month lag. The regression lines are for each data set individually. Since each data set has a different mean energy and associated mean wind stress, Figure 10b shows the same data plotted relative to the mean values; i.e., energy anomaly and wind stress anomaly are plotted. The regression lines now all pass through a common origin, giving a better sense of the slope of the correlation.
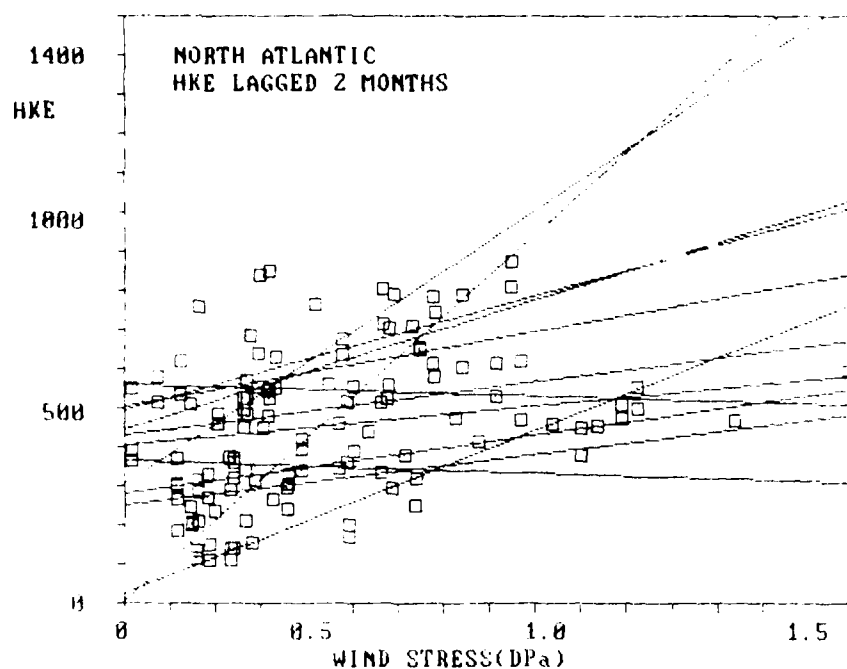
Fig. 10a. High-frequency monthly horizontal kinetic energy for each of the
13 North Atlantic data sets plotted versus monthly wind stress at the
same site. The monthly energy values are lagged two months later than
the wind stress values. The linear regression lines are for each of the
13 data sets individually; see Table 2b.
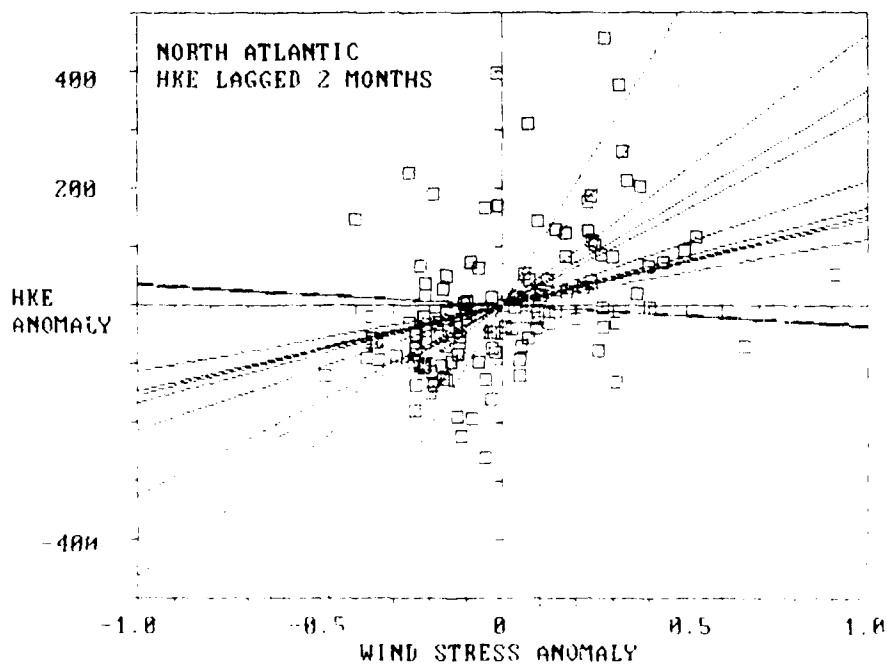
Fig. 10b. The same as Figure 10a, except each data set is plotted relative
to its mean value of energy and stress. The regression lines have the
same slopes as in Figure 10a, but now all pass through a common point.

Table 2a lists the correlation coefficients for each of the 13 data sets in the North Atlantic (except the JASIN data, which are only for 1 month), for lags of 0 to 6 months; only correlations different from zero at 95 percent confidence are shown. Lags of 2 and 3 months produce the highest correlations, although lags of 0 to 4 months all yielded at least 1 positive correlation. Data sets 8, 9, and 10 are the only sets extending for at least a year, so their lagged correlations are the most meaningful; they strongly center on 2 month lags. Table 2b gives the rest of the statistical information for the 2-month lagged North Atlantic data, including t-test confidence limits on the slopes.

Lumping together all the North Atlantic data, including JASIN, Figure 11a gives the overall regression line for the energy versus stress anomalies; the (significantly non-zero) correlation is 0.36, the R-squared value is 0.13 (i.e., 13 percent of the variance is explained by the linear regression), the slope is 219 microJ/kg per dPa, and the t-test 90 percent confidence limits on the slope are 87. Figure 11b plots the same data and regression but without removing the means of each data set; the regression is, of course, the same.

This is the principal result of this paper: a significant correlation results from comparing North Atlantic monthly average wind stress with monthly average internal wave high-frequency kinetic energies at 100–300 m, normalized by annual average Brunt-Väisälä frequencies at 250 m for each site. The correlation suggests the changes in kinetic energy lag the wind stress changes by 2 to 3 months. Of the 13 sites examined, 8 had 10 or more months of data, and 5 of those 8 yielded significant correlations. The average slope of the entire 13-site data set was 219 ± 87 microJ/kg per 1 dPa; the slopes of the 5 individually correlated data sets varied from 167 to 1043, averaging 462 (weighted by the number of months in each data set).

All these regressions have discussed the changes in the energy relative to the changes in the wind stress; Figure 12 shows the mean (over the number of months in each data set) kinetic energy plotted versus the mean wind stress for the same number of months but starting 2 months earlier. The radius of each circle is proportional to the standard deviation of the energy within that data set. The range of variation from the bottom of the lowest circle to the top of the highest circle is about 100–800 microJ/kg; this is a quantitative statement of the lack of universality in the energy of the internal wave field.

DISCUSSION

The correlation developed above between wind stress and internal wave energy with 2–3 month time lags is weak but significant, and quite unexpected. Of the mechanisms described to put wind energy into the

Table 2a. Lagged Correlation Coefficients (Kinetic energy lags stress)

DATA SET	MONTHS DURATION	MONTHS LAG						
		0	1	2	3	4	5	6
1	11	0.62						
2	7							-0.88
3	8				0.87	0.78		
4	5			0.89	0.93			
5	10							
6	10	-0.79				0.71		
7	10							
8	15		0.54	0.82	0.67			
9	15			0.55				
10	13*		0.77	0.90	0.71			
11	1							
12	6							
13	10		0.75	0.87	0.83			
No. of positive correlations		1	3	5	5	2	0	0

Table 2b. 2-Month Lagged Correlations (significant values underlined)

DATA SET	MONTHS DURATION	R	R^2	SLOPE	OFFSET	t	± SLOPE
1	11	0.36	0.130	366	446	1.16	
2	7	0.12	0.015	152	430	0.28	
3	8	0.50	0.248	147	252	1.41	
4	5	_0.89_	_0.788_	_781_	_303_	_3.34_	_550_
5	10	0.49	0.237	114	405	1.58	
6	10	0.43	0.185	213	506	1.35	
7	10	-0.13	0.018	-32	560	-0.38	
8	15	_0.82_	_0.670_	_167_	_281_	_5.14_	_119_
9	15	_0.55_	_0.300_	_325_	_497_	_2.36_	_58_
10	13*	_0.90_	_0.817_	_464_	_26_	_7.01_	_244_
11	1						
12	6	-0.01	0.000	-35	367	-0.02	
13	10	_0.87_	_0.765_	_1043_	_6_	_5.10_	_350_

* Too short for a regression

146
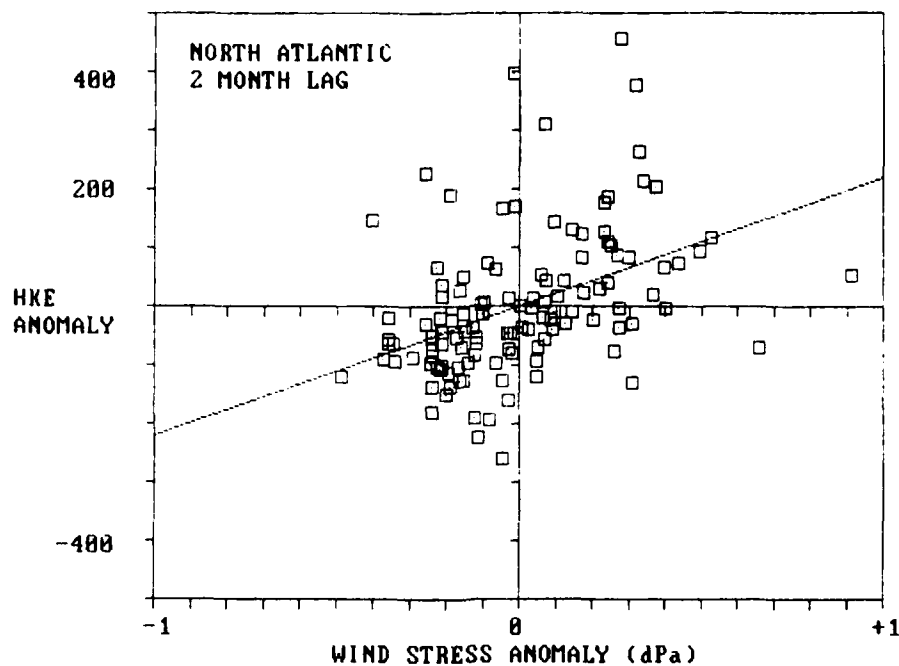
Fig. 11a. The same as Figure 10b, except that only one regression line is
fit to the ensemble of data points. There are 121 months of data shown,
with an ensemble mean of 0.44 dPa and 453 microJ/kg. The line has slope
219 microJ/kg per 1 dPa, a y-intercept of 356 microJ/kg, and an R-value
of 0.36 (0.179 is significantly non-zero at the 95 percent level). The
t-value is 4.2 (1.66 is significant at the 90 percent level), giving
confidence limits on the slope of ± 87.
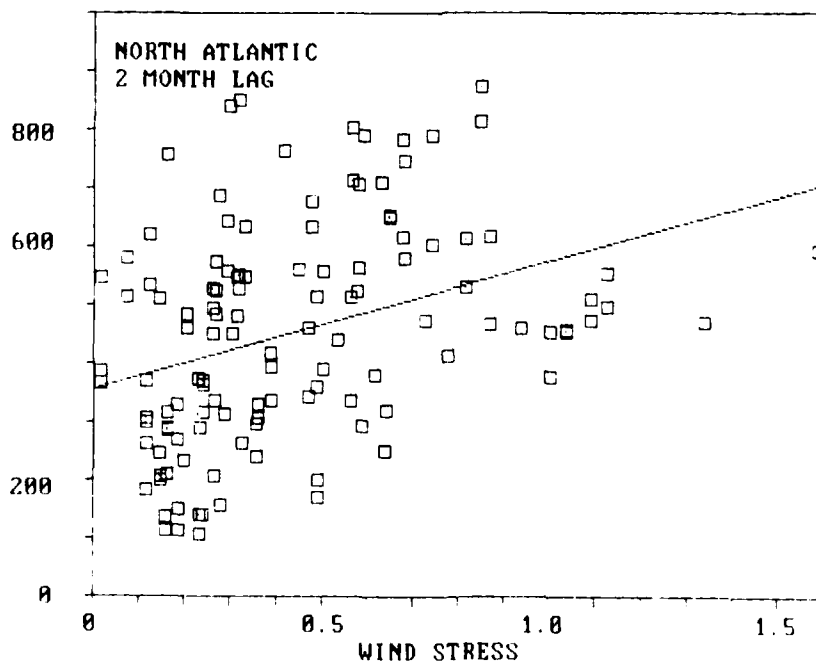
Fig. 11b. The same as Figure 10a, except that only one regression line is
fit to the ensemble of data points. The line is the same line as shown
in Figure 11a; here the actual energy and stress values are plotted
instead of the anomalies from the data set means.
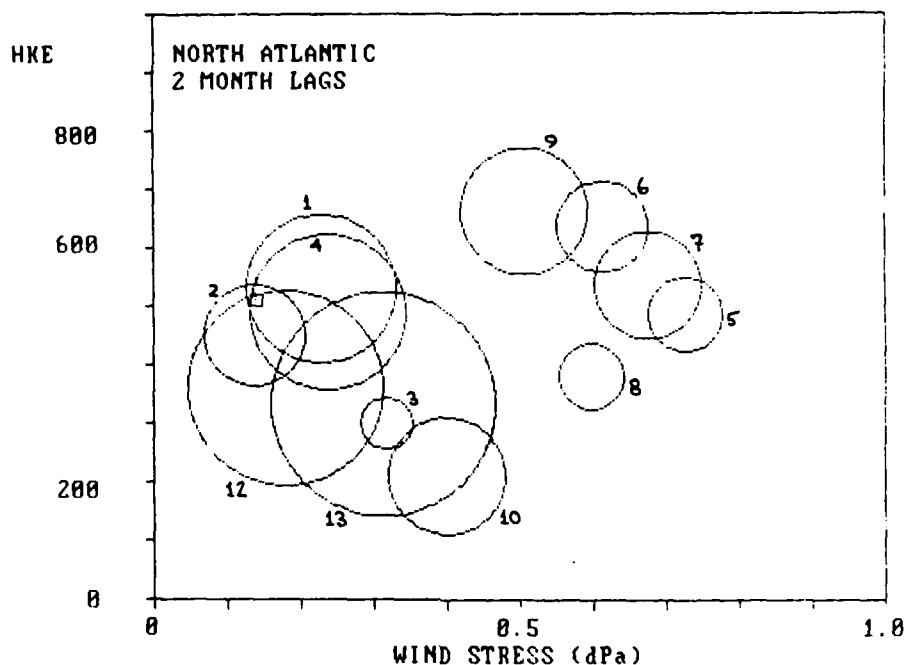
Fig. 12. The record-mean high-frequency horizontal kinetic energy for each of the 13 North Atlantic data sets, plotted against the mean wind stress at each site for the same length record but starting two months earlier. The radius of each circle is proportional to the standard deviation of the monthly kinetic energy values for that dat set; one tic-mark on the energy axis corresponds to a standard deviation of 100 microJ/kg, the same scale as the means are plotted on. The numbers beside each circle correspond to the data sets in Table 1. The JASIN data (set 11) are only for 1 month; hence are plotted as a small square since the standard deviation cannot be calculated.

internal wave field, only the one involving the mesoscale eddy field as an intermediate process seems likely because it has the correct time lags and it permits the observed spatial inhomogeneity of the internal wave energy to exist. However, if mesoscale eddies are the actual source of the internal wave energy, then the observed seasonal modulation of the internal wave energy demands that the mesoscale eddies also have a seasonal modulation, and that the correlations seen here between internal waves and wind stress should be at least as good for internal waves versus eddies and for eddies versus wind. Although there are even fewer data (permitting tests of seasonal effects) for eddies than for internal waves, Müller (1983) re iews the evidence and concludes that the seasonal modulation of eddies is observationally supported, at least away from regions of strong currents where eddy generation mechanisms other than the wind are dominant.

148

It follows that in those regions where the eddy field is produced by instabilities of large-scale currents (near western boundaries, for example), the internal wave field might have little relation to the wind stress. For the North Atlantic data emphasized in this paper, the deep water sites (Figure 4) closest to intense eddy regions (Wyrtki et al. 1976) are data sets 1 and 2 near the Gulf Stream, and set 7 near the Atlantic North Equatorial Current. None of these 3 data sets gave a significant correlation between wind stress and internal wave energy. On the other hand, the sites farthest from strong eddy regions are data sets 3 near Bermuda, 10 (the Local Dynamics Experiment), and 5,6,8, and 9 (the two Polymode clusters near the mid-Atlantic Ridge). Of these 6 sites, 3 gave significant correlations. These results are supportive of the idea that monthly average wind stress and high-frequency internal wave energy tend to be related in regions where the eddy field is weak, and therefore most likely to have been atmospherically generated.

The weakest aspect of this present study is the need to use the Hellerman and Rosenstein (1983) wind stress; it seems unlikely that the 106-year average monthly wind is a good descriptor of the actual monthly wind at a particular site during a particular year. This may be the source of much of the variability in Figures 10 and 11, and the reason why only one of the two data sets at each of 3 sites yields a significant correlation. That is, sets 5 and 8 are both in the central Atlantic just west of the mid-Atlantic ridge in 1977 and 1978, respectively; set 8 gives a good correlation, set 5 does not. Similarly, 6 and 9 are just east of the mid-Atlantic ridge, also during 1977 and 1978, respectively, and set 9 gave a significant correlation while 6 did not. Note that there were only 3 data sets in 1978 with more than 1 month of data (8,9, and 10) and all 3 gave good correlations between wind stress and internal wave energy. Perhaps 1978 had Atlantic winds like the 106-year average, and 1977 did not.

ACKNOWLEDGEMENTS

REFERENCES

Briscoe, M.G., 1983: Observations on the energy balance of internal waves during JASIN. Phil. Trans. R. Soc. Lond. A, 308, 427-444.

Briscoe, M.G., and R.A. Weller, 1984: Preliminary results from the Long-Term Upper Ocean Study (LOTUS). Dyn. Atmos. Oceans, in press.

Brown, E.D., and W.B. Owens, 1981: Observations of the horizontal interactions between the internal wavefield and the mesoscale field. J. Phys. Oceanogr., 11, 1474-1480.

Garrett, C., 1979: Mixing in the ocean interior. Dyn. Atmos. Oceans, 3, 239-265.

Garrett, C.J.R., and W.H. Munk, 1972: Space-time scales of internal waves. Geophys. Fluid Dyn., 2, 225-264.

Garrett, C., and W.H. Munk, 1979: Internal waves in the ocean. A. Rev. Fluid Mech., 11, 339-369.

Hellerman, S., and M. Rosenstein, 1983: Normal monthly wind stress over the world ocean with error estimates. J. Phys. Oceanogr., 13, 1093-1104.

Henyey, F., 1984: Transport of small-scale internal waves toward microstructure. Proceedings, Second 'Aha Huliko'a Hawaiian Winter Workshop, Hawaii Institute of Geophysics, Honolulu, HI, (this volume).

Käse, R.H., and R.A. Clarke, 1978: High frequency internal waves in the upper thermocline during GATE. Deep Sea Res., 25, XXX-XXX.

Levitus, S., 1982: Climatological atlas of the world ocean. NOAA Professional Paper 13. Geophysical Fluid Dynamics Laboratory, Princeton, NJ, 172 pp.

Müller, P., 1983: Evidence for the direct atmospheric forcing of mid-ocean eddies. The Role of Eddies in the General Ocean Circulation. Hawaii Institute of Geophysics Special Publication, University of Hawaii, Honolulu, HI, 113-127.

Müller, P., and C. Frankignoul, 1981: Direct atmospheric forcing of geostrophic eddies. J. Phys. Oceanogr., 11, 287-308.

Müller, P., and C.H. McComas, 1981: Dynamics and energy balance of internal waves. Nonlinear Properties of Internal Waves. American Institute of Physics Conference Proceedings no. 76, 181-201.

Munk, W., 1981: Internal waves and small-scale processes. Evolution of Physical Oceanography. MIT Press, Cambridge, MA, 264-291.

150

Olbers, D.J., 1983: Models of the oceanic internal wave field. Rev. Geophys. Space Phys., 21, 1567-1606.

Olbers, D.J., and K. Herterich, 1979: The spectral transfer from surface waves to internal waves in the ocean. J. Fluid Mech., 92, 349-379.

Sgouros, T.A., and T. Keffer, 1983: The CAMS interactive atlas package. A computerized program for the archiving and presentation of oceanographic data. Technical Report WHOI-83-39. Woods Hole Oceanographic Institution, Woods Hole, MA, 51 pp.

Weller, R.A., 1982: The relation of near-inertial motions observed in the mixed layer during the JASIN (1978) experiment to the local wind stress and to the quasi-geostrophic flow field. J. Phys. Oceanogr., 12, 1122-1136.

Wunsch, C., 1976: Geographical variability of the internal wave field: a search for sources and sinks. J. Phys. Oceanogr., 6, 471-485.

Wunsch, C., and S. Webb, 1979: The climatology of deep ocean internal waves. J. Phys. Oceanogr., 9, 235-243.

Wyrtki, K., L. Magaard, and J. Hager, 1976: Eddy energy in the oceans. J. Geophys. Res., 81, 2641-2646.

INTERNAL WAVE CLIMATOLOGY: AN UPDATE

Murray D. Levine

College of Oceanography, Oregon State University
Corvallis, Oregon 97331

ABSTRACT

Recent observations of the internal wave frequency spectrum are examined along with historical data. The "universality" of the spectral level is discussed. The greatest deviations from the Garrett-Munk spectrum are the high levels found near topography and the low levels found in the Arctic Ocean. Evidence is presented which suggests that the Garrett-Munk spectrum should not depend upon the Coriolis parameter. No significant qualitative difference is found between scaling the internal wave spectral level by energy per unit area or by energy per unit volume.

INTRODUCTION

More than a decade has passed since Garrett and Munk's pioneering work organizing diverse internal wave observations into a unified theoretical framework (Garrett and Munk, 1972, 1975; hereafter referred to as GM). These observations came from a variety of sources, from time series of current in the Atlantic to horizontal temperature profiles in the Pacific. The data sets are obviously not synoptic, yet a surprising result was discovered: the different types of data are generally consistent with each other under the assumption of linear free internal waves. The statistical measures of the internal wave field--the spectral shape and level and the coherence structure--are remarkably uniform in space and constant in time.

In light of the recent increase in internal wave data, it is instructive to take another look at the type of evidence that led to the original formulation of the GM model. As the quantity of data increases, it should be possible to categorize with greater precision the similarities and differences of the ubiquitous internal wave field. Careful examination of the variations of the wave field may help to identify the still unknown sources and sinks of internal

152

waves (Wunsch, 1975). While it is impractical to conduct an experiment whose sole purpose is to sample many realizations of the wave field from many diverse locations, the attempt to synthesize existing data remains a potentially fruitful pursuit.

The modest goal of this paper is to report on the recent compilation of temperature and velocity frequency spectra by Levine et al. (1984). The level of observed frequency spectra are discussed--the variations of other spectral measures are left for another time. Several different quantities are calculated from the observations in an attempt to find the quantities that are most "universal" as well as to identify data that deviate from the average.

OBSERVATIONS AND MODELS

The results from Wunsch (1976) and Wunsch and Webb (1979) (hereafter referred to as WW) form the foundation of this analysis. Additional data that have been reported in the literature are also included. To be cautious, WW chose not to combine temperature and velocity measurements in the same comparison; here this precaution is abandoned in favor of a broader data base.

The observed spectral levels are expressed in terms of the parameters of the GM model. Specifically, we use the form of the horizontal velocity spectrum, $S_u(\omega)$, and vertical displacement spectrum, $S_\zeta(\omega)$, given by Munk (1981)

$$S_\zeta(\omega) = \frac{2}{\pi}\, r\, \frac{f}{N}\, \frac{(\omega^2 + f^2)^{1/2}}{\omega^3} \tag{1}$$

$$S_u(\omega) = S_{u_1} + S_{u_2} = 8\pi r f N\, \frac{(\omega^2 + f^2)}{\omega^3\,(\omega^2 - f^2)^{1/2}} \tag{2}$$

where f is the Coriolis parameter and $N(z)$ is the buoyancy frequency. A combination of parameters in the GM model has been recast into a single parameter r as suggested by Desaubies (1976)

$$r = Eb^2 N_0$$

where E is the non-dimensional energy level, b is the vertical scale of N, and N_0 is the buoyancy frequency scale. Since the kinetic and potential energy are both proportional to r [eqs. (1) and (2)], the parameter r is proportional to the total internal wave energy

(integrated from f to N) per unit mass per unit <u>volume</u>—a physically
relevant quantity. It is useful to define for future reference the
total internal wave energy per unit mass per unit <u>area</u>

$$\bar{E} = 4\pi^2 \; r \int_{bottom}^{surface} N(z) \; dz \quad \times \; (3600)^{-2} \qquad (3)$$

in units of joules $(kg \; m^2)^{-1}$ for $N \gg f$. Note that the units of
frequency used throughout this paper are cycles per hour (cph).

The aim of this survey is to look for a scaling of the
frequency spectrum that best represents the data. Three quantities,
r, rf, and E, are estimated from the same set of historical data and
discussed below.

<u>Estimates of r</u>. Estimates of r were made from the data using a
variety of procedures. Typically, the spectral level was estimated
in a frequency band between the tidal and buoyancy frequencies, e.g.,
WW report the velocity spectral level in a band centered at 0.2 cph.
These estimates of spectral level were then converted to values of r
using the local N(z) and eq. (1) or (2). Of course, this comparison
is model-dependent; the essential purposes of the model are to relate
horizontal velocity spectra to vertical displacement spectra and to
scale the observations in depth by N and in latitude by f.

The estimates of r are presented graphically vs the local N(z)
in Fig. 1. The sources of the data are given in Table 1. No
dependence of spectral level with N(z) is meant to be implied by this
figure. Note, however, that slopes of -1 on this log-log plot
represent lines of constant rN(z), which is proportional to the total
internal wave energy per unit volume (Munk, 1981).

If the value of r were "universal," then the observations
should lie along a single horizontal line. The GM value of $r = 320$
m^2 cph is plotted for reference and is obtained by choosing $E = 6.3 \times 10^{-5}$, $b = 1300$ m, and $N_0 = 3$ cph (Munk, 1981). The variation in
estimates of r is large—three orders of magnitude. However, most
observations are within a factor of 3 of the GM level.

The lower levels of internal wave energy in this survey tend to
be from observations in the Arctic Ocean. Although there are few
observations, the spectral levels measured below the pack ice are
lower than those at low latitude. This result is based on
measurements in the upper ocean (to 200 m) (#1-4) as well as the deep
ocean (1200 m) (#5).

154

Table 1. Source of data displayed in Figs. 1, 2, and 3.
The type of observation is indicated by the abbreviations
T and V, representing temperature and velocity, respectively.

NUMBER	LOCATION Lat.°N, Long.°W	PRIMARY and ADDITIONAL REFERENCES	DATA TYPE	DURATION, days	INSTRUMENT DEPTH, m	WATER DEPTH, m	surface $\int N(z)\,dz$, cph m bottom
1	81.8, -4.0 Fram 3	This Report Morison (1983)	T	4	50-150	800	1070
2	75.4, 140.3 Ice Island T-3	Yearsley (1966) Morison (1983)	T	4	60, 125	3000	2800
3	85.0, 95.0 Ice Island T-3	Bernstein (1972) Morison (1983)	V	70	40, 60	1500	2000
4	85.3, 97.8 Ice Island T-3	Neshyba et al. (1972) Morison (1983)	T	1	250	1500	2000
5	89.2, 141.5 Arctic	Aagaard (1981)	V	35	1240, 1415	1500	2000
6	46.6, 145.1 MILE, NE Pacific	Levine et al. (1983a)	T,V	19	30-175	4000	3300
7	8.8, 22.9 GATE, Atlantic	Käse and Siedler (1980) Roth et al. (1981)	T,V	18-60	18-60	4900	4700
8	25.0, 159.0 Pacific	Pinkel (1975) Roth et al. (1981)	T	10	110	4000	4900
9	59.0, 12.5 JASIN, NE Atlantic	deWitt et al. (1984) Levine et al. (1983b)	T	40	50	1500	1950
10	16.0, 65.0 St. Croix	Tarbell et al. (1977) Roth et al. (1981)	T,V	32	95-243		
11	42.0, 70.0 Cape Cod	Zenk and Briscoe (1974) Roth et al. (1981)	T,V	21	59, 84	500	
12	59.0, 12.5 JASIN, NE Atlantic	Weller (1982) Weller and Halpern (1983)	V	33	82, 100	1550	1950
13	JASIN Area NE Atlantic	Gould et al. (1984) Levine et al. (1983b)	V	27-52	200-1500	1500	1950
14	46.6, 130.2 MATE, NE Pacific	Levine and Irish (1981)	T,V	23	880-1300	2200	4000
15	38.3, 70.0 39.2, 69.0 Under Gulf Stream	Luyten (1977) Wunsch and Webb (1979)	V	230	200-2800	3000	4000
16	28.0, 69.6 MODE Center	Wunsch (1976) Wunsch and Webb (1979)	V		4000	5400	4100
17	33.5, 62.5 Muir Seamounts	Wunsch (1976) Wunsch and Webb (1979)	V	150	2100-3000	3000-4400	
18	39.9, 68.9 Hydrographer Canyon	Wunsch (1976) Wunsch and Webb (1979)	V		320-710	350-700	
19	38.0, -5.0 Mediterranean	Perkins (1972) Wunsch and Webb (1979)	V	60	1200	2700	1800
20a 20b	1.5, -53.0 0 to 0.05, -50 to -57 Indian Ocean	Wunsch and Webb (1979) Eriksen (1980)	V	60-200	1500, 3600 1500, 3600	5100 4700-5100	4700 4700
21	39.5, 72.3 Hudson Canyon	Hotchkiss and Wunsch (1982)	V	105	100-700	300-700	
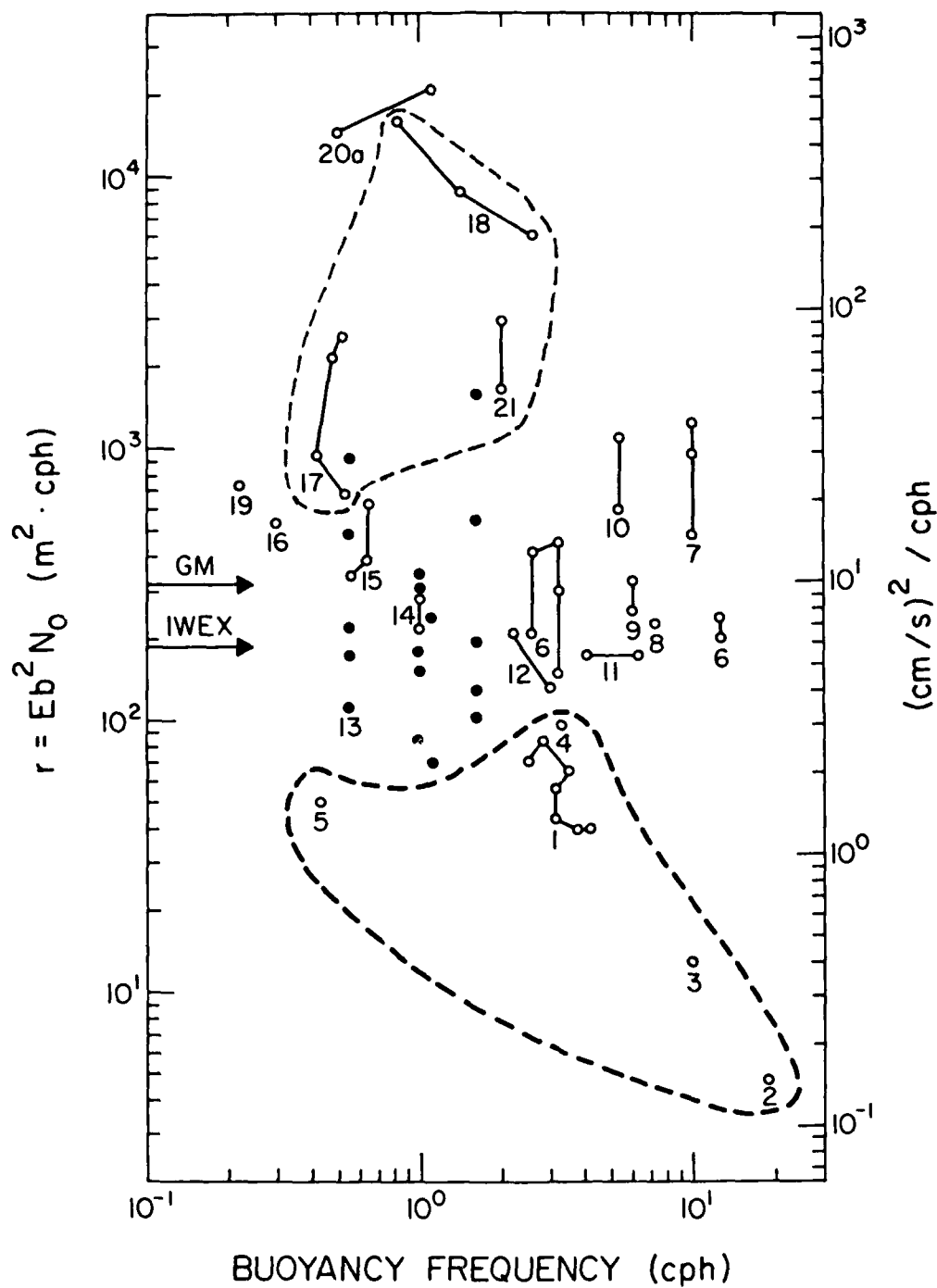
Figure 1. Estimates of the spectral level, reported
in units of $r = Eb^2 N_0$, are plotted vs local buoyancy
frequency. The numbers refer to the data sources listed
in Table 1. The estimates from the Arctic Ocean and near
steep topography are enclosed by a dashed line. Lines
with slope of -1 are isolines of total internal wave
energy per unit volume.

As discussed by WW, high energy levels occur near large topographic features, e.g., Muir Seamounts (#17), Hydrographer Canyon (#18), Hudson Canyon (#21), Ymir Ridge and Lousy Bank (highest values of #13). Values at low latitude also tend to be high, e.g., 16°N (#10), 8.8°N (#7) and 1.5°N (#20a), and estimates of r very near the equator are too large to be plotted, e.g., 0 to 0.05°N (#20b). The high values of r at low latitude are not due to anomalously high spectral levels, but are a consequence of the scaling by f in eqs. (1) and (2); this is demonstrated in the next section.

Estimates of rf. To examine the effect of eliminating the f-scaling from the GM model, the quantity r' = rf is calculated and plotted in Fig. 2 for the same data used in Fig. 1. The scatter among the data is significantly reduced--values from low latitude, e.g., 8.8°N (#7), 16°N (#10), 0-1.5°N (#20a,b), now agree better with mid-latitude observations. However, the observations from high latitude and near topography remain distinct. This evidence supports the suggestion by Munk (1981) that the f-scaling of the GM model frequency spectrum could be eliminated. The consequences of reformulating the entire GM model in a consistent manner without f-scaling is deferred to another forum.

Estimates of $\bar{E}$ and $\bar{E}f$. In the search for another quantity that might be more universal than either r or r', another scaling based on the total internal wave energy per unit surface area was tested. To estimate E, the integral of N(z) from the surface to the bottom is needed (eq. 3). Profiles of N(z) were obtained from the original papers where possible. If sufficient data were not available, historical averages were used (e.g., Levitus, 1982). Hence, estimates of $\int N\,dz$ must be considered coarse. In general, variations of $\int N\,dz$ are not large--all are within a factor of 4 (Table 1). If the data are plotted as a function of E (not shown), there is not much qualitative change in the scatter of the values from Fig. 1; the values from the Arctic are still low and those near topography are high.

Since removing the f-scaling in the GM model reduced the scatter among the data (Fig. 2), the quantity Ef is perhaps a more logical candidate to test for universal scaling than E. Estimates of Ef are shown in Fig. 3. Note some of the data were not used because profiles of N(z) could not be found, mostly near topography. There is about the same amount of scatter in Ef as rf. Even with more accurate estimates of $\int N\,dz$, it does not appear likely that this scaling would be preferable to rf. Conversely, there is no evidence that E is any worse than r in scaling the internal wave frequency spectrum.
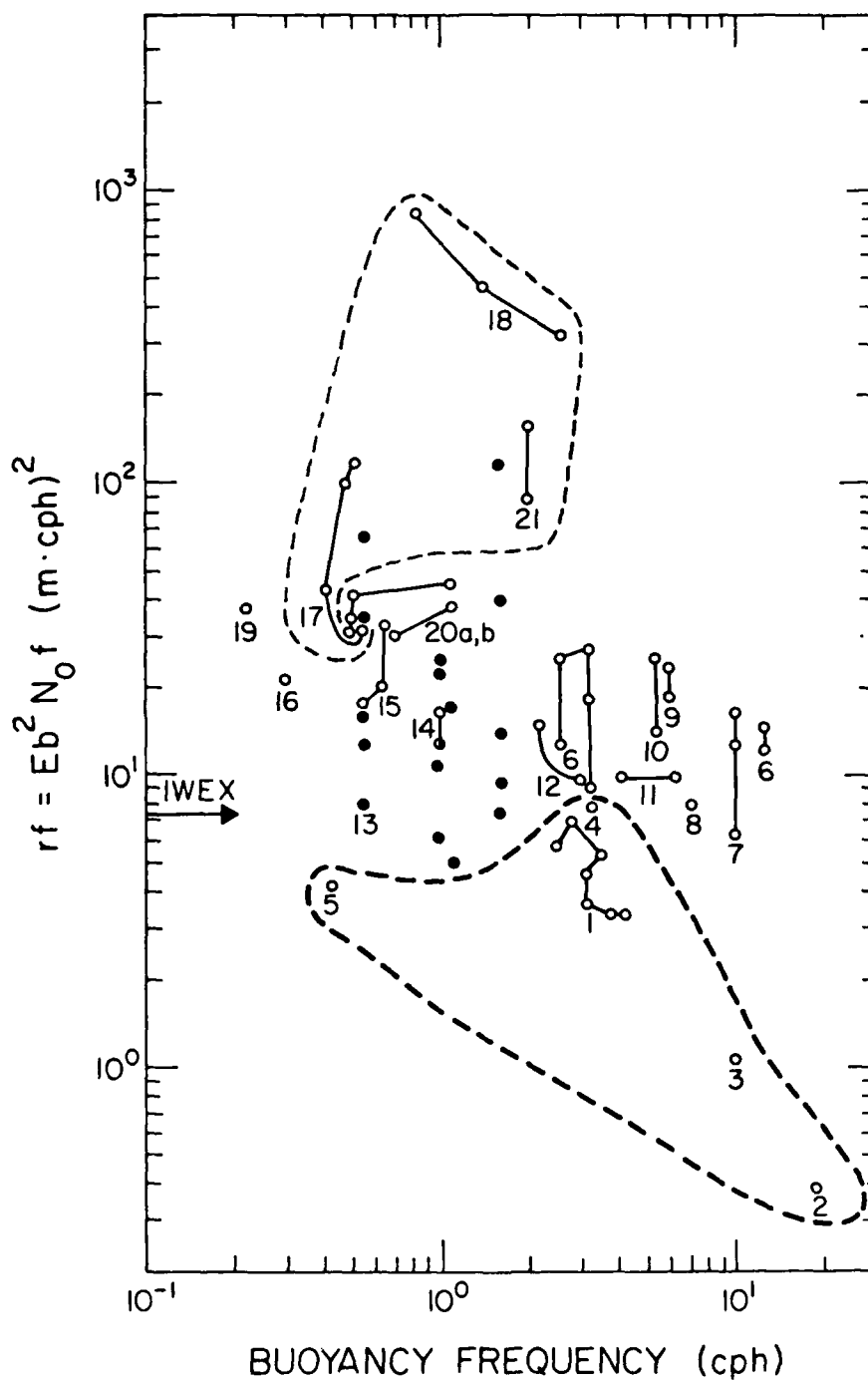
Figure 2. Same data as shown in Fig. 1 with ordinate re-scaled by r' = rf.

158
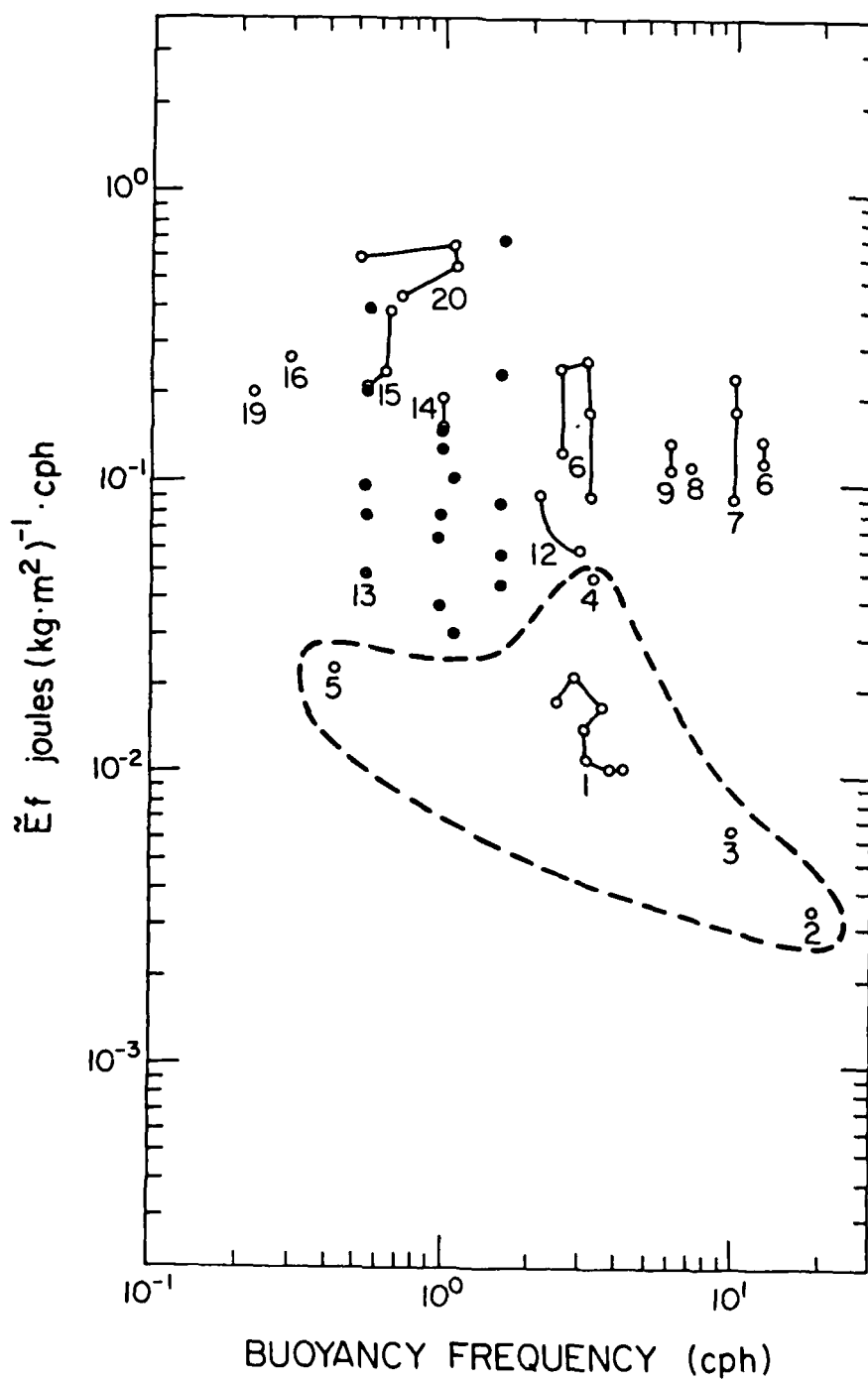
Figure 2. Same data as shown in Fig. 1 with ordinate re-scaled by Ef.

CONCLUSIONS AND CONJECTURE

The purpose of this paper was to discuss some aspects of the notion of "universality" in internal wave observations. This study focused on a survey of historical observations of internal wave frequency spectra of horizontal velocity and vertical displacement. Estimates were made of different quantities in an attempt to determine the best candidate for universality and at the same time to identify data that differ significantly from the universal.

Comparisons of estimates of r, rf, and $\bar{E}f$ for the s...e set of data support the following conclusions (Figs. 1, 2, 3):

   • The frequency spectral level is not a function of f. This is in contrast to the GM model spectrum which scales as $1/f$ (eqs. 1 and 2).

   • The spectral levels in the Arctic Ocean are below the average; levels measured near steep topography are higher than the average.

   • There is little difference in the scatter of the data between scaling by the total energy per unit volume (r) or by the total energy per unit area (E).

The high levels of internal wave energy near topography have been recognized previously by WW. While it is tempting to infer that the topography acts as a generator of internal waves, the high levels are apparently due to the kinematic adjustment of the wave field from reflection off the bottom (Eriksen, 1982) or focusing in canyons (Hotchkiss and Wunsch, 1982).

The recently reported evidence of relatively low energy levels in the Arctic Ocean invites speculation as to possible causes. Perhaps the lower energy can be related to the unique forcing and dissipation processes that are present in the Arctic:

   • The ice-cover damps the internal wave field via a turbulent bour...ry layer.

   • Surface forcing is weaker due to weaker winds and due to the loss of momentum to the coast by internal ice stress.

   • The nature of the stress transfer through the ice is different from an ice-free ocean. The generation of internal waves may depend critically on the geometry of the underside of the ice; momentum transfer from surface waves to internal waves is not possible.

• The internal tides which may transfer energy to other
frequency bands in the temperate oceans are generally
small in the Arctic Ocean.

The significance of these processes in shaping the internal wave
field is not yet known; more thorough investigations are needed.

ACKNOWLEDGEMENTS

REFERENCES

Aagaard, K., 1981: On the deep circulation in the Arctic Ocean.
Deep-Sea Res., 28A, 251-268.

Bernstein, R. L., 1972: Observations of currents in the Arctic Ocean.
Tech. Report No. 7, Contract N-00014-67-A-0108-0016.
Lamont-Doherty Geological Observatory of Columbia University.
Palisades, New York.

Desaubies, Y. J. F., 1976: Analytical representation of internal wave
spectra. J. Phys. Oceanogr., 6, 976-981.

deWitt, L. M., M. D. Levine, C. A. Paulson and W. V. Burt, 1984:
Internal waves in JASIN: Moored observations of isotherm
displacement. J. Phys. Oceanogr. (To be submitted).

Eriksen, C. C., 1980: Evidence for a continuous spectrum of
equatorial waves in the Indian Ocean. J. Geophys. Res., 85,
3285-3303.

Eriksen, C. C., 1982: Observations of internal wave reflection off
sloping bottoms. J. Geophys. Res., 87, 525-538.

Garrett, C. J. R., and W. Munk, 1972: Space-time scales of internal
waves. Geophys. Fluid Dyn., 2, 255-264.

_____, and _____, 1975: Space-time scales of internal waves: A
progress report. J. Geophys. Res., 80, 291-297.

Gould, W. J., A. N. Cutler and D. Weddell, 1984: (Internal report, in
preparation). Institute of Ocean Sciences, Wormley, England.

Hotchkiss, F. S., and C. Wunsch, 1982: Internal waves in Hudson Canyon with possible geological implications. Deep-Sea Res., 29, 415-442.

Käse, R. H., and G. Siedler, 1980: Internal wave kinematics in the upper tropical Atlantic. Deep-Sea Res., Suppl. to Vol. 26, 161-189.

Levine, M. D., and J. D. Irish, 1981: A statistical description of temperature finestructure in the presence of internal waves. J. Phys. Oceanogr., 11, 676-691.

Levine, M. D., R. A. deSzoeke and P. P. Niiler, 1983a: Internal waves in the upper ocean during MILE. J. Phys. Oceanogr., 13, 240-257.

Levine, M. D., C. A. Paulson, M. G. Briscoe, R. A. Weller and H. Peters, 1983b: Internal waves in JASIN. Phil. Trans. R. Soc. Lond. A, 308, 389-405.

Levine, M. D., C. A. Paulson and J. H. Morison, 1984: Internal waves in the Arctic Ocean: comparison with lower-latitude observations. J. Phys. Oceanogr., (Submitted).

Levitus, S., 1982: Climatological atlas of the world ocean. NOAA Professional Paper 13, U.S. Department of Commerce.

Luyten, J. R., 1977: Scales of motion in the deep Gulf Stream and across the Continental Rise. J. Mar. Res., 35, 49-74.

Morison, J., 1983: Internal waves in the Arctic Ocean: A review. Geophysics of Sea Ice, edited by N. Untersteiner. (In press).

Munk, W., 1981: Internal waves and small-scale processes. Evolution of Physical Oceanography, edited by B. A. Warren and C. Wunsch, MIT Press, Cambridge, 264-290.

Neshyba, S. J., V. T. Neal and W. W. Denner, 1972: Spectra of internal waves: In situ measurements in a multiple-layered structure. J. Phys. Oceanogr., 2, 91-95.

Perkins, H., 1972: Vertical oscillations in the Mediterranean. Deep-Sea Res., 19, 289-296.

Pinkel, R., 1975: Upper ocean internal wave observations from FLIP. J. Geophys. Res., 80, 3892-3910.

Roth, M. W., M. G. Briscoe and C. H. McComas, III, 1981: Internal waves in the upper ocean. J. Phys. Oceanogr., 11, 1234-1247.

162

Tarbell, S., S. Payne and R. Walden, 1977: A compilation of moored current meter data and associated mooring action data from mooring 592. Vol XIV (1976 Data), WHOI-77-41, Woods Hole Oceanographic Institution, 122 pp.

Weller, R. A., 1982: The relation of near-inertial motions observed in the mixed layer during the JASIN (1978) experiment to the local wind stress and to the quasi-geostrophic flow field. J. Phys. Oceanogr., 12, 1122-1136.

Weller, R. A., and D. Halpern, 1983: The velocity structure of the upper ocean in the presence of surface forcing and mesoscale oceanic eddies. Phil. Trans. R. Soc. Lond. A, 308, 327-340.

Wunsch, C., 1975: Deep ocean internal waves: what do we really know? J. Geophys. Res., 80, 339-343.

Wunsch, C., 1976: Geographical variability of the internal wave field: A search for sources and sinks. J. Phys. Oceanogr., 6, 471-485.

Wunsch, C., and S. Webb, 1979: The climatology of deep ocean internal waves. J. Phys. Oceanogr., 9, 235-243.

Yearsley, J. R., 1966: Internal waves in the Arctic Ocean. Master's Thesis, Mechanical Engineering Department, University of Washington, Seattle, WA.

Zenk, W., and M. G. Briscoe, 1974: The Cape Cod experiment on near-surface internal waves. WHOI Ref. 74-87, Woods Hole Oceanographic Institution, 52 pp.

ESTIMATES OF CROSS-ISOPYCNAL DIFFUSIVITIES FROM CLIMATOLOGICAL HYDROGRAPHIC DATA

D. J. Olbers
Max-Planck Institut fuer Meteorologie, Hamburg

J. Willebrand and M. Wenzel
Institut fuer Meereskunde, Kiel

ABSTRACT

Estimates of cross-isopycnal diffusivities obtained by applying a beta-spiral method to the climatological hydrographic atlas of Levitus (1982) reveal values of 10^{-5} m^2/s in the low current regions of the North Atlantic. Most of the values are not statistically different from zero, however, since standard deviations are of the same order of magnitude. We thus conclude that diffusivities appropriate to the actual state of the ocean are much lower than the traditional value of 10^{-4} m^2/s.

INTRODUCTION

Microstructure measurements obtained in the recent years suggest that vertical mixing rates are much lower than Munk's (1966) recipe of $K_v = 10^{-4}$ m^2/s estimated from a balance of upwelling and vertical diffusion in temperature, salinity, and passive tracer profiles. This 1 cgs milestone was accepted by the oceanographic community for about a decade although it was well-known that the balance of upwelling and diffusion was too simplistic to explain the thermocline circulation in which horizontal advection cannot be ignored. With the more advanced diagnostic methods such as the beta-spiral method (Stommel and Schott, 1977), mixing coefficients can in principle be inferred from hydrographic data without any presumption about the importance of the advective and diffusive terms in the tracer balance. We give here a brief survey of results obtained for cross-isopycnal mixing by applying a beta-spiral scheme to data from the climatological hydrographic atlas of Levitus (1982). The cross-isopycnal mixing coefficients estimated from these data are less than 10^{-5} m^2/s in the subtropical gyre and attain larger values in the region of strong currents but, by and large, all values are smaller than their standard deviations. The results of the beta-spiral analysis are thus consistent with microstructure estimates of mixing. A more detailed description of our analysis, including long-isopycnal mixing and mixing of vorticity, will shortly be published (Olbers et al., 1984).

METHOD

The beta-spiral method is based on the thermal wind relations, the
linearized vorticity balance and the balance of a tracer Ψ

$$\underset{\sim}{u}_z = - \frac{g}{f} \underset{\sim}{k} \times \nabla \rho \tag{1}$$

$$w_z = \frac{\beta}{f} v \tag{2}$$

$$\underset{\sim}{u} \cdot \nabla \Psi + w \Psi_z = G \tag{3}$$

where G represents the effect of mixing which we parameterize in terms of
long and cross-isopycnal diffusion. We are interested here with mixing
effects which might be associated with internal waves and thus restrict the
discussion to cross-isopycnal mixing. The most convenient tracer for this
purpose is potential density σ as long-isopycnal mixing drops out of the
balance (if non-linear effects as cabling are ignored). Then G is given by

$$G = A_c (\nabla^2 + \partial_z^{\ 2})\sigma \cong A_c \sigma_{zz} \tag{4}$$

where the cross-isopycnal diffusion coefficient A_c is assumed to be a
constant with depth.

Integrating (1) and (2) from an arbitrary reference level $z = z_0$ where
$\underset{\sim}{u} = \underset{\sim}{u}_0$ and $w = w_0$ and inserting the result into (3) we get the
beta-spiral equations

$$\underset{\sim}{u}_0 \cdot \nabla \sigma + w_0 \sigma_z - A_c \sigma_{zz} + v_0 \frac{\beta}{f} \sigma_z (z - z_0)$$

$$= \frac{g}{f} \left\{ J_{xy} \left[\sigma, \int_{z_0}^z dz' \rho \right] - \frac{\beta}{f} \sigma_z \int_{z_0}^z dz' (z' - z_0)\rho_x \right\} \tag{5}$$

which can be used to estimate the unknown reference velocitites $\underset{\sim}{u}_0$ and w_0
and the diffusion coefficient A_c by a least-squares fit of the linear
velocities (5) at different levels to data of gradients of potential
density σ and density ρ. If these data are given at levels $z = z_j$ ($j =$
1, . . ., J) the equations to be solved are of the form

$$D_{jk} P_k - b_j = \varepsilon_j \tag{6}$$

where $(P_k) = (u_0, w_0, A_c)$, $k = 1, \ldots, K$ are unknown parameters,
D_{jk} and b_j are the known coefficients appearing in (5) and ε_j is the
imbalance due to data noise and imperfections of the model. Minimizing the
weighted square sum

$$\varepsilon^2 = \sum_{i,j} \varepsilon_i W_{ij} \varepsilon_j \tag{7}$$

the solution is simply

$$\underset{\sim}{P} = (\underset{\approx}{D}^{+}\underset{\approx}{W}\underset{\approx}{D})^{-1}\underset{\approx}{D}\underset{\approx}{W}\underset{\sim}{b} \tag{8}$$

This solution may yield negative diffusion coefficients. Then, (8) was not used but a minimum of ϵ^2 was searched with the constraint of positive diffusion coefficients. The weighting matrix W_{ij} is the only subjective element in the method. For a thorough discussion and geometrical interpretation we refer to Muller et al. (1978). In this study we choose W_{ij} diagonal and inversely proportional to the variance of the imbalance at each level, i.e.

$$W_{ij} = \delta_{ij} / <\epsilon_i^2> \tag{9}$$

so that each of the equations (6) is weighted by its corresponding data noise. The quantity $< \epsilon_i^2 >$ was estimated by a Monte Carlo simulation.

As the parameters P_k are estimated from noisy data (both, the vector b and the matrix D, are obtained from data) they are contaminated by data noise. Parameters variances can be obtained from (8), a rough approximation being

$$<\delta P_k \delta P_l> = \frac{<\epsilon^2>}{J_{eff} - K} (\underset{\approx}{D}^{+}\underset{\approx}{W}\underset{\approx}{D})^{-1}_{kl} \tag{10}$$

where J_{eff} is the number of statistically independent ϵ_j, which is unknown. Replacing this number by $J > J_{eff}$ underestimates the covariances by a factor of 2 to 3.

THE CROSS-ISOPYCNAL DIFFUSION COEFFICIENT

The analysis was applied to the North Atlantic part of Levitus' (1982) atlas. For the actual fit only data below the maximum mixed layer depth (about 100-200 m in the subtropic increasing to about 1000 m in high latitudes) and above 2000-m depth were used. Since the mixing coefficient was expected to vary with depth this part of the water column was divided again. In the first run u_o, v_o, w_o and A_c were computed from the deeper part (800 m - 2000 m). The reference velocities were then fixed in the second run which determined A_c for the upper part between the mixed layer base and 800-m depth.

Maps of A_c and its standard deviation are given in Fig. 1 and 2. Apparently, the coefficient A_c is of order 10^{-5} m^2/s in the low velocity regimes within the subtropical gyre and north of the North Atlantic current system. This current appears very broad due to climatological averaging of the actual data, as shown by the geostrophic velocities at 100 m in Fig. 3. Within the strong current regime cross-isopycnal mixing becomes more important and A_c attains values of order 10^{-4}m^2/s. The standard deviations of A_c shown in Fig. 1b and 2b reveal a similar pattern as the coefficient itself and the magnitudes are as large as or even larger than A_c. Notice that the noise pattern in Fig. 2 closely resembles the
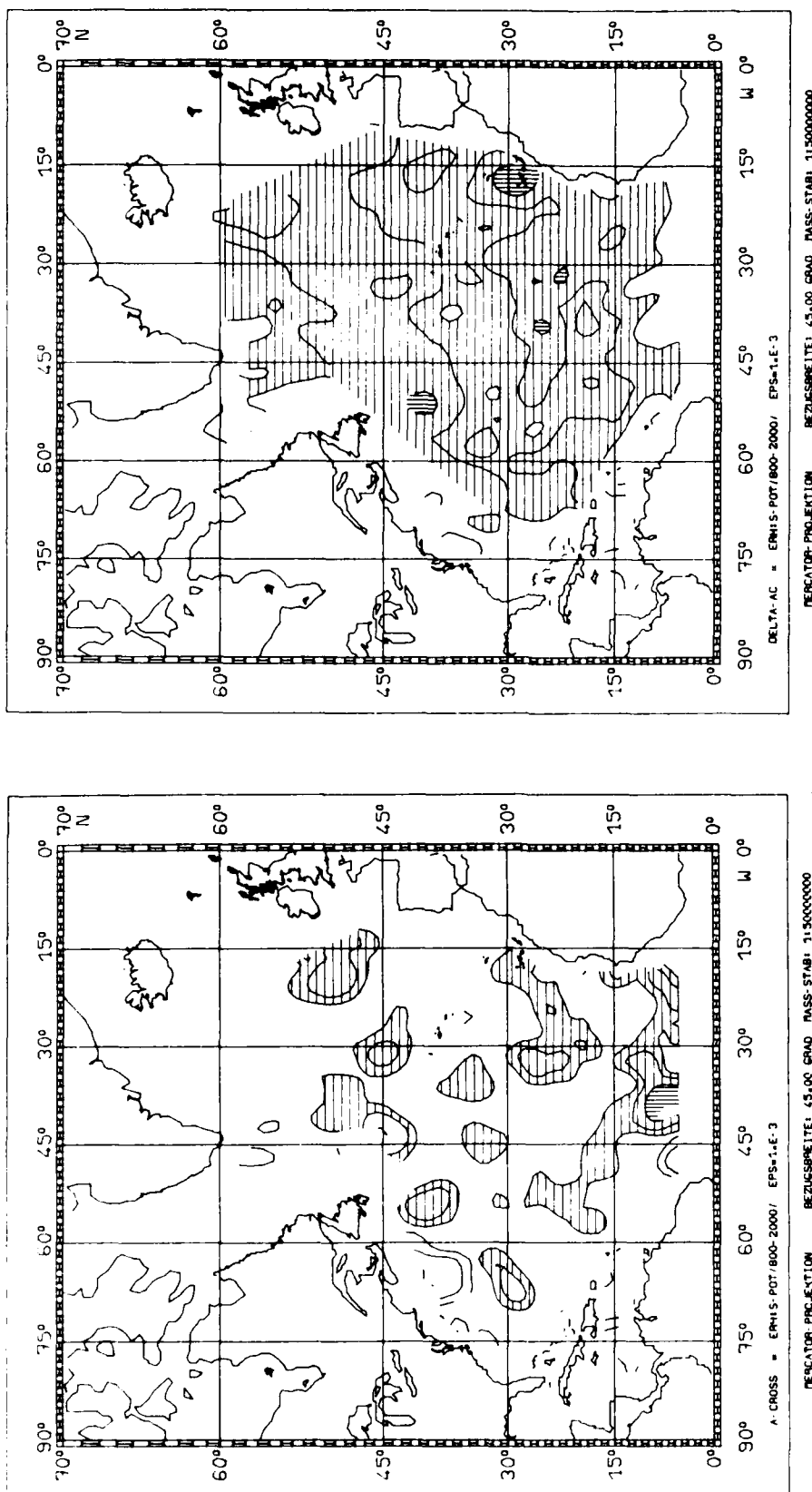
Fig. 1 Isolines of the cross-isopycnal diffusion coefficient A_c (a) and its standard deviation (b) for the depth range 800 m to 2000 m. Vertical hatching: larger than $10^{-4} m^2 s^{-1}$; horizontal hatching: larger than $10^{-5} m^2 s^{-1}$ and smaller than $10^{-4} m^2 s^{-1}$; blank: smaller than $10^{-5} m^2 s^{-1}$.

167
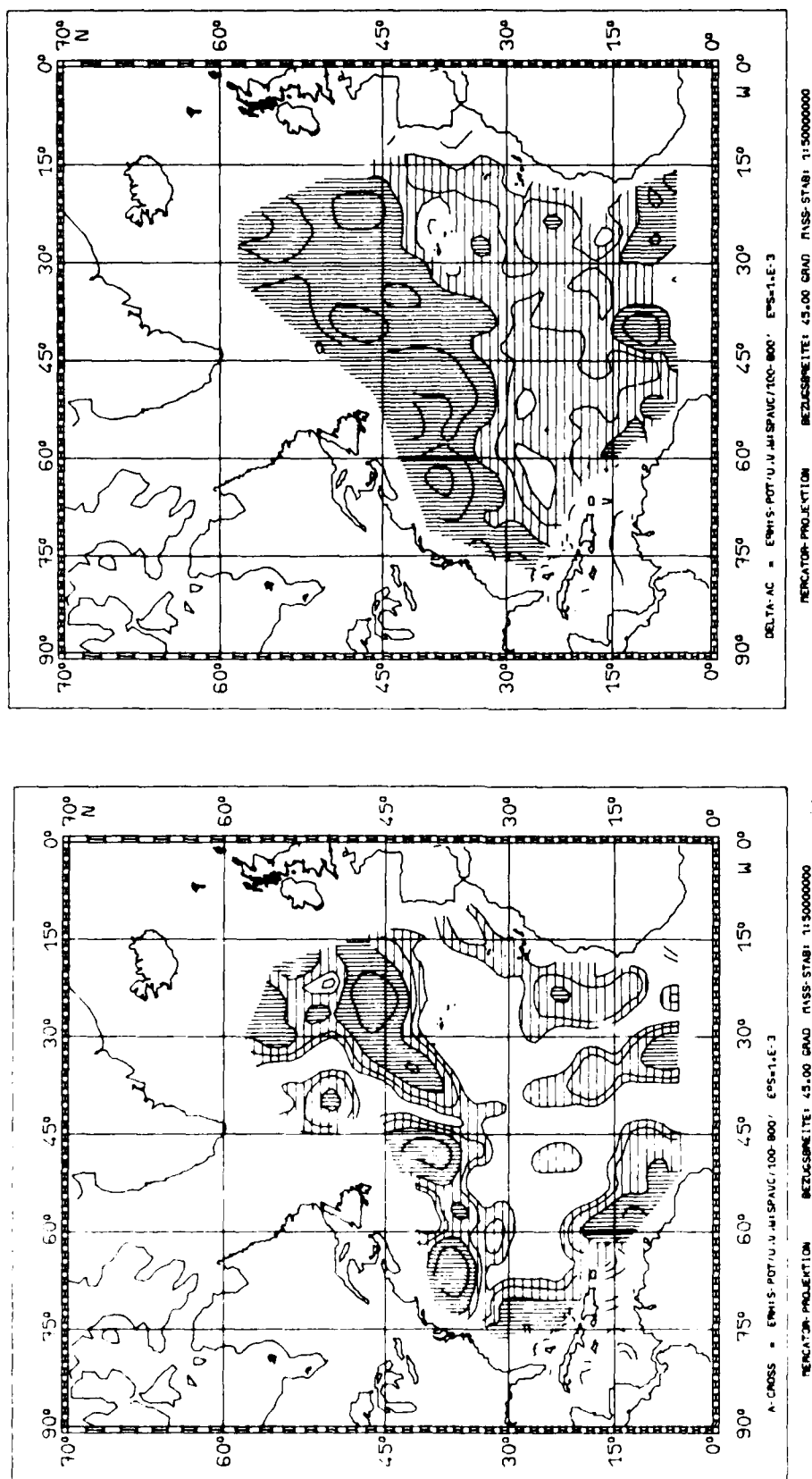
Fig. 2 Same as Figure 1, but for the depth range mixed layer base to 800 m.
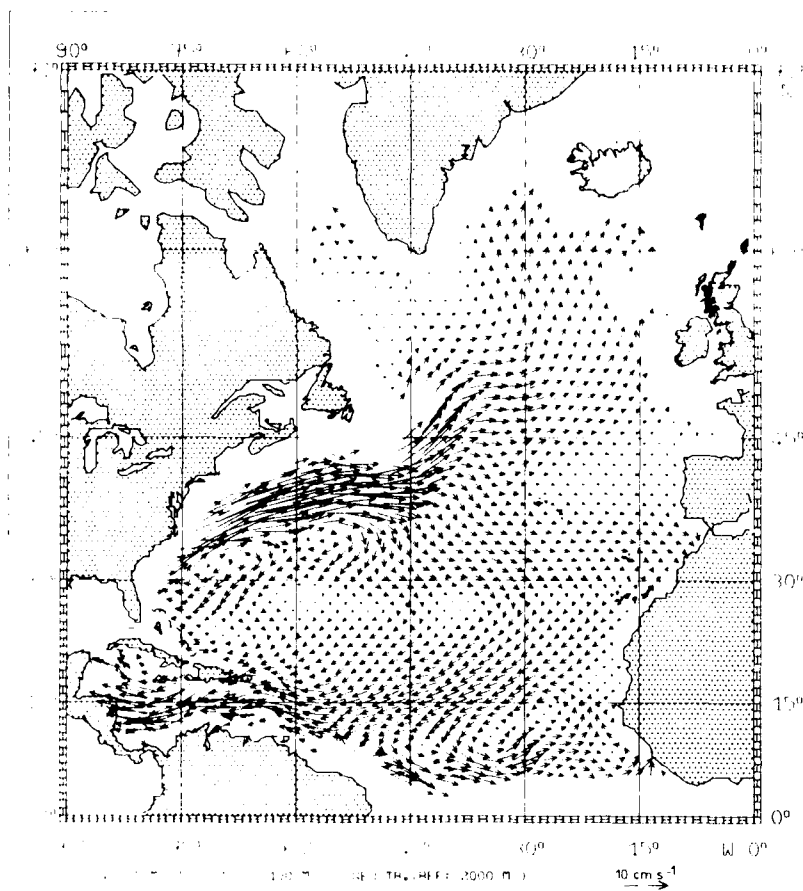
Fig. 3 Geostrophic velocities at 100 m relative to
2000 m inferred from Levitus' (1962) atlas.

eddy statistics of the temperature field as computed e.g. by Dantzler (1976).
(In fact the quantities are closely related.) Remembering that the
variances of A_c are underestimated by factors of 2 to 3 we have to
conclude that none of the values of A_c is statistically different from
zero.

To summarize, outside strong current regimes the estimates of cross-isopycnal
mixing coefficients obtained in this analysis are significantly lower (about
an order of magnitude) than Munk's abyssal recipe of $10^{-4}m^2/s$ and,
further, most values are statistically not different from zero. The results
for long-isopycnal mixing not shown here revealed long-isopycnal diffusion
coefficients in the range $10^2m^2/s$ to $10^3m^2/s$ which are above the
standard deviation in the region of the Mediterranean tongue. The balance
of heat and salinity within the domain of our analysis (mainly the
themocline down to 2000 m) is thus consistently described by advection and
diffusion along isopycnals with no (or very little) cross-isopycnal

transport. In this respect our results seems to confirm the low mixing rates estimated from microstructure measurements. This result appears to hold even more strongly for the actual ocean state because the coefficients we have determined are likely to be biased toward larger values by climatological averaging.

ACKNOWLEDGMENTS

REFERENCES

Dantzler, H. L. Jr., 1976: Geographic variations in intensity of the North Atlantic and North Pacific oceanic eddy fields. Deep Sea Res., 23, 783-794.

Levitus, S., 1982: Climatological atlas of the world ocean. NOAA Professional Paper.

Muller, P., D. J. Olbers and J. Willebrand, 1978: The Iwex Spectrum. J. Geophys. Res., 83, 470-500.

Munk, W. H., 1966: Abyssal recipes. Deep Sea Res., 13, 707-730.

Olbers, D. J., J. Willebrand and M. Wenzel, 1984: The inference of North Atlantic circulation parameters from climatological hydrographic data. To be published.

Stommel, H. and F. Schott, 1977: The beta-spiral and the determination of the absolute velocity field from hydrographic station data. Deep Sea Res., 24, 325-329.

PARAMETERIZING THE EFFECTS OF INTERNAL WAVES: SIMPLE IDEAS AND THINGS WE NEED TO KNOW

Christopher Garrett

Department of Oceanography
Dalhousie University
Halifax, Nova Scotia
Canada B3H 4J1

ABSTRACT

A number of observed properties and theoretical ideas
concerning internal waves and microstructure seem to be
consistent with a vertical eddy diffusivity, due to
breaking internal waves, of no more than about $10^{-5} m^2 s^{-1}$ in
the main thermocline and away from ocean boundaries. The
depth dependence of K_v is uncertain, with kinematic
arguments for wave breaking not suggesting any strong N-
dependence. Values for other parameters representing the
secondary effects of internal waves are even more
uncertain, but are needed for models of some mesoscale
features.

INTRODUCTION

Internal waves may be a source of endless fascination for
most of us at this meeting, but for many of our colleagues
they are merely a messy bit of sub-grid-scale physics that
has to be parameterized. Do we now have an adequate
understanding of oceanic internal waves to provide values
of internal-wave-induced eddy diffusivity and eddy
viscosity coefficients (if these are appropriate concepts)
in terms of external parameters (such as wind-stress) or
internal parameters (such as current shear) that are
resolved on a scale of, say, 10 m vertically and 10 km
horizontally?

As I have argued elsewhere (Garrett, 1984), several
different factors associated with the oceanic internal wave
field and oceanic mixing seem to be consistent with each
other and with a small vertical eddy diffusivity in the
main thermocline. I shall summarize this lowest order view
in the next section before expanding on one aspect of it,
the kinematic arguments connecting the internal wave field

and the vertical eddy diffusivity K_v. This leads on to a
contribution to the important debate, pursued by others at
this meeting, on the dependence of K_v on the mean
stratification or depth. The answer is still not clear,
but the paper concludes by pointing out that we know even
less about how to parameterize the effective eddy
viscosities associated with the interaction of internal
waves with shear flows.

A ZEROTH ORDER VIEW

The sketch in Figure 1 is an attempt to summarize arguments
that kinematic and dynamic estimates of the frequency and
energetics of internal wave breaking, along with some
degree of universality in time and space, are consistent
with a vertical eddy diffusivity, K_v, of less than about
$10^{-5} m^2 s^{-1}$, as typically obtained from microstructure
measurements away from boundaries or regions of strong mean
shear. An additional consistency check for this scenario
is in the typical overturning scale, as calculated from a
kinematic approach to breaking internal waves or measured
in the ocean.
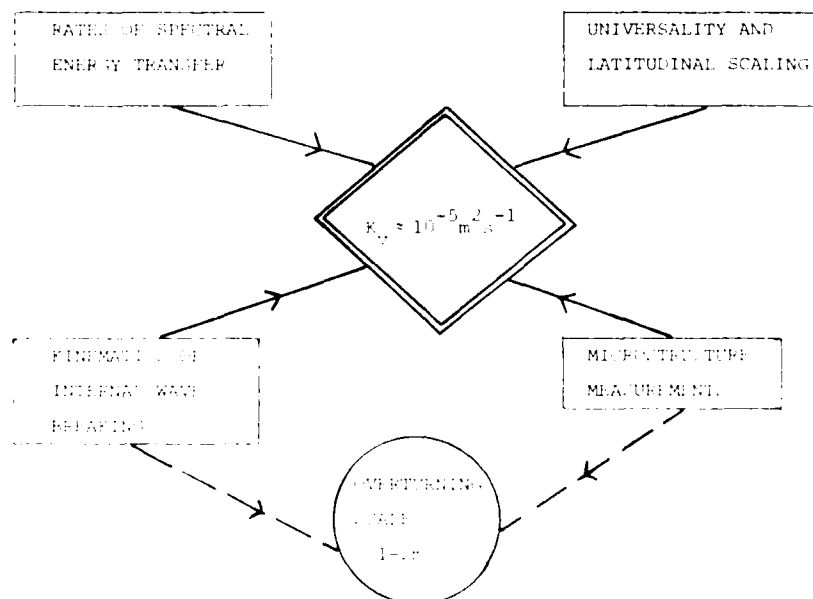
Figure 1. Schematic of a zeroth order view in which a
    number of observed and theoretical properties of
    internal waves and microstructure are consistent with
    each other.

Whether this is a useful lowest order view, or a myth that will shortly be destroyed, is uncertain, but the picture does at least point out the different elements that must be reconciled in any other simple view.

Most of my discussion will be of the kinematic approach, but let me first briefly summarize the other elements of Figure 1:

Dynamics

The most comprehensive computations, so far, of energy fluxes within the typically observed internal wave field are those by McComas and Müller (1981). As they point out, the time for wave-wave interactions to drain the energy of the dominant low-mode waves is of the order of 50 to 100 days. If this energy eventually leads to shear instability at high wavenumbers, with 80% being dissipated and 20% appearing as potential energy (Osborn, 1980; Oakey, 1982), then

$$K_v \rho_0 N^2 \simeq 0.2 \ E/(50 \text{ to } 100 \text{ days}) \tag{1}$$

where E is the local internal wave energy density. This leads to K_v of a few $\times 10^{-6} m^2 s^{-1}$.

Universality

It has been argued by several authors that this rather long time constant leads to a smoothing of temporal variations in internal wave generation. Moreover, starting from estimates by Cox and Johnson (1978), it seems likely that in 100 days a patch of high wave energy would spread about 1,000 km (although this number is far from certain) so that there is also some spatial smoothing. The long lifetime (or equivalently, small K_v) is thus consistent with the alleged absence of internal wave "calms" between places and times of strong generation, and with the fact that, to some extent, internal waves scale with latitude, as well as depth, in a manner that can be associated purely with propagation (Eriksen, 1980; Fu, 1981; Munk, 1980).

KINEMATICS OF WAVE BREAKING

A simple-minded kinematical model for the effects of sporadic shear instability of the internal wave field was introduced by Garrett and Munk (1972). They assumed that a shear instability would occur at some shear maximum where the Richardson number dropped below 1/4, and spread to mix a layer with a bulk Richardson number of about 0.4.

174

The net vertical eddy diffusivity was given roughly by $1/12H^2 T_e^{-1}$, with T_e the time between mixing events in each depth H, with the thickness H of the mixing events related to the vertical shear spectrum S(m) by

$$H \simeq 0.7 \; \pi \; [\int S(m)dm/\int m^2 S(m)dm]^{1/2}. \tag{2}$$

This, of course, is just an estimate of the typical thickness of a mixing event; estimating the probability distribution of H probably requires Monte-Carlo simulations such as those of Desaubies and Smith (1982).

Gargett et al.(1981) point out that the vertical wavenumber spectrum S(m) may be represented well by a spectrum that is white between some small wavenumber and a wavenumber m_0, and proportional to m^{-1} between m_0 and some higher wavenumber m_1 (Figure 2). (Beyond m_1 the shear seems to be associated with small-scale turbulence.) If we insert this form for S(m) in (2) we obtain

$$H \simeq 3.1 \; m_1^{-1} \; [1 + \ln(m_1/m_0)]^{1/2} \tag{3}$$

and for Gargett et al's (1981) choice of m_0 = 0.1 cpm, m_1 = 1 cpm, we have $H \simeq 1$ m. This estimate for the thickness of a mixing event is broadly consistent with observations (e.g. Gregg and Briscoe, 1979).
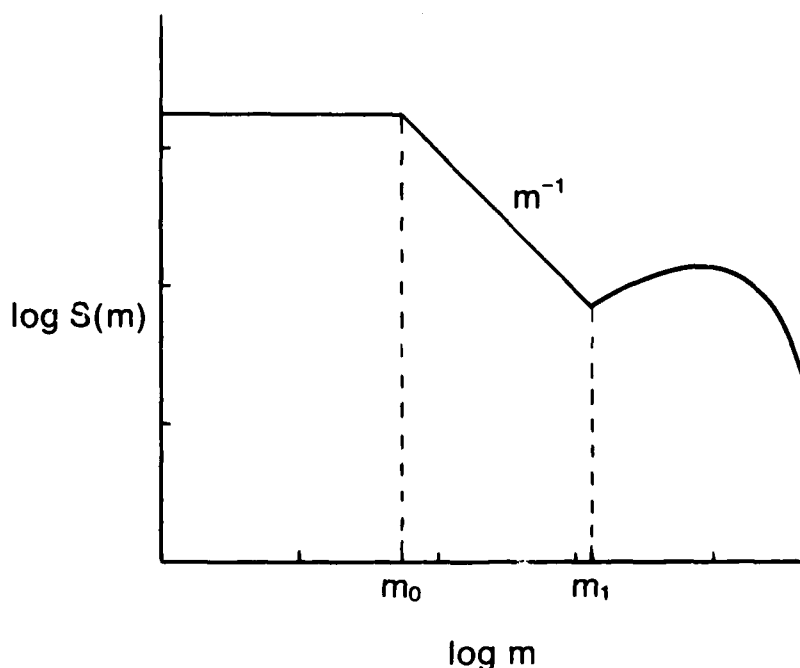
Figure 2. Schematic of the vertical wavenumber spectrum of the vertical shear of horizontal current due to internal waves (after Gargett et al, 1981).

The idea of shear instability on this sort of scale is also consistent with the long-recognized fact that the Richardson number based on the average N^2 and the shear spectrum integrated to a high wavenumber can be comparable with the critical value of 0.25 (e.g. Garrett and Munk, 1975; Garrett, 1979). For the spectrum of Gargett et al. (1981) the Richardson number is about 1 for the shear to m_0 = 0.1 cpm or about 0.3 if the integration is continued to $m_1 \simeq 1$ cpm.

It is difficult to decide what the time interval T_e between mixing events should be. One might take it to be the time interval between shear maxima. For a typical frequency spectrum this is 0.8 times the geometric mean of the inertial and Väisälä periods (Garrett and Munk, 1972), leading to K_v of no more than about $10^{-5} m^2 s^{-1}$, again roughly consistent with microstructure measurements.

It has been pointed out (e.g. Osborn, 1978; Gregg, 1980) that overturning events, while not more than a metre or two thick, tend to occur in active regions that may be 10's of metres thick. This is consistent with the model runs of Desaubies and Smith (1982), or with one's expectations for a shear field that contains a considerable amount of low-wavenumber shear. Indeed, I find it quite plausible that the change in slope of the shear spectrum at $m_0 \simeq 0.1$ cpm (Gargett et al, 1981) is a transition from inertio-internal waves to finestructure. If one envisages a situation with no shear for $m > m_0$, a rare instability on the scale of m_0^{-1} will presumably generate density finestructure with $m^0 > m_0$ which will subsequently lead to shear with $m > m_0$. This situation could then, perhaps, perpetuate itself, with the internal waves having $m < m_0$ leading to clusters of instabilities with overturning scales given by the scale of the finestructure.

One might then want to argue that overturning events could occur more frequently if a large-scale ($> m_0^{-1}$) shear is imposed, with the time scale of a few times N^{-1} given by the time for development of Kelvin-Helmholtz instability. Perhaps the mixing events occur in clusters in time as well as space, with the clusters separated by $O(f^{-1})$ in time.

Mixed Region Collapse

The kinematic arguments above assume a one-dimensional view of the vertical mixing due to internal wave breaking. However, some of the potential energy gained in an isolated mixing event may be lost if the mixed region subsequently collapses (Figure 3). Garrett (1984) calculated that if each mixed region of horizontal scale ℓ collapses to a

(a)

$\rho(z)$

(b)

H

Mixed

ℓ

(c)

L
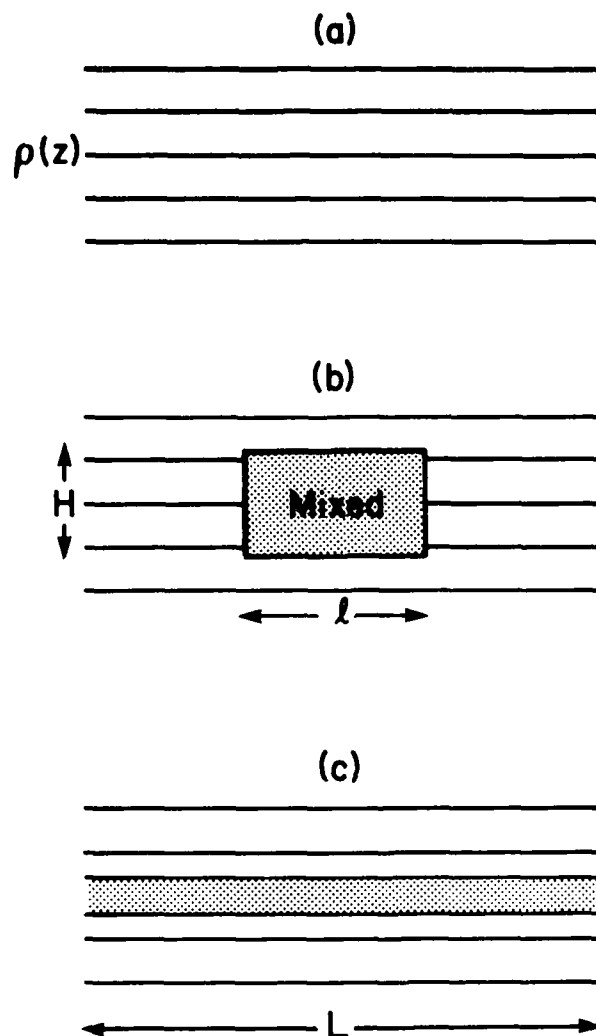
Figure 3. Schematic of the mixing, over a horizontal
distance ℓ, and subsequent collapse to a distance L,
of a region of stratified ocean.

scale L ℓ, the effective K_v is reduced by a factor
$1/2(1+\ell/L)$ from that calculated neglecting collapse. This
factor tends to $1/2$ as $\ell/L \to 0$. Mel Briscoe asked, during
this meeting, if this result still applies if the mixed
region spreads in both horizontal directions, rather than
just one. The answer is easily seen to be yes; ℓ/L is
simply replaced by the ratio of the initial to final
horizontal areas occupied by the mixed patch.

DEPTH DEPENDENCE OF K_v.

As discussed above, there are a number of features of
oceanic microstructure and the internal-wave field in the
ocean which are consistent with an average K_v of no more
than about $10^{-5} m^2 s^{-1}$. This is an important result, in that
it is an order of magnitude less than the $10^{-4} m^2 s^{-1}$ which
is often required in model fits to large-scale ocean
features (e.g. Munk, 1966). There is not really a conflict
here, as most of these model results are for depths greater
than the bulk of the microstructure measurements.

Gargett and Holloway (1984) have made the very interesting
and important suggestion that $K_v \propto N^{-1}$, and have assembled
microstructure data that do seem to point in this direction
(although weakly still, given the limited range of N). Is
this N^{-1} dependence compatible with any of the discussions
of internal waves so far in this paper?

Energetics

If N decreases exponentially with depth (a reasonable first
approximation) and the rate of loss of energy from the
internal wave field is $5K_v \rho N^2$ at any depth, then the depth-
integrated rate of loss of energy is only twice as much for
$K_v = K_0 N_0 N^{-1}$ (with N_0 the near-surface value of N) as for
$K_v = K_0$ throughout. A scenario with the internal-wave-
induced $K_v < 10^{-5} m^2 s^{-1}$ in the main thermocline, increasing
like N^{-1} with depth, is thus not inconsistent with the long
lifetime of the internal-wave field that is, in turn,
consistent with some degree of universality.

Dynamics

McComas and Müller (1981) find an energy flux to high
wavenumbers that scales like N^2 if the bandwidth of the
energy-containing waves scales in a WKB fashion. This
would give K_v independent of N^2. However, the timescale
for these interactions is longer than the timescale for
significant vertical propagation, so this argument is
probably not very relevant

Kinematics

If the internal waves scale with depth according to the WKB
approximation, then

$$S(\omega,m;N) = (N^2/N_0^2)S(\omega, mN/N_0; N_0) \qquad (4)$$

and the integrated shear out to some WKB-scaled wavenumber
is proportional to N^3. However, Gargett et al. (1981) find

that the transition wavenumber m_0 seems to remain constant with depth (although only for two values of N that differ by less than a factor of 2) so that the integrated shear scales like N^2 and the associated Richardson number is independent of N.

One thus envisages a scenario with WKB scaling in the vertical, apart from a constant transition wavenumber (rather than one proportional to N) maintained, presumably by wave-wave interactions. If the m^{-1} dependence of the shear spectrum for $m > m_0$ is also maintained, then one is left with the two results:

(i) the wavenumber to which one must integrate to achieve a certain integral shear (or equivalent Richardson number) is independent of N, and

(ii) the associated vertical scale from eq.(2) is independent of N.

In the kinematic approach to wave breaking the only quantity left to have N-dependence is T_e. The simple argument cited earlier suggested that $T_e \propto (Nf)^{-1/2}$ so that $K_v \propto N^{1/2}$. One might equally well argue $T_e \propto f^{-1}$ so that K_v is independent of N, but it is hard to see how the kinematic arguments can be reconciled with $K_v \propto N^{-1}$.

The key assumption in the above argument is that the low wavenumber part of the internal wave spectrum follows WKB-scaling. In areas where the spectrum is enhanced (as by reflection off a sloping bottom (Eriksen, 1982)), the vertical scale associated with a critical Richardson number can be much larger and the associated K_v much greater. It should certainly be borne in mind that one interesting measure of a proposed or observed internal wave spectrum is the vertical wavenumber to which one has to integrate the shear to obtain an O(1) Richardson number.

My own guess is that some years from now we will settle on a scenario in which internal wave breaking leads to a small K_v everywhere in the ocean interior away from boundaries, but that close to a sloping bottom the enhancement of the reflected internal wave field (Eriksen, 1982) leads to considerable internal wave breaking and a very effective form of "near-boundary" mixing that has a significant effect on the distribution of ocean properties.

OTHER PARAMETERS

Diapycnal mixing by internal waves, as represented by the eddy diffusivity, K_v, may be their most important effect that has to be represented in a large-scale ocean

circulation model, although A_v, the vertical eddy
viscosity, could also be important. The dominant
horizontal (or isopycnal) transfer of scalars or momentum
is probably dominated by mesoscale eddies. However, in
considering the dynamics of the eddies themselves, or of
isolated lenses or fronts, we will need to parameterize the
role of internal waves in the vertical and horizontal
transfer of mass and momentum. Assuming that these
processes can be represented using eddy coefficients A_h,
K_h, A_v, K_v, with A for momentum, K for mass and subscripts
h and v for horizontal and vertical, the equation for the
buoyancy $b = -g\rho_0^{-1}(\rho-\rho_0)$ in a two-dimensional situation is

$$b_{xxt} + [(f^2/N^2)b_t]_{zz} = (A_v b_x)_{xzz} + (A_h b_{xx})_{xx} +$$
$$[(f^2/N^2)(K_h b_x)_x]_{zz} + [(f^2/N^2)(K_v b_z)_z]_{zz} \qquad (5)$$

subject to hydrostatic and Boussinesq assumptions and with
the Rossby number small and also much less than the Burger
number $N^2H^2(f^2L^2)^{-1}$, with H and L typical vertical and
horizontal scales. It has also been assumed that A_h is
independent of z, but otherwise the eddy coefficients may
be functions of x,z and t. The equation simplifies
somewhat if all the eddy coefficients are independent of x
and z (Müller, 1976).

Our knowledge of appropriate values for these coefficients
is rudimentary. Müller's (1976) theory, in which internal
waves play a role in momentum transfer analogous to that of
molecules in the kinetic theory of gases, led to a
prediction of about 0.4 m^2s^{-1} for A_v. However, Ruddick and
Joyce (1979) evaluated the vertical momentum flux from data
and showed that $|A_v|<0.02$ m^2s^{-1}, with uncertain sign. They
also give possible reasons for the breakdown of Müller's
(1976) theory.

Brown and Owens (1981) find data weakly in support of A_h of
order 100 m^2s^{-1}, a value which they themselves admit is too
large to be compatible with the long observed lifetime of
some mesoscale features.

The relationship of A_v and A_h to the energetics of the
internal wave field, discussed by Müller (1976), as well as
to the dynamics of low-frequency flows, must be borne in
mind. Too large a proposed value of A_v or A_h, multiplied
by the mean square low frequency shear, may not be
compatible with the long lifetime of internal waves implied
by universality.

The horizontal mixing of a scalar by internal waves may be
due to shear dispersion, with $K_h \approx (N^2/f^2)K_v$ (Young et al,
1982), but this formula is dependent on a knowledge of K_v,
so we have come full circle.

180

CONCLUSIONS

We may have a reasonably consistent zeroth-order view of
internal waves and the vertical mixing of density that they
cause, at least in the main thermocline not too close to
boundaries. However, we are still woefully uncertain about
the depth-dependence of K_v or the values of other
parameters such as eddy viscosity coefficients.
Determining how to parameterize the effects of internal
waves on lower frequency, large-scale flows remains the
central oceanographic problem connected with internal
waves.

REFERENCES

Brown, E.B. and W.B. Owens, 1981: Observations of the
horizontal interactions between the internal wave
field and the mesoscale flow. J. Phys. Oceanogr.,
11, 1474-1480.

Cox, C.S. and C.L. Johnson, 1978: Inter-relations of micro-
processes, internal waves, and large scale ocean
features. Unpublished manuscript, Scripps Institution
of Oceanography.

Desaubies, Y. and W.K. Smith, 1982: Statistics of
Richardson number and of instability in oceanic
internal waves. J. Phys. Oceanogr., 12, 1245-1259.

Eriksen, C.C., 1980: Evidence for a continuous spectrum of
equatorial waves in the Indian Ocean. J. Geophys.
Res., 85, 3285-3303.

Eriksen, C., 1982: Observations of internal wave reflection
off sloping bottoms. J. Geophys. Res., 87, 525-538.

Fu, L.-L., 1981: Observations and models of inertial waves
in the deep ocean. Rev. Geophys. and Space Phys., 19,
141-170.

Gargett, A.E. and G. Holloway, 1984: Dissipation and
diffusion by internal wave breaking. J. Mar. Res., 42 (1).

Gargett, A.E., P.J. Hendricks, T.B. Sanford, T.R. Osborn
and A.J. Williams, III, 1981: A composite spectrum of
vertical shear in the upper ocean. J. Phys. Oceanogr.,
11, 1258-1271.

Garrett, C.J.R., 1984: Turning points in universal
speculation on internal waves. In A Celebration in
Geophysics and Oceanography 1982 , Scripps Institution
of Oceanography Reference Series 84-5, 38-46.

Garrett, C.J.R., 1979: Mixing in the ocean interior. _Dyn. Atmos.Oceans_, _3_, 239-265.

Garrett, C.J.R. and W.H. Munk, 1972: Oceanic mixing by breaking internal waves. _Deep-Sea Res._, _19_, 823-832.

Garrett, C.J.R. and W.H. Munk, 1975: Space-time scales of internal waves: a progress report. _J. Geophys. Res._, _80_, 291-297.

Gregg, M.C., 1980: Microstructure patches in the thermocline. _J.Phys. Oceanogr._, _10_, 915-943.

Gregg, M.C. and M.G. Briscoe, 1979: Internal waves, finestructure, microstructure, and mixing in the ocean. _Rev. Geophys. and Space Phys._, _17_, 1524-1548.

McComas, C.H. and P. Müller, 1981: The dynamic balance of internal waves. _J. Phys. Oceanogr._, _11_, 970-986.

Müller, P., 1976: On the diffusion of momentum and mass by internal gravity waves. _J. Fluid Mech._, _77_, 789-823.

Munk, W.H., 1966: Abyssal recipes. _Deep-Sea Res._, _13_, 707-730.

Munk, W.H., 1980: Internal wave spectra at the buoyancy and inertial frequencies. _J. Phys. Oceanogr._, _10_, 1718-1728.

Oakey, N.S., 1982: Determination of the rate of dissipation of turbulent energy from simultaneous temperature and velocity shear microstructure measurements. _J. Phys. Oceanogr._, _12_, 256-271.

Osborn, T.R., 1978: Measurements of energy dissipation adjacent to an island. _J. Geophys. Res._, _83_, 2939-2957.

Osborn, T.R., 1980: Estimates of the local rates of vertical diffusion from dissipation measurements. _J. Phys. Oceanogr._, _10_, 83-89.

Ruddick, B.R. and T.M. Joyce, 1979: Observations of interaction between the internal wavefield and low frequency flows in the North Atlantic. _J. Phys. Oceanogr._, _9_, 498-517.

Young, W.R., P.B. Rhines and C.J.R. Garrett, 1982: Shearflow dispersion, internal waves and horizontal mixing in the ocean. _J. Phys. Oceanogr._, _12_, 515-527.

HOW MUCH INTERNAL WAVE ENERGY IS REDISTRIBUTED OR LOST THROUGH BOTTOM REFLECTION?

Charles C. Eriksen

Department of Earth, Atmospheric and Planetary Sciences
Massachusetts Institute of Technology, Cambridge, Massachusetts 02139

ABSTRACT

A linear internal wave model for reflection off a sloping bottom applied to a field of downgoing horizontally isotropic waves typical of the deep ocean leads to a strongly perturbed frequency-vertical wavenumber energy spectrum. The spectrum is dominated by a non-integrable singularity at the internal wave critical frequency characteristic of the environment and bottom slope. An observational requirement that the internal wave spectrum near the bottom relaxes to the open deep ocean level and shape within a few hundred meters vertically implies a flux imbalance normal to the boundary. The flux which must be redistributed over the internal wave spectrum or lost from it amounts to 0 (10^{-2} W/m^2), larger than for most other energy transfer mechanisms estimated for internal waves. A small fraction of this flux imbalance applied to mixing can account for a basin-averaged effective vertical diffusivity of 10^{-4} m^2/s. Bottom reflection represents not only a likely and powerful sink for internal wave energy, but a mechanism which may be important to the oceanic general circulation through its contribution to mixing.

INTRODUCTION

Internal wave reflection from sloping bottom topography has been documented observationally at several sites where near-bottom measurements have been made (Eriksen, 1982). In all cases, the spectrum of internal wave motions is perturbed from its open deep ocean form. (See the reviews by Munk (1981) , Olbers (1983) for discussions of the spectrum of internal waves in the deep ocean away from boundaries.) The bottom-reflection perturbed spectrum exhibits strong enhancement and horizontal anisotropy over a band of frequencies centered at the frequency where rays are inclined the same as the bottom slope, the critical frequency. These features are predicted by linear theory. Within a few hundred meters of the bottom, the spectrum is observed to relax to the shape and level characteristic of the deep ocean interior. This adjustment is not predicted by linear theory.

Rather, the adjustment must be due to non-linear processes which redistribute internal wave energy throughout the spectrum and/or transform it into potential energy via mixing. The degree to which the internal wave spectrum is perturbed by bottom reflection and its implications are the subject of this theoretical study.

Near-bottom moored observations indicate spectral enhancement and cross-isobath alignment of motions near the critical frequency, but not to the degree predicted by linear theory. Spectral intensification decays roughly exponentially from the ocean bottom with a scale of about 100 m (Eriksen, 1982). Moored vertical difference estimates of shear and buoyancy frequency near the bottom show that Richardson numbers over scales as large as 50 m have distributions which cut off at roughly Ri = 0.25 near the bottom from gradients enhanced by reflection. Profile measurements of currents also indicate near-bottom spectral changes. Hogg, Katz, and Sanford (1978) found that the spectrum of vertical shear of horizontal currents is slightly diminished at vertical wavelengths longer than about a kilometer and somewhat enhanced at shorter wavelengths in approaching Bermuda from the open ocean at thermocline and subthermocline depths. Similarly, Johnson and Sanford (1980) found a transition from clockwise to anti-clockwise polarization of horizontal current variance in the same data in approaching Bermuda, a transition which can be interpreted as a transition from a preponderance of downward to upward internal wave energy flux. They also found currents polarized normal to isobaths in shallower water. Although frequency spectra and vertical wavenumber spectra both show evidence for perturbations of the internal wave spectrum by reflection, the behavior of the joint frequency-wavenumber spectrum of internal wave motions near a sloping bottom has not been measured. Further substantial progress on the reflection process as it actually occurs in the ocean requires attempts to make such measurements.

The purpose of this study is to extend the results of single wave reflection from an arbitrary sloping plane bottom to reflection of a full spectrum of waves and examine the implications of such a calculation for processes of wave interaction both with other waves and with the mean stratification. We imagine a downward flux of internal wave energy with a given spectrum which is incident on a sloping bottom. The energy density of the total (incident plus reflected) wave field can be calculated from the reflection rules for single wave components. The basic problem for estimating the amount of internal wave energy involved in reflection is that linear theory leads to a non-integrably singular spectrum for energy density of the wave field. However, since the observed total spectrum some distance off the bottom is not demonstrably different from the interior spectrum, a flux imbalance is implied between the incident and reflected parts of the wave field. The nature and strength of this flux imbalance is the ultimate subject of this study.

Some remarks on sea floor topography are in order, since the distribution of bottom slopes in a range of horizontal scales has direct bearing on the importance of bottom reflection to the oceanic

internal wave spectrum. Basically, for the scales of importance to internal waves, most of the ocean bottom is sloping rather than flat. Abyssal hills cover a sizeable majority of the ocean floor. According to Bell (1975a) the rms slope of the sea floor for horizontal wavenumbers less than 0.75 cpkm is 0.07. Slopes in the range 0.1 to 0.5 are common on islands and seamounts. Slopes at the low end of this range are typical for mid-ocean ridges, which cover a sizeable portion of the sea floor. For a more detailed discussion of sea floor bathymetry, the reader is referred to Bell (1975b).

This paper is an abstracted version of a manuscript submitted for publication (Eriksen, 1984), to which the reader is directed for details. Only a brief discussion of the calculation and results is given here.

A SPECTRUM OF REFLECTED WAVES

The kinematics of internal wave reflection are presented in Eriksen (1982) along with observational evidence for spectral enhancement. The basic features of reflection which are important for a spectrum of waves are that a reflected wave typically has vertical wavenumber and horizontal propagation direction (azimuth) different than the incident wave. These transformations are most extreme near the critical frequency $\sigma_c = ((N^2 s^2 + f^2)/(1+s^2))^{1/2}$ (where N = buoyancy frequency, f = Coriolis frequency, and s = bottom slope), but the effect on a spectrum of waves is apparent an octave or more above and below σ_c. Since group speeds and ray tube widths both vary inversely with wavenumber, energy density must vary as the square of wavenumber amplification in order to conserve energy flux normal to a sloping boundary.

To illustrate the collective effect of bottom reflection on a spectrum of waves, the Garrett-Munk model GM79 is used to specify the incident spectrum (Munk, 1981). For reference to observations made near Muir Seamount (Eriksen, 1982), the incident spectrum of energy density and energy flux over a flat bottom are plotted in Figure 1. The part of this spectrum incident over a sloping bottom is drawn in Figure 2a. Figures 1 and 2a differ because in the sloping case waves incident from some azimuths are blocked by the topography. Figure 2b illustrates intensification of the reflected wave spectrum near the critical frequency. Intensification is most apparent at high wavenumbers. The frequency spectrum is sharply peaked near σ_c, but the peak is broad enough to be felt nearly throughout the internal wave band. The wavenumber spectrum is nearly flat, rather than red. In Figure 3b, the sum of incident and reflected wave spectra is drawn. This spectrum is dominated by reflected waves at high wavenumbers and by incident waves at low wavenumbers near the critical frequency. At the extremes of the internal wave range (f and N), the spectrum is relatively unaffected.

186
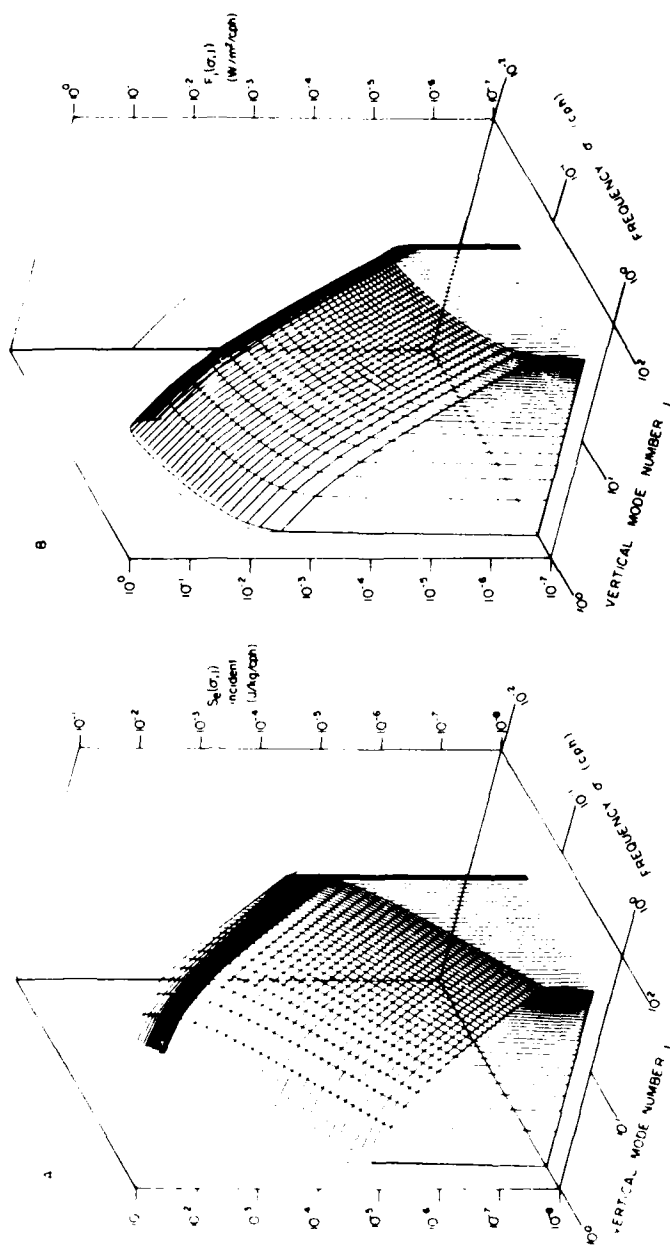
Fig. 1. Energy spectrum $S_e(\sigma,j)$ (a) and flux spectrum $F_i(\sigma,j)$ (b) of internal waves incident on a flat bottom (s=0) specified by GM79 with N = 0.605 and latitude = 33°30'. Spectra are evaluated on a discrete grid of vertical wavenumbers j = 1,32 and frequencies logarithmically equispaced in two domains above and below 1.1f, respectively. Unconnected curves drawn in the planes of the ordinate and lowest vertical mode number are frequency spectra; corresponding curves in the opposite plane are wavenumber spectra.
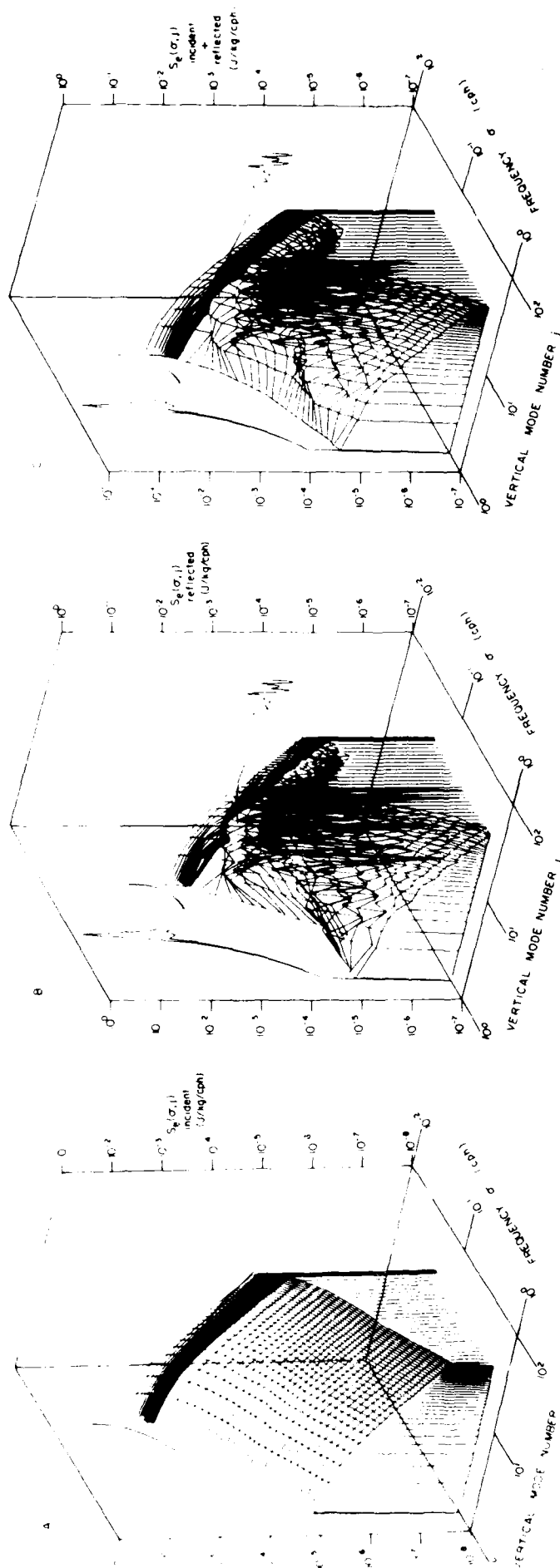
Fig. 2. Energy spectra $S_e(\sigma,j)$ of internal waves over a bottom with slope $s = 0.3$ calculated and drawn as in Figure 1a. a) Incident isotropic spectrum of all possible downward-travelling waves according to GM79. b) Corresponding reflected spectrum, c) Sum of incident plus reflected spectra.
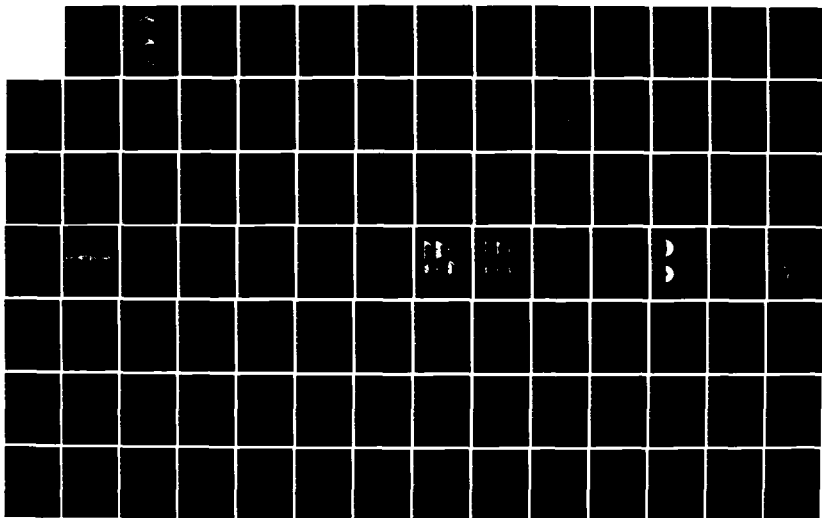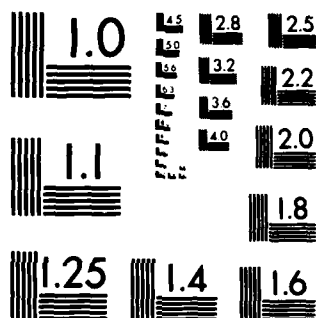
MICROCOPY RESOLUTION TEST CHART

NATIONAL BUREAU OF STANDARDS-1963-A
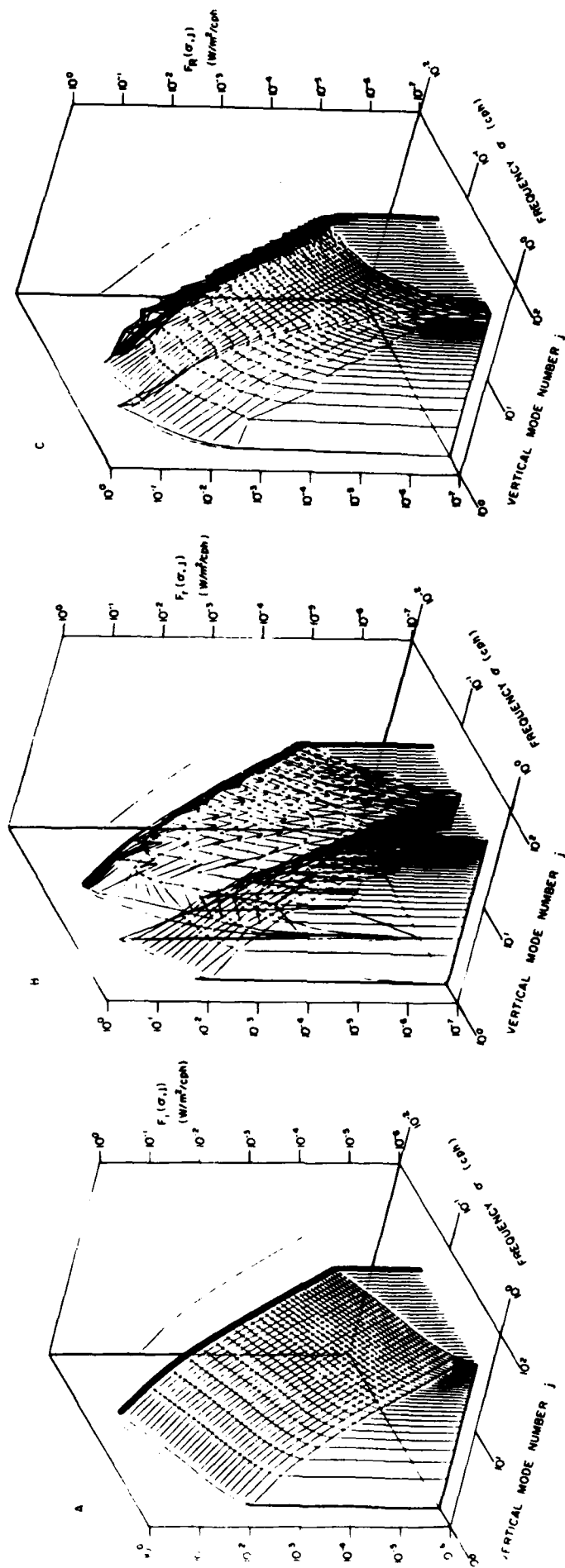
Fig. 3. Flux spectra normal to bottom with slope s = 0.3 for incident waves
specified by GM79 and drawn as in Figure 1b, assuming reflected waves take
on the GM79 energy density appropriate to their reflected wavenumber, as
discussed in the text. a) Incident flux spectrum $F_i(\sigma,j)$, b) Reflected
flux spectrum, $F_r(\sigma,j')$, c) Redistributed flux spectrum $F_R(\sigma,j)$.

FLUX REDISTRIBUTION

The observed internal wave spectra indicate that spectral intensification is limited to within a few hundred meters of the bottom. The spectral peak near σ_c decays roughly exponentially from the bottom with a scale about 100 m (Eriksen, 1982). This suggests that a nonlinear adjustment to the internal wave spectrum taks place near the bottom. Incident waves presumably change wavenumber and energy density through reflection, conserving their energy flux normal to the bottom. The decay of energy density perturbations with height off the bottom implies a redistribution of energy flux. If reflected wave components are prescribed to take on the Garrett-Munk energy level appropriate to their new (reflected) wavenumber, their flux normal to the boundary is generally different than for the incident components from which they originate. The flux difference between incident and reflected waves may be of either sign. Below σ_c, incident exceeds reflected flux. Above σ_c, the opposite is true for low wavenumbers. The absolute value of the difference between incident and reflected flux integrated over all azimuths gives the spectrum of redistributed flux. Presumably some of this flux difference is lost from the wave field into mixing.

The spectra of incident, reflected, and redistributed flux are drawn in Figure 3 for the same f, N, and s as the energy density spectra of Figure 2. Since fluxes are normal to a sloping bottom, there is no dropoff in the spectrum at f (compare Figure 3a with Figure 1b). The reflected flux (Figure 3b) has a sharp minimum near the critical frequency. This is because wavenumbers are amplified most extremely near σ_c and the GM79 wavenumber spectrum is red so that there is a deficit of reflected flux relative to incident flux. The redistributed flux (the absolute value of the flux difference between each incident and reflected wave pair, integrated over azimuth) spectrum in Figure 3c is comparable in level to both the incident and reflected fluxes. In fact, summed over frequency and wavenumber, the total redistributed flux (34.56 mW/m^2) exceeds both the total incident flux (30.82 mW/m^2) and total reflected flux (20.39 mW/m^2). Redistributed flux can exceed incident flux because incident waves travelling downslope at high frequency can reflect into lower wavenumbers, thus implying a net gain of flux out of the bottom.

Flux calculations vary with varying bottom slope s for given values of f and N. Figure 4 summarizes the variation of total incident, total reflected, and total redistributed flux for the midlatitude f and N values used in the previous examples. Total redistributed flux has a broad maximum roughly centered between slopes f/N<s<1. Inside this range, total redistributed flux varies between about 20-35 mW/m^2. Outside this range, it falls off roughly linearly with slope.
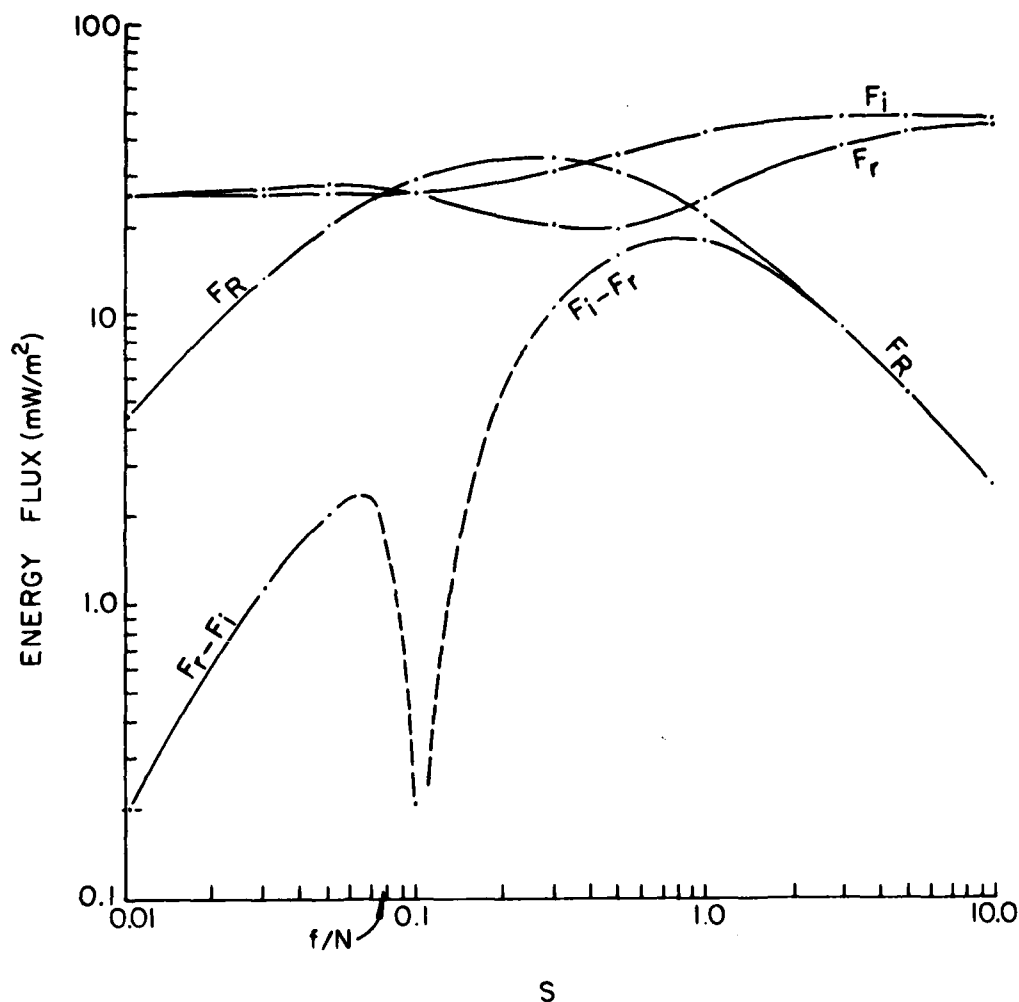
Fig. 4. Total flux (flux spectra integrated over all frequencies and summed over all vertical mode numbers $j=1, 32$ with incident waves specified by GM79) versus slope s for f,N as in Figures 2 and 3. Subscripts i,r, and R correspond to incident, reflected, and redistributed fluxes, as in spectra of Figure 3.

DISCUSSION

The relevance of the calculations presented in the previous section to the oceanic internal wave field depends on several assumptions whose validity may be questioned. These range from the appropriateness of linear theory to the choice of parameters which characterize the internal wave flux spectrum. Comments on the validity of these assumptions and the implications of the flux redistribution calculation for internal wave interactions and deep ocean mixing will be presented here.

The relevance of flux estimates calculated assuming linear
internal waves is not established observationally, mostly because
identification of phase propagation is rather difficult. Several
studies of weakly interacting waves have been done for the oceanic
internal wave field, but objections to their validity have been raised
by Holloway (1980), (1982). Olbers (1983) summarizes these studies. In
estimating fluxes associated with various processes, most authors
estimate flux by the product of energy density times (linear wave)
group velocity, perhaps for want of a better method. In following
suit, our flux estimates are at least made in a manner consistent with
others, even if they may not be strictly correct in describing oceanic
conditions.

The redistributed flux value attained by integrating the flux
spectrum depends on various parameterizations of the wave field. In
particular, it depends on latitude in two ways. As mentioned, the
redistributed flux varies relatively weakly with slope s for given f
and N. Since observations suggest that the level of the oceanic
internal wave spectrum is relatively independent of latitude and
buoyancy frequency (rather than being proportional to f, as in GM79;
see footnote 14 in Munk, 1981), the total flux of the wave field varies
roughly inversely as f. In addition, the closer s falls to the range
f/N<s<1, the larger the flux redistribution will be for given f and N.
Thus latitudes $\theta \lesssim \sin^{-1}(sN/2\Omega)$, where Ω is the earth's rotation rate,
are likely to be the sites of greatest flux redistribution. For
typical values (s~0.07, benthic N(z)~0.5 cph), this leads to $\theta \lesssim 25°$,
which corresponds to roughly half of the world ocean. The other
important parameterization of the wave field is energy content at the
gravest vertical scales. Most flux to be contributed by only the
lowest few modes of the spectrum. If, for some reason, these long
wavelengths are not part of the incident spectrum, the incident (thus
redistributed) flux will be accordingly smaller. The low wavenumber
form of GM79 has not been verified observationally, so the incident
flux employed in the reflection calculations is uncertain. However,
since theoretical calculations by others also assume GM79 as a
canonical spectrum, the results from this study are on an equal basis.
That is, although the flux redistributions calculated here may be
different than those in the actual ocean, their relative value compared
to other theoretically postulated fluxes is consistent.

The partition between energy lost from the internal wave field to
mixing and energy simply redistributed within the spectrum requires an
extension to the reflection model. No such extension will be offered
here, only a reminder that shears become sufficiently high in
reflection to drive Richardson numbers to very low values. Following
Munk (1981) we define an inverse Richardson function

$$Ri^{-1}(j_u) = \sum_{j=1}^{j_u} \int_f^N (S_{u_z}(\sigma,j)/N^2)d\sigma$$

which is the inverse Ri resulting from a shear spectrum S_{u_z} summed to

upper mode number j_u. Since $S_{u_z} = m(\sigma^2+f^2)\sigma^{-2}S_e(\sigma,j)$, it is clear that

$Ri^{-1}(j_u)$ will reach a fixed value (say, unity) for a lower j_u for waves reflecting off a sloping bottom than off a flat one. Just as with the energy spectrum, though, $Ri(j_u) \to 0$ as $\sigma \to \sigma_c$ independent of j_u because of the (non-integrable) singularity. Whereas in the flat bottom case most shear variance is contributed by near-inertial frequencies, over a sloping bottom most of the shear is near the critical frequency σ_c. Thus most mixing events should take place at a preferred frequency $\sigma \equiv \sigma_c$ and near the bottom. Unlike the interior case, breaking due to bottom reflection can be expected locally in depth (near the bottom) but not in time. Rather, it should be local in frequency, instead. Such periodic near-bottom mixing does occur in laboratory experiments of critical frequency reflection (Cacchione and Wunsch (1974)).

The range of redistributed flux in the examples we have used is about 3-30 mW/m^2 for $0.01<s<10$, but also at least 20 mW/m^2 for $f/N<s<1$. This is very large compared to estimates for generation, spectral transfer, or dissipation mechanisms for internal waves. It exceeds the estimates for individual mechanisms of these three processes by an order of magnitude, according to Olbers (1983). Observations suggest that this flux redistribution must take place over $O(100$ m$)$ vertically, as was mentioned above.

Internal waves have long been examined as an agent of mixing the deep ocean to produce the basin-wide vertical diffusivities needed to maintain the thermocline in balance with mean vertical advection. Garrett (1979a) reviewed the mechansms proposed to produce the desired "classical" value of 10^{-4} m^2/s, finding "no clear answers yet to the problems of understanding and parameterizing vertical mixing in the ocean". Internal waves in the deep ocean interior do not appear to provide enough mixing to account for the desired diffusivity. Garrett (1979a) and Armi (1978), as did Munk (1966), suggested that boundary mixing across isopycnals coupled with horizontal mixing by mesoscale eddies provides the needed effective mixing. Armi proposed turbulent bottom drag as a mechanism for boundary mixing, but Garrett (1979b) objected that realistic efficiency of conversion of kinetic to potential energy prevented this mechanism from providing sufficient buoyancy flux. In reply, Armi (1979) suggested roll waves or obstacle wakes as other mechanisms, but without a model for their mixing efficacy. His observations of deep mixed layers detached from the bottom and chemical tracer distributions in them strongly suggest that robust mixing at topographic features is, in fact, taking place.

Internal wave reflection off a sloping bottom may well provide the desired mixing mechanism. If a fraction ε of the total redistributed flux F goes in to potential energy change, the basin averaged rate of potential energy creation is $\varepsilon FA/V$ where A is the area over which the flux is applied and V is the basin volume. This can be regarded as a topography-weighted rate of potential energy creation. It is equal to the effective vertical diffusivity K times $\rho_0 N^2$, where turbulent buoyancy flux has been parameterized by turbulent diffusion. Thus

$$K = \varepsilon FA/\rho_0 VN^2$$

For typical basin-averaged values, $A/V \sim (depth)^{-1}$ and $N \sim 1$ cph, giving

$$K \sim \varepsilon \cdot 1.3 \times 10^{-3} \text{ m}^2/\text{s}$$

for $F = 20$ mW/m^2 and depth = 5 km. This implies only an efficiency of 8% is needed to provide the desired basin-averaged vertical diffusivity of 10^{-4} m^2/s. The traditional estimate for production of potential energy from shear instability is 25% (Thorpe, 1973) (although viscous effects in the laboratory experiments used to make this estimate cast it in some doubt (Thorpe, personal communication, 1984)). Thus only about 32% of the total redistributed flux F need undergo shear instability in order to produce enough mixing. (The remaining flux presumably rejoins the internal wave spectrum). As mentioned above, the absolute magnitude of flux is not well known, due to uncertainty about the energy level of low mode number waves participating in reflection. Nevertheless, the calculation is in the fortunate position of needing a rationale to reduce ε, rather than increase F to get the desired result.

By these calculations it appears that internal waves reflecting off the rough topography of the world's ocean basins are a likely mechanism for boundary mixing, and are, as such, the likely link in effecting basin scale vertical diffusivity via the boundaries.

194

REFERENCES

Armi, L., 1978, Some evidence for boundary mixing in the deep ocean, J. Geophys. Res., 83, 1971-1979.

Armi, L., 1979, Reply to comments by C. Garrett, J. Geophys. Res., 84, 5097-5098.

Bell, T.H., Jr., 1975a, Topographically generated internal waves in the open ocean, J. Geophys. Res., 80, 320-327.

Bell, T.H., Jr., 1975b, Statistical features of sea-floor topography, Deep-Sea Res., 22, 883-892.

Cacchione, D. and C. Wunsch, 1974, Experimental study of internal waves over a slope, J. Fluid Mech., 66, 223-239.

Eriksen, C.C., 1982, Observations of internal wave reflection off sloping bottoms, J. Geophys. Res., 87, 525-538.

Eriksen, C.C., 1984, Implications of Ocean Bottom Reflection for internal wave spectra and mixing, J. Phys. Oceanogr., submitted.

Garrett, C., 1979a, Mixing in the ocean interior, Dyn. Atmos. Oceans, 3, 239-265.

Garrett, C., 1979b, Comment on 'Some evidence for boundary mixing in the deep ocean' by Laurence Armi, J. Geophys. Res., 84, 5095.

Hogg, N.G., E.J. Katz, and T.B. Sanford, 1978, Eddies, islands, and mixing, J. Geophys. Res., 83, 2921-2938.

Holloway, G., 1980, Oceanic internal waves are not weak waves, J. Phys. Oceanogr., 10, 906-914.

Holloway, G., 1982, On interaction time scales of oceanic internal waves, J. Phys. Oceanogr., 12, 293-296.

Johnson, C.L., and T.B. Sanford, 1980, Anomalous behavior of internal gravity waves near Bermuda, J. Phys. Oceanogr., 10, 2021-2034.

Munk, W.H., 1966, Abyssal recipes, Deep Sea Res., 13, 207-230.

Munk, W.H., 1981, Internal waves and small scale processes, in Evolution of Physical Oceanography Scientific Surveys in Honor of Henry Stommel, edited by B.A. Warren and C. Wunsch, pp. 264-291, MIT Press, Cambridge, Mass.

Olbers, D.J., 1983, Models of the oceanic internal wave field, Rev. Geophys. Space Phys., 21, 1567-1606.

Thorpe, S.A., 1973, Turbulence in stably stratified fluids: a review of laboratory experiments, Boundary Layer Meteorol., 5, 95-119.

INTERACTION OF INTERNAL WAVES OF NEAR INERTIAL FREQUENCIES

Kenneth M. Watson

Marine Physical Laboratory of the
Scripps Institution of Oceanography
University of California, San Diego
San Diego, California, 92093

ABSTRACT

A model to describe the internal wave spectrum has been proposed by McComas and Müller. When supplemented by the mesoscale diffusion (MSD) mechanism, a global model for a quasi-steady internal wave field is obtained. The model predicts a sufficient energy flow from the mesoscale field to the internal wave field to replenish the latter within a month or so.

INTRODUCTION

A little more than a decade ago Garrett and Munk (1972, 1979) suggested that the internal wave (IW) field is in a "near steady state". They proposed a specific spectral form which has evolved into what is now termed "GM 76" (see, for example, Munk 1981). Several variations on the "GM theme" have also been proposed. A number of efforts have been made to understand the mechanisms that determine the IW spectrum. Olbers (1976), McComas and Bretherton (1977) and McComas (1977) have used a Hasselmann (1967) transport equation. Pomphrey et al (1980) employed a more empirical approach but obtained results equivalent to the earlier work. A "global" description of the IW spectrum, which synthesizes the earlier models, has been presented by McComas and Müller (1981).

DESCRIPTION OF IW TRANSPORT PROCESSES

The "global" description of McComas and Müller (1981) is based on simple limiting mechanisms proposed by McComas and Bretherton (1977). This is illustrated in Fig. (1), where the domain of the IW field is shown in a frequency-vertical wavenumber plot. (Here the inertial frequency is taken as $f = 7 \times 10^{-5}$ rad/sec, k_z is the vertical wavenumber, ω the angular frequency, and $B = 1200$ m is the GM scale length.)

WAVELENGTH (meters)
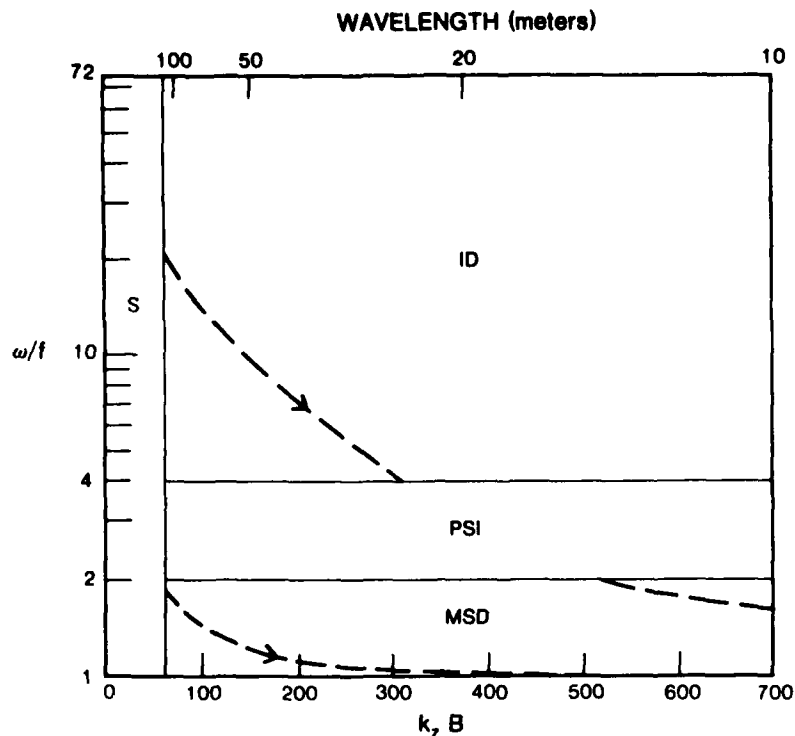
Fig. 1. Representation of the McComas Müller model of internal wave transport processes.

Referring to Fig. (1), the model of McComas (1978) and of McComas and Müller (1981) assumes a source to supply IW energy to region "S". Wave energy (or wave action) diffuses along lines of constant horizontal wavenumber k_h by the "induced diffusion" (ID) mechanism. This occurs in the domain labelled as "ID", where a typical path of constant k_h is illustrated.

The ID mechanism becomes ineffective for $\omega/f < 4$. In the McComas Müller (1981) model IW action is pumped by the "parametric subharmonic instability" (PSI) mechanism from the ID regime to that labelled as MSD, corresponding to $\omega/f < 2$.

The label MSD refers to the mechanism of "mesoscale diffusion" suggested by Watson (1984). By this mechanism IW action can diffuse to the regime $k_z B > 700$, where hydrodynamic instabilities are thought to dissipate the IW energy (see, for example, the review by Munk, 1981). Watson (1984) found that diffusion in both the k_z and k_h directions must be taken into account using the MSD mechanism. He also concluded that the mesoscale field represents a significant source of energy for the IW field.

The regime labelled ID in Fig. (1) is also that of the "elastic scattering" (ES) mechanism of McComas and Bretherton (1977). The ES mechanism tends to equalize fluxes of upward and downward moving internal waves. It is operative, however, only in the indicated domain of ω and k_z.

THE LANGEVIN APPROACH

Pomphrey et al (1980) used the Langevin equation and the fluctuation-dissipation theorem in discussing IW transport. A more formal version of this was used by Meiss and Watson (1982) who used a general theory of Van Kampen (1974).

To illustrate the Langevin approach, let us suppose the action amplitudes to be represented by the Fourier expansion

$$A(x,t) = \sum_k a_k \ \exp[i(k \cdot x - \omega_k t)]. \tag{1}$$

The action spectrum $F(k)$ is determined from the relation

$$\int F(k)d^3k = \sum_k <|a_k|^2>, \tag{2}$$

where $<...>$ represents an ensemble average over a set of realizations of the fluid system.

The Langevin equation is of the form

$$\frac{d}{dt} <a_k> = -\nu <a_k>, \tag{3}$$

where ν is the "Langevin rate constant." Closely related to (3) is the Van Kampen transport equation

$$\frac{\partial F(k)}{\partial t} = \int d^3k' \ K(k,k')\Big[F(k')-F(k)\Big]. \tag{4}$$

Here K is the Van Kampen kernel.

The time scale of the McComas (1978) "bump experiment" is $(2\nu)^{-1}$. Meiss and Watson (1982) found that in the ID regime the ν obtained from the Van Kampen theory differed significantly from that of weak interaction theory.

The effect of mesoscale current interactions on the Langevin rate constant has been described by Watson (1983). Calculated rate constants for the MSD regime are shown in Fig. (2).

For the ID mechanism equation (4) can be reduced to the diffusion equation of McComas and Bretherton (1977). For the MSD mechanism equation (4) can reduced to the form

$$\frac{\partial}{\partial t} F(k_h,k_z) = \frac{\partial}{\partial k_h} \ V_h \ \frac{\partial}{\partial k_h} F + \frac{\partial}{\partial k_z} V_z \frac{\partial}{\partial k_z} F, \tag{5}$$
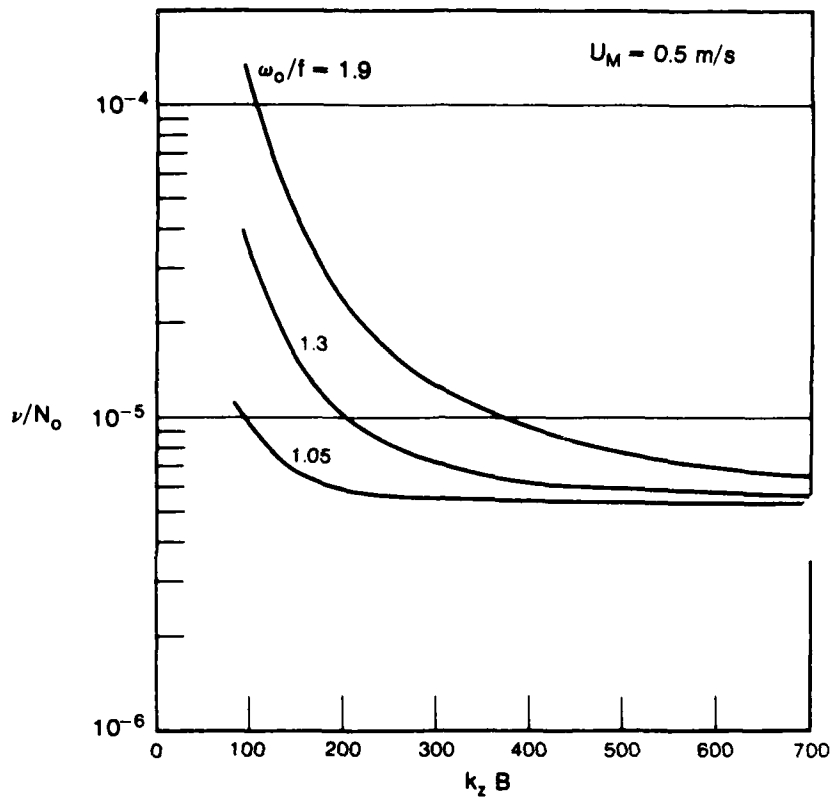
Fig. 2. The Langevin rate constant resulting from mesoscale internal wave interaction in units of $N_o{=}5x10^{-3}$ rad/sec. The curves are labelled by ω_o , the angular frequency at $k_z B{=}20\pi$, with a constant value of k_h for each curve. The rms mesoscale current assumed is $U_M = 0.05$ rm/sec.

where V_h and V_z are appropriate diffusion constants (a similar equation has been obtained by Müller, 1977).

For the ES mechanism, equation (4) may be simplified to give (compare Watson, 1981)

$$\frac{\partial F_+}{\partial t} = 0, \frac{\partial F_-}{\partial t} = -2\nu F_- \tag{6}$$

$$F\pm = \tfrac{1}{2}\left[F(k_z) \pm F(-k_z) \right], \tag{7}$$

in agreement with McComas and Bretherton (1977).

CONCLUSIONS

The model of McComas and Müller (1981), when augmented with the MSD mechanism, provides a plausible "global" description of the IW spectrum. Missing is a systematic description of energy sources and sinks (these are introduced phenomenalogically). Also, reliance on some form of weak interaction theory limits the quantitative interpretation of the McComas Müller model.

References

Garrett, C. J. R. and W. H. Munk, 1972: Space-time scales of internal waves. *Geophys. Fluid Dyn.* , *2*, 225-264

-----, ----- 1979: Internal waves in the ocean, in *Annual Review of Fluid Mechanics*, edited by M. Van Dyke, J. V. Wehousen, and J. L. Lumley, Annual Reviews, Palo Alto, CA.

Hasselmann, K., 1967: Nonlinear interactions treated by the methods of theoretical physics. *Proc. Roy. Soc. London A229*, 77-100.

McComas, C. H. 1977: Equilibrium mechanisms within the oceanic internal wave field. *J. Phys. Oceanogr.*, *7*, 836-845.

----- and F. P. Bretherton, 1977: Resonant interaction of oceanic internal waves. *J. Geophys. Res.*, *82*, 1397-1412.

----- and P. Müller, 1981: The Dynamic balance of internal waves. *J. Phys. Oceanog.*, *11*, 970-986.

Meiss, J. D. and K. M. Watson, 1982: Internal-wave interactions in the induced-diffusion approximation. *J. Fluid Mech.*, *117*, 315-341.

Munk, W. H., 1981: Internal waves and small-scale processes, in *Evolution of Physical Oceanogrpahy*, Warren, B. A. and C. Wunsch editors. The MIT Press, Cambridge, Mass.

200

Olbers, D. J., 1976: Non-linear energy transfer and energy balance of the internal wave field in the deep ocean. *J. Fluid Mech., 74,* 375-399.

Pomphrey, N., J. D. Meiss and K. M. Watson, 1980: Description of nonlinear internal wave interactions using Langevin methods. *J. Geophys. Res., 85,* 1085-1094.

Van Kampen, N. G., 1974: Stochastic Differential equations. *Physica, 74,* 215-251.

Watson, K. M., 1981: in Nonlinear properties of internal waves, Edited by B. J. West, Amer. Inst. of Physics Conf. Proc., No. *76.*

-----, 1983: Relaxation processes for internal waves in mesoscale flow. *Proc. Natl. Acad.Sci., USA., 80,* 1144-1146.

-----, 1984: Internal wave mesoscale flow interaction. Submitted to *J. Phys. Oceanogr..*

TRANSPORT OF SMALL-SCALE INTERNAL WAVES TOWARD MICROSTRUCTURE

Frank Henyey

La Jolla Institute
Center for Studies of Nonlinear Dynamics
8950 Villa La Jolla Drive, Suite 2150
La Jolla, California 92037

ABSTRACT

The "Eikonal-Monte-Carlo" technique is used to model transport properties of small-scale oceanic internal waves. The waves being investigated interact with a flow field of given statistical properties, presently those given by the Garrett-Munk spectrum. Weak interaction transport theory is inadequate to handle the small-scale waves. Spectral properties of the small scale waves are predicted, as are microstructure patch statistics. Internal wave instabilities are associated with highly nonlinear processes.

INTRODUCTION

This paper reviews previous work our group has done on the eikonal method of small-scale internal wave transport, and presents preliminary new results concerning the relation between internal wave transport and microstructure statistics. The completed work was done primarily in collaboration with Neil Pomphrey, with contributions from Jim Meiss, Jon Wright, and George Carnevale. The current studies are being carried out in collaboration with Stan Flatté and Jon Wright.

THE EIKONAL METHOD

This approach was presented by Henyey and Pomphrey (1983), in which the equations were derived and preliminary calculations were reported. The results of the calculations led the authors to suggest a picture of small-scale internal wave transport rather different, and apparently inconsistent with, the old picture of induced diffusion.

The eikonal, or ray-tracing, approach is based on a dynamical system describing "wave packets," each carrying a fixed amount of wave action A, and each having both a position and wavenumber (defined to an accuracy of $\Delta x\, \Delta k_z \sim 1$). These

wave packets are referred to as test waves, and the ambient flow field which causes their properties to change is called the background. The background consists, in all calculations performed to date, of all internal waves present, described in an approximate way. There is no fundamental reason to exclude the vortical mode (Müller, these proceedings), although phenomenological models of the vortical mode on internal wave scales are just beginning to be formulated. The eikonal technique could be, but hasn't been, used to study the interaction with mesoscale and other larger scale vortical motion. From the work of Watson (these proceedings) we expect this interaction to be important.

The ray equations are the dynamical equations of a Hamiltonian system (Henyey and Pomphrey, 1983), with the Hamiltonian being the test wave frequency, ω, expressed as a function of the canonical variables $\vec{r}$, the position, and $\vec{k}$, the wavenumber. A factor of the wave action A of the packet can multiply both ω and $\vec{k}$, converting them to energy and momentum, without changing the equations. The frequency ω is observed at a fixed point, and includes both the intrinsic frequency σ and the Doppler shift:

$$\omega(\vec{r}, \vec{k}) = \sigma(\vec{k}, N(z)) + \vec{u}(\vec{r}, t) \cdot \vec{k} \tag{1}$$

where $\vec{u}$ is the background flow. The intrinsic frequency is given by the usual expression

$$\sigma = \sqrt{\frac{N^2 k_H^2 + f^2 k_V^2}{k_H^2 + k_V^2}} \tag{2}$$

The interaction of the test wave with other waves (and vortical flows) is entirely in the Doppler shift. (We have neglected effects such as the addition of the background vorticity to the planetary vorticity, which Kunze (1984) finds important in the interaction of near-inertial waves with geostrophic flows).

The ray equations which result are

$$\vec{v} = \frac{\partial \omega}{\partial \vec{k}} = \frac{\partial \sigma}{\partial \vec{k}} + \vec{u} \quad , \tag{3}$$

group velocity plus advection, and

$$d_t \vec{k} = -\frac{\partial \omega}{\partial \vec{x}} = -\frac{\partial \sigma}{\partial N} \nabla N - \nabla \vec{u} \cdot \vec{k} \tag{4}$$

"WBK Scaling" of the wavenumber plus shearing.

In the calculations performed to date, the background flow $\vec{u}$ was modeled as the horizontal component of a Garret-Munk spectrum evolving linearly and the buoyancy frequency N was modeled as an exponential profile

$$N = N_0 e^{z/B} \tag{5}$$

The flow $\vec{u}$ was chosen at random from the G-M spectrum and depends on all three coordinates of space as well as time.

For a given flow, and given initial conditions, we numerically integrate the six equations for $\vec{r}(t)$ and $\vec{k}(t)$. We repeat the integration many times over with differently chosen realizations of the G-M spectrum and/or with different initial conditions.

The picture that emerged from the early calculations of Henyey and Pomphrey (1983) was transport dominated by "critical layer events," i.e., by segments of time over which the vertical wavenumber changed significantly, reasonably closely following the simple critical layer approach expressions. Dependence of $\vec{u}$ on horizontal position and time eventually terminates such critical layer events, unless the test wave first reaches instability scales, in which case it is assumed to dissipate.

COMPARISON WITH WEAK INTERACTION TRANSPORT

Since this picture is so different from the induced diffusion picture, it was decided to compare the results with the weak interaction approach [Henyey, Pomphrey, and Meiss (1984)]. Comparison was made both with induced diffusion and the refinement of the weak interaction theory by Meiss and Watson. Care was taken to ensure that the stratification and background flow was identical in the different approaches, so that differing results could be attributed to differences in the approximation. Moreover, the ocean model was taken to guarantee the correctness of the eikonal approach, while having the strength of the background flow and other features be appropriate for the real ocean. Thus, the weak theories were being tested.

It was found that the Meiss-Watson theory was rather similar to induced diffusion, with only two differences. One difference is that Meiss and Watson did not make the scale separation assumption. For the model used, this was of almost no significance; the validity of scale separation for more realistic ocean models is discussed below. The other difference is that the Meiss-Watson theory has an initial transient due to the assumed absence of correlations between the initial test wave conditions and the background flow. The effect of this transient is to postpone the transport by a small fraction of an inertial period; otherwise it follows the induced diffusion results.

Figure 1 shows the comparison of the eikonal calculations with the weak models (induced diffusion rather than Meiss-Watson is shown). Both the mean vertical wavenumber and its rms deviation from the mean are shown. The initial condition was $k_V \sim 0.05\ rad/m$. The results show well-defined differences. The most significant effect is that the weak theories predict a rapid exponential equilibration while the eikonal shows significant "memory" of the initial conditions for several inertial periods, shown particularly in the $<k_V>$. The wiggles in the eikonal $<k_V>$ may be artifacts of the Monte-Carlo numerics, and it is not possible to determine from this curve whether the relaxation is exponential. The decrease of the variance at about one inertial period is significant, and is completely impossible in a diffusion model. The asymptotic level of the weak interaction variance is not of significance since it is caused by resonant kinematics coupled with a scale truncation in the model, which was imposed to
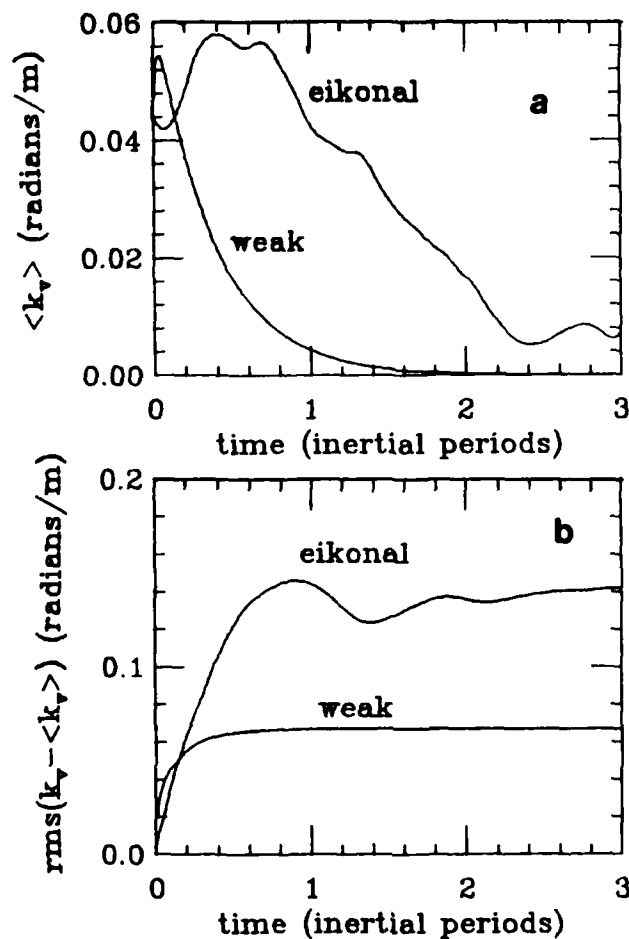
Figure 1. The comparison of the eikonal calculation with weak
interaction transport theory. Shown are the average verti-
cal wavenumber and its rms spread. Important
differences are the much slower relaxation of the eikonal
$<k_V>$ and the decrease of its variance after about an iner-
tial period, both of which are "memory" effects missed by
the weak theory.

guarantee the correctness of the eikonal approach. The different long-time level
of the eikonal curve shows that it does not respect resonant kinematics, and the
level is set by the imposed dissipation scale.

The shortcomings of the weak interaction transport theory can also be exhibited
within the context of a perturbation expansion of which the weak interaction
theory is the lowest order. Henyey, Pomphrey, and Meiss (1984) use a formalism
due to Van Kampen (1974) to calculate the next order term. Actually, the next
order contains, in the expression for the action flux through wavenumber space,

terms proportional to both the action-gradient $\partial_{k_v} a$ and the action curvature $\partial_{k_v} a^2$. Only the coefficient of the former can be described as a diffusivity , and it is this correction to the diffusivity that Henyey, Pomphrey, and Meiss calculate. They use a model almost identical (except that the scale truncation is slightly smeared) to that of the comparison to the eikonal and find that the second order term is not small compared to the lowest order. It is clear that the perturbation expansion is not converging rapidly, and there is no reason to expect the lowest order equation to resemble the actual transport. The disagreement with the eikonal is entirely consistent with the lack of convergence of the perturbation expansion. Internal wave interactions are just too strong for induced diffusion.

VALIDITY OF THE EIKONAL

The eikonal approach requires the assumption of scale separation, while weak interaction theory only makes this approximation as a convenience.

The model used in the comparison had scale separation, and therefore the eikonal was correct and weak theory not. It is possible that in a more realistic model that the eikonal fails because there is inadequate scale separation, leaving us with no reasonable approach.

This question was investigated by Henyey, Wright, and Carnevale (1984). The approach they took was to compare statistical properties of eikonal calculations which were nearly identical. Background waves were discarded if their vertical wavenumber was greater than some fixed number φ times the test wave vertical wavenumber; the different calculations correspond to different choices of φ. As the text wave evolved, new background waves were included or discarded based on this value of φ. In any case, low mode background waves were never discarded, in order that the text wave would continue to evolve at small wavenumber.

The choice $\varphi = \infty$ corresponds to all waves being kept, $\varphi = 1$ corresponds to all waves bigger than the test wave being kept, and $\varphi = 1/2$ corresponds to no wave within a factor of two of the test wave being effective. Waves smaller than the test wave probably are not effective in transport, and their effect is almost certainly modeled very poorly by the eikonal technique. Waves more than twice the size of the test wave are probably modeled correctly, and those within a factor of two are open to some question. The most reasonable choice of φ is somewhere near $\varphi = 1$. Agreement of $\varphi = \infty$ and $\varphi = 1$ calculations are required for the basic validity of the eikonal, and one could be very confident of such validity if the $\varphi = 1/2$ would also agree.

Figure 2 shows the comparison between the three values of φ. As in Figure 1, $\langle k_V \rangle$ and the square root of its variance are shown. The $\varphi = 10 \ (\approx \infty)$ and the $\varphi = 1$ curves are in good agreement, so the eikonal remains viable. Unfortunately, however, the $\varphi = 1/2$ curves are smaller; those background waves between one and two times the test wave size account for somewhere around half the transport. The ability of the eikonal to deal with such small scale

206

separation is debated. My personal opinion is that asymptotic techniques, of which the eikonal is an example, tend to become good rapidly and I think that the background waves included in $\varphi = 1$ but excluded in $\varphi = 1/2$ do have about the effect that the eikonal attributes to them.
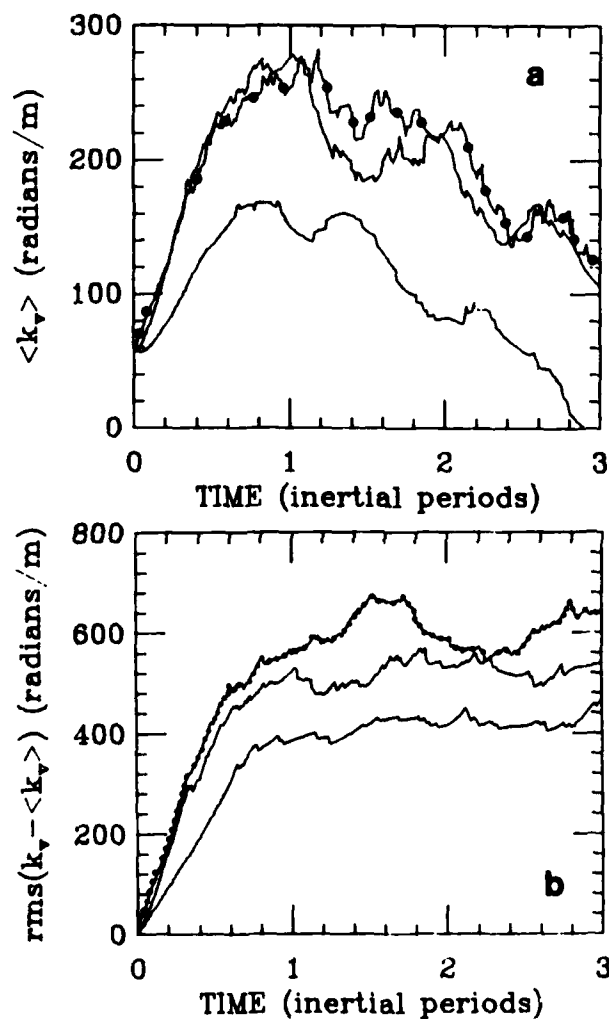
Figure 2. Test of the scale separation assumption. Background wave are discarded if $K_V > \varphi k_V$, with K_V and k_V the wave-numbers of the background and test waves. Results at $\varphi = 10$ (curve with dots), $\varphi = 1$, and $\varphi = 1/2$ (lowest curve) are shown. Background waves smaller than the test wave (which are incorrectly handled by the eikonal) are relatively unimportant, but those within a factor of two (which are handled fairly well, but not extremely well) are moderately important.

INTERNAL WAVE SPECTRA

Stan Flatté, Jon Wright, and I have started a program of seriously investigating the predictions of the eikonal theory to ocean phenomena. We are examining both predictions of the internal wave spectrum and predictions of microstructure. The remainder of this paper presents some preliminary results of these studies.

We follow Henyey and Pomphrey (1983) in imposing a high wavenumber cutoff on the test wave in order to model dissipative processes very roughly. This "poor man's" stability theory accepts the picture described by Munk (1981), which attributes the break in slope in the internal wave vertical wavenumber spectrum at about a vertical wavelength of 10 meters to occurrence of Richardson numbers of about 1/4 and therefore instability (breaking and/or Kelvin-Helmholz) at this scale. This instability is assumed to lead to turbulence and eventually to microstructure. We choose a cutoff slightly smaller than the observed break; our cutoff is at a 5-meter vertical wavelength.

In order to study the spectrum of test waves, we must choose a spectrum of initial conditions. We choose a horizontal wavelength of one kilometer at which to specify the initial conditions, since the eikonal approximation is probably unreliable at larger scales. We attempt to duplicate the Garrett-Munk spectrum in the initial conditions. The action density of the initial conditions should be chosen to be the action flux of the spectrum; i.e., the initial conditions are dA/dt and the spectrum is dA/dk_H, with a ratio of dk_H/dt. We calculate dk_H/dt assuming no correlation between the test waves and the background. This assumption is true of our initial conditions but is not exactly true in nature. In any case, the results are not particularly sensitive to the initial conditions.

Our phase space is bounded by

$$k_H > 2\pi/1km$$

$$k_V < 2\pi/5m$$

In this region we examine the distribution as a function of k_H, k_V, ω, etc.

Figure 3 shows the fraction of the action which has not yet reached the $k_V = 2\pi/5m$ limit. It is approximately exponential with an e-folding time of around 130 hr. (~ 5-1/2 inertial periods).

Figure 4 shows the horizontal wavenumber distribution, and the comparison with the Garrett-Munk spectrum. We see that large k_H is populated in about the right amount. We did not expect this result, but rather we expected k_H to remain small while most transport occurred in k_V. It appears that horizontal shears are large during the critical layer events when vertical shears are large.

Greg Holloway (discussion, these proceedings) expressed the belief that internal wave sources should be at low frequency, and he was puzzled that the transport theories seemed to indicate a decrease of frequency rather than an increase. In

208
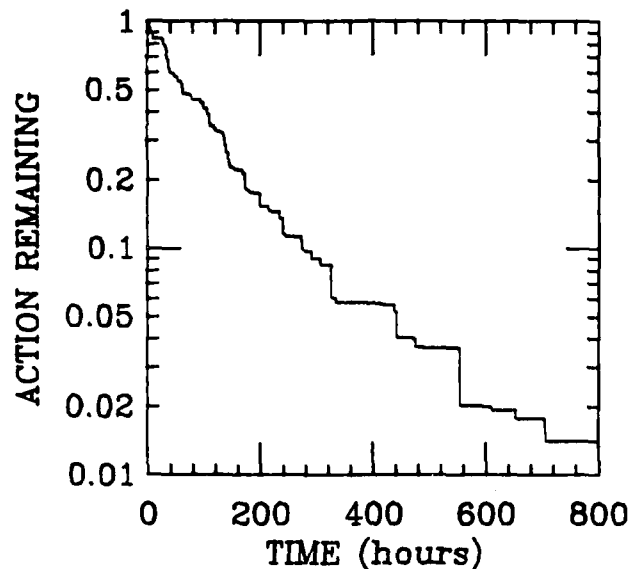
Figure 3. The fraction of the action remaining from the time the wave had a
horizontal wavelength of 1 km. The rest of the action reaches a vertical
wavelength of 5 m, where it is assumed to dissipate by instabilities.

our eikonal calculation we find that k_H evolves rapidly, suggesting that some-
thing interesting might be happening with the frequency. Figure 5 (calculated
after I returned from the meeting) shows the distribution of the intrinsic fre-
quency σ, compared to the distribution at the initial time. There has been an
increase of σ as the evolution has proceeded, supporting the view that perhaps
the sources are low frequency.

INSTABILITY AND MICROSTRUCTURE

The predictions for microstructure of the eikonal calculations come from exa-
mining the properties of the distribution in space and time of the points at
which the test waves reach the 5-meter cutoff, and correlating these points with
properties of the background. This part of the project is in the stage of
discovering the qualitative features of the predictions of the eikonal calcula-
tions. We try series of runs with the same initial conditions but different back-
grounds and others with the same background but different initial conditions.

One set of runs consisted of a single initial condition in a large number of reali-
zations of the background. The background velocity u_x, shear $\partial_z u_x$, and verti-
cal positions z of the test wave when the 5m cutoff was reached were tabu-
lated. (The initial test wave horizontal wavenumber was in the x direction.) Fig-
ure 6 shows the distribution of the position. The test wave was started at 1-km
depth, moving upward. The distribution is a superposition of upward-going waves
and those reflected off the surface. As will become clear later, very few waves
reach the 5m point going in the opposite direction (vertically) from which they
start, unless they reflect from the surface.
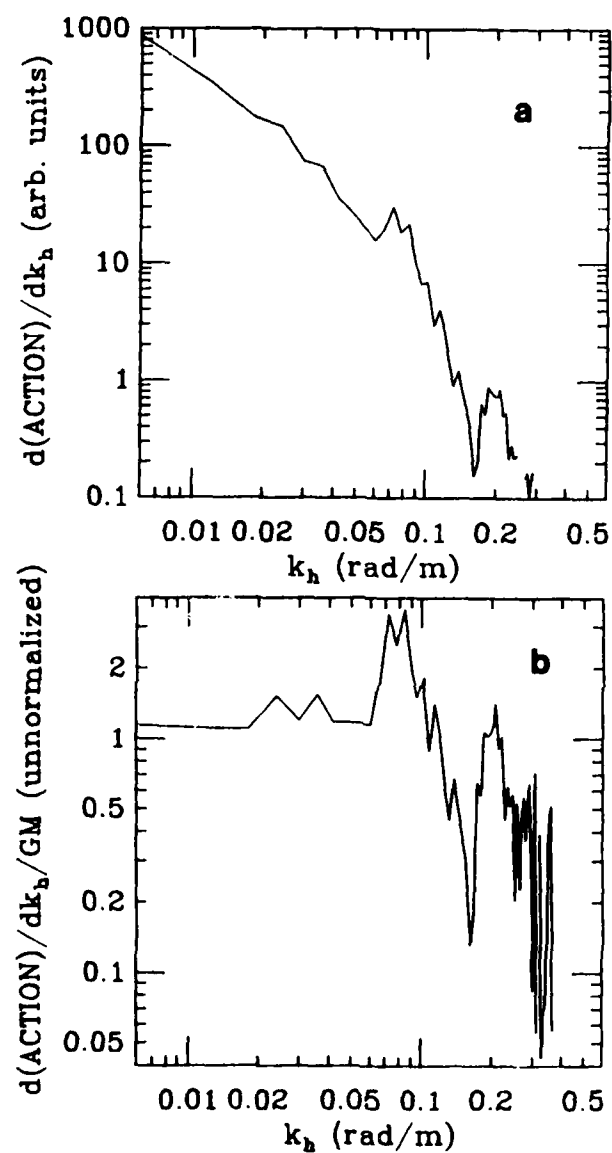
Figure 4. The calculated horizontal wavenumber spectrum of
action. Figure 4a shows the spectrum and Fig. 4b shows its
ratio to the Garrett-Munk spectrum. The two agree in the
region in which our statistics are adequate.
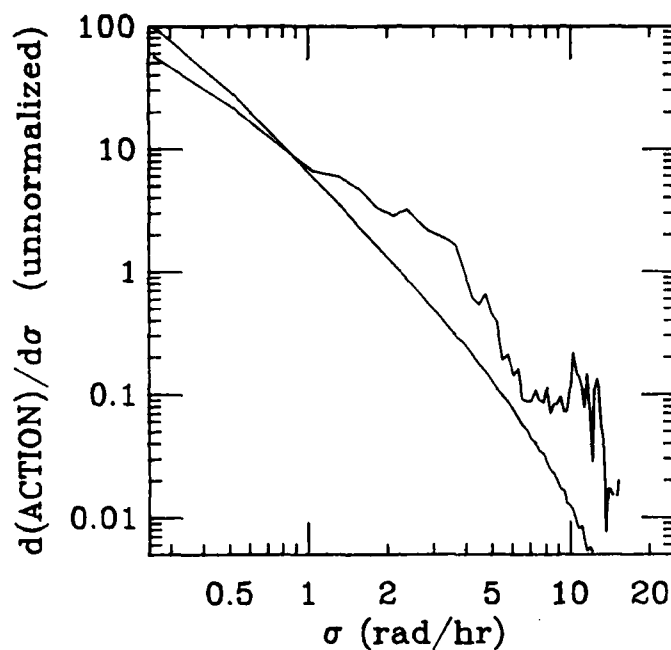
Figure 5. The intrinsic frequency spectrum averaged over time (jagged curve) compared to the initial condition spectrum (smooth curve). The initial conditions are chosen at k_H = 1 cycle/km.
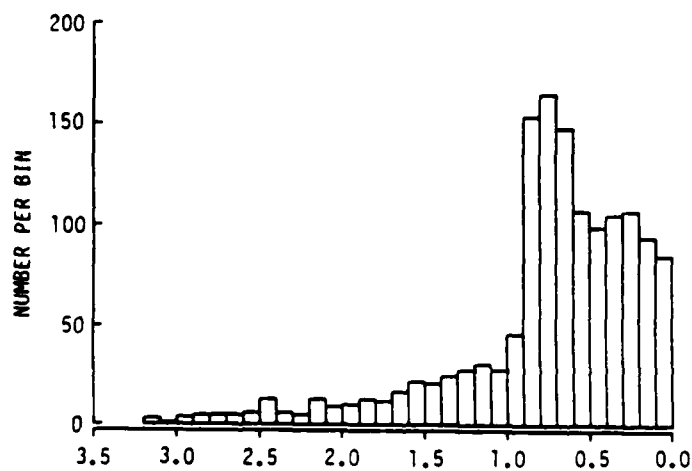
Figure 6. The distribution of depths (nondimensionalized with B = 1.3 km) of critical layers for a wave starting at a depth of 1. Critical layers deeper than 1 are largely due to waves reflected off the surface.

Figure 7 shows the velocity distribution at the 5m point compared to the velocity distribution at a randomly chosen point. It is clear that velocity is not a good indicator of these events, since these distributions are so similar.
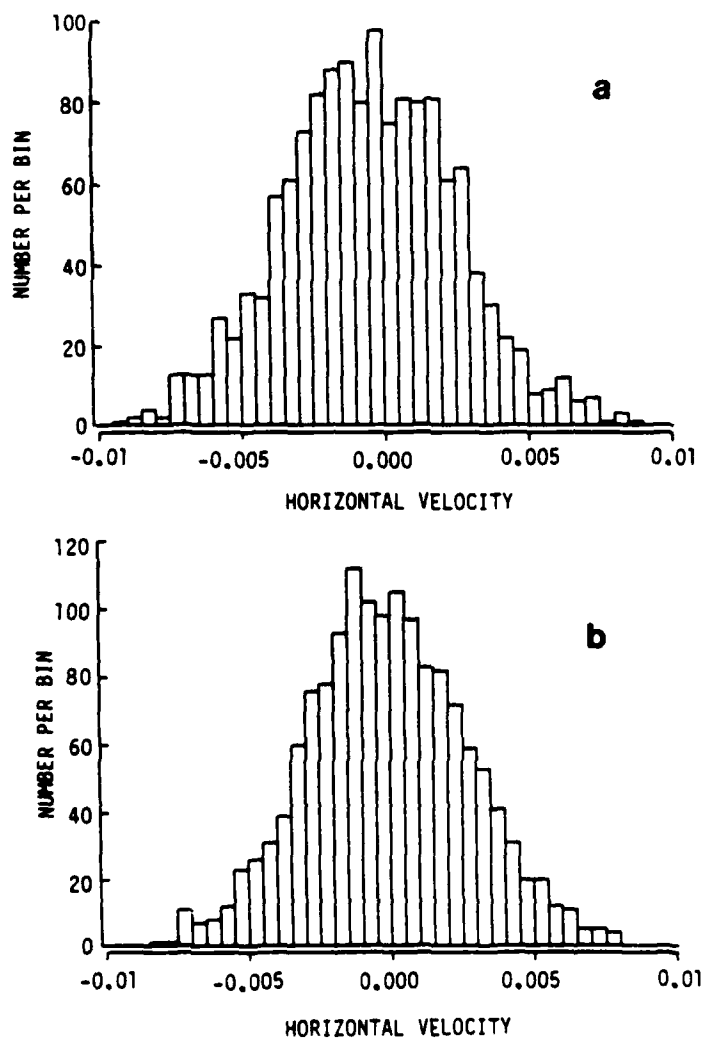
Figure 7. The distribution of horizontal velocity (nondimensionalized with $B = 1.3$ km, $N_{0} = 3$ cycles/hr) for critical layers (a) compared to random points (b). Critical layers do not seem to select out special values of velocity.

Figure 8 shows the shear distribution. The test wave wavenumber changes primarily in response to shear, so it is very unlikely that 5 meters will be reached at a point at which the shear is small.
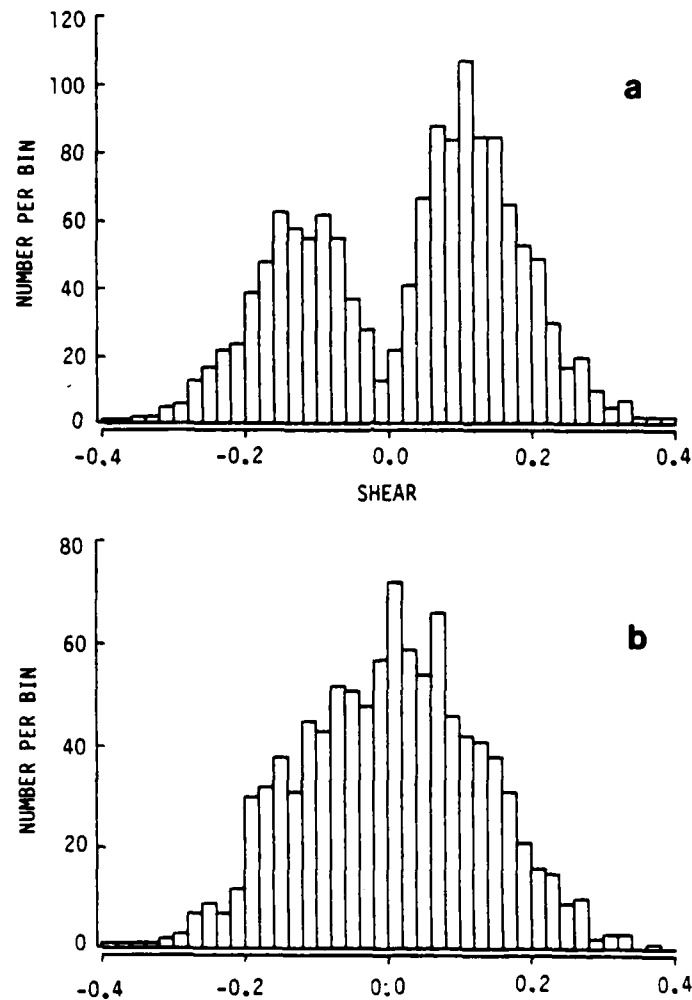
Figure 8. The distribution of shear for critical layers (a) compared to random points (b). Critical layers do select high shear values. The two peaks would be even more asymmetric if there were no high surface reflection.

Figure 9 shows the joint distributions between pairs of these variables. It appears that the velocity is irrelevant in the sense that the distribution factorizes:

$$\rho(u_z, \partial_z u_z, z) = \rho_1(u_z)\rho_2(\partial_z u_z, z)$$

The shear-position joint distribution shows that almost all of the upward-going events are above the source, and the downward-going distribution decreases smoothly from the surface, with no apparent indication of the source depth. Thus, except for reflections, the waves "remember" the direction they should be moving. This memory effect is probably one of the most important features missing from the weak interaction theory, and may well account for the differences, discussed above, between the weak theory and the eikonal.

We have also carried out many runs with different initial conditions in the same realization of the background. The purpose of such calculations is to study the patchiness of the breaking and of the resulting microstructure. Figure 10 shows a typical series of runs in one background. The depth and one horizontal coordinate of those points at which the test wave reaches a 5-meter wavelength are shown. Such plots show that the breaking events tend to cluster in "critical layers." For this particular background there is a very prominent critical layer at about 800-m depth, as well as several smaller ones.

What is it about the background which causes the critical layers? In order to begin to answer this question, we concentrate on a small sublayer of this big critical layer, and on a small time interval. We find that the kinematic configurations of the upward-going test waves that reach 5 meters wavelength in this Δz, Δt region are rather similar. In particular, Figure 11 shows their k_z, k_y distributions (their initial values were $k_z \neq 0$, $k_y = 0$). We rotate the axes as shown in Figure 11, and plot the background flow components at a horizontal position in the middle of the critical sublayer along the rotated axes in Figure 12. The component in the direction of the final $\vec{k}$ is shown in Fig. 12a, with the critical layer at 780 m indicated. The perpendicular component (Fig. 12b) is anomalously featureless. The critical sublayer, as indicated in Fig. 12a,is at a point of high shear. However, there are other high shear regions in both Fig. 12a and Fig. 12b. The distinguishing characteristics of the critical layer are (1) that this high-shear region is embedded in a much larger region with an average shear which is large and of the same sign as the smaller scale shear and (2) that this region is not "shadowed" by a velocity peak, as is a shear region 50-100 meters higher up.

These results suggest a new picture of the instability and dissipation of internal waves. At certain positions and times in the ocean, the conditions are appropriate for the occurrence of a critical layer. Among the conditions is that the shear is large. The critical layer has a large vertical extent -- it is perhaps 20 meters thick. Small scale waves arrive at this layer by nonlinear transport processes. Their evolution closely resembles the approach to critical layer absorption. The concentration of small-scale waves causes the small scale shear

214
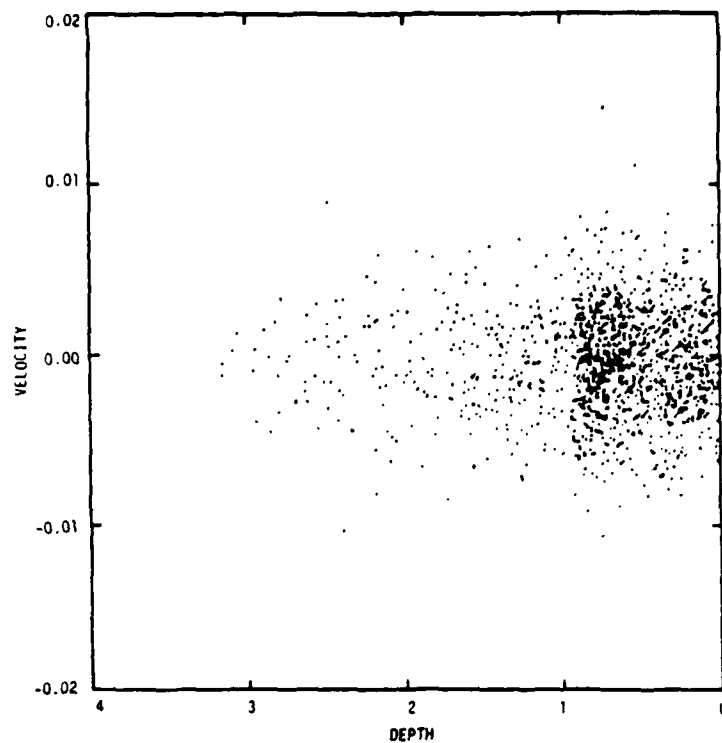
Figure 9a. The joint distribution of velocity and depth of critical layers, showing independence of the separate distributions.
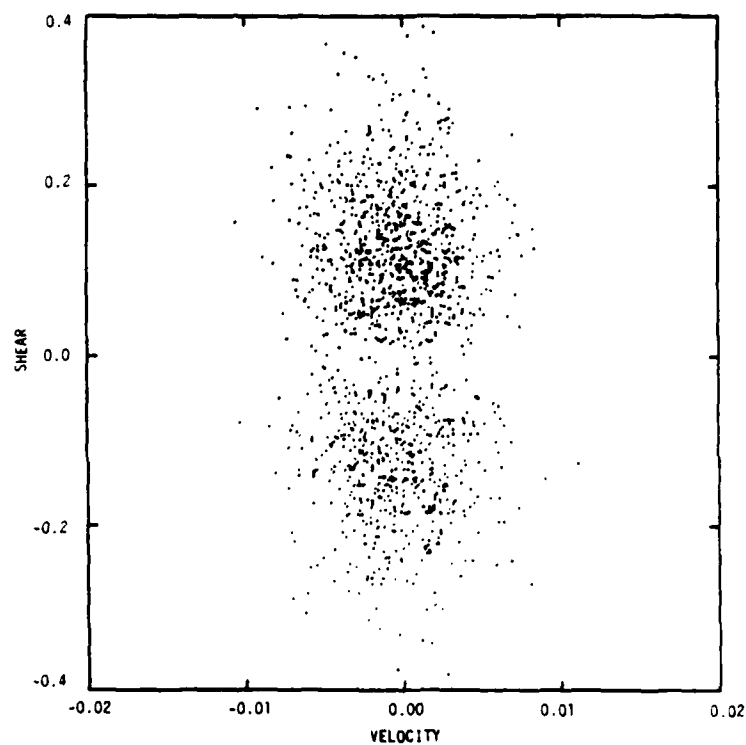
Figure 9b. The joint distribution of velocity and shear. This figure, along with Figures 7 and 9a, strongly suggests an absence of any correlation with velocity.
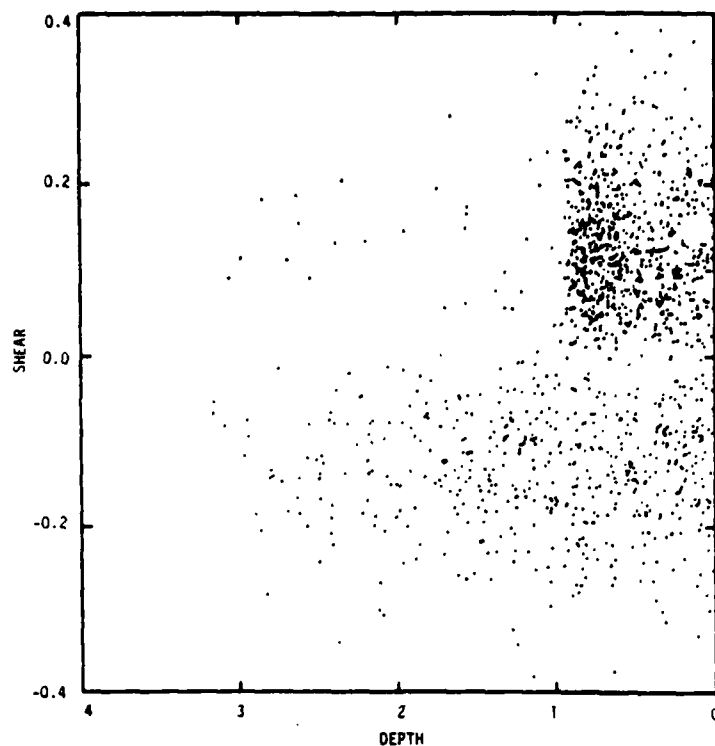
Figure 9c. The joint distribution of shear and depth of critical layers.
The starting point is clearly visible for upward going critical layers but
absent from downward going critical layers. Therefore, most downward
going critical layers involve waves reflected off the surface.
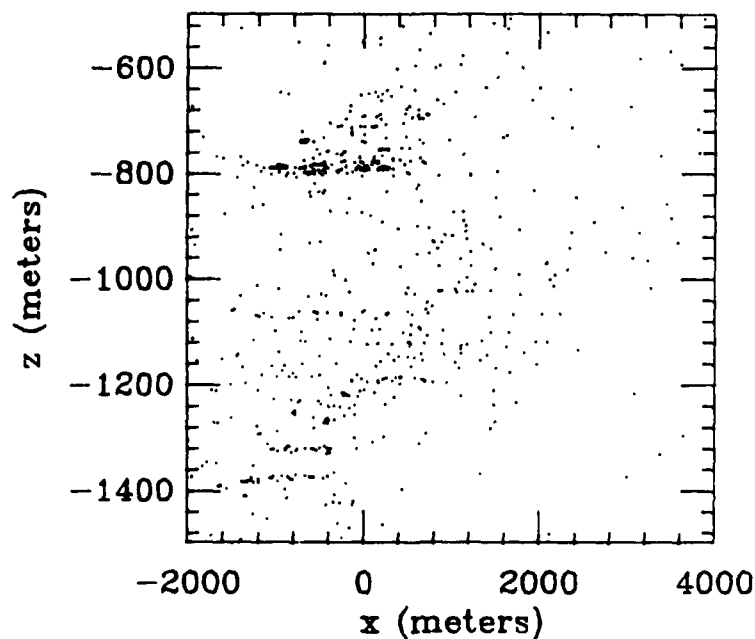
Figure 10. The distribution of positions of waves reaching $k_y = 2\pi/5m$, in one
realization of the background, but many initial conditions. The points are patchy,
and tend to occur in "critical layers." The initial conditions were chosen with
-1600 m < z < -1300 m and -1000 m < x < 0, near the lower left corner.
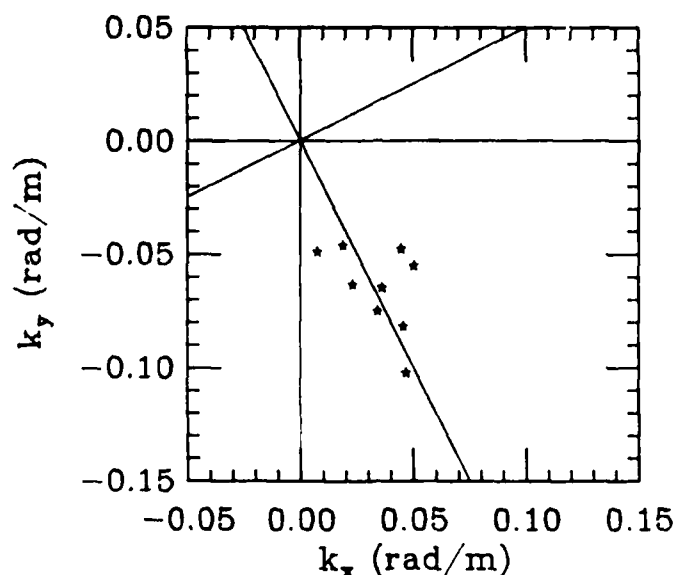
Figure 11. The horizontal wavenumber distribution of upward-moving waves
reaching the 5-m cutoff in a small vertical region near 780 m (see Fig. 10)
in a small time interval. New horizontal axes are defined as shown.

to be large. At appropriate phases of the small scale waves, their shear will add
to the large-scale shear, causing an instability. This instability has a thickness
which is a small fraction of the vertical wavelength of the small-scale waves. If
the wavelength of the small scale is somewhat under 10m, and if the instability
region is somewhat less than one radian of small-scale phase, the instability
region would be on the order of one-meter thick. This instability would lead to a
one-meter-thick turbulent region. As time goes on, the instability regions occur
more or less randomly in the 20-meter patch, filling it with microstructure.
Thus the patches are much larger than the individual instability events.

Our picture of the occurrence of instability events is very different from that of
Desaubies (these proceedings). He assumes Gaussian statistics for the wave
function, which is equivalent to (nearly) linear wave transport. For him, high
inverse Richardson number occurs as a fluctuation of the Gaussian statistics.
We, on the other hand, rely on very nonlinear processes and therefore strongly
non-Gaussian statistics. Our high inverse Richardson number is associated
largely with dynamical processes. One consequence of this difference is our
result that the individual unstable regions should be smaller than those that
would occur by Gaussian statistics, and are imbedded in a larger layer.

The results shown in Figure 10-12 have been for initial conditions at a consider-
able depth, with the waves started upward. We started some waves downward
from the surface, at the same point but with different wavenumbers, and found

that they reached the 5-meter cutoff at positions as shown in Figure 13. The patches are not as layered as in the upward going waves. The reasons for this difference are currently under investigation. Figure 14 shows the trajectories of a chosen selection of these test waves. It is seen that they tend to stay together
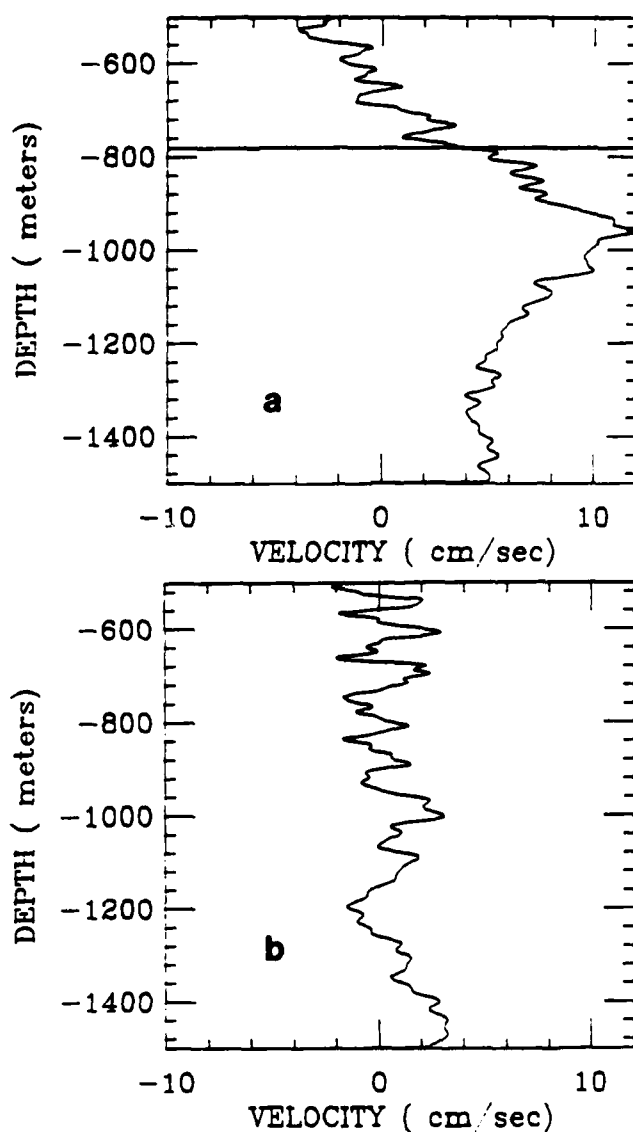
Figure 12. Horizontal velocity components along the axes defined
Figure 11, and at a horizontal position (and time) at the center
of the cluster of critical layer events used in Figure 11.
Figure 12a shows the component in the direction of the cluster
of $\vec{k}_H$ values of the critical events, with the critical layer depth
(780 m) indicated. Figure 12b shows the perpendicular
component.

218
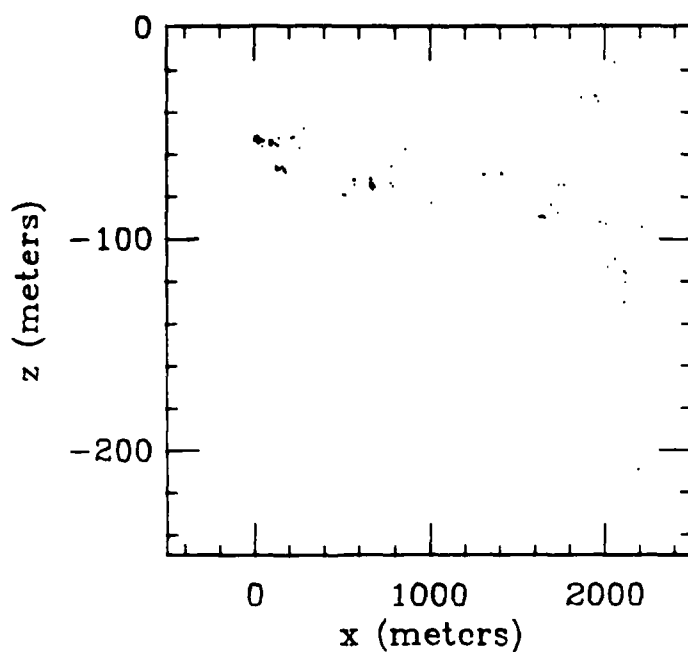
Figure 13. Distribution of 5-m cutoff points for waves starting at the surface (and x = 0), with a variety of wavenumbers in a single realization of the background.
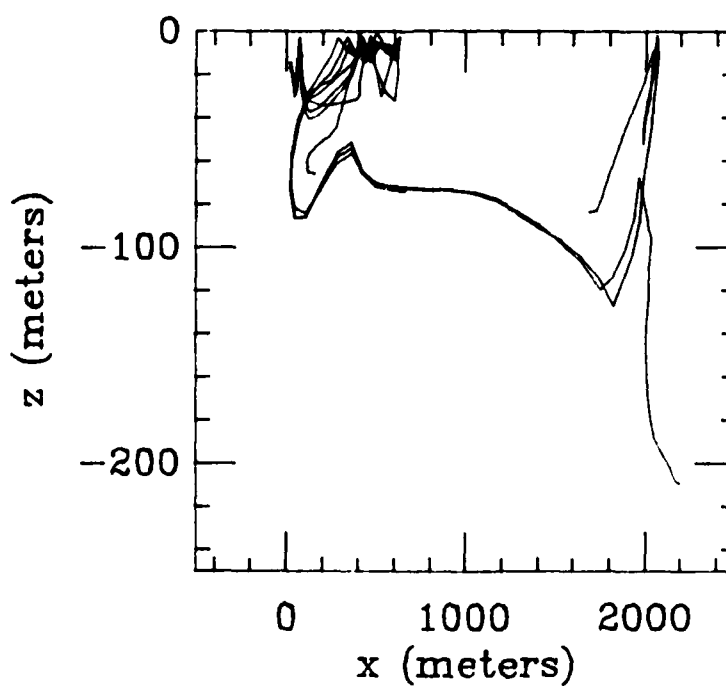
Figure 14. The trajectories a few waves took to reach the points shown in Figure 13. Although they change direction several times, they "remember" that they should be moving downward.

except at unstable "hyperbolic points," at which nearly identical wave packets can go in very different directions. Notice the "memory" effect: all waves shown achieve their 5-meter cutoff going downward, even though they might have reversed direction (aside from surface reflections) several times.

CONCLUSIONS

The research program I have discussed is in a preliminary state as far as quantitative results are concerned, but has yielded a number of qualitative results. We find that weak interaction transport theory is inadequate for the transport of small-scale internal waves in the ocean. On the other hand, the eikonal approximation seems to be fairly well satisfied, although comparisons with numerical integration of the wave equation would be desirable. The ultimate fate of small-scale waves in breaking events is rather complex, and the correlation of these events with single point ambient properties of the background flow leaves out important features. The breaking events occur in patchy layers, and these layers are probably correlated with high shears on more than one vertical scale. The initial conditions are important to the evolution of the small-scale waves; a remarkable "memory" effect persists clear to the instability point, indicating that the statistics of microstructure patches might tell us something about internal wave source mechanisms.

ACKNOWLEDGEMENTS

220

REFERENCES

Henyey, F. and N. Pomphrey, 1983: Eikonal description of internal wave interactions: A non-diffusive picture of induced diffusion. Dyn. Atmos. and Oceans, 7, 189.

Henyey, F., N. Pomphrey and J. Meiss, "Comparison of Short Wavelength Internal Wave Theories," submitted for publication.

Henyey, F., J. Wright, and G. Carnevale, "Validity of the Eikonal Approximation for Transport of Small Scale Internal Waves", in preparation.

Kunze, E. (1984), "Near-Inertial Wave Propagation in Geostrophic Shear", Univ. of Washington preprint.

Munk, W. H. (1981), Internal waves and small-scale processes. In: B. A. Warren and C. Wunsch (Editors), Evolution of Physical Oceanography, MIT Press, Cambridge, p. 264-291.

Van Kampen, N. G. (1974), A cumulant expansion for stochastic linear differential equations, Physica 74, 215-230.

PROBING THE INTERNAL WAVE STRONG INTERACTION REGIME BY NUMERICAL
EXPERIMENTATION

Greg Holloway

Institute of Ocean Sciences
Sidney, B.C., Canada V8L 4B2

ABSTRACT

Direct numerical simulations are used to examine nonlinear
interaction within a spectrum of internal gravity waves. The motion
field is constrained to lie in a vertical plane, permitting experiments
which resolve interactions among widely disparate scales of motion.
By means of external forcing and damping, statistically stationary wave
fields are obtained which exhibit different levels of nonlinearity.
When nonlinearity as measured by a 'wave Richardson number' is of order
unity, density overturnings are observed. A more surprising result is
that, even at weak levels of nonlinearity, a significant vertical mass
flux is supported by wave-wave interaction. Wavenumber and frequency
spectra are exhibited and transfers and conversions of kinetic and
potential energies are examined. Implications with respect to recent
theoretical studies are discussed.

MOTIVATION AND BACKGROUND

The ubiquitous presence of internal wave energy throughout the
world's oceans is well known. Statistics of velocity and temperature
fluctuations over a wide range of space and time scales are observed to
vary in systematic, reproducible ways with respect to such parameters as
latitude or ambient stratification. On length scales from tens to
hundreds of meters and time scales from the inertial to buoyancy
frequencies, the fluctuation statistics have been synthesized in GM
model (Garrett and Munk, 1972, 1975; Cairns and Williams, 1976;
Desaubies, 1976; Munk, 1981). On smaller scales down to molecular
dissipative cutoffs, further systematic variations are observed as
described, e.g., by Gregg (1977) or Gargett et al. (1981). Participants
at this workshop are elaborating upon further and more recent observa-
tions.

The ubiquitous, systematic and reproducible nature of the
observations make this a tantalizing field for theoretical study.
Immensely practical questions, ranging from the small—scale mixing of

dissolved substance up to the interaction with mesoscale or even basin scale circulation, tend to focus attention upon the so-called internal wave field. Here "so-called" raises a fundamental question: to what extent can observed fluctuations on different scales be characterized as internal inertial-gravity waves? To what extent are geostrophic or "vortical" modes entwined with internal waves on all scales (Riley et al., 1981; Holloway, 1981, 1983; Lilly, 1983)?

Despite great interest and effort, the theoretical problem seems awesome in its impenetrability. Perhaps others at this workshop are in the process of proving me wrong here! The core difficulty is, to my mind, that the fluctuation fields are neither close to very small amplitude waves nor close to fully excited turbulence but rather hang tenaciously in the poorly understood middle ground. The entwined vortical modes question provides further complexity.

Theoretical efforts to date have focussed mainly upon a perturbative expansion about a "ground state" consisting of linearized, hence non-interacting, internal waves with vortical modes omitted. The formalism of resonant interaction (RI) theory (Hasselmann, 1962; Benney and Saffman, 1966) has been exercised with respect to internal waves by Müller and Olbers (1975), Olbers (1976), McComas and Bretherton (1977), McComas (1977) and Pomphrey et al. (1980). Detailed dynamical accounts for the internal wave field have been generated. However, at amplitudes given by GM, RI calculated interaction rates are very substantially too fast, contradicting the RI premise (Holloway, 1980). The point is further discussed by McComas and Müller (1981a, b), DeWitt and Wright (1982), Holloway (1982), Carnevale and Frederiksen (1983, hereafter CF), Henyey and Pomphrey (1983) and Frederiksen and Bell (1983a, b, hereafter FB). While there remain points of ambiguity, I believe that the conclusion is that RI is at least dangerous, if not inapplicable, at GM amplitude.

With earlier optimism bruised, where are we now? Theoretical efforts such as DeWitt and Wright (1982) or CF indicate some measure of the challenge ahead. In principle, the problem of essentially strong nonlinear wave interactions is treated by Kadomtsev (1965) or Holloway (1979). Practically, the accomplishment of testable quantitative results is most demanding. Moreover, except in the RI limit, finite amplitude interaction theories are not deductively grounded by rest upon uncertain assumptions. Even the RI limit may prove to be a singular limit as suggested by CF.

Despite these challenges, or perhaps on account of these challenges, there is reason to expect good theoretical progress in the years ahead. However, success will surely depend upon the availability of adequate means for theory testing. Direct field tests, while essential, are fundamentally limited by incompleteness of data. Full resolution of the four-dimensional wavevector-frequency spectrum, for example, seems almost certainly unattainable; let alone the more difficult matter of

bispectra (McComas and Briscoe, 1980). Laboratory testing likewise
suffers uncertainties as described during this meeting by Prof. Thorpe.
In this article I turn to yet a third source for testing, namely direct
numerical simulations. Illustrations will be drawn from recent work by
Dr. C. Shen and myself (Shen and Holloway, 1984, hereafter SH).

Use of numerical simulation to explore internal wave phenomena has
been extensively developed. Applications have included Kelvin-Helmholtz
evolution, critical layer interactions, vortex dynamics on interfaces,
stability of standing waves, etc. For the problem of wave-wave inter-
actions within a broad band spectrum, previous works have consisted of
the experiments of Orlanski and Cerasoli (1980, 1981, hereafter OC),
Weissman et al. (1981) and FB, each of which has adopted the idealiza-
tion of motion constrained to lie in a vertical plane. Riley et al.
(1981, hereafter RMW) report simulations for fully three-dimensional
(3D) spectra.

When viewing the simulations which follow, the reader is well
advised to keep in mind that there may arise wide differences between
"numerical physics" and "true physics". Even on the world's largest,
fastest machines, uncomfortable compromises are required. The method
of discrete representation of fluid continuum equations is important.
Customary schemes for finite differencing may exhibit unphysical
defects. In particular, difference methods may limit the phase speeds
of short waves. Numerical distortion of wave group speeds will be even
more severe. A method which avoids distortion of phase and group speeds
is the pseudo-spectral simulation (Orszag, 1971).

Apart from method of representation, even the largest computers can
only practically calculate the time evolution of about 10^5 dependent
variables. The result is that one is limited in the range of scales
that can be resolved. For the 3D simulations of RMW, the resolved
range of scales was only 15, i.e. the longest wavelength resolved is
only 15 times the shortest. Yet the cost was so large as to limit RMW
to consider only short-time, rapidly decaying evolution from a few
randomly chosen initial conditions. A further penalty due to coarse
resolution is the need to impose a large damping in order to remove
variance which would accumulate on the shortest resolved scales. The
result is that numerical experiments are run at low to modest effective
Reynolds or Peclet numbers.

Higher resolution and weaker damping, as well as lower cost
permitting longer time integrations in order to explore statistical
stationarity, become possible if we consider motion constrained such
that variations may occur only in a vertical plane (2D). Relative to
computational capability, efforts to date in 2D have been quite modest.
The computations of OC were performed by finite differences, yielding
an effective resolution range that would not be greater than about 20.
Pseudo-spectral computations of Weissman et al. (1981) were at resolu-
tion of 60 but were carried only to the point of preliminary results, as

224

their authors remark. Pseudo-spectral computations of FB are at reso-
lution 30 while those of SH are at 30 and 60. Higher resolutions,
certainly in 2D and to some extent in 3D, are available,though the
scientific cost-benefit at this time may be questionable.

For what follows, we will be limited to discussion of SH, i.e. to
2D. The immediate question arises, and will arise recurringly through-
out this paper: to what extent does 2D violate oceanic reality? Rather
than attempting an answer at the outset, I will reserve this for the
concluding section.

MODEL FORMULATION

Consider incompressible flow under Boussinesq approximation. We
imagine a background density stratification which will be taken to be a
simple uniform gradient, such that $R = |\partial \bar{\rho}/\partial z|$ is a constant. Fields are
constrained to vary only in the vertical plane defined by coordinates
x and z, as shown in Fig. 1. A component of flow along the normal
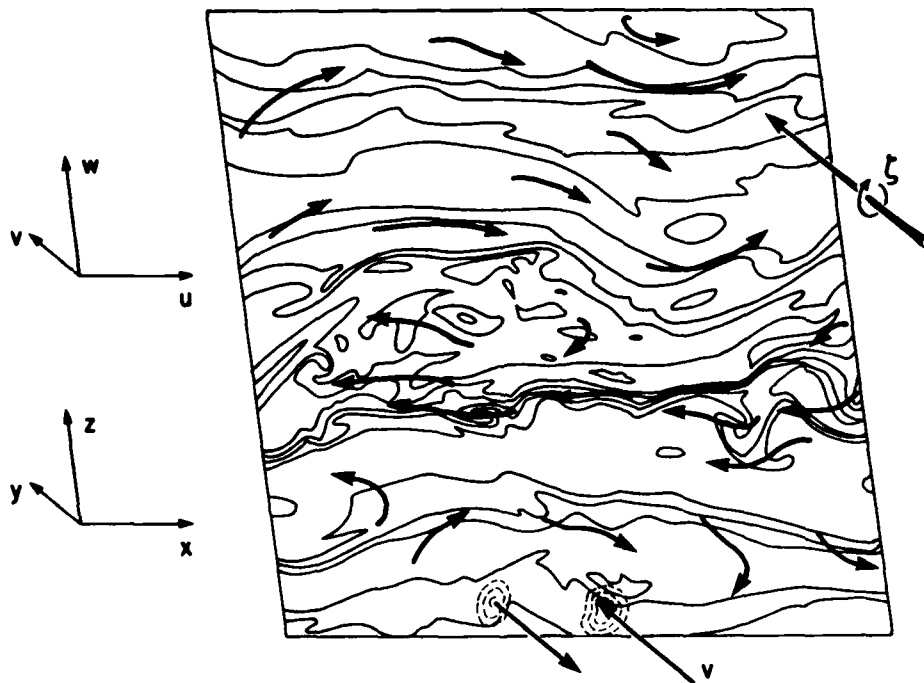
Fig. 1. An orientation sketch shows the vertical x - z plane with
density variation and u - w flow lying in the plane. Normal or v
flow is also sketched along with the y component of vorticity,
$\zeta = \partial_z u - \partial_x w$.

coordinate y is allowed but no variation along y is permitted. Hence velocity components u, w in the vertical plane are definable from a normal component of vorticity $\zeta = \hat{y} \cdot \nabla x \underline{u}$, under suitable boundary conditions. Those boundary conditions are that all perturbations from a quiescent state with uniform density gradient will be periodic in both x and z. In this way we envisage Fig. 1 as a little "piece" of ocean (albeit 2D!), removed from boundaries.

Equations of motion are

$$\partial_t \zeta + J(\psi,\zeta) - g\partial_x \rho \quad - f\partial_z v = F_\zeta - D_\zeta \tag{1}$$

$$\partial_t \rho + J(\psi,\rho) + R\partial_x \psi \quad\quad = F_\rho - D_\rho \tag{2}$$

$$\partial_t v + J(\psi,v) \quad\quad + f\partial_z \psi = F_v - D_v \tag{3}$$

A streamfunction ψ is here defined by $\nabla^2 \psi = \zeta$. Jacobian determinants $J(\psi,q)$ represent advection of any property q. ρ is the departure of density from uniform gradient R, and f is Coriolis parameter.

Right-hand sides of (1), (2), (3)* list symbolically any forcing and dissipation that may be applied to the perturbation fields. Uncertinty and arbitrariness already appear. What kind of energetic sources do we suppose act upon our little "piece" of ocean? Plausibly (we hope), SH have chosen to excite the low vertical wavenumber, horizontal flows by means of F_ζ. Three kinds of forcing were tested: (1) purely random external torques are applied to excite vertically sheared, horizontal flows; (b) artificial self acceleration of horizontal flows according to a prescribed rate of energy supply; and (c) random excitation of both ζ and ρ, with the excitation at low wavenumbers but distributed isotropically with respect to vertical and horizontal. Our purpose in exploring such a variety of forcing was to see how sensitive are the results to choice of forcing. Happily, we have found surprisingly little sensitivity of flow statistics to the manner of forcing. However, one important point, apropos of Dr. Briscoe's comments during the workshop, is that we have confined forcing to very low wavenumbers. Forcing might have been moved to intermediate scales, as OC, but we have not done so. I will return to this point.

Dissipation admits the possibility of further artifice. One straightforward scheme is to appeal to molecular diffusion, i.e. to ∇^2 operators on the right of (1), (2), (3). However, given the limited resolution available, sufficient ∇^2 diffusion to smooth the fields at grid spacing will produce very strongly damped fields. Since our goal is to look at internal wave interactions, we would prefer to think that

---

* Equations (1), (2), (3) have been coded as listed, with demonstration runs executed for verification. However, for production runs to be described here, we take f = 0 and omit equation (3).

226

direct molecular diffusion is unimportant. In this case we would be
obliged to introduce a 'subgridscale parameterization'. None is known
reliably. OC explore one ad hoc scheme. SH have explored another; we
replace ∇^2 by $-\nabla^4$. There is no theoretical excuse for this except that
the higher derivative form concentrates dissipative effects into the
higher wavenumber portion of the spectrum. As with the forcing issue,
when uncertain about one's assumptions, it is best to try different
possibilities. Dr. Shen and I have made some intercomparisons of ∇^2
and ∇^4 dissipation. We observed no qualitative differences of
phenomenology except for the stronger damping by ∇^2.

Numerical experiments of SH are initiated from a random wave field
with a prescribed spectrum suggestive of GM. For details see SH.
Forcing is applied at low wavenumbers and time integrations are carried
forward until an approximate condition of statistical stationarity is
achieved. I believe that the statistical character of the solutions
long after initialization is effectively independent of the initial
conditions. However, apropos of comments from Dr. Abarbanel during the
workshop, I should say that the question of independence from initial
conditions has not been tested systematically. Results which are
discussed throughout the rest of this paper are taken from the approx-
imately stationary regime of SH.

PHENOMENOLOGY

In setting out these numerical experiments, my goal has been 'to
see what happens' with as little theoretical prejudice as possible. We
may ask how phenomena change as flow fields are made increasingly
energetic, hence more strongly nonlinear. As a measure of strength, SH
adopt a kind of inverse Richardson number $Ri^{-1} \equiv \overline{(\partial u/\partial z)^2}/N^2$. There is
no defined mean flow for these problems and $\overline{(\partial u/\partial z)^2}$ is the variance
density of vertical shear averaged over the flow domain. Velocity
component v is absent, with equation (3) omitted. $N^2 = gR$ is prescribed
and we consider time to be scaled such that $N^2 = 1$.

By varying the strength of forcing, SH explore the vicinity of four
values of Ri^{-1}:

$$Case\ 1 \qquad Ri^{-1} \approx 0.01$$

$$Case\ 2 \qquad Ri^{-1} \approx 0.1$$

$$Case\ 3 \qquad Ri^{-1} \approx 1.$$

$$Case\ 4 \qquad Ri^{-1} \approx 7.$$

In Fig. 2, representative instantaneous fields are shown for streamfunc-
tion ψ, vorticity ζ and total density $\rho + Ry$, along with the horizontally
averaged density as a vertical profile. Vorticity and density fields are

in statistical balance. For small to modest Ri^{-1}, behavior appears to be plausible. Small vorticity in Case 1 leads to almost imperceptible deformations of isopycnals. Increasing vorticity leads to stronger deformation until, near $Ri^{-1} \sim 1$, we begin to encounter significant overturnings. This rather tidy result is found throughout our work and appears to be fairly insensitive to choices of forcing and dissipation. In other terms, a strain parameter such as that discussed by Dr. Desaubies will apparently take values near unity at scales such that resolved Ri^{-1} comes near unity, at least here in 2D. At still larger Ri^{-1}, as Case 4, overturning is ubiquitous. The 2D idealization is, presumably, a severe affront to dynamics in Case 4; the reader may be amused to consider at how much smaller amplitude is 2D likely a problem.

Also shown in Fig. 2, row (a) are the locations of nine moorings. Time series and frequency spectra from these moorings will be discussed later.

While viewing pictures, Fig. 3 is included in order to display in more detail, and at 128 x 128 resolution, some of the morphology of near-overturning 2D structures. A sense of time evolution may also be seen in Fig. 3. Units of time here and throughout are nondimensionalized by buoyancy frequency $N^2 = gR$; hence the frames in Fig. 3 are separated by just more than half a buoyancy period ($\Delta t = 3.61$). A couple of noteworthy features are (1) the similarity of small-scale vorticity and density features, and (2) some tendency for "breaking" to occur near a velocity extremum rather than a shear extremum. (However, high levels of vorticity fluctuation will also be generated near large isopycnal deformations or overturnings.) Incidentally, during the sequence shown in Fig. 3, Ri^{-1} ranged over about 1.5 to 1.6, as is consistent with the evident propensity for breaking.

WAVENUMBER AND FREQUENCY SPECTRA

For more quantitative descriptions we turn to spectra in both wavenumber and frequency domains. Fig. 4 shows wavenumber spectra of kinetic and potential energies for the four cases as seen in Fig. 2. Here and throughout, potential energy (PE) refers to 'available potential energy' of the fluctuation density field. For the present problem with prescribed uniform background stratification, PE is just proportional to total density fluctuation variance. Spectra are given in total wavenumber $k = (k_x^2 + k_z^2)^{\frac{1}{2}}$; marginal spectra in k_x and k_z are also given. Cases 1 and 2 exhibit near equipartition of KE and PE, as would be expected of weakly nonlinear, nonrotating, internal gravity waves. Direct forcing of KE but not of PE in modes $k_x = 0$, $|k_z| < 4$ accounts for most (but not all!) nonequipartition seen in Cases 1 and 2. Wavenumber spectral slopes for Cases 1 and 2 appear to range around a -3 exponent, roughly consistently with FB. (As well as I can judge from their publications, experiments by FB fall in the range of SH Cases 1 to 2. In particular, it seems doubtful to me that FB experiments would have exhibited any overturning.)

228
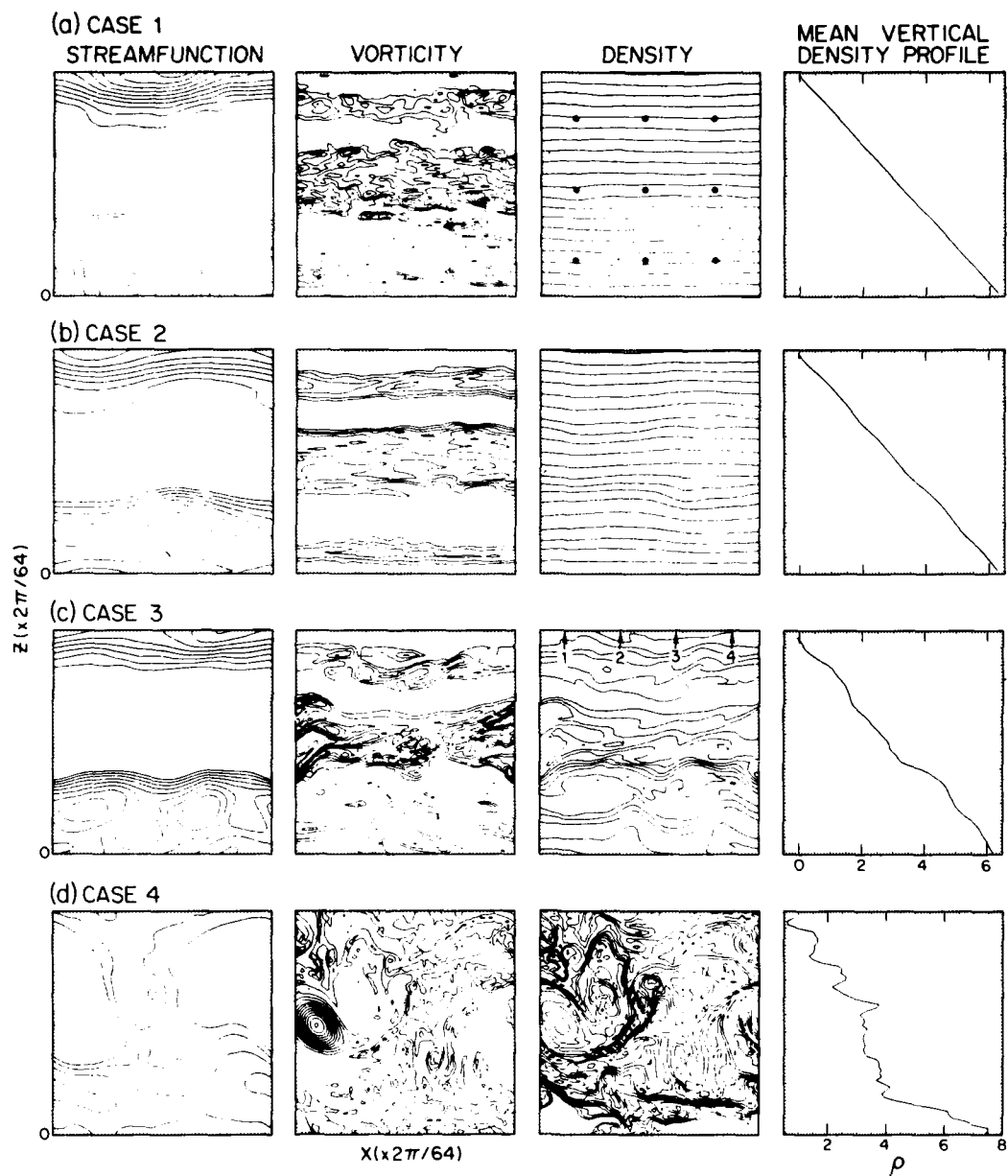
Fig. 2. Instantaneous fields of streamfunction, vorticity and density
are shown, along with vertical profiles of horizontally averaged
density, for four cases. Also shown in row (a) are locations of
nine moorings. Locations for release of four dropped probes are
shown in row (c). From SH.

T = 33.39   37.00   40.62   44.23

STREAMFUNCTION
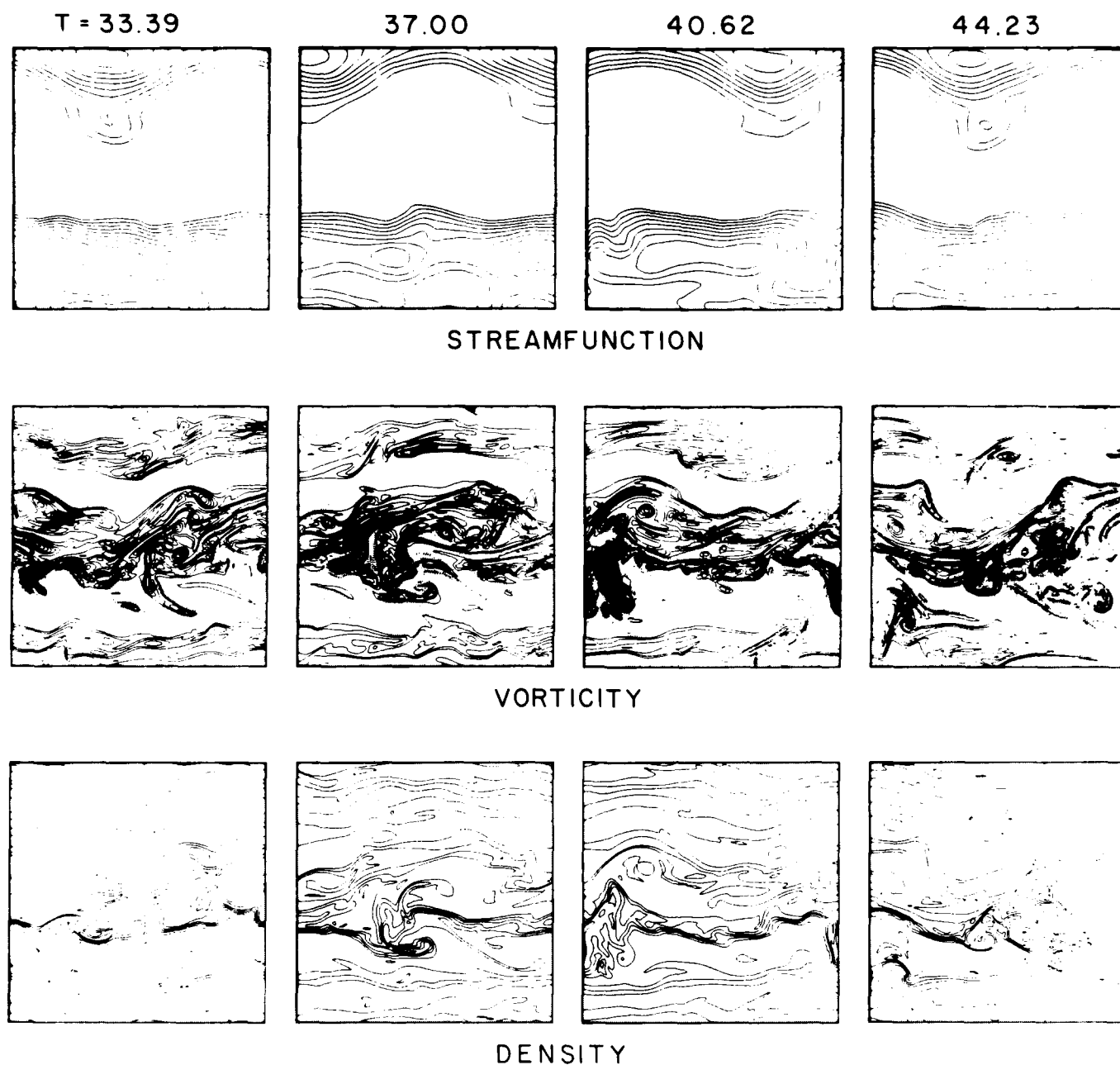
VORTICITY

DENSITY

Fig.   3. Fields of streamfunction, vorticity and density are shown at
successive times. Time is scaled by the mean buoyancy frequency.
Positive streamfunction is contoured in solid lines; negative
streamfunction dashed. Sense of flow is here defined such as to
keep more positive streamfunction to left.

230
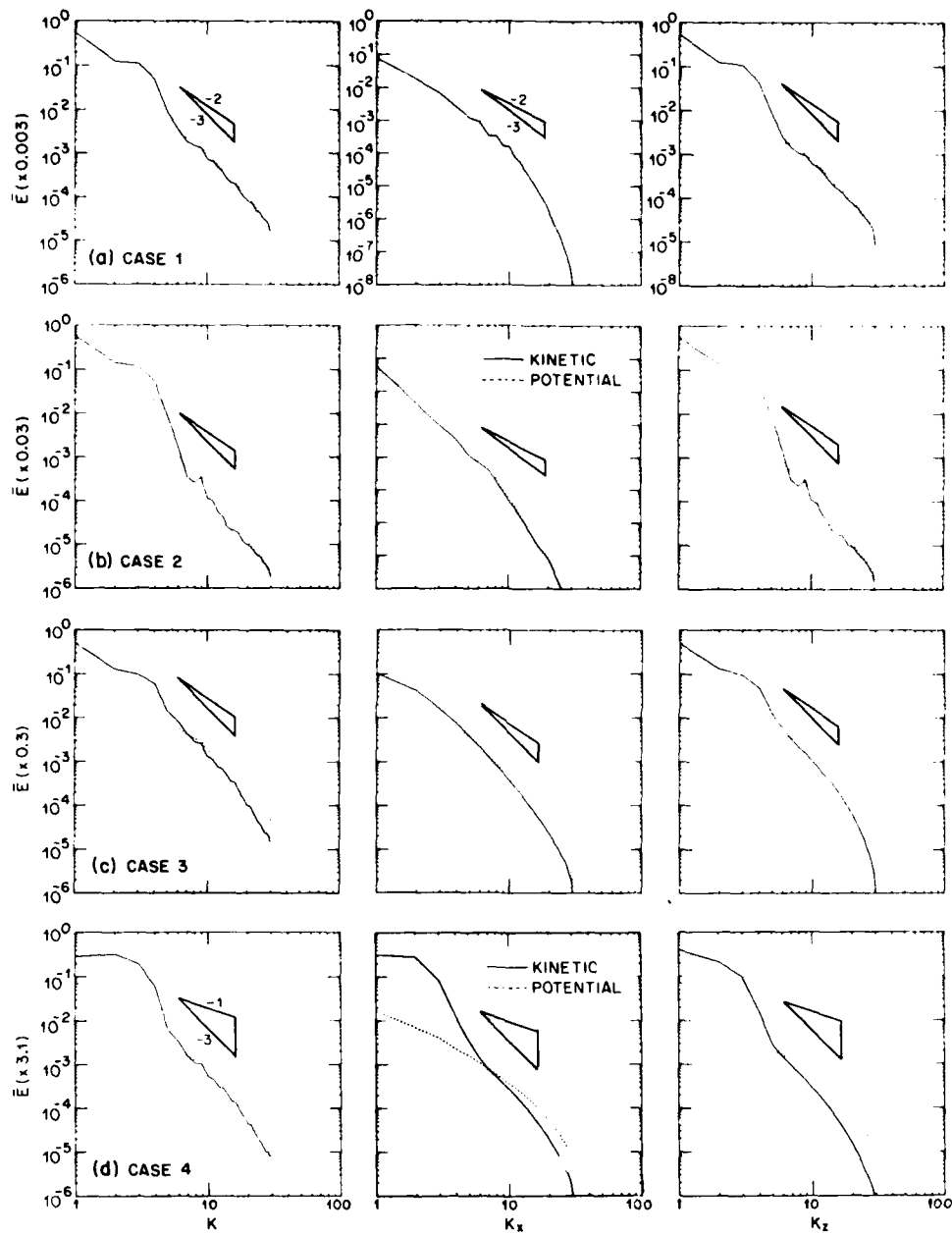
Fig. 4. Wavenumber spectra of kinetic and potential energy are shown for the four cases seen in Fig. 2. From SH.

Near Ri^{-1} unity (Case 3), where we recollect that substantial over-turning has begun, wavenumber spectra begin to exhibit significant departure from equipartition. KE fall off more steeply while PE fall off less steeply at larger wavenumbers. One consequence is that direct dissipation rate of PE exceeds the direct dissipation rate of KE in Cases 3 and 4, contrary to oceanic observations such as those of Oakey (1982). For Case 4, spectra of KE and PE are quite dissimilar, exhibiting spectral slopes a bit steeper than k^{-3} and k^{-1}, respectively. Such slopes are in fact what one may expect in the enstrophy cascading sub-range of 2D turbulence (Kraichnan, 1967) with density acting effectively as a passive tracer (Lesieur et al., 1981) at this large Ri^{-1}.

Frequency spectra obtained from the nine moorings seen in Fig. 2 are shown in Fig. 5. Spectra are shown for PE, vertical KE and horizontal KE. Cases 1, 2 and 3 exhibit tendencies to produce spectral peaks near the buoyancy frequency, here given by $\omega = 1$. These tendencies are particularly noteworthy since the stratification is uniform; hence turning point considerations (Desaubies, 1975) do not apply. Moreover, the energy source is in HKE at very low frequency. Other noteworthy features are that an approximate ω^2 scaling from PE to VKE is found in Case 1 for $\omega < 1$, but that this scaling already fails at Case 2. Last we observe that increasing Ri^{-1} is accompanied by greater energy accumulation in $\omega > 1$, i.e. at frequencies above the internal wave band.

ENERGY BALANCE

A merit of numerical experiments is the possibility of resolving fully all of the processes which together produce a phenomenon. Spectra seen in Fig. 4 represent some energy balance between forcing, redistribution and dissipation. Although details will differ, a similar kind of balance may hold in oceanic reality. Important differences are that in the numerical experiments we know the sources and sinks exactly and we can calculate exactly the rates of redistribution of energy.

Energy redistribution for the present problem may be decomposed into three parts:

1) KE transfer. This is the rate at which KE increases or decreases at any wave vector k due to nonlinear transfer of KE to or from other regions of the spectrum. Summed over the spectrum, the transfer vanishes; this is a pure redistribution with no overall gain or loss of KE

2) PE transfer. This is the rate of PE increase or decrease at any k due to transfer and is a pure redistribution with no overall gain or loss of PE

FREQUENCY SPECTRA

(a) $\overline{PE}$ (b) $\overline{VKE}$ (c) $\overline{HKE}$

CASE 1

CASE 2

CASE 3

CASE 4

$\overline{E}(\times 0.003)$

$\overline{E}(\times 0.03)$

$\overline{E}(\times 0.3)$

$\overline{E}(\times 3.1)$

ω
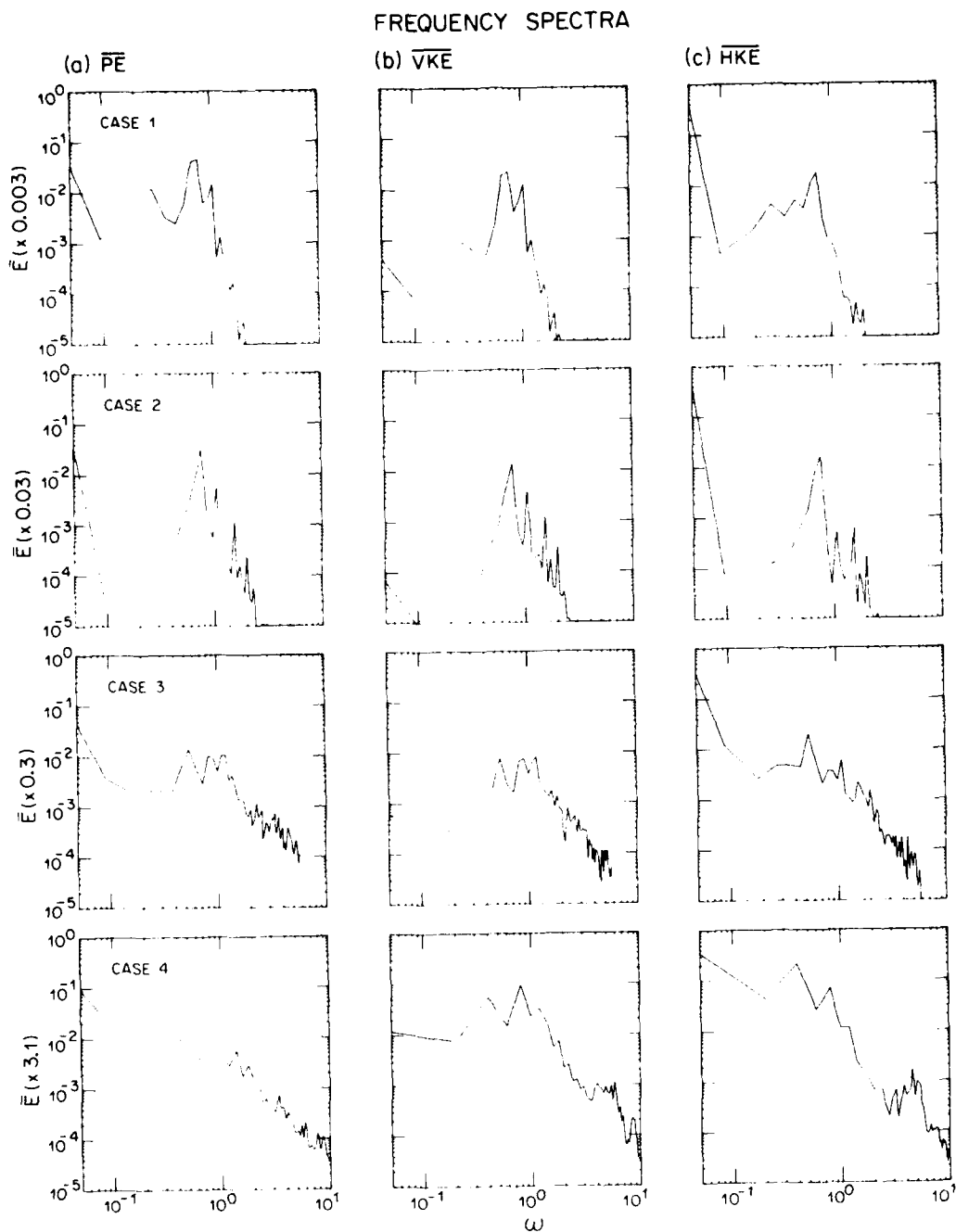
Fig. 5. Frequency spectra of potential energy, vertical kinetic energy and horizontal kinetic energy are shown for the four cases, based upon time series collected at nine moorings. From SH.

3) KE - PE conversion. In a stratified fluid under gravity, KE and PE
   may be exchanged by means of vertical mass flux $\overline{\rho w}$. Upward flux
   $\overline{\rho w} > 0$ is a sink for KE and corresponding source for PE.

   In Fig. 6 the two transfers and the conversion are shown for Case 3,
graphed separately against k_x, k_z and total k. All quantities have been
time averaged through several buoyancy periods. KE transfer exhibits a
pattern of KE loss at intermediate scales with compensating gains at
large and small scales. This pattern is characteristic for 2D flows in
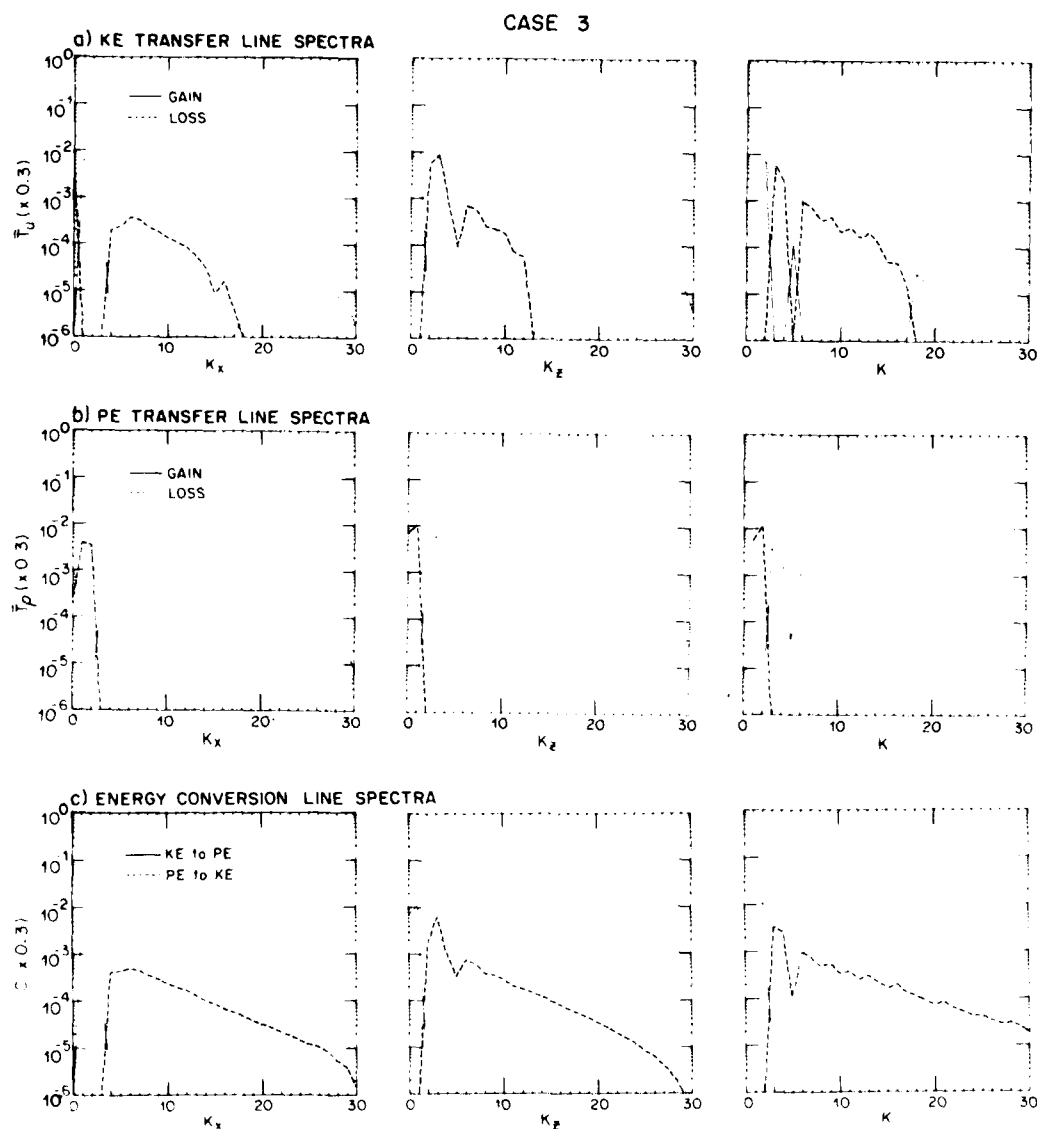
Fig.   6. Time averaged rates of transfer of kinetic energy and of
   potential energy are shown, as well as conversion rate from KE to PE.
   From SH.

234

which KE transfer alone conserves both overall KE <u>and</u> overall vorticity
variance. Although vorticity at each fluid element may change on account
of gravitational torques, KE transfer is nonetheless constrained
(Fjørtoft, 1953; Kraichnan, 1967).

PE transfer is somewhat simpler since no secondary conservation
constraints occur as in the case of KE. PE is removed at low wave-
numbers and supplied to higher wavenumbers by the physical process of
shearing and deforming larger scale density features into smaller scale
features.

When we come to KE – PE conversion, we encounter what may be either
a rude shock or a fascinating suggestion, depending upon one's predispo-
sition. 'Conventional wisdom' (according to me) holds that vertical mass
flux in an internal wave field results from overturning and ensuing
mixing; thus $\rho w > 0$ should be associated with the scales of motion involved
most directly in the apparent overturnings seen in Fig. 2. Now the
surprise, perhaps, is that Fig. 6 shows KE to PE conversion, i.e. $\overline{\rho w} > 0$;
occurs at the very lowest wavenumbers, i.e. at the largest resolved
scales of motion. Over the smaller scales, including those which one
might associate with overturning, mass is falling back, i.e. $\overline{\rho w} < 0$ or
reconversion of PE to KE.

Another view of these transfers and conversions may be seen in Fig.
7 where quantities are displayed in greytones in $k_x - k_z$ space. Again
Case 3 is shown. In the top panels, positive transfers and conversion
($\overline{\rho w} > 0$) are shown, with darker shades denoting greater intensity.
Negative transfer and conversion ($\overline{\rho w} < 0$) are shown in lower panels.
Anistropy of the transfers is apparent. Removal of KE at intermediate
scales with transfer to smaller and larger scales is seen to contrast
with PE, which is removed near the origin and transferred to higher wave-
numbers. However, the clearest and most startling signal is in the
KE – PE conversion where $\overline{\rho w} > 0$ is supported by a very tight region at
small k_x and near $k_z = 0$. Reconversion ($\overline{\rho w} < 0$) is dominantly at inter-
mediate scales.

The results we have just discussed become even more surprising
when it is remarked that the patterns of transfer and conversion appear
to be qualitatively similar in all four Cases 1–4. Especially in Cases
1 and 2 for which overturning does not occur, one may ask how (or if!)
waves can maintain non-zero $\overline{\rho w}$. In fact $\overline{\rho w}$ exhibits more oscillatory
behavior at smaller Ri^{-1} so that time averaging only slowly resolves a
reliable mean signal. An example, averaged over many periods, is shown
in Fig. 8 for Case 2. While the patterns are less distinct, it may be
seen that they are broadly similar to those in Fig. 7.
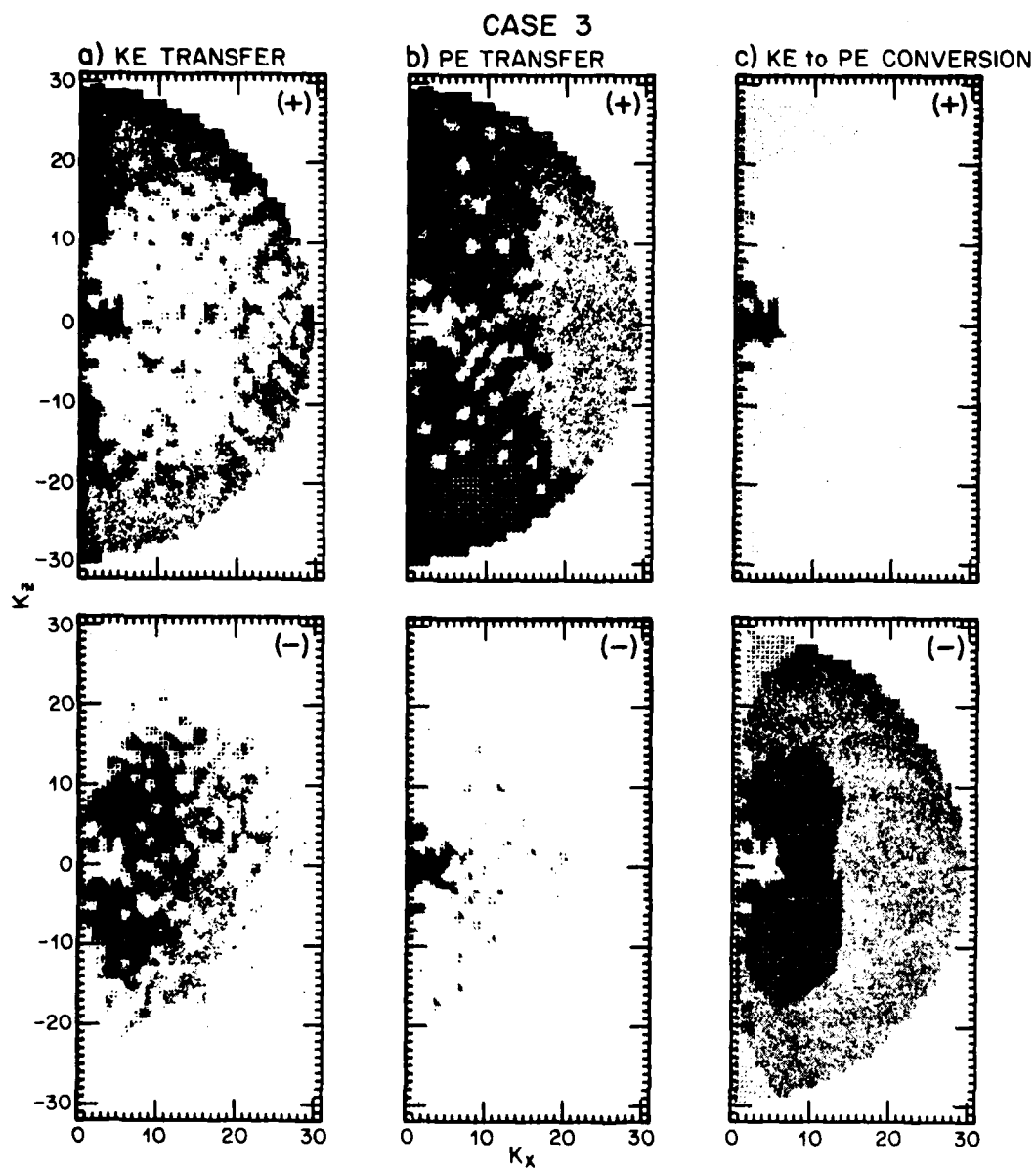
Fig. 7. Time averaged rates of transfer and conversion of KE and PE
in case 3 are here shown as greytones in k_x, k_z - space. Darker
shades indicate greater intensity. From SH.

236
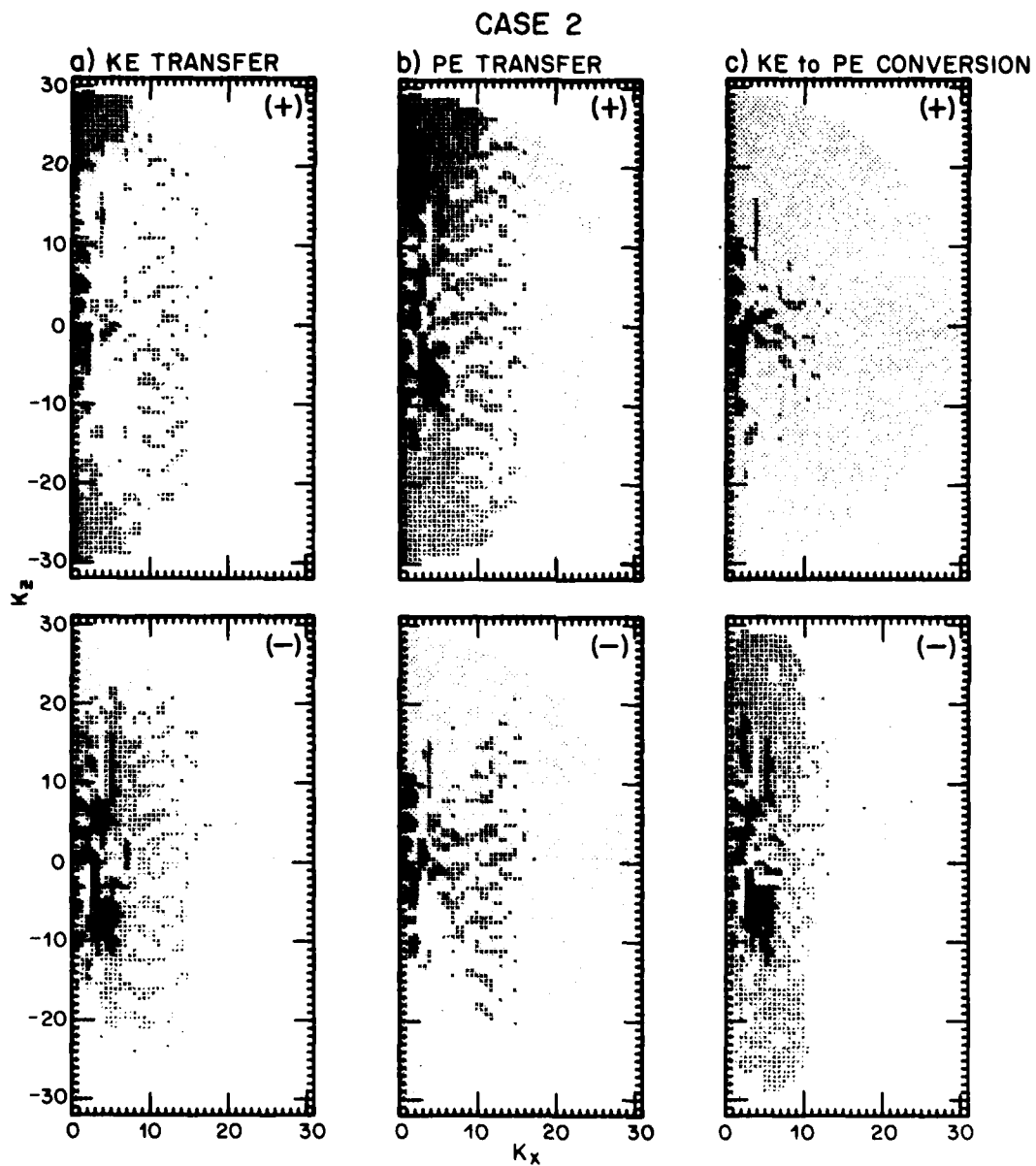
Fig.   8.   Same as Fig. 7, here shown for case 2.   From SH.

We have arrived at an unusual result that internal waves even with no manifest overturning (Cases 1 and 2) sustain systematic vertical mass flux. Is this consistent with previous work such as OC or FB? The analysis was not reported by OC. However, FB do experiments in the range of present Case 1 to Case 2. It is my opinion that results of FB do exhibit systematically non-zero mass flux, although the signal is weak and considered to be unreliable by FB.

As a last point in this section, let us consider how dissipation rates change with increasing energy level. Such a relationship, if it were known for the case of oceanic reality, would bear upon the question of possible saturation control of the GM spectrum (Munk, 1981). In fact SH find dissipation to be a strongly increasing function of Ri^{-1}, particularly when close to the onset of overturning. However, there is a point of ambiguity: at larger Ri^{-1} the generation of small-scale features is more intense and the coefficients of explicit dissipation operators must be increased to prevent excessive accumulation of small-scale variation. This is taken into account in Fig. 9 where dissipation rate is divided by the coefficient of dissipation operator and graphed against Ri^{-1}.
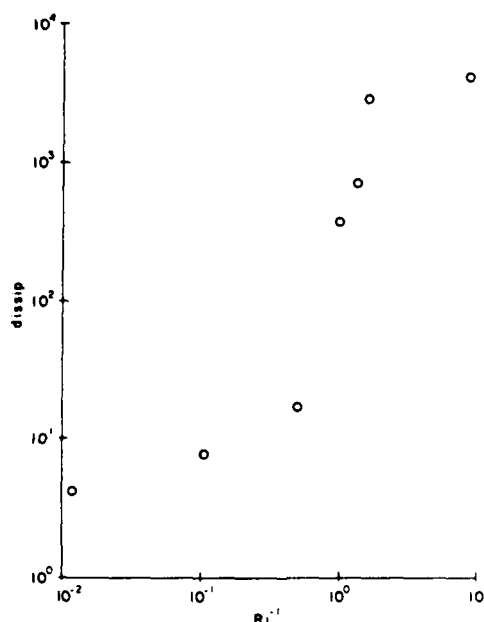
Fig. 9. Dissipation rate of total energy, divided by the coefficient of dissipation operator, is graphed against Ri^{-1}. The viewer is strongly cautioned from quantitative interpretation of this figure on account of the 2D idealization underlying the computation.

FREQUENCY DISPERSION

A premise underlying RI is that the wave field can be described approximately as a superposition of freely propagating waves. Each wave will then propagate with a frequency very near to its natural frequency. This thesis is easily tested over Cases 1 to 4 to see at what level it fails.

Streamfunction and density fields may be combined to fields of up- and down-going waves $a_{\underline{k}}^{\pm} = k\psi_{\underline{k}} \pm \rho_{\underline{k}}$ where $\psi_{\underline{k}}$ and $\rho_{\underline{k}}$ are expansion coefficients of ψ and ρ. In a limit of very weak interaction one expects $a_{\underline{k}}^{\pm} \sim A_{\underline{k}}^{\pm} e^{i\theta_{\underline{k}}^{\pm}}$ with $A_{\underline{k}}^{\pm}$ only weakly time dependent and $\theta_{\underline{k}}^{\pm} \sim \pm \Omega_{\underline{k}} t$ with $\Omega_{\underline{k}} = k_x/k$, where time is scaled so that buoyancy frequency is unity. In the numerical simulations we observe the time rates of evolution of $\theta^{\pm}$. Observed frequency $\omega^{\pm} = d\theta^{\pm}/dt$ varies erratically due to nonlinear inter-action, giving a spread of values within which the means of ω are not demonstrably different from Ω. Standard deviations σ_{ω} are plotted in Fig. 10, both in greytones and as a line graph against total k. Here Cases 1 and 4 are shown, exhibiting similar behavior consisting of roughly linear increase of σ_{ω} with k. Greytones show σ_{ω} to be anistropic in Case 1, but more isotropic in Case 4. This distribution of σ_{ω} may be explained as resulting from random Doppler shifting of phases, roughly as

$$\sigma_{\omega}^2 \sim \sum_{\underline{p}} U_{\underline{p}} \ |\hat{\underline{p}} \times \hat{\underline{y}} \cdot \underline{k}|^2 \tag{4}$$

where $U_{\underline{p}}$ is velocity variance at wavevector $\underline{p}$. From (4), σ_{ω} varies linearly with k and, in Case 1 where U is concentrated near the k_z axis, σ_{ω} increases more strongly along k_x.

One point particularly to be noted in Fig. 10 is that, even for Case 1, $\sigma_{\omega} > 1$ over much of the wave space, i.e. the spread of frequency at given $\underline{k}$ exceeds the buoyancy frequency.

IMPLICATIONS AND INTERPRETATIONS

As was discussed at the outset, the primary motivation for numerical experimentation such as described here is not the direct application to oceanic reality. Limited resolution and the 2D idealization are obvious shortcomings. Rather, present experiments bear upon the testing of theoretical approaches which, in turn, may apply to reality. However,
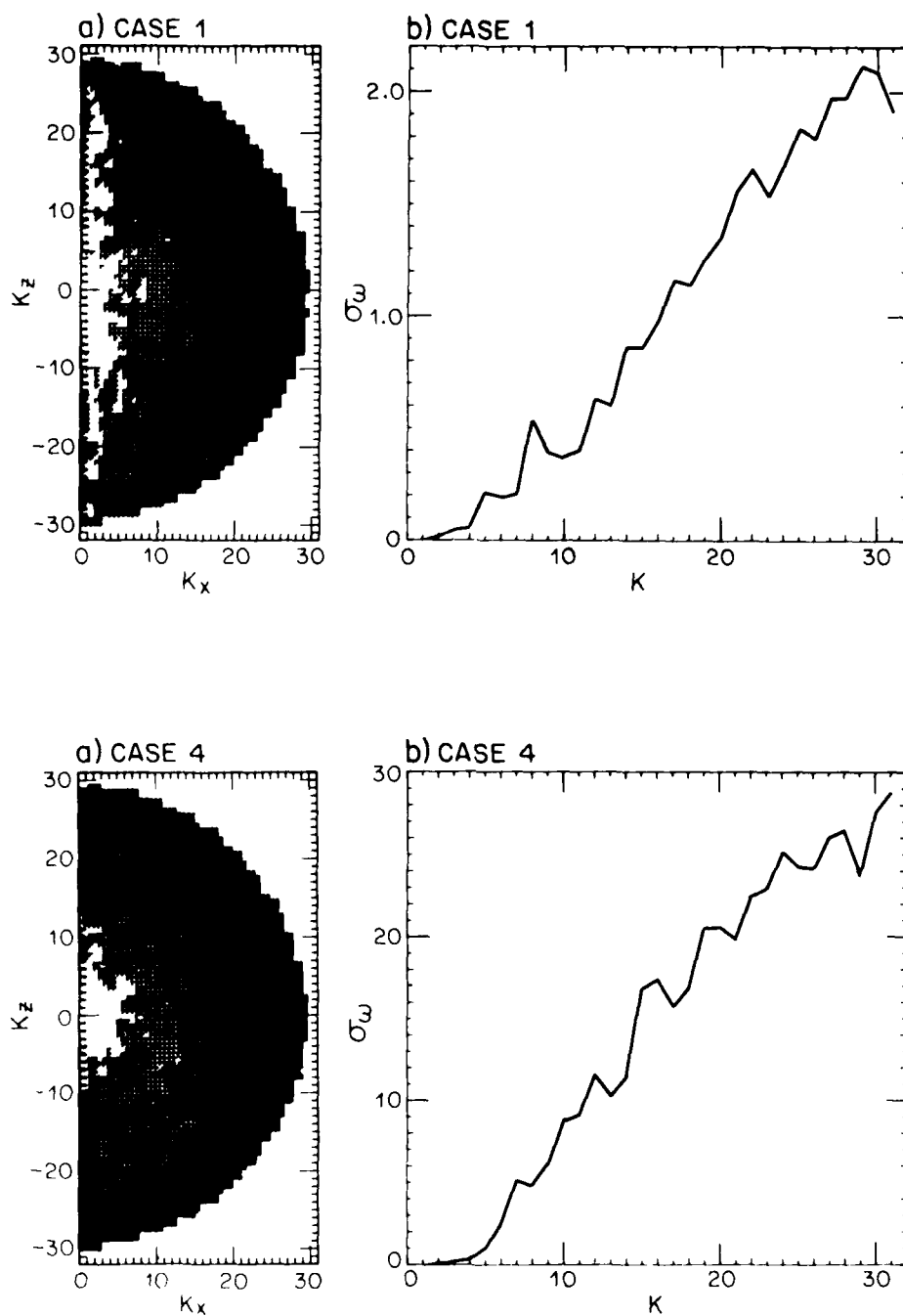
Fig. 10. Standard deviation of frequency distributions are plotted in greytones in k_x, k_z - space and as a line graph in total k. Cases 1 and 4 are shown. From SH.

the only theory which is well developed to date is RI. In Fig. 10 we have seen one basis for skepticism about RI: the frequencies of interacting waves are not narrowly distributed close by their natural frequency. Even at the very low amplitudes seen in Case 1 in Fig. 2, σ_ω in Fig. 10 are so large as to make precise frequency resonance unnecessary for sustained wave interaction.

There is a simpler comparison with RI available. RI has a tendency (Hasselmann, 1967) that energy flows from higher frequency modes to lower frequency modes. This is consistent with the several RI studies of internal waves and is construed to imply that energetic sources for oceanic internal waves must include significant high-frequency content. However, experiments performed here have known energy sources. In most instances, SH have forced only the horizontal flows and have applied forcing at very low frequencies. Nonetheless, and even at the low amplitudes of Case 1, wave-wave interactions scatter energy up into higher frequency modes.

If RI isn't applicable, then what? CF and FB explore a theory which goes beyond RI. However, as a matter of convenience, an assumption termed diagonal dominance (DD) has been adopted. DD is equivalent to the assumption that there is no correlation between up- and down-going waves, which further implies the absence of vertical mass flux. Yet we have seen that systematic mass flux does arise in wave fields of small amplitude. It would appear that DD is a hazardous assumption even at small amplitude. The assumption is not essential though, and a theory such as proposed by CF can be evaluated without taking DD.

Let me now return to the vertical mass flux issue since it seems so surprising and, to some, offensive. How can such a flux be sustained even without wave breaking? (Fortran error? I think not. In fact it is a possibility that I suggested in Holloway (1981), with an eye then to controversy.) There are two ways of explanation which are related, though perhaps not apparently so. One approach is to consider two oppositely travelling waves a^+ and a^-. Nonlinear interaction gradually broadens the frequency distribution associated with each wave until the two overlap, as sketched in Fig. 11. Overlapping frequency distributions permit the possibility for cross-correlation a^+a^- which may support mass flux.

A second explanation may be more physically appealing. Consider a large-scale standing wave, exchanging KE and PE by means of oscillatory $\overline{\rho w}$. Let a background spectrum of waves be present, interacting with the standing wave. During the phase when energy accumulates in PE, large-scale density features are generated which are susceptible to deformation-scattering by the background waves, resulting in loss of PE from the standing wave. During the phase of accumulation of KE, large-scale velocity features are generated. However, in 2D such velocity fields resist deformation-scattering because of tendency to conserve vorticity

$$\omega_0 = \sqrt{N^2 \cos^2\phi + f^2 \sin^2\phi}$$

$$\tan\phi = k_z/k_h$$

$\omega = +\omega_0$

$\omega = 0$

$\omega = -\omega_0$
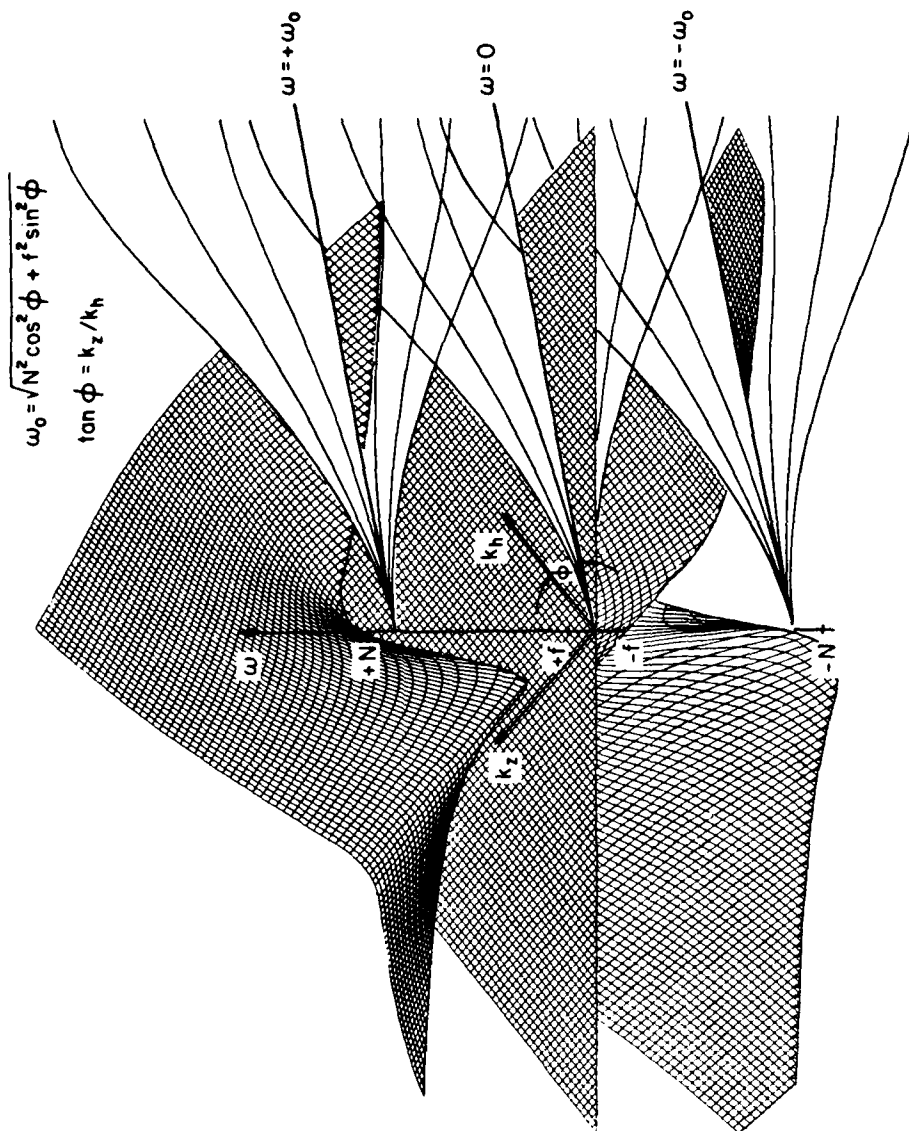
Fig. 11. Solution surfaces for the linear dispersion relation $\omega = \pm\Omega$ and the surface $\omega = 0$ are shown as hatched surfaces in ω, k_x, k_z - space. For a particular aspect ratio $k_z/k_x = \tan\phi$, the natural frequencies $\omega = \pm\omega_0$ and $\omega = 0$ are given by the intersection of the dispersion relations (hatched surfaces) and the plane $k_z/k_x = \tan\phi$. These intersections are straight lines labelled $\omega = +\omega_0$, $\omega = 0$ and $\omega = -\omega_0$. Because of non-linear interactions, energy will be distributed about the natural frequencies. That relative distribution of energy is sketched as fan-like curves, which may be regarded as contours of relative energy density, decreasing away from the natural frequencies. At large wavenumbers, the fans become very broad, with the different branches overlapping. The figure emphasizes the continuous transition from more wavelike dynamics at small wavenumbers to more turbulent dynamics at large wavenumbers (from Holloway, 1983).

variance. Hence the large wave preferentially loses PE,which is
presumably resupplied by external forcing of KE, PE or both. (In most
experiments of SH, large scale forcing was of KE type so the need for
conversion to PE might be considered to be obvious. However, SH did also
supply random forcing at equal rates to PE and to KE with no significant
change in the resulting dynamics.)

Overall energy balance is sketched in Fig. 12. Energy supplied at
low wavenumber either in KE or in KE + PE is dominantly converted to PE
by $\overline{\rho w} > 0$. PE is then efficiently scattered to higher wavenumber where
PE is lost either to direct dissipation or to reconversion by $\overline{\rho w} < 0$
back to KE. This is a noteworthy and curious point: most manifest over-
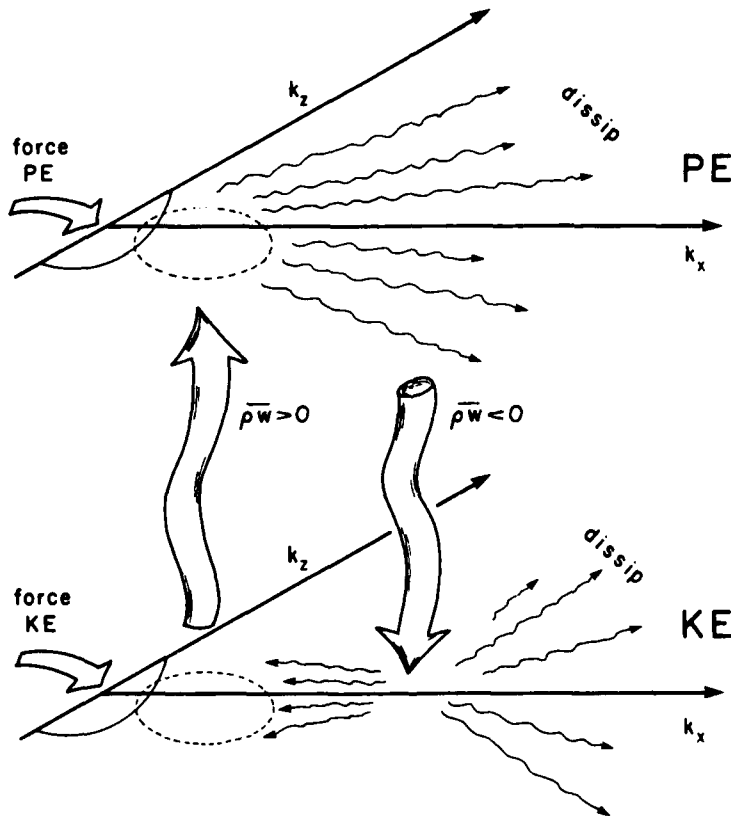
Fig. 12. A sketch depicts the energy balance on two planes, one
representing kinetic energy, the other prepresenting potential energy.
External forcing of KE and, sometimes, of PE apply at low wavenumbers.
KE is converted to PE at low wavenumbers by $\overline{\rho w} > 0$. Then PE is
scattered to higher wavenumbers where some is reconverted to KE by
$\overline{\rho w} < 0$. KE is then distributed to both low and high wavenumbers.

turning may be associated with reconversion $\overline{\rho w} < 0$; i.e. mass falling back. KE acquired by reconversion is transferred simultaneously back to low wavenumber and also to higher wavenumber, thereby conserving vorticity variance. Note that the combination $\overline{\rho w} > 0$ at low wavenumber with $\overline{\rho w} < 0$ at higher wavenumber provides vorticity variance generation for these 2D experiments. Recalling Dr. Briscoe's comment, I'll speculate that if forcing in KE or in KE + PE were moved to intermediate wavenumbers, things would not change greatly. KE supply in 2D must be transferred both to low and high wavenumber. Then KE arriving at low wavenumber can only be disposed by conversion ($\overline{\rho w} > 0$) to PE, thereafter scattering to high wavenumber. Another noteworthy point is that PE finds a direct path to dissipation whereas KE is obliged to follow a more circuitous path to dissipation. Consequently, rates of PE dissipation are higher than rates of KE dissipation.

Let us now address the question of 2D restriction. First, it may be said that solutions in 2D are also solutions in 3D although the solutions, when embedded in 3D, might be unstable and might not be selected by 3D reality. More importantly, vorticity variance generation by direct vortex stretching in 3D would open a direct path for KE transfer to high wavenumber. The rather surprising patterns of $\overline{\rho w} > 0$ and $\overline{\rho w} < 0$ as observed in 2D remain possible in 3D but may be unlikely. My guess, without dynamical support, is that 3D does behave very differently. Elsewhere (Holloway, 1983) I have tried to construct a dynamically consistent account of oceanic internal waves and small-scale processes on the premise that ρw is not energetically important at any scale. Such an account is certainly contrary to SH!

As mentioned previously 2D simulations were really performed for the purpose of theory testing. Here we have found RI failing at very small amplitude. We have also found DD failing at small amplitude. Recall too that we have found frequency spectra from moorings exhibiting characteristic 'bumps' near the buoyancy frequency in an environment which does not support turning levels. The 2D simulations also suggest phenomenology such as overturning accompanying $Ri^{-1} \approx 1$. Rapid increase of dissipation near $Ri^{-1} \approx 1$ is also noteworthy although the quantitative relation is suspect in 2D.

Finally, what next? I believe 2D simulations have an important role left to play in the testing of theoretical approaches beyond RI and DD. There may also be some interesting phenomenology to explore when equation (3) is retained. However, the main thrust of numerical experimentation should, in my opinion, move to fully 3D where present-day computational power makes resolution range up to 30 available.

244

ACKNOWLEDGEMENTS

REFERENCES

BENNEY, D.J. and P.G. SAFFMAN (1966): Nonlinear interactions of random waves in a dispersive medium. Proceedings Royal Society, A289, 301-320.

CAIRNS, J.L. and G.O. WILLIAMS (1976): Internal wave observations from a midwater float. 2. J. Geophys. Res., 81, 1943-1950.

CARNEVALE, G.F. and J.S. FREDERIKSEN (1983): A statistical dynamical theory of strongly nonlinear internal gravity waves. Geophys. Astrophys. Fluid Dyn., 23, 175-207.

DESAUBIES, Y.J.F. (1975): A linear theory of internal wave spectra and coherences near the Väisälä frequency. J. Geophys. Res., 80, 895-899.

DESAUBIES, Y.J.F. (1976): Analytical representations of internal wave spectra. J. Phys. Ocean., 6, 976-981.

DeWITT, R.J. and J. WRIGHT (1982): Self-consistent effective-medium theory of random internal waves. J. Fluid Mech., 115, 283-302.

FJØRTOFT, R. (1953): On the changes in the spectral distribution of kinetic energy for two-dimensional nondivergent flow. Tellus, 5, 225-230.

FREDERIKSEN, J.S. and R.C. BELL (1983): Statistical dynamics of internal gravity waves - turbulence. Geophys. Astrophys. Fluid Dyn., 26, 257-301.

FREDERIKSEN, J.S. and R.C. BELL (1983): Energy and entropy evolution of interacting internal gravity waves and turbulence. Geophys. Astrophys. Fluid Dyn., in press.

GARGETT, A.E., P.J. HENDRICKS, T.B. SANFORD, T.R. OSBORN and A.J. WILLIAMS, III, (1981): A composite spectrum of vertical shear in the upper ocean. J. Phys. Ocean. 11, 1258-1271.

GARRETT, C.J.R. and W.H. Munk (1972): Space-time scales of internal waves. Geophys. Fluid Dyn., 3, 225-264.

246

GARRETT, C.J.R. and W.H. MUNK (1975): Space-time scales of internal waves: a progress report. J. Geophys. Res., 80, 291-297.

GREGG, M.C. (1977): A comparison of fine-structure spectra from the main thermocline. J. Phys. Ocean., 7, 33-40.

HASSELMANN, K. (1962): On the nonlinear energy transfer in a gravity wave spectrum. Part 1. General Theory. J. Fluid Mech., 12, 481.

HASSELMAN, K. (1967): Nonlinear interactions treated by the methods of theoretical physics. Proc. Royal Society, A299, 77-100.

HASSELMAN, K. (1967): A criterion for nonlinear wave stability. J. Fluid Mech. 30, 737-739.

HENYEY, F.S. and N. POMPHREY (1983): Eikonal description of internal wave interactions: a non-diffusive picture of induced diffusion. Dyn. Atmos. Oceans, 7, 189-208.

HOLLOWAY, G. (1979): On the spectral evolution of strongly interacting waves. Geophys. Astrophys. Fluid Dyn., 11, 271-287.

HOLLOWAY, G. (1980): Oceanic internal waves are not weak waves. J. Phys. Ocean., 10, 906-914.

HOLLOWAY, G. (1981): Theoretical approaches to interactions among internal waves, turbulence and finestructure. In Nonlinear Properties of Internal Waves, B.J. West, ed., Amer. Inst. Phys., 79-112.

HOLLOWAY, G. (1982): On interaction time scales of oceanic internal waves. J. Phys. Ocean., 12, 293-296.

HOLLOWAY, G. (1983): A conjecture relating oceanic internal waves and small-scale processes. Atmos.-Ocean, 21, 107-122.

KADOMTSEV, B.B. (1965): Plasma Turbulence. Academic Press, London 149 pp.

KRAICHNAN, R.H. (1967): Inertial ranges in two-dimensional turbulence. Phys. Fluids, 10, 1417-1423.

LESIEUR, M., J. SOMMERIA and G. HOLLOWAY (1981): Zones inertielles du spectre d'un contaminant passif en turbulence bidimensionelle. Comptes-Rendu, II-20.

LILLY, D.K. (1983): Stratified turbulence and the mesoscale variability of the atmosphere. J. Atmos. Sci., in press.

McCOMAS, C.H. (1977): Equilibrium mechanisms within the oceanic internal wave field. J. Phys. Ocean., 7, 836-845.

McCOMAS, C.H. and F.P. BRETHERTON (1977): Resonant interaction of oceanic internal waves. J. Geophys. Res., 83, 1397-1412.

McCOMAS, C.H. and M.G. BRISCOE (1980): Bispectra of internal waves. J. Fluid Mech., 97, 205-213.

McCOMAS, C.H. AND P. MÜLLER (1981): Time scales of resonant interactions among oceanic internal waves. J. Phys. Ocean., 11, 139-147.

McCOMAS, C.H. and P. MÜLLER (1981): The dynamic balance of internal waves. J. Phys. Ocean., 11, 970-986.

MÜLLER, P. and D.J. OLBERS (1975): On the dynamics of internal waves in the deep ocean. J. Geophys. Res., 80, 3848-3860.

MUNK, W.H. (1981): Internal waves and small-scale processes. In Evolution of Physical Oceanography, B.A. Warren and C. Wunsch, ed., MIT Press, 264-291.

OAKEY, N.S. (1982): Determination of the rate of dissipation of turbulent energy from simultaneous temperature and velocity shear microstructure measurements. J. Phys. Ocean., 12, 256-271.

OLBERS, D.J. (1976): Non-linear energy transfer and the energy balance of the internal wave field in the deep ocean. J. Fluid Mech., 74, 375-399.

ORLANSKI, I. and C.P. CERASOLI (1980): Resonant and non-resonant wave-wave interactions for internal gravity waves. Marine Turbulence. J.C.J. Nihoul, ed., Elsevier, Amsterdam, 65-100.

ORLANSKI, I. and C.P. CERASOLI (1981): Energy transfer among internal gravity modes: weak and strong interactions. J. Geophys. Res., 86, 4103-4124.

ORSZAG, S.A. (1971): Numerical simulation of incompressible flows within simple boundaries. I. Galerkin (spectral) representations. Studies in Applied Math., 50, 293-327.

POMPHREY, N., J.D. MEISS and K.M. WATSON (1980): Description of non-linear internal wave interactions by Langevin methods. J. Geophys. Res., 85, 1085-1094.

RILEY, J.J., R.W. METCALFE and M.A. WEISSMAN (1981): Direct numerical simulations of homogeneous turbulence in density-stratified fluids. In Nonlinear Properties of Internal Waves, B.J. West, ed., Amer. Inst. Phys., 79-112.

SHEN, C. and G. HOLLOWAY (1984): A numerical study of the frequency and the energetics of nonlinear internal gravity waves; preprint.

WEISSMAN, M.A., R.W. METCALFE and J.J. RILEY (1981): Non-linear internal wave interactions. Nonlinear Properties of Internal Waves, B.J. West, ed., Amer. Inst. Phys., 253-266.

SMALL-SCALE VORTICAL MOTIONS

Peter Muller

Department of Oceanography and Hawaii Institute of Geophysics
University of Hawaii at Manoa, Honolulu, Hawaii 96822

ABSTRACT

Internal gravity waves do not provide a complete description of an
incompressible one-component fluid. A "vortical" mode must be added which
carries the potential vorticity of the flow. The dynamic balance of the
vortical mode depends on its Rossby number and aspect ratio. At large and
meso scales it represents geostrophic or quasi-geostrophic motion, but it
also exists at small scales. I suggest that oceanic current finestructure
is a manifestation of the vortical mode.

1. INTRODUCTION

An incompressible one-component fluid supports three modes of motion. Two
modes represent internal gravity waves. The third mode represents an
entirely different type of motion with well-defined, distinct dynamics.
Unlike internal gravity waves, this mode carries potential vorticity. It
has been termed "vortical" by Muller et al. (1984) and is the topic of this
note.

The vortical mode of motion is a familiar mode at large and meso scales,
representing geostrophic and quasi-geostrophic flows. It also exists at
small scales. This fact has been overlooked in the past; it was only
recently pointed out by Riley et al. (1981), Holloway (1981, 1983) and
Muller et al. (1984). There are two reasons for this oversight. In the
linear case, the vortical mode has zero frequency (on a f-plane) and was
therefore assumed not to play any role at small scales. Second, all of the
nonlinear calculations (recently reviewed by Muller et al. (1984)) have used
either the resonant interaction approximation (Olbers, 1976; McComas and
Bretherton, 1977; Pomphrey et al., 1980) or direct numerical modelling
(Orlanski and Cerasoli, 1981; Riley et al., 1981; Shen and Holloway, 1984).
The resonant interaction approximation uses a Lagrangian approach. When the
Lagrangian is expanded about an equilibrium state the vortical mode is
eliminated, for reasons discussed by Ripa (1981). Most of the numerical
studies are two-dimensional and simulate the motion on a nonrotating
vertical plane. These simplifications also eliminate the vortical mode of
motion. The only three-dimensional study, to our knowledge, is the one by
Riley et al. (1981). They indeed found the vortical mode in their
simulation and showed the partition of energy between the vortical and
internal gravity mode of motion.

The existence of the vortical mode at small scales has also been realized in meteorology. There, the vortical mode is called "stratified two-dimensional turbulence". The atmospheric mesoscale spectrum is assumed to represent stratified two-dimensional turbulence. The observed slope is roughly consistent with an upscale energy cascading inertial range (Lilly, 1983).

We first discuss the role of the vortical mode in the normal mode analysis of an incompressible one-component fluid. Internal gravity waves do not provide a complete description of an arbitrary motion field. Another mode of motion must be added, which is the vortical mode. In section 3 we show how the vortical mode can be isolated in the fully nonlinear case. Depending on the value of the Rossby number and aspect ratio, we obtain geostrophic, quasi-geostrophic, or stratified 2-D turbulence balances. In section 4 we suggest that current finestructure is a manifestation of the vortical mode at small scales.

2. NORMAL MODE ANALYSIS

We assume that the fluid motion is incompressible. We also neglect all double diffusive effects and regard sea water as a one-component system. To construct a complete set of normal modes we disregard dissipation and forcing mechanisms and linearize the equations of motions. The f-plane equations then take the form

$$\partial_t u - fv + \frac{1}{\rho_0} \partial_x p = 0 \qquad (2.1a)$$

$$\partial_t v + fu + \frac{1}{\rho_0} \partial_y p = 0 \qquad (2.1b)$$

$$\partial_t w + \frac{\rho g}{\rho_0} + \frac{1}{\rho_0} \partial_z p = 0 \qquad (2.1c)$$

$$\partial_t \zeta - w \frac{\rho_0}{g} N^2 = 0 \qquad (2.1d)$$

$$\partial_x u + \partial_y v + \partial_z w = 0 \qquad (2.1e)$$

Here u, v, and w denote the velocity components, ρ and p the deviations from the background density and pressure fields, f the (constant) Coriolis frequency, N the Brunt-Väisälä frequency, ρ_0 a constant reference density and g the gravitational acceleration. The equations contain only three prognostic variables. The three momentum equations are not independent because of the incompressibility constraint (2.1e). Usually, the variables u, v, and ζ are taken as prognostic. The vertical velocity w can then be determined diagnostically from the incompressibility condition. The pressure can be determined from the divergence of the momentum balance which yields

$$(\partial_x\partial_x + \partial_y\partial_y + \partial_z\partial_z)p = \rho_0 f(\partial_x v - \partial_y u) - g\partial_z \rho \qquad (2.2)$$

It is sometimes more convenient to introduce the vertical displacement ζ as

a dependent variable and define the density by

$$\rho(x,t) = \bar\rho(z') - \bar\rho(z) \qquad (2.3)$$

where $\tilde{\rho}(z)$ is the background density and

$$z' = z - \zeta(x,y,z',t) \qquad (2.4)$$

This transformation only changes the character of the nonlinearities. In the linear case the density ρ and the displacement ζ are equivalent and are related by

$$\rho = \frac{\rho_0}{g} N^2 \zeta \qquad (2.5)$$

For simplicity, let us assume a constant Brunt-Väisälä frequency. Solutions to equation (2.1) are then proportional to $\exp\{i(k\cdot x - \omega t)\}$. Non-trivial solutions of the resulting algebraic equations require the determinant to be zero. As there are three prognostic variables the determinant is a cubic polynomial in the frequency ω. The three roots correspond to three independent modes of motion.

Two of the roots give the dispersion relation for internal waves

$$\omega_\pm = \pm \left(\frac{N^2\alpha^2 + f^2\beta^2}{k^2} \right)^{\frac{1}{2}} \qquad (2.6)$$

where the plus sign corresponds to upward and the minus sign to downward propagating waves. Here α, β and k are the moduli of the horizontal, vertical, and total wavenumber, respectively. The third root is

$$\omega_0 = 0 \qquad (2.7)$$

and represents (degenerated) Rossby waves on a f-plane.

The internal wave variables at a given wavenumber are given by

$$(u,v,\zeta) = \left(U_{\underset{\sim}{k}}^{\pm}, V_{\underset{\sim}{k}}^{\pm}, Z_{\underset{\sim}{k}}^{\pm} \right) a_{\underset{\sim}{k}}^{\pm} e^{i(\underset{\sim}{k}\cdot\underset{\sim}{x} - \omega_\pm t)} \qquad (2.8)$$

where

$$\begin{pmatrix} U_{\underset{\sim}{k}}^{\pm} \\\\ V_{\underset{\sim}{k}}^{\pm} \\\\ Z_{\underset{\sim}{k}}^{\pm} \end{pmatrix} = \begin{pmatrix} (\omega_\pm k_x + if k_y)k_z \\\\ (\omega_\pm k_y - if k_x)k_z \\\\ -i\alpha^2 \end{pmatrix} \qquad (2.9)$$

is the polarization vector and $a_{\underset{\sim}{k}}^{\pm}$ the wave amplitude. The dispersion relation (2.6) and the polarization vector (2.9) characterizes linear

internal waves. From (2.9) it follows that the potential vorticity

$$\Pi = \left[\partial_x v - \partial_y u \right] - f\partial_z \zeta \qquad (2.10)$$

vanishes for internal waves

$$\Pi_{\underset{\sim}{k}}^{\pm} = ik_x V_{\underset{\sim}{k}}^{\pm} - ik_y U_{\underset{\sim}{k}}^{\pm} - fik_z Z_{\underset{\sim}{k}}^{\pm} = 0 \tag{2.11}$$

The $\omega_0 = 0$ mode is the mode that carries the potential vorticity of the flow. Its variables at a given wavenumber are

$$(u,v,\zeta) = \left[U_{\underset{\sim}{k}}^{0}, V_{\underset{\sim}{k}}^{0}, Z_{\underset{\sim}{k}}^{0} \right] a_{\underset{\sim}{k}}^{0} e^{i\underset{\sim}{k}\cdot\underset{\sim}{x}} \tag{2.12}$$

with

$$\begin{Bmatrix} U_{\underset{\sim}{k}}^{0} \\ V_{\underset{\sim}{k}}^{0} \\ Z_{\underset{\sim}{k}}^{0} \end{Bmatrix} = \begin{Bmatrix} -k_y \\ k_x \\ -\dfrac{f}{N^2} k_z \end{Bmatrix} \tag{2.13}$$

and its potential vorticity is

$$\Pi_{\underset{\sim}{k}}^{0} = i\left(\alpha^2 + \frac{f^2}{N^2} \beta^2 \right) a_{\underset{\sim}{k}}^{0} \tag{2.14}$$

In the rotating case, $f \neq 0$, this mode is in geostrophic and hydrostatic balance, *satisfies the thermal wind relations* $\frac{f}{N^2}\partial_z u = \partial_y\zeta$ and $\frac{f}{N^2}\partial_z v = -\partial_x\zeta$ and is horizontally non-divergent, $\partial_x u + \partial_y v = 0$. Hence, it is the usual geostrophic mode; however, it also exists in the non-rotating case $f = 0$. In this case the flow is not in geostrophic and hydrostatic balance. The fields ζ and hence ρ and p vanish. The flow consists of steady horizontal vortices with an arbitrary vertical structure. The mode is still the one that carries the potential vorticity of the flow. To include this case, this $\omega_0 = 0$ mode has been termed "vortical".

In the actual nonlinear case, dispersion relations for the internal wave and vortical mode may not exist. In this case we can use the polarization vectors as a convenient definition to distinguish between the two modes.

The three polarization vectors $\left(U_{\underset{\sim}{k}}^{+}, V_{\underset{\sim}{k}}^{+}, Z_{\underset{\sim}{k}}^{+}\right)$, $\left(U_{\underset{\sim}{k}}^{-}, V_{\underset{\sim}{k}}^{-}, Z_{\underset{\sim}{k}}^{-}\right)$ and $\left(U_{\underset{\sim}{k}}^{0}, V_{\underset{\sim}{k}}^{0}, Z_{\underset{\sim}{k}}^{0}\right)$

represent a complete set of basis vectors in the Fourier space of $\{u, v, \zeta\}$. Thus, all observed fields can be uniquely decomposed into a component

along $\left\{U_{\underset{\sim}{k}}^{+}, V_{\underset{\sim}{k}}^{+}, Z_{\underset{\sim}{k}}^{+}\right\}$ and $\left\{U_{\underset{\sim}{k}}^{-}, V_{\underset{\sim}{k}}^{-}, Z_{\underset{\sim}{k}}^{-}\right\}$, the internal gravity component, and

into a component along $\left\{U_{\underset{\sim}{k}}^{0}, V_{\underset{\sim}{k}}^{0}, Z_{\underset{\sim}{k}}^{0}\right\}$, the vortical component. This is a

decomposition into a component that does not carry potential vorticity and one that carries potential vorticity. The geometry of this decomposition is shown in Figure 1 for the nonrotating case. For a given wavenumber $\underset{\sim}{k}$, the Fourier transform $u_{\underset{\sim}{k}}$ of the velocity vector must lie in a plane perpendicular to $\underset{\sim}{k}$, because of the incompressibility condition $\underset{\sim}{k}\cdot u_{\underset{\sim}{k}} = 0$.

The component u_k^v, which lies in the intersection of this plane with the horizontal plane, is the vortical component. The component u_k^i perpendicular to it is the internal gravity component (see also Riley et al. 1981).

If one expands all field variables in terms of the three polarization vectors the equations of motion become equations for the amplitudes. In the (u, v, ρ) representation these amplitude equations take the form

$$\partial_t a_k^s + i\omega_k^s a_k^s = Q^s \qquad s = +,-,0 \qquad (2.15)$$

where the Q's are quadratic interaction terms that describe the self- and cross-interactions of the different modes. The derivation of the Q's is straightforward but tedious. Explicit expression can be found in Shen and Holloway (1982) for the case of two-dimensional fluid motion.
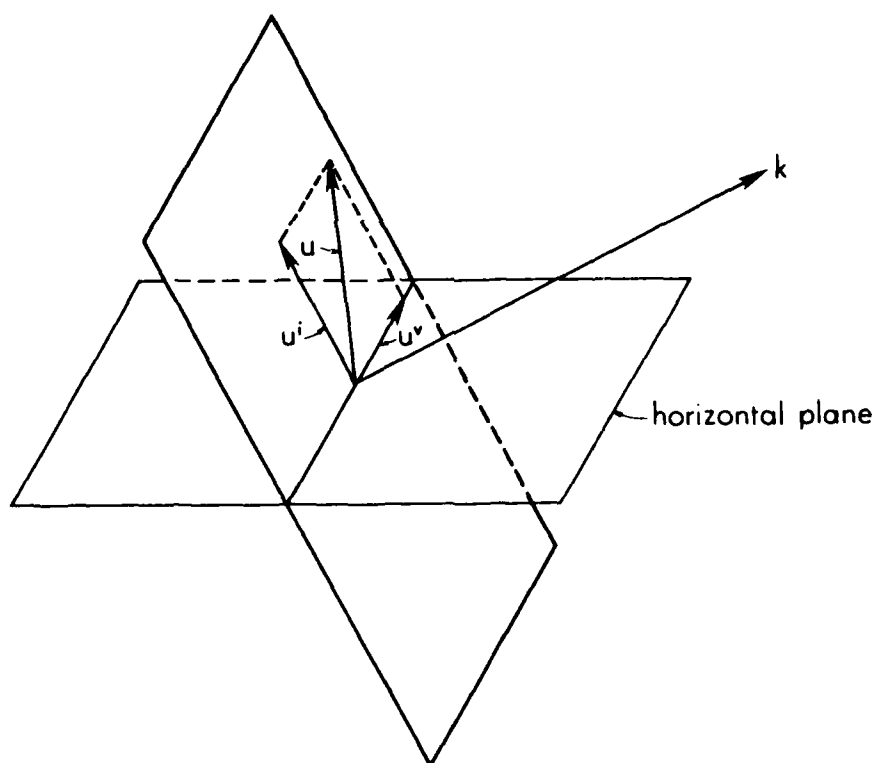
Fig. 1. Decomposition of the velocity vector into its internal gravity and vortical component for the nonrotating case. Because of incompressibility, the vector u must lie in the plane perpendicular to the wavenumber vector k. The vector u can be decomposed into two orthogonal components. The component u^v lies along the intersection of the horizontal and k-plane. This component represents the vortical mode. The component u^i perpendicular to it represents the internal gravity mode.

3. THE VORTICAL MODE

Here we derive approximations to the fully nonlinear equations of motion
that isolate the vortical mode. For an incompressible one-component fluid
the nonlinear equations have the form

$$\partial_t u + u\partial_x u + v\partial_y u + w\partial_z u - fv + \frac{1}{\rho_0}\partial_x p = 0 \tag{3.1a}$$

$$\begin{array}{cccccc}\varepsilon & Ro & Ro & Ro & 1 & r\end{array}$$

$$\partial_t v + u\partial_x v + v\partial_y v + w\partial_z v + fu + \frac{1}{\rho_0}\partial_y p = 0$$

$$\begin{array}{cccccc}\varepsilon & Ro & Ro & Ro & 1 & r\end{array} \tag{3.1b}$$

$$\partial_t w + u\partial_x w + v\partial_y w + w\partial_z w + \frac{\rho g}{\rho_0} + \frac{1}{\rho_0}\partial_z p = 0$$

$$\begin{array}{cccccc}\varepsilon\delta^2 & Ro\delta^2 & Ro\delta^2 & Ro\delta^2 & r/q & r\end{array} \tag{3.1c}$$

$$\partial_t \rho + u\partial_x \rho + v\partial_y \rho + w\partial_z \rho - w\frac{\rho_0}{g}N^2 = 0$$

$$\begin{array}{ccccc}\varepsilon\gamma^2 & Ro\gamma^2 & Ro\gamma^2 & Ro\gamma^2 & q/r\end{array} \tag{3.1d}$$

$$\partial_x u + \partial_y v + \partial_z w = 0$$

$$\begin{array}{ccc}1 & 1 & 1\end{array} \tag{3.1e}$$

The potential vorticity of the flow is defined by

$$\Pi = f\partial_z\tilde\rho + f\partial_z\rho + \omega_z\partial_z\tilde\rho + \omega_i\partial_i\rho \tag{3.2}$$

$$\begin{array}{cccc}q & r\gamma^2 Ro & qRo & r\gamma^2 Ro^2\end{array}$$

where $\omega = \nabla\times u$ is the vorticity and $\tilde\rho = \tilde\rho(z)$ the background density. The
potential vorticity Π is conserved, i.e. $(\partial_t + u\partial_x + v\partial_y + w\partial_z)\Pi = 0$.
If we introduce the vertical displacement ζ, instead of the density ρ,
the potential vorticity Π can be written in the form

$$\rho_0\Pi = \partial_z\tilde\rho(z-\zeta)\tilde\Pi \tag{3.3}$$

where

$$\tilde\Pi = f - f\partial_z\zeta + \omega_z - \omega_i\partial_i\zeta \tag{3.4}$$

$$\begin{array}{cccc}q & r\gamma^2 Ro & qRo & r\gamma^2 Ro^2\end{array}$$

The quantity $\tilde\Pi$ is also referrred to as potential vorticity. It is also
conserved.

We assume that the fluid motion has a typical time scale T, horizontal
length scale L, vertical length scale H, horizontal velocity scale U,
vertical velocity scale $W = \frac{H}{L}U$ (from incompressibility), pressure scale P
and density scale D. The different terms in the equation of motion and
potential vorticity then scale as indicated in (3.1), (3.2), and (3.4). The
dimensionless parameters are $\varepsilon = \frac{T^{-1}}{f}$, $Ro = \frac{U}{fL}$ (Rossby number), $\delta = \frac{H}{L}$
(aspect ratio), $r = \frac{P}{\rho_0 fLU}$, $q = \frac{P}{gHD}$ and $\gamma = \frac{L}{R_i}$ where $R_i = \frac{N}{f}H$ is the

internal Rossby radius of deformation. The ratios r and q compare the pressure force to the Coriolis and buoyancy force, respectively. Other

nondimensional parameters are the Froude number $F = Ro\gamma = \dfrac{U}{NH}$ and the

Richardson number $Ri = F^{-2} = \dfrac{N^2}{U^2} H^2$. Note that the parameter $\gamma = \dfrac{f}{N}\dfrac{L}{H} = \dfrac{f}{N}\dfrac{1}{\delta}$ also compares the aspect ratio to the ratio of Coriolis to Brunt-Vaisala frequency.

We restrict our analysis to flows with small aspect ratios so that we can make the hydrostatic approximation and set q = 1. We also assume that the local time scales are comparable to the advective time scales and set $\varepsilon \sim Ro$. The balance in the horizontal momentum equation is then determined by the Rossby number Ro and the balance in the density equation by the parameter γ or aspect ratio δ. Depending on the values of these two parameters we can distinguish three cases, shown schematically in Figure 2.
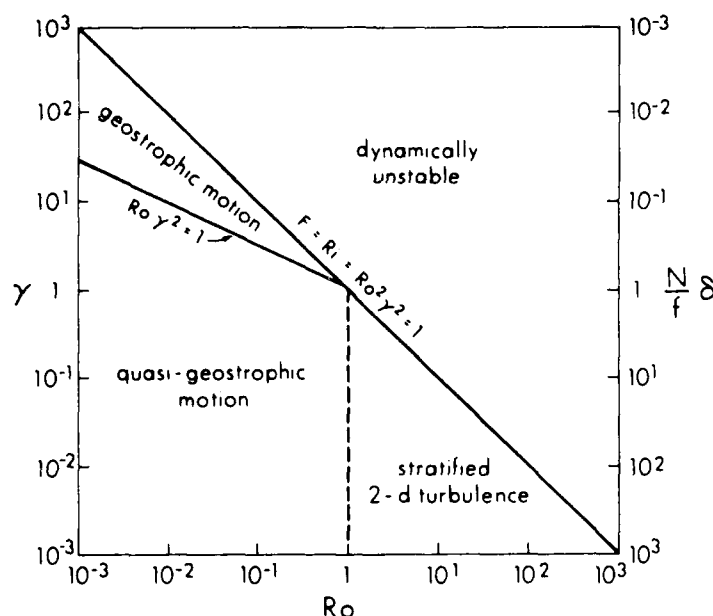
Fig. 2. Schematic diagram showing the dynamic balance of the vortical mode as a function of Rossby number Ro and the

parameters $\cdot = L/R_i$ or $\gamma^{-1} = \dfrac{N}{f}\delta$. The vortical mode has geostrophic

dynamics for Ro $\ll$ 1 and Ro $\cdot$ $\sim$ 1, quasi-geostrophic dynamics for Ro $\ll$ 1 and Ro $\cdot$ $\ll$ 1, and stratified 2-D turbulence dynamics for Ro $\gg$ 1 and $Ro^2\gamma^2 \ll$ 1. For Ri $\ll$ 1 the flow is dynamically unstable.

Geostrophic motions

Consider motions with a small Rossby number, Ro << 1. The horizontal momentum balance then reduces to the geostrophic balance (r = 1). If the horizontal length scale L is much larger than the internal Rossby radius of deformation, i.e. if $\gamma^2 \gg Ro^{-1}$, the gradients of the density fluctuations are much larger than the gradients of the background density. For these motions the equtions (3.1) reduce to the geostrophic equations on a f-plane.

$$-fv + \frac{1}{\rho_0} \partial_x p = 0 \qquad (3.5a)$$

$$fu + \frac{1}{\rho_0} \partial_y p = 0 \qquad (3.5b)$$

and

$$\rho g + \partial_z p = 0 \qquad (3.5c)$$

$$\left\{ \partial_t + u\partial_x + v\partial_y + w\partial_z \right\}\rho = 0 \qquad (3.5d)$$

$$\partial_x u + \partial_y v + \partial_z w = 0 \qquad (3.5e)$$

On planetary scales these equations are used to describe the thermohaline circulation. The equations contain only one prognostic equation, the density equation (3.5d). The pressure can be determined from the hydrostatic balance, the horizontal velocity from the geostrophic balance, and the vertical velocity from the incompressibility condition. The density equation can be rewritten as

$$\left\{ \partial_t + u\partial_x + v\partial_y + w\partial_z \right\}\Pi_\ell = 0 \qquad (3.6)$$

where

$$\Pi_\ell = f \cdot \partial_z \qquad (3.7)$$

In this form the conserved quantity Π_ℓ is the Ro << 1 , $Ro\gamma^2 \gg 1$ limit of the potential vorticity (3.2). The equations (3.5) hence represent the vortical mode of motion.

Quasi-geostrophic motion

Consider motions Ro 1 with . These motions have horizontal length scales comparable to the internal Rossby radius of deformation. In this case the density equation (3.1d) implies w = 0. The equations of motion become degenerate. They determine u, v, w, and ρ in terms of the pressure but do not provide an evolution equation for the pressure. The evolution of the pressure is determined by higher order ageostrophic terms and can be obtained by a systematic perturbation expansion of (3.1) in ε and Ro (Pedlosky, 1979). The resulting equations are the quasi-geostrophic

equations on a f-plane. The prognostic equation has the form

$$\left\{ \partial_t + u\partial_x + v\partial_y \right\} \Pi_m = 0 \tag{3.8}$$

where

$$\Pi_m = (\partial_x \partial_x + \partial_y \partial_y)\psi + \partial_z \frac{f^2}{N^2} \partial_z \psi \tag{3.9}$$

Here ψ is the streamfunction. The diagnostic equations

$$u = -\partial_y \psi \tag{3.10a}$$

$$v = \partial_x \psi \tag{3.10b}$$

$$w = -\frac{f}{N^2}(\partial_t + u\partial_x + v\partial_y)\partial_z \psi \tag{3.10c}$$

$$\rho = -\frac{\rho_0 f}{g} \partial_z \psi \tag{3.10d}$$

$$p = \rho_0 f \psi \tag{3.10e}$$

determine the field variables in terms of the streamfunction.

The quantity Π_m can also be written as

$$\Pi_m = \partial_x v - \partial_y u - f\partial_z \zeta \tag{3.11}$$

and is the $Ro \ll 1, \gamma^2 \ll Ro^{-1}$ limit of the potential vorticity $\tilde{\Pi}$, except for the irrelevant constant (on a f-plane) planetary contribution f. The quasi-geostrophic equations (3.8) and (3.10) hence represent vortical motion.

Stratified two-dimensional turbulence

Consider motions with large Rossby numbers $Ro \gg 1$, which implies $r = Ro$. If these motions have horizontal length scales such that $\gamma^2 \ll Ro^{-2}$ (or equivalently $F \ll 1$ or $Ri \gg 1$) the equations (3.1) reduce to (Riley et al., 1981; Lilly, 1983)

$$\partial_t u + u\partial_x u + v\partial_y u - fv + \frac{1}{\rho_0} \partial_x p = 0 \tag{3.12a}$$

$$\partial_t v + u\partial_x v + v\partial_y v + fu + \frac{1}{\rho_0} \partial_y p = 0 \tag{3.12b}$$

$$\rho g + \partial_z p = 0 \tag{3.12c}$$

$$w = 0 \tag{3.12d}$$

$$\partial_x u + \partial_y v = 0 \tag{3.12e}$$

and describe a flow called stratified two-dimensional turbulence by Lilly (1983).

The two horizontal momentum equations are not independent because of the incompressibility constraint (3.12e). Taking the divergence and curl of

(3.12a) and (2.12b) we can replace these two equations by

$$\left[\partial_x\partial_x + \partial_y\partial_y\right]p = \rho_0 f_0\left[\partial_x v - \partial_y u\right] \tag{3.13}$$

$$- \partial_x u\partial_x u - \partial_x v\partial_y u - \partial_y u\partial_x v - \partial_y v\partial_y v$$

and

$$\left[\partial_t + u\partial_x + v\partial_y\right]\Pi_s = 0 \tag{3.14}$$

where

$$\Pi_s = \left[\partial_x v - \partial_y u\right] \tag{3.15}$$

The quantity Π_s is the Ro $\gg 1$ limit of the potential vorticity Π for $w = 0$. Hence, the equations (3.12) describe the vortical mode of motion. In this limit the vortical mode of motion has the following properties:

(i) The local and advective time scales are smaller than the Coriolis period and thus comparable to internal wave periods.

(ii) The horizontal scales are much smaller than the internal Rossby radius of deformation. The aspect ratio is small.

(iii) The vertical velocity vanishes (to lowest order). The horizontal velocity field is nondivergent. The flow field hence consists of two dimensional vortices.

(iv) The horizontal momentum balance is not geostrophic. The basic balance occurs between the pressure and the nonlinear advection term. If the nonlinear terms are neglected, the frequency of the vortical mode vanishes (Section 2). The pressure is a nonlinear function of the horizontal velocity field (see 3.13). Rotation does not significantly affect the momentum balance. Small-scale vortical motions behave the same both with and without rotation.

(v) The time evolution is governed by equation (3.14), the conservation of potential vorticity. Since the flow is horizontally nondivergent we can introduce a streamfunction ψ such that $u = -\partial_y\psi$ and $v = \partial_x\psi$ and rewrite (3.14)

$$\left[\partial_t + u\partial_x + v\partial_y\right]\left[\partial_x\partial_x + \partial_y\partial_y\right]\psi = 0 \tag{4.13}$$

This equation is the evolution equation for two-dimensional turbulence. It applies to every horizontal plane separately. The motion hence represents stacked or layered two-dimensional turbulence. The turbulence in each horizontal plane is independent from the turbulence in the other planes. The pressure and density field, which are dynamically passive, adjust to the velocity field and can be calculated from the diagnostic relation (3.13) and (3.12c).

4. CURRENT FINESTRUCTURE

Vortical motion is known to exist at large and meso scales, representing geostrophic and quasi-geostrophic flows. The vortical mode must also be expected to be excited at small scales, thoroughly intertwined with the internal gravity mode. To decompose the observed fluctuations into its internal wave and vortical component we need to measure potential vorticity, an extremely difficult measurement. One major attempt to perform the decomposition into internal wave and vortical motion was Muller et al.'s (1978) analysis of the three legged IWEX mooring. Using consistency tests and a least square fit to a total of 1444 cross spectra, they determined the amount of energy in the internal wave field and in various "contaminations". Their result is shown in Figure 3. The part denoted internal waves is that energy consistent with free, linear, internal wave motions on a smooth background profile. The contaminations consist of a finestructure contamination of the displacement field and a finestructure and noise contamination of the current field. The current finestructure contamination is a substantial part of the observed fluctuations. It represents about 15% of the horizontal kinetic energy. The IWEX array did not have enough resolution to allow determination of the complete kinematical structure of the contaminations. The current and temperature finestructure contaminations are viewed as being due to the vertical advections of passive finestructure past the sensors by mainly high-frequency internal waves (e.g. Phillips, 1971; Garrett and Munk, 1971). The advected finestructure is a two-dimensional field and has vertical coherence scales smaller than 10 m and horizontal coherence scales larger than a few hundred meters. The question then becomes: what is this finestructure that is being advected?

Temperature finestructure is generally assumed to be part of the irreversible background stratification. It is the result of past mixing events that occur randomly in space and time and persist for times longer than internal wave periods. The low-gradient regions are the sites of mixing events. The high-gradient regions are the boundaries between mixing events. In its purest form this model becomes the sheet and layer model (Woods, 1968) but, as shown by Desaubies and Gregg (1981), mixing events are rarely complete and produce only minor modifications of the stratifiction.

Current finestructure is assumed to carry most of the vertical shear and to be the major contributor to the order one Richardson number (Gargett et al. 1981). No consistent model exits for current finestructure. Garrett and Munk (1971) view current finestructure as a manifestiation of long internal waves whose horizontal velocity field contains finestructure because of the finestructure in the background stratification. Their arguments lead to a relative current finestructure contamination which is equal to the relative temperature finestructure contamination. This is inconsistent with observations which show that there is more current than temperature finestructure contamination (see Figure 3). Muller (1984) argues that internal waves on a rugged background stratification should show less current than temperature finestructure contamination, even more inconsistent with the observations. As a possible way out of this dilemma we offer that current finestructure is a manifestation of the vortical mode.
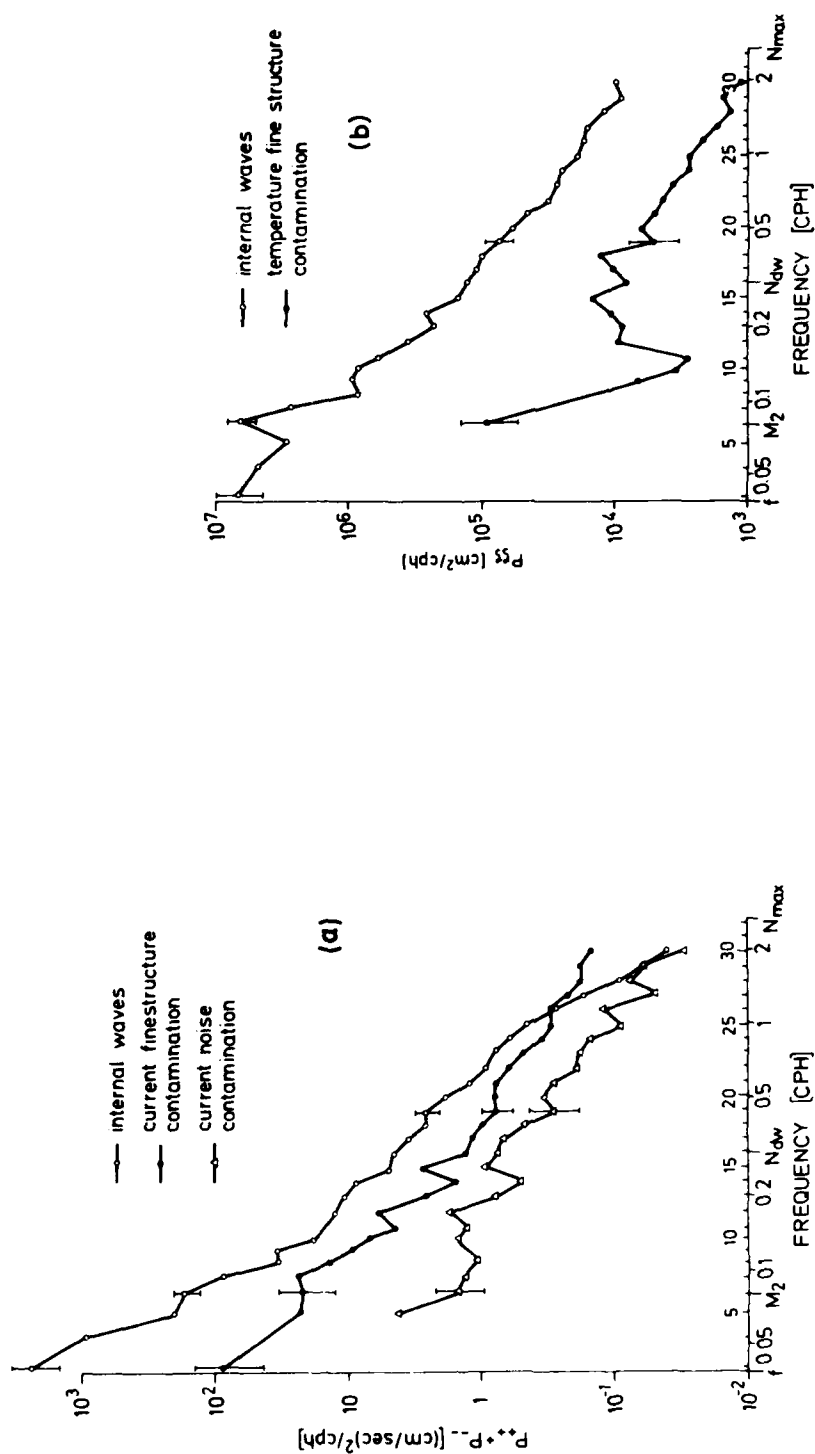
Fig. 3. Partition of the observed horizontal current and vertical displacement spectrum into internal waves, current and temperature finestructure, and current noise (from Muller et al. 1978).

At the IWEX site $N = 5 \times 10^{-3}$ s^{-1} and $f = 7 \times 10^{-5}$ s^{-1}, hence $\frac{f}{N} = 1.4 \times 10^{-2}$. The IWEX analysis indicates $U \simeq 2$ cm s^{-1}, $H \leq 10$ m and $L \geq 300$ m for current finestructure. If we further assume $Ri = \frac{N^2}{U^2} H^2 = 1$, i.e. that all shear resides in the current finestructure, we find $Ro \leq 1$ and $\gamma \geq 1$ and it is not clear which specific dynamic balance might apply to current finestructure. To test the conjecture that current finestructure represents vortical motion and to determine its specfic dynamic balance we need to develop techniques to measure potential vorticity on small scales.

5. SUMMARY AND CONCLUSIONS

Internal gravity waves do not provide a complete description of an arbitrary flow field. There exists another mode of motion that carries the potential vorticity of the flow. At large and mesoscales this vortical motion represents geostrophic and quasi-geostrophic flows. The vortical mode also exists at scales traditionally associated with internal waves. Its specific dynamic balance depends on its Rossby number and aspect ratio.

The implication of the existence of the vortical mode have not yet been explored. The vortical mode must be excited at all scales, thoroughly intertwined with the internal gravity mode. At each scale we need to sort out how much of the observed variability is internal gravity and how much is vortical motion. This requires the measurement of potential vorticity on small scales which is not possible yet. The vortical mode must also be expected to interact with the internal gravity mode. We must include this cross-interaction into our nonlinear interaction calculations in order to sort out how much the internal gravity and vortical mode contribute to the overall energy and enstrophy cascade and to mixing in the ocean.

REFERENCES

Desaubies, Y. J. F. and M . G. Gregg: 1981. Reversible and irreversible finestructure. J. Phys. Oceanogr., 11, 541-566.

Gargett, A. E., T. J. Hendricks, T. B. Sanford, T. R. Osborne and A. J. Williams III: 1981. A composite spectrum of vertical shear in the upper ocean. J. Phys. Oceanogr., 11, 1258-1271.

Garrett, C. J. R. and W. H. Munk: 1971. Internal wave spectra in the presence of finestructure. J. Phys. Oceanogr., 1, 196-202.

Holloway, G.: 1981. Theories of statistical balance among internal waves. In: Nonlinear Properties of Internal Waves, B. West (Ed.), American Institute of Physics Conference Proceedings, 76, 47-77.

Holloway, G.: 1983. A conjecture relating oceanic internal waves and small-scale processes. Atmosphere-Ocean, 21, 107-122.

Lilly, D. K.: 1983. Stratified turbulence and the mesoscale variability of the atmosphere. J. Atmos. Sci., 40, 749-761.

McComas, C. H. and F. P. Bretherton: 1977. Resonant interaction of oceanic internal waves. J. Geophys. Res., 82, 1397-1412.

Muller, P.: 1984. On current finestructure and vortical motions. (submitted to J. Phys. Oceanogr.).

Muller, P., D. J. Olbers and J. Willebrand: 1978. The IWEX Spectrum, J. Geophys. Res., 83, 479-500.

Muller, P., G. Holloway, F. Henyey, and N. Pomphrey: 1984. Nonlinear interations among internal gravity waves (to be submitted to Rev. Geophys. Space Phys.)

Olbers, D. J.: 1976. Nonlinear energy transfer and the energy balance of the internal wave field in the deep ocean. J. Fluid Mech., 74, 375-399.

Orlanski, I. and C. P. Cerasoli: 1981. Energy transfer among internal gravity modes: Weak and strong interactions. J. Geophys. Res., 86, 4103-4124.

Pedlosky, J.: 1979. Geophysical Fluid Dynamics. Springer Verlag, Berlin and New York.

Phillips, O. M.: 1971. On spectra measured in an undulating layered medium. J. Phys. Oceanogr., 1, 1-6.

Pomphrey, N., J. D. Meiss and K. M. Watson: 1980. Description of nonlinear internal wave interactions using Langevin methods. J. Geophys. Res., 85, 1085-1094.

Riley, J. J., R. W. Metcalfe and M. A. Weissman: 1981. Direct numerical simulations of homogeneous turbulence in density-stratified fluids. In: Nonlinear Properties of Internal Waves, B. J. West (Ed.), American Institute of Physics Conference Proceedings, 76, 79-112.

Ripa, P.: 1981. Symmetries and conservation laws for internal gravity waves. In: Nonlinear Properties of Internal Waves, B. J. West (Ed.), American Institute of Physics Conference Proceedings, 76, 281-306.

Shen, C. and G. Holloway: 1982. Spectral formulation of internal wave interaction. Technical Report No. 392, School of Oceanography, University of Washington.

Shen, C. and G. Holloway: 1984. A numerical study of the frequency and the energetics of nonlinear internal gravity waves (in press, J. Geophys. Res.).

Woods, J. D.: 1968. Wave induced shear instability in the summer thermocline. J. Fluid Mech., 32, 791-800.

STABILITY OF INVISCID STRATIFIED FLOWS UNDER NONLINEAR PERTURBATIONS

Henry D. I. Abarbanel

University of California, San Diego
Marine Physical Laboratory of the
Scripps Institution of Oceanography
La Jolla, California 92093

ABSTRACT

A method developed by V. I. Arnol'd for investigating the stability of inviscid flows under nonlinear deformations is applied to stratified flows in two and three dimensions with and without rotations. The method is discussed in some detail for the example of Arnol'd: two dimensional homogeneous incompressible flow and contrasted with the usual Rayleigh equations arising from linear stability theory.

In the study of stratified flows we find that any flow in a two dimensional stratified fluid is unstable to finite perturbations unless the mean flow vanishes and the buoyancy frequency is positive, i.e., usual internal waves are allowed. In usual language this means that only flows with infinite Richardson number are stable. In three dimensions with and without rotations stable flows can arise, and necessary and sufficient conditions are given for this situation.

INTRODUCTION

The stability of stratified fluid flow is an issue of central importance in the study of internal gravity waves. Internal waves, after all, are excitations of a fluid in the presence of a background stratification $\rho_e(\vec{x})$ and background flow $\vec{u}_e(\vec{x})$. ($\vec{x} = (x,y,z)$ and $\vec{u} = (u,v,w)$; the e stands for equilibrium or steady state.) The usual method for study of these excitations is to presume a ρ_e and $\vec{u}_e$ and then seek solutions for the full density field $\rho_e + \rho(\vec{x},t)$ and velocity field $\vec{u}_e + \vec{u}(\vec{x},t)$ by linearizing the equations of motions in ρ and $\vec{u}$. [Useful references for the conventional approach are Phillips (1977) and Drazin and Reid (1982).] The stability of these linear, and therefore infinitesimal, motions can roughly be characterized by a Richardson number:

$$Ri = N^2/(\partial u/\partial z)^2, \tag{1}$$

where N^2 is the buoyancy frequency and $\partial u/\partial z$ is the vertical shear of the background current in the x direction. A criterion for stability, by now widely accepted, is that Ri should exceed $\frac{1}{4}$ (Drazin and Reid, 1982; Chandrasekhar, 1961). Indeed, there is persuasive observational evidence (Erickson, 1978) that this rule holds in oceanic motions.

This paper is a summary of work done in collaboration with D. Holm, J. Marsden, and T. Ratiu on the extension of the conventional linear stability analysis to the study of finite motions of an inviscid stratified fluid around a given $\rho_e(\vec{x})$, $\vec{u}_e(\vec{x})$. We will, in this note, report only on work considering incompressible flow of such a fluid under the Boussinesq-Overbeck approximation. The latter restrictions can be lifted (see Abarbanel et al. (1984) -- to be referred to as AHMR subsequently), but to date the method is restricted to the stability of finite perturbations around the time-independent states of inviscid fluids. Good ideas are needed to extend the present theory to viscous and time-dependent flows.

We begin this report by describing the method, due to V. I. Arnol'd (1965, 1969) and others (see AHMR for references), using the example of two-dimensional homogeneous incompressible fluids analyzed by Arnol'd. After explaining the technique we contrast the result to the linear stability analysis first done in Rayleigh (1880).

With the method in hand we turn to stratified flows in two and three dimensions with and without rotations. Our key result here is that in two dimensions stratified flows are not nonlinearly stable unless the background flow is constant, which by the Galilean invariance of the theory is equivalent to $\vec{u}_c = 0$. In three dimensions nonlinearly stable flows are possible, and we give the necessary and sufficient conditions under which that stability is possible.

In using the Arnol'd method there are certain technical issues connected with the precise meaning of stability and with the fact that for the evolution of fluids an infinite number of degrees of freedom are involved. These issues are addressed in the appendix (and in AHMR) so as not to interrupt the pedagogical purposes of this contribution to the 'Aha Huliko'a Workshop.

Two final notes of some importance before proceeding with the technical details:

(1) Linear stability theory is most persuasive and useful in telling when a given flow is unstable. If a certain setup is unstable to infinitesimal perturbations, it is certainly unstable. If, however, a flow is stable to infinitesimal perturbations, it could well still be unstable to finite perturbations.

The method described here is in some sense complimentary. Within the environment of the technical issues in the appendix having primarily to do with our knowledge (or ignorance) of the global equilibria of a flow, if a setup is stable to finite perturbations, it is certainly stable.

In between these possibilities lies a very intriguing middle ground: flows that are nonlinearly unstable and linearly stable! Suitable conjectures for the dynamics gourmet are made in AHMR and later in this article.

(2) In the method of infinitesimal perturbations or linear stability theory one examines in detail a linear partial differential equation to determine the sign of a certain eigenvalue which governs the temporal growth of the perturbation.

The method described here eventually ends up with the same task but with a different interpretation of the eigenvalue and with a different differential equation. So the issue of nonlinear stability is found to revolve around the analysis of a linear problem.

THE METHOD AND AN EXAMPLE TO ILLUSTRATE IT

The method put forward by Arnol'd (1965, 1969) and others (see AHMR for references) replaces the equations of motion method of linear stability analysis by turning attention to a variational principle which extremizes the energy subject to the constraints imposed by the conserved quantities for the flow. In effect, one constructs a Liapunov functional (Guckenheimer and Holmes, 1983) for the system. Since we restrict our attention to inviscid fluids, the system is Hamiltonian (see AHMR for details) and the energy is a natural Liapunov functional. Since there are conserved quantities, the flow on the energy surface of the Hamiltonian system is restricted to lie on orbits preserving these quantities. It is natural then to seek extrema of the energy subject to the conservation laws.

Flesh appears on these bare bones when we consider our illustrative example of inviscid, incompressible, homogeneous flow in two spatial dimensions. Choosing the density to be unity, since it plays no role here, we are invited to investigate the solutions of the Euler equation

$$\frac{\partial}{\partial t} u(x,t) + u \cdot \nabla u(x,t) = -\nabla p \tag{2}$$

along with

$$div \ u(x,t) = 0. \tag{3}$$

Here we imagine a co-ordinate system $x = (x, y)$ and a two-vector flow $u(x,t) = (u(y,t), v(x,t))$. Since u is solenoidal, only one component is independent, and we express this in the usual way by introducing the stream function

$$u(x,t) = (-\partial_y \psi(x,t), \partial_x \psi(y,t)), \tag{4}$$

and by curling the Euler equation we find the familiar

$$\frac{\partial}{\partial t} \omega(x,t) + \left\{ \psi(x,t), \omega(x,t) \right\} = 0 \tag{5}$$

where the z vorticity $\omega(x,t)$ is

$$\omega(x,t) = \nabla^2 \psi(x,t) \tag{6}$$

and the Poisson bracket $\left\{ A, B \right\}$ is

$$\left\{ A, B \right\} = \partial_x A \partial_y B - \partial_y A \partial_x B. \tag{7}$$

As a useful sidenote here we remark that this equation for w is precisely the Liouville equation for the phase space density $F(p,q,t)$ with Hamiltonian $\psi(x,y,t)$ and canonical co-ordinates $(x=p, y=q)$. The canonical equations are

$$\dot{x} = u = -\partial_y \psi \tag{8}$$

and

$$\dot{y} = v = \partial_x \psi.$$

If this helps the reader, it should give some substance to the more abstract remarks about Hamiltonia made above.

A consequence of the evolution equation for $\omega(xt)$ is the conservation of

$$\int d^2x \ G(\omega(x,t)) \tag{9}$$

for an arbitrary function $G(\omega)$. This is demonstrated directly by

$$\frac{\partial}{\partial t} \int d^2x \ G(\omega) = \int d^2x \ \frac{\partial \omega}{\partial t} G'(\omega) \tag{10}$$

$$= \int d^2x \left\{ \omega, \psi \right\} G'(\omega) \tag{11}$$

$$= \int d^2x \left(\partial_x \omega \ \partial_y \psi - \partial_y \omega \ \partial_x \psi \right) G'(\omega) \tag{12}$$

$$= \int d^2x \left(\partial_x G(\omega) \partial_y \psi - \partial_y G(\omega) \partial_x \psi \right) \tag{13}$$

$$= \int dy \ G(\omega) \partial_y \psi \Big|_{\substack{surface \ at \\ fixed \ x}} - \int dx \ G(\omega) \partial_x \psi \Big|_{\substack{surface \ at \\ fixed \ y}} \tag{14}$$

Since the x velocity $(-\partial_y \psi)$ must vanish at a surface of fixed x and the y velocity $(\partial_x \psi)$ must vanish at a surface of fixed y, the right-hand side of eq. (14) vanishes.

266

Now we examine the extrema of the energy:

$$\int d^2x \; \tfrac{1}{2}(u)^2 = \int d^2x \, \tfrac{1}{2}(\nabla\psi)^2 = -\tfrac{1}{2}\int d^2x \; \omega \frac{1}{\nabla^2}\omega \tag{15}$$

constrained by the constancy of eq. (9). Form the functional

$$A(\omega) = \int d^2x \left[-\tfrac{1}{2}\omega \frac{1}{\nabla^2}\omega + G(\omega) \right] \tag{16}$$

and vary it with respect to ω. The first variation must vanish at an equilibrium solution $\omega_e(x)$:

$$\delta A(\omega)\big|_{\omega_e} = \int d^2x \; \delta\omega(x) \left[-\frac{1}{\delta^2}\omega_e(x) + G'(\omega_e) \right] = 0, \tag{17}$$

which identified $G'(\omega_e)$ as the stream function ψ_e and is really no more than the information that for a time-independent flow we must satisfy

$$\left\{ \omega_e, \psi_e \right\} = 0, \tag{18}$$

which is done by ψ_e, an arbitrary function of ω_e.

The second variation of $A(\omega)$ around ω_e must be of a definite sign for all possible variations $\delta\omega$. If it were positive for some $\delta\omega$ and negative for others, then ω_e would be a saddle point in the infinite dimensional $(\omega(x))$ space and ω_e would not be stable. (The subtleties of stability are taken up in the Appendix.) So we now examine

$$\delta^2 A(\omega)\big|_{\omega_e} = \int d^2x \; \delta\omega(x) \left[-\frac{1}{\nabla^2} + G''(\omega_e) \right] \delta\omega(x). \tag{19}$$

Since the operator $-\dfrac{1}{\nabla^2}$ is positive, a SUFFICIENT condition for stability is:

$$G''(\omega_e) > 0. \tag{20}$$

However, if $G''(\omega_e)$ is negative, the operator $\dfrac{-1}{\nabla^2}$ may be bounded enough that $\delta^2 A$ remains positive. This may not seem so cryptic a comment if one recalls the meaning of $\dfrac{-1}{\nabla^2}$ as an operator on any function $f(x)$:

$$-\frac{1}{\nabla^2} f(x) = \int \frac{d^2k}{(2\pi)^2} \, e^{ik\cdot x} \frac{1}{k^2} \, f(k), \tag{21}$$

where $f(k)$ is the two-dimensional Fourier transform of $f(x)$. If the wavenumbers k have a minimum size so that k^2 is bounded, then a negative $G''(\omega_e)$ in eq. (19) may result in a negative definite $\delta^2 A(\omega_e)$.

The more precise statement of the condition to be met is to remark that the total operator

$$M = -\frac{1}{\nabla^2} + G''(\omega_e(x)) \tag{22}$$

must be strictly positive or strictly negative. This is realized by requiring that the eigenvalues of M be either all positive or all negative. Suppose those eigenvalues are called λ and the eigenfunctions called $\phi_\lambda(x)$:

$$M\psi_\lambda(x) = \lambda\psi_\lambda(x), \tag{23}$$

then writing

$$\delta w(\omega) = \sum_{\lambda} a_{\lambda} \psi_{\lambda}(x) \tag{24}$$

and assuming an orthonormality relation between $\psi_{\lambda}(x)$ and $\psi_{\lambda}(x)$, the expression for $\delta^2 A(\omega_c)$ is

$$\delta^2 A(\omega_c) = \sum_{\lambda} \lambda (a_{\lambda})^2. \tag{25}$$

This makes explicit the statement about the sign of the eigenvalues.

If we now write the eigenfunctions $\psi_{\lambda}(x)$ as $\nabla^2 X_{\lambda}(x)$ to raise the $-\dfrac{1}{\nabla^2}$ from integral to differential operator status, we arrive at the study of the eigenvalue equation

$$\left[G''(\omega_c(x)) - \lambda \right] \nabla^2 X_{\lambda}(x) - X_{\lambda}(x) = 0. \tag{26}$$

With appropriate boundary conditions, this linear equation determines the nonlinear stability of the flow $\omega_c(x)$.

As an example of this exercise suppose the flow is a shear flow $U(y)$ in the x direction. We have

$$w_c(x,y) = -U'(y)$$

and

$$\frac{d}{d\omega_c} G'(\omega_c) = \frac{dy}{d\omega_c} \frac{d\psi_c}{dy} = U(y)/U''(y). \tag{27}$$

Our SUFFICIENT condition tells us that if

$$U''(y)/U(y) > 0, \tag{28}$$

this shear flow is nonlinearly stable. This adds a nice touch to the classical result, Rayleigh (1880), for two-dimensional shear flow.

When $U''(y)/U(y)$ is negative, we must find out when all λ satisfying

$$\left[U(y) - \lambda U''(y) \right] \left[\frac{d^2}{dy^2} - k^2 \right] X_{\lambda}(k,y) - U''(y) X_{\lambda}(k,y) = 0 \tag{29}$$

are negative. A Fourier transform in x with x wave number k has been performed here. This last result is to be compared to the classical Rayleigh equation (Drazin and Reid, 1982, p. 130).

$$(U(y)-c) \left[\frac{d^2}{dy^2} - k^2 \right] \Psi(y) - U''(y)\Psi(y) = 0, \tag{30}$$

which, again with appropriate boundary conditions on the perturbation stream function $\Psi(y)$, is to be solved for the perturbation phase velocity c. When $\text{Im} c > 0$, the flow $U(y)$ is unstable.

Though eqs. (29) and (30) look similar and pose mathematical challenges of a similar nature, their interpretation and the meaning of the eigenvalues (λ or c, respectively) are quite different. As noted in the Introduction, however, both are linear eigenvalue problems.

To close this "review" section we consider an example of $G''(\omega_c) < 0$, again lifting shamelessly from Arnol'd (1965). We take the same shear flow $u = (U(y),0)$ and allow the flow to live in a channel $0 \leqslant y \leqslant Y$. The positive quantity

$$\int d^2x \, \delta\omega(x) \frac{-1}{\nabla^2} \delta\omega(x) \tag{31}$$

appearing in $\delta^2 A$ is expressible in Fourier space as:

$$\int \frac{d^2k}{(2\pi)^2} \delta\omega(k) \frac{1}{k^2} \delta\omega(k). \tag{32}$$

The minimum value which can be achieved by $k^2 = k_x^2 + k_y^2$ is realized when $k_x = 0$ (as there are no boundaries in x) and $k_y = \pm \frac{\pi}{Y}$. This means

$$\frac{1}{k^2} < \frac{Y^2}{\pi^2} \tag{33}$$

and

$$\delta^2 A < \int d^2x \; \frac{Y^2}{\pi^2} \; (\delta\omega(x))^2 - \int d^2x \; (\delta\omega(x))^2 |G''(w_c)|. \tag{34}$$

$\delta^2 A$ is certainly negative if for all y:

$$\left| \frac{U(y)}{U''(y)} \right| > \frac{Y^2}{\pi^2}.$$

A 1927 example from Tollmein where $U(y) = U_o \sin ay$, so $U''/U = -a^2$ is recounted by Arnol'd.

The variational method clearly incorporates classical results such as the Rayleigh inflection point theorem and includes much beyond.

Now we depart from this example which I hope was indeed illustrative, and turn to stratified flows which, after all, are the subject of the present gathering.

TWO-DIMENSIONAL STRATIFIED FLOWS

With no need for lengthy explanation in this audience we consider incompressible flow of a stratified fluid in the Boussinesq approximation. We have the Euler equation:

$$\frac{\partial}{\partial t} u(x,t) + u \cdot \nabla u(x,t) = - \nabla p - \rho g z \tag{35}$$

and the mass conservation equation:

$$\frac{\partial}{\partial t} \rho(x,t) + u \cdot \nabla \rho(x,t) = 0 \tag{36}$$

to satisfy where we have set the background density $\rho_o = 1$. The coordinates $x = (x, z)$, and because $div\ u = 0$ we introduce the stream function $\psi(x, z, t)$ such that

$$u(x, z, t) = (\partial_z \psi(x, z, t), - \partial_x \psi(x, z, t)). \tag{37}$$

Then we can write the coupled evolution equations for the two independent fields $\psi(x,t)$ (or $\omega(x,t) = \nabla^2 \psi$) and $\rho(x,t)$

$$\frac{\partial}{\partial t} \omega(x,t) + \left\{ \omega, \psi \right\} = g \; \frac{\partial}{\partial x} \rho(x,t) \tag{38}$$

and

$$\frac{\partial}{\partial t} \rho(x,t) + \left\{ \rho, \psi \right\} = 0, \tag{39}$$

where the Poisson brackets are

$$\left\{ A, B \right\} = \partial_x A \partial_z B - \partial_z A \partial_x B. \tag{40}$$

(We are using some of the same notation as in the previous section; hopefully the reader will

be able to maintain any confusion at a low level.)

We have the conserved energy

$$\int d^2x \left[\frac{1}{2}\,(u)^2 + \rho gz \right] = \int d^2x \left[-\omega \frac{1}{\nabla^2}\omega + \rho gz \right] \tag{41}$$

as usual, and it happens that

$$\int d^2x \left[\omega F(\rho) + G(\rho) \right], \tag{42}$$

where $F(\rho)$ and $G(\rho)$ are arbitrary functions of ρ, is also conserved when

$$\int d^2x\,\rho\,\frac{\partial}{\partial x}\,F(\rho) = 0, \tag{43}$$

which we henceforth assume. This is certainly true for either periodic flows or flows where ρ vanishes at $|x|\to\infty$.

Now we seek the extrema of the Arnol'd functional

$$A(\omega,\rho) = \int d^2x \left[-\frac{1}{2}\omega\frac{1}{\nabla^2}\omega + \rho gz + F(\rho)\omega + G(\rho) \right] \tag{44}$$

under variations of ω and ρ. The first variation is

$$\delta A(\omega,\rho)\Big|_{\omega_c,\rho_c} = 0 = \int d^2x \left\{ \delta\omega \left[-\frac{1}{\nabla^2}\,\omega_c + F(\rho_c) \right] \right.$$
$$\left. + \delta\rho \left[gz + \omega_c F'(\rho_c) + G'(\rho_c) \right] \right\}, \tag{45}$$

which implies

$$F'(\rho_c) = \psi_c \tag{46}$$

and

$$gz + \omega_c F'(\rho_c) + G'(\rho_c) = 0. \tag{47}$$

These remind us that ψ_c is a function of ρ_c only for time-independent solutions of the continuity eq. (39), and eq. (47) is just Long's equation (Dubreil-Jacotin, 1935; Long, 1953) for a Boussinesq flow. The usual form of Long's equation is

$$\nabla^2\psi_c + \left[\frac{d\rho_c}{d\psi_c} \right] gz = arbitrary\ function\ of\ \rho_c \tag{48}$$

which follows easily from eq. (46) and eq. (47).

Now, buoyed by the rediscovery of past work, we make the required second variation on $A(\omega,\rho)$:

$$\delta^2 A(\omega_c,\rho_c) = \int d^2x \left\{ \delta\omega \left[-\frac{1}{\nabla^2} \right]\delta\omega + 2\delta\omega\,\delta\rho\,F'(\rho_c) + \delta\rho\,A\,\delta\rho \right\}, \tag{49}$$

where we have introduced the shorthand notation

$$A = -g\,\frac{\partial z}{\partial\rho_c} - \frac{\partial\omega_c}{\partial\rho_c}\,\frac{\partial F(\rho_c)}{\partial\rho_c}. \tag{50}$$

If $\delta^2 A$ has a definite sign, it is positive. This we see by considering the direction $(\delta\omega,0)$ in $(\delta\omega,\delta\rho)$ space. So a necessary condition for nonlinear stability is $A>0$ as we see from looking in the direction $(0,\delta\rho)$. With these observations we complete the square in eq. (49) to write

$$\delta^2 A(\omega_c,\rho_c) = \int d^2x \left\{ \delta\omega \left[-\frac{1}{\nabla^2} - (F'(\rho_c))^2/A \right]\delta\omega \right. \tag{51}$$

$$+ \left[\sqrt{A}\ \delta\rho + (F'(\rho_e)/\sqrt{A})\delta\omega \right]^2 \Big\}.$$

The second term here is always positive. However, if we allow variations in $\delta\omega$ of arbitrary high wave number, then the contribution to the first term from $\delta\omega(-1/\nabla^2)\delta\omega$ can be as small as we like. In the direction

$$\delta\rho = -(F'(\rho_e)/A)\delta\omega, \tag{52}$$

the second variation $\delta^2 A$ is negative for high wave number variations. We conclude then that unless $F'(\rho_e) = 0$, which means no mean flow in the background, $\delta^2 A$ is not of definite sign and two-dimensional incompressible Boussinesq stratified flow is not nonlinearly stable. Neither incompressibility nor the Boussinesq approximation are important; the result holds without them.

Absence of viscosity and the time independence of the state u_e, ρ_e are important, and, to date, it is not known how to extend the present method or the present results to include their effect. Viscosity makes the system non-Hamiltonian so that flows are no longer restricted to constant energy surfaces and the other conserved quantities become nonconserved. That might not be so bad if one could establish a Liapunov function to take the place of $A(w,\rho)$ in eq. (44), but so far the search continues. However, to make a success out of a paradox one can view the result here as giving its own signal for its limitations. Only high wave number excitations are found to be unstable and at high enough wave number the inviscid theory is not valid. The result here tells us that for wave numbers

$$k^2 \approx A/F'(\rho_e)^2, \tag{53}$$

where the right-hand side is to be interpreted in an averaged sense, stability is no longer assured. If this k is less than a realistic dissipative k_D for the flow, it is likely to be unstable. If this $k \sim k_D$, viscous effects may induce stability. Rigorous statements are absent so far.

The time independence of the basic state may possibly be circumvented by introducing a constrained action principle in place of the constrained energy principle used here. This idea is under investigation, and we have nothing to report for or against it.

THREE-DIMENSIONAL FLOWS IN A ROTATING SYSTEM

Having neatly disposed of two-dimensional flows we turn to flows in three spatial dimensions. Again we consider only incompressible fluids in Boussinesq approximation. The equations are the Euler equation

$$\frac{\partial}{\partial t}\vec{v}(\vec{x},t) + \vec{v}\cdot\nabla\vec{v}(\vec{x},t) = -\nabla p - \rho g\vec{z} + \vec{v}\times\vec{f} \tag{54}$$

or

$$\frac{\partial}{\partial t}\vec{v}(\vec{x},t) = -\nabla(p + \vec{v}^2/2 + \rho gz) + gz\nabla\rho + \vec{v}\times\vec{\Omega}, \tag{55}$$

with

$$\vec{\Omega} = curl\ \vec{v} + \vec{f}, \tag{56}$$

and the continuity equation

$$\frac{\partial}{\partial t}\rho(\vec{x},t) + \vec{v}\cdot\nabla\rho(\vec{x},t) = 0, \tag{57}$$

along with

$$div\ \vec{v} = 0. \tag{58}$$

The vector $\vec{f}$ will be taken to be $f(x,y)\vec{z}$, and the centrifugal potential is in the pressure

$p(\vec{x},t)$. As ever the background density $\rho_0 = 1$.

In this system there are two quantities conserved along orbits: the density $\rho(\vec{x},t)$ and the potential vorticity Pedlosky (1979), q:

$$q(\vec{x},t) = \vec{\Omega} \cdot \nabla \rho. \tag{59}$$

In addition to the conserved energy

$$\int d^3x \left[\tfrac{1}{2}\vec{v}^2 + \rho g z \right], \tag{60}$$

the integral

$$\int d^3x \, F(q,\rho) \tag{61}$$

is conserved where $F(q,\rho)$ is an arbitrary function of ρ and q. We thus form the Arnol'd functional

$$A(\vec{v},\rho) = \int d^3x \left[\tfrac{1}{2}\vec{v}^2 + \rho g z + F(q,\rho) \right] \tag{62}$$

and vary $\vec{v}$ and ρ within the class of velocity fields satisfying $div \ \vec{v} = 0$.

The first variation is

$$\delta A(\vec{v}_e,\rho_e) = 0 = \int d^3x \left\{ \delta \vec{v} \cdot \left[\vec{v}_e - (\nabla \rho_e \ x \ \nabla q_e) F_{qq} \right] \right.$$
$$\left. + \delta \rho \left[gz + F_\rho - \vec{\Omega}_e \cdot \nabla F_q \right] \right\}, \tag{63}$$

where F_{qq}, F_ρ, and F_q denote partial derivatives with respect to the indicated subscripts. The first term in eq. (63) requires

$$\vec{v}_e = F_{qq}(q_e,\rho_e) [\nabla \rho_e \ x \ \nabla q_e], \tag{64}$$

which is implied by the time independent statments of conservation

$$\vec{v}_e \cdot \nabla \rho_e = \vec{v}_e \cdot \nabla q_e = 0, \tag{65}$$

An exception occurs when $\nabla \rho_e \ x \ \nabla q_e = 0$ as occurs in several quite interesting examples; more about this later. The second piece of eq. (63) means

$$gz + F_\rho(q_e,\rho_e) = \vec{\Omega}_e \cdot \nabla F_q(q_e,\rho_e). \tag{66}$$

Once we know how to determine $F(q,\rho)$, eq. (66) becomes the three-dimensional version of Long's equation, which has thus far escaped being named.

To learn $F(q,\rho)$ we note that the Bernoulli function

$$B = p + \tfrac{1}{2} \vec{v}^2 + \rho g z \tag{67}$$

satisfies

$$\vec{v}_e \cdot \nabla B_e = 0 \tag{68}$$

for a time-independent flow. This follows from the second form of Euler's equation, eq. (55), and $\vec{v}_e \cdot \nabla \rho_e = 0$. To satisfy this we take B_e to be a function of q_e and ρ_e only. Then some uninteresting algebra leads to

$$F(\rho,q_e) = q_e \int^{q_e} dq \ B_e(\rho,q)/q^2 + function \ of \ \rho_e. \tag{69}$$

With this determination of $F(\rho,q)$ from the properties, ρ_e, q_e and B_e of the time-dependent flow, eq. (66) takes on an appearance similar to Long's equation.

The second variation of $A(\vec{v},\rho)$ around $\vec{v}_e,\rho_e$ is

$$\delta^2 A(\vec{v}_e,\rho_e) = \int d^3x \left[(\delta\vec{v})^2 + (\delta q,\delta\rho) \begin{pmatrix} F_{qq} & F_{q\rho} \\ F_{q\rho} & F_{\rho\rho} \end{pmatrix} \begin{pmatrix} \delta q \\ \delta\rho \end{pmatrix} \right], \tag{70}$$

where F_{qq}, etc. are evaluated at q_e, ρ_e. From this a sufficient condition for nonlinear stability is that the 2 by 2 matrix in (70) have only positive eigenvalues. This means

$$F_{qq}(q_e,\rho_e) > 0, \tag{71}$$

and

$$F_{qq} F_{\rho\rho} - (F_{q\rho})^2 > 0. \tag{72}$$

Fortunately, a single Rossby-like wave with stream function $\psi(x,y,t) = \psi_0 \sin k_1 x \sin k_2 y \, e^{-i\omega t}$ has $F_{qq} < 0$ so one must inquire into the necessary and sufficient condition for nonlinear stability. To this end we choose independent fields to be $u_3(\vec{x},t)$, the vertical component of $\delta\vec{v}, w_3(\vec{\omega},t)$, the vertical vorticity $(curl\,\delta\vec{v})\cdot z$, and $\delta\rho$. A routine struggle with algebra gives for $\delta^2 A$

$$\delta^2 A(\vec{v}_e,\rho_e) = \int d^3x \, (u_3,\omega_3,\delta\rho) \, (M) \begin{pmatrix} u_3 \\ \omega_3 \\ \delta\rho \end{pmatrix}. \tag{73}$$

where M is a 3 by 3 operator given in AHMR for the hardy. The requirement that the eigenvalues of M be all positive or all negative is now a linear problem whose solution determines the nonlinear stability of $(\vec{v}_e,\rho_e)$. Example and further commentary is in AHMR.

NONROTATING THREE-DIMENSIONAL FLOWS

In trying to apply the machinery of the previous section to the standard example of shear flow: $\vec{v}_e = (U(z), V(z), 0)$ in a vertical density profile: $\rho_e(\vec{x}) = \rho(z)$, one encounters the irritating fact that $\nabla\rho_e$ and ∇q_e are parallel so only $\vec{v}_e \propto \nabla\rho_e \times \nabla q_e = 0$ is permitted. To encompass as much of the standard example as possible we first recall that the $\vec{v}_e$ and ρ_e just noted do not, in fact, solve the Euler equations when $\vec{f} = f(x,y)z$ is nonzero. So we turn off rotations for the remainder of this section. From the internal wave viewpoint this restricts our attention to frequencies large compared to inertial motions.

When $\vec{f} = 0$, the horizontal shear flow does satisfy the equations of motion. We also encounter an additional constant of the motion, the helicity:

$$\int d^3x \, \vec{v}(\vec{\omega},t)\cdot\vec{w}(\vec{\omega},t); \quad \vec{\omega} = curl\,\vec{v}. \tag{74}$$

We are thus invited to add to our Arnol'd functional of eq. (62) and vary

$$A(\vec{v},\rho) = \int d^3x \left[\tfrac{1}{2}\vec{v}^2 + \rho gz + F(q,\rho) - \frac{a}{2}\vec{v}\cdot\vec{\omega} \right], \tag{75}$$

in which $q = \vec{\omega}\cdot\nabla\rho$ since $\vec{f}=0$, and a is just a constant. Now the first variation of A is:

$$\delta A(\vec{v}_e,\rho_e) = 0 = \int d^3x \left\{ \delta\vec{v}\cdot\left[\vec{v}_e - a\,\vec{w}_e - (\nabla\rho_e \times \nabla q_e)F_{qq} \right] \right.$$

$$\left. + \delta\rho\left[gz + F' - \vec{w}_e\cdot\nabla F_q \right] \right\}. \tag{76}$$

So we have

$$\vec{v}_e = a\,\vec{\omega}_e + (\nabla\rho_e \times \nabla q_e)\,F_{qq} \tag{77}$$

and

$$gz + F\rho = \vec{\omega}_e \cdot \nabla F_q \tag{78}$$

at the stationary flow.

Since we are interested in the case where $\vec{v}_e = (U(z), V(z), 0)$ and $\rho_e(\vec{x}) = \rho(z)$, we look for the restrictions implied by $\nabla \rho_e \times \nabla q_e =$; indeed, $q_e = 0$ for this flow. We then have

$$\vec{v}_e = a\, \vec{\omega}_e, \tag{79}$$

or

$$\nabla^2 \vec{v}_e = -\frac{1}{a^2} \vec{v}_e, \tag{80}$$

or

$$\frac{d^2}{dz^2}(U(z), V(z)) = -\frac{1}{a^2}(U(z), v(z)), \tag{81}$$

with

$$\partial_z U = \frac{1}{a} V(z). \tag{82}$$

The solution is

$$U(z) = U_0 \sin(z/a + \phi_0) \tag{83}$$

and

$$V(z) = U_0 \cos(\frac{z}{a} + \phi_0), \tag{84}$$

with V_0 a velocity scale and ϕ_0 a phase. Clearly a could be complex so a mixture of sin, cos, sinh, and cosh is permitted.

The second variation of $\delta^2 A$ is altered in only one respect from the earlier result, eq (70); namely to the term quadratic in $\delta \vec{v}$ is added $-a\delta\vec{v}\cdot(curl\ \delta\ \vec{v})$ which is not naturally positive so the sufficient conditions for nonlinear stability, eqs. (71) and (72), must be discarded. Turning to the necessary and sufficient conditions of eq. (73) we find a change $-(a/2)\,u_3(\nabla^2/\nabla^2)w_3$, $\nabla^2 = \partial_1^2 + \partial_3^2$, in the uw elements of the matrix operator M.

By considering flows which are very nearly parallel, we have been able to demonstrate that the flow $\vec{v}_e = (U(z),0,0)$, $\rho_e = \rho(z)$ is stable to nonlinear perturbations when the Richardson number with respect to density

$$Ri_\rho = N^2(z)/\left[\frac{\partial\rho}{\partial z}\right]^2 \frac{\partial^2}{\partial\rho^2}\left[\frac{1}{2} U^2\right] \tag{85}$$

exceeds unity. The details are available in our paper in Physical Review Letters, 52, 2352 (1984). This result opens the very interesting realm $\frac{1}{4} < Ri < 1$ for theoretical and experimental study.

DISCUSSION

In this report I have presented the method of Arnol'd and others for the analysis of the STABILITY of inviscid stratified fluid flows under nonlinear deformations of a time-independent equilibrium flow $\vec{v}_e(\vec{x})$, $\rho_e(\vec{x})$. The emphasis here on stability is crucial since it is a major contrast with the familiar linear stability method which is able to establish the INSTABILITY of a flow to infinitesimal disturbances. One may wonder what is the situation when a given flow is nonlinearly unstable (more precisely not nonlinearly stable) and simultaneously linearly stable. In AHMR is a suggested conjecture to cover this case. We guess there that in this intermediate arrangement a phenomenon occurs known as Arnol'd

274

diffusion, which is a slow random-walk-like process away from the original $\overline{v}_e$, ρ_e resulting in a slow visitation of the energetically allowed state space.

The key results reported here are the absence of nonlinear stability of two-dimensional stratified flows with $u_e \neq 0$ and the setup, with many details omitted, of the linear equations determining the issue of nonlinear stability for the three-dimensional case. We hope to report on the investigation of special cases in the near future.

We close this report by repeating an important feature of the "Arnol'd" method and the limitations known to us:

(1) The decision whether a given flow is NONLINEARLY STABLE rests on the investigation of a LINEAR eigenvalue problem. Examples in the main body of this report are typified by the equation, eq. (29), which must be studied for two-dimensional homogeneous flow.

(2) The method, to date, is restricted to the stability analysis of time-independent flows of inviscid fluids. Perhaps these limitations can be lifted by a generalization of the energy principle variational technique to an action principle and by the invention of a Liapunov functional for the dissipative setup.

(3) Perhaps more troublesome is the limitation to flows which neatly arise from consideration of the invariants of the motion (potential vorticity, helicity,...). As indicated the familiar example of plane parallel shear flow is not yet included.

Acknowledgements

APPENDIX

This appendix is for the dynamics gourmet or for completeness, if you like. This is not to make light of the issue raised and answered here (Arnol'd, 1969) but to prevent defocusing on the computationally more difficult issues treated in the main text.

When one has an infinite dimensional system, such as a fluid, then the unique sign of the second variation of the Arnol'd functionals is not enough to mathematically guarantee the stability of the equilibrium flow. The simple positivity or negativity is labeled formal stability by AHMR. To go beyond formal stability we require a convexity argument of the sort made by Arnol'd (1965). Here we indicate how it goes for our example of two-dimensional homogenous incompressible flow.

We form the quantity (see eq. (16) for A) $A_2(\Delta w) = A(w_e + \Delta_w) - DA(w_e)\Delta w$ which is an invariant under the flow. If the quantity $G''(w_e)$ is bounded by

$$0 < C_L \leqslant G''(w_e) \leqslant C_u < \infty, \tag{A.1}$$

then we can define two norms which give a sense of size to the deviation from w_e.

$$||\Delta w||_{L,U} = \int d^2x \; \tfrac{1}{2} \Delta w \left[-\frac{1}{\nabla_2} + C_{L,U} \right] \Delta w, \tag{A.2}$$

and since $A_2(\Delta w(x,t)) = A_2(\Delta w(x,0))$ we have

$$A_2(\Delta w(x,t)) \leqslant \Delta w(x,0||_u, \tag{A.3}$$

and

$$A_2(\Delta w(x,t)) \geqslant ||\Delta w(x,0)||_L. \tag{A.4}$$

More precisely than in the text we conclude that for $\Delta w(x,0)$ for which the norms in eq. (A.2) are finite, the flow is stable since

$$||\Delta w(x,t)||_L \leqslant ||\Delta w(x,0)||_u. \tag{A.5}$$

276

References

Abarbanel, H. D. I., Holm, D. D., Marsden, J. E., and Ratiu, T., submitted: Stability analysis of stratified incompressible fluid flow. *J. Fluid Mech.*. Referred to as AHMR.

Arnol'd, V. I., 1965: Conditions for nonlinear stability of stationary plane cirvilinear flows of an ideal fluid. *Doklady Nat. Nauk*, **162**, 773-777.

Arnol'd, V. I., 1969: On an *a priori* estimate in the theory of hydrodynamical stability. *Am. Math Soc. Transl.*, **79**, 267-269.

Chandrasekhar, S., 1961: *Hydrodynamic and Hydromagnetic Stability*. Oxford University Press.

Drazin, P. G. and Reid, W. H., 1982: *Hydrodynamic Stability*. Cambridge University Press, 527 pp.

Dubreil-Jacotin, M. L., 1935: Complément à une note anteriéure sur les ondes de type permanent dans les liquides hétérogènes. *Atti. Accad. Lincei Rend. Cl. Sci. Fis. Mat. Nat.*, **21**, 344-346.

Erickson, C. C., 1978: Measurements and models of fine structure, internal gravity waves, and wave breaking in the deep ocean. *J. Geophys. Res.*, **83**, 2989-3009.

Guckenheimer, J. and Holmes, P., 1983: *Nonlinear Oscillations, Dynamical Systems, and Bifurcations of Vector Fields*. Springer-Verlag, 453 pp.

Long, R. R., 1953: Some aspects of the flow of stratified fluids. I. Theoretical investigation. *Tellus*, **5**, 42-57.

Pedlosky, J., 1979: *Geophysical Fluid Dynamics*. Springer-Verlag, 624 pp.

Phillips, O. M., 1977: *The Dynamics of the Upper Ocean*. Vol. 2nd Ed., Cambridge University Press, 336 pp.

Rayleigh, Lord, 1880: On the stability, or instability of certain fluid motions. *Proc. London Math. Soc.*, **11**, 57-70.

CLOSURE FOR TURBULENT VELOCITY/PRESSURE-GRADIENT CORRELATIONS IN NONUNIFORM FLOWS

Brent Gallagher

Department of Oceanography and Hawaii Institute of Geophysics,
University of Hawaii, Honolulu, 96822

ABSTRACT

Turbulent velocity/pressure gradient correlations arise in nonuniform
flows through the interaction of the turbulence with the mean strain rate
field. We have developed a rational closure to represent the influence
of these correlations on the behavior of the Reynolds stress tensor. The
closure permits us to obtain good agreement between observed and
numerically modeled Reynolds stress components as they evolve under the
influence of uniform shear and plane strain.

INTRODUCTION

In the past decade there have been important advances in the modeling of
turbulent fluxes which rest on treating the turbulence closure problems
at the level of second and higher order moments in physical space.
Developments have shown the possibility that higher order closure can
lead to sets of equations that allow prediction of turbulent fluxes as
well as mean flow variables. This is clearly important and exciting both
for oceanography and for fluid dynamics in general. However, there
remain several difficulties that must be overcome in order to put the
methods on a firm footing and to know their limitations.

One of the major difficulties is that the equations governing one-point
second order moments (such as Reynolds stress) contain unknown
correlations between the turbulent pressure and other fluctuating
quantities in the flow. In many cases these correlations have an
important influence on the turbulent fluxes, and there has been a real
need for improvement in the way they are modeled. Earlier closure
expressions for the pressure correlations failed to produce agreement
with observations; others did better but were somewhat arbitrary
constructions. After summarizing existing approaches, Mellor and Herring
(1973) concluded that there did not yet seem to be a way of making a
rational elaboration of the pressure-related correlations. In his review
of numerical turbulence models, Reynolds (1974) reached the similar
conclusion that further development was needed in the treatment of these
terms.

We began our work in this area several years ago. We started with the intention of applying the higher-order closure methods to problems in physical oceanography, but soon found that such applications would not be meaningful until some fundamental improvements were made in the closures for pressure-related correlations — especially those that arise when the mean flow field is inhomogeneous. We therefore undertook work on this more basic problem and succeeded in developing a rationally based closure for turbulent velocity pressure-gradient correlations in the presence of non-uniform mean currents (Gallagher, Magaard, and Gutteling, 1981). Since then we have extended the development and tested the closure to see how well it would allow us to predict the measured evolution of turbulence in wind tunnels. The purpose of this was to confirm the validity of the closure with high-quality observations before moving into the less well controlled realm of the ocean.

SUMMARY OF THEORETICAL DEVELOPMENT

The Reynolds stress tensor $< u_i u_j >$ is governed by the equation

$$\partial_t <u_i u_j> + U_k \partial_k <u_i u_j> + <u_j u_k> \partial_k U_i + <u_i u_k> \partial_k U_j + \partial_k [<u_i u_j u_k>$$

$$- \nu \partial_k <u_i u_j>] = - \frac{1}{\rho} <u_j \partial_i p + u_i \partial_j p> - 2\nu <\partial_k u_i \partial_k u_j> . \qquad (1)$$

The first term on the right-hand side is the one for which we want to help develop a closure. It can be represented as a sum of two parts, corresponding to the fact that turbulent pressure fluctuations arise in two ways — by interactions of the turbulent velocity field with itself and with the mean strain rate field. The second of these is the source of the effects we wish to model here, and the corresponding velocity/pressure-gradient correlation can be found analytically. Naming the correlation P_{IIij}, we have

$$P_{IIij}(\underline{x}) = - \frac{1}{2\pi} \int_{\underline{x}'} <u_j \partial_i' \partial_k' u_n' + u_i \partial_j' \partial_k' u_n'> \partial_n' U_k' \frac{dV}{|\underline{x}-\underline{x}'|} ,$$

where primed variables are evaluated at $\underline{x}'$ and unprimed variables at $\underline{x}$. When the mean strain rate does not change too greatly over an integral scale of the turbulence, one can approximate:

$$P_{IIij} \simeq 2(a_{ijkn} + a_{jikn}) \partial_n U_k .$$

The closure problem is now that of finding an expression for

$a_{ijkn} = - \frac{1}{4\pi} \int_{\underline{x}'} <u_j \partial_i' \partial_k' u_n'> \frac{dV}{r}$. The development up to this point is due to Chou (1945) and to Rotta (1951).

Early workers in this field attempted to approximate a_{ijkn} with various ad hoc formulas. Some of these seemed to work in certain circumstances, but none rested on a firm, rational base. We were able to provide such a base and showed that under some fairly unrestrictive conditions one could write

$$a_{ijkn} + a_{jikn} = [2C_1\lambda_k\lambda_n + (-C_1-C_2+C_3)\mu_k\mu_n + (-C_1+C_2-C_3)\theta_k\theta_n]\lambda_i\lambda_j$$

$$+ [(-C_1-C_2+C_3)\lambda_k\lambda_n + 2C_2\mu_k\mu_n + (C_1-C_2-C_3)\theta_k\theta_n]\mu_i\mu_j \quad (2)$$

$$+ [(-C_1+C_2-C_3)\lambda_k\lambda_n + (C_1-C_2-C_3)\mu_k\mu_n + 2C_3\theta_k\theta_n]\theta_i\theta_j .$$

Here $\underline{\lambda}$, $\underline{\mu}$, $\underline{\theta}$ are eigenvectors of $< u_i u_j >$, and

$$C_1 = -\frac{1}{4\pi} \int_{\underline{x}'} < \partial_\lambda' \partial_\lambda' u_\lambda u_\lambda' > \frac{dV}{|\underline{x}-\underline{x}'|} ,$$

where the subscript λ indicates derivatives and velocities in the λ direction. C_2 and C_3 are similarly defined with respect to $\underline{\mu}$ and $\underline{\theta}$. Expression (2) establishes the geometrical structure of the closure, and we have progressed significantly toward our goal. We must still specify the scalars C_1, C_2, and C_3, whose definitions continue to contain some residual of the original closure problem. The development up to this point is given more fully in Gallagher et al. (1981).

In our most recent work we have developed expressions for C_1, C_2, and C_3, based on the following:

(a) From its definition, C_1 will approach $\frac{1}{15} <u_i u_i>$ when $< u_i u_j >$ becomes isotropic.

(b) From its definition, C_1 will be zero when $< u_\lambda u_\lambda >$ is zero.

(c) From its definition, C_1 will be zero if the turbulence becomes one-dimensional with all motion in the λ-direction. This means C_1 vanishes as $(2E - <u_\lambda u_\lambda>)$ vanishes, where $E = 1/2 <u_i u_i>$.

(d) If the turbulence becomes two-dimensional, no component of $< u_i u_j >$ can approach 2E, and C_1 will not contain the factor $(2E- <u_\lambda u_\lambda>)$.

(e) From the observations of wind tunnel turbulence, to be described later, we found that the strength of the turbulent pressure effects increased rapidly when the anisotropy of $<u_i u_j>$ exceeded a certain moderate level. This suggested that C_1 increased rapidly with anisotropy of $< u_i u_j >$.

In building an expression involving the foregoing properties, we need to specify the amount and type of anisotropy present in $< u_i u_j >$. For this we consider its anisotropic part $b_{ij} = <u_i u_j> - \frac{2}{3} E \delta_{ij}$. The second invariant of this, II, is a quadratic measure of the degree of anisotropy present, and the sign of the third invariant indicates whether $<u_i u_j>$ is tending toward one-dimensionality (III > 0) or two-dimensionality (III < 0). Using these conveniences we construct an expression for C_1

that has all the features (a)-(e):

$$C_1 = \frac{3}{20} <u_\lambda u_\lambda> E^{-1} G(<u_\lambda u_\lambda>, III), \ H(II),$$

where $G(<u_\lambda u_\lambda>, III) = 2E - <u_\lambda u_\lambda>$ when $III > 0$

$$= \frac{4}{3} \qquad \text{when } III \leq 0,$$

and $H(III) = 1$ when $II \leq II_c$

$$= 1 + \alpha(II-II_c) \qquad \text{when } II > II_c.$$

The constants α and II_c were found empirically to be about 70. and .08, respectively.

The foregoing expression for C_1 and parallel ones for C_2 and C_3 are employed in equation (2) to complete the closure model for P_{IIij}. The closure is then employed in equation (1) and tested by comparing numerical solutions for $<u_i u_j>$ with observations .

THE TEST RESULTS

Two wind tunnel tests were used. They are physically quite different, and together they test the performance of the closure in the two fundamentally different kinds of mean flow distortion. The wind tunnel observations of Champagne, Harris and Corrsin (1970) are used to check how well our models can predict all components of the Reynolds stress tensor as a grid-generated turbulence evolves downstream in the presence of a constant mean shear flow. To test the closure as turbulence evolves under the influence of pure straining of the mean flow, we use the observations of Tucker and Reynolds (1968), in which the mean flow is subjected to simultaneous contraction and dilation in directions normal to the flow.

Observations and our computed results are pictured in figure 1 for the uniform shear flow of Champagne, Harris, and Corrsin. The three independent, non-zero components of $<u_i u_j> /E$ are shown, and model results reported by other authors are sketched in for comparison. There are three phases in the evolution of the energy components, and they can be seen in the S-shapes of the curves in figure 1. At first, while $<u_1 u_2> /E$ is still small, the turbulence energy components drift only slowly away from their initial, nearly isotropic values. In the second phase, when $- <u_1 u_2> /E$ reaches about 0.25, the energy components grow almost explosively away from isotropy. During this phase P_{IIij} is opposing the growth of anisotropy, but not strongly enough to prevent it. In the third phase P_{IIij} becomes larger more rapidly and suppresses further anisotropic growth; the energy components roll off sharply to their steady state levels.
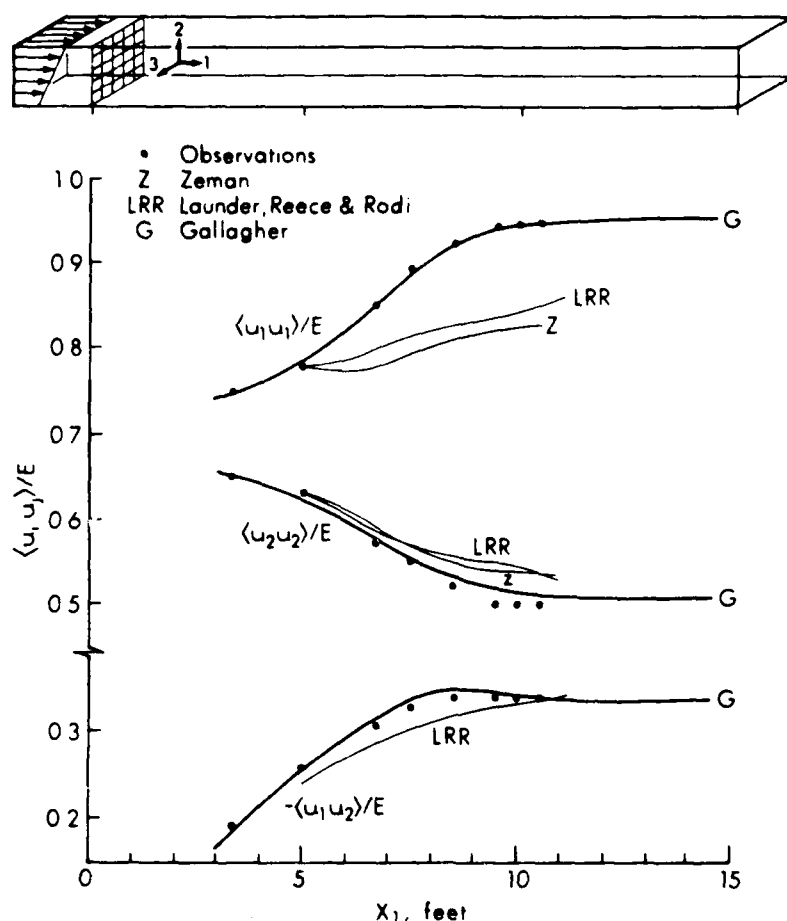
Fig. 1. Reynolds stress components evolving in uniform
shear flow — as observed by Champagne, Harris, and
Corrsin and as predicted by various models.

The distortion of turbulence by plane straining is illustrated in figure
2, where the observations of Tucker and Reynolds are shown together with
model results. The type of anisotropy produced here is different from
that in the shear flow example. There, the turbulence was distorted
toward one-dimensionality with one energy component dominating and the
other two falling below isotropic values $(III > 0)$. Here, under plane
straining the turbulence is pushed toward two-dimensionality; two energy
components are above isotropic values, and one lies well below $(III < 0)$.
The turbulence starts to become two-dimensional about one-third meter
into the distoring section and remains so thereafter. The Tucker and

Reynolds experiment showed that the performance of the P_{IIij} closure
can be improved by accounting for differences in the shape of the
distorted Reynolds stress tensor. This was done by allowing III to play
a role in the structuring of C_1, C_2, and C_3, as noted in our
discussion of equation (5). As it did in the previous test, P_{IIij} acts
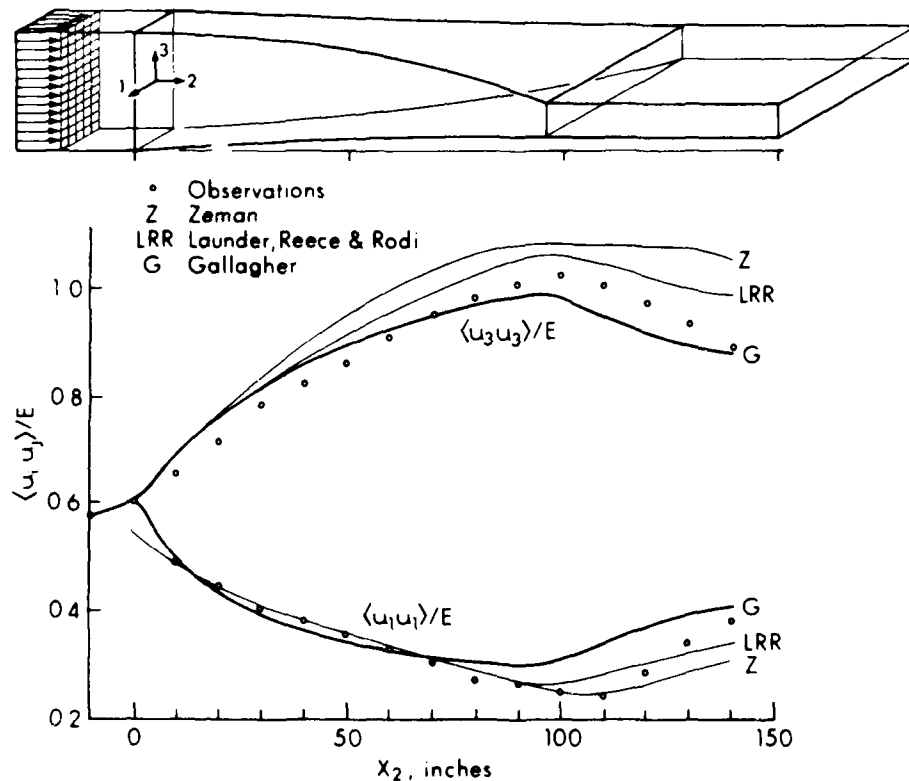here to resist the production of anisotropy.

Fig. 2. Reynolds stress components evolving under plane
strain -- as observed by Tucker and Reynolds and as
predicted by various models.

DISCUSSION

Considering the results of both tests, we conclude that our closure for
P_{IIij} seems to work acceptably. It allows the observed Reynolds stress
components to be computed fairly closely, and in several instances it
clearly does much better than earlier models.

Since the closure for $P_{III_{ij}}$ has been rationally based, its structure
encourages physical interpretations. $P_{III_{ij}}$ is a very particular type
of restoring effect that acts to reduce anisotropy of the Reynolds stress
tensor. Our work has at least begun to indicate what this behavior
depends on and to suggest some details of its structure. At this point
we might describe things by imagining that turbulent motions in
themselves constitute a sort of hypersubstance. Then through its
interaction with the background motion field (the nonuniform mean flow)
the hypersubstance gains resiliency. Like an ordinary material, the
hypersubstance resists distortion — but it does so in a strongly
nonlinear, anisotropic manner. The resilience increases with the amount
of distortion, and very strongly so when the distortion exceeds a certain
moderate level. Further, when elements of hypersubstance are distorted
toward cylindrical shapes, the resilience is somewhat less than when the
distortion is toward disk-like shapes. P_{II} gives a quantitative
specification of all these behaviors, and it might be viewed as a sort of
rheological function for turbulence-material.

ACKNOWLEDGEMENT

REFERENCES

Champagne, F. H., V. G. Harris, and S. Corrsin, 1970: Experiments on nearly
    homogeneous turbulent shear flow, J. Fluid Mech., 41, 81-139.

Chou, P.Y., 1945: On Velocity Correlations and the Solutions of the
    Equations of Turbulent Fluctuations, Quart. Appl. Math., 3, 38-54.

Gallagher, B., L. Magaard, and E. Gutteling, 198 : Closure for velocity/
    pressure-gradient correlations in turbulent shear flow, Phys. Fluids, 24,
    1605-1610.

Mellor, G. and H. Herring, 1973: A survey of mean turbulent field closure
    models, AAIA Journal, 11, 590-599.

Reynolds, W.C., 1974: Recent advances in the computation of turbulent
    Flows, Adv. Chem. Engr., 9, 193-246.

Rotta, J., 1951: Statistische Theorie nichthomogener Turbulenz, Z. Physik,
    129, 547-572.

Tucker, H. J. and A. J. Reynolds, 1968: The distortion of turbulence by
    irrotational plane strain, J. Fluid Mech., 32, 657-673.
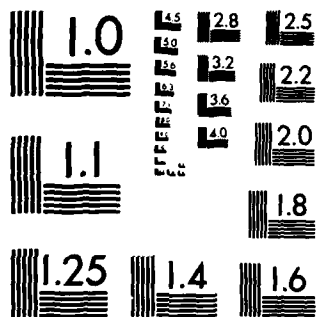
MICROCOPY RESOLUTION TEST CHART

NATIONAL BUREAU OF STANDARDS-1963-A

THE ATMOSPHERIC NOISE SPECTRUM--WAVES OR STRATIFIED TURBULENCE?

Douglas K. Lilly

University of Oklahoma, Norman, Oklahoma

ABSTRACT

Recent observational data show the horizontal and vertical spectra of atmospheric motions and temperature to be well defined and fairly constant in the middle and upper troposphere and lower stratosphere, and to have similarities with the corresponding spectra in the ocean. Two proposed rationalizations of these structures are reviewed, one adapted from and similar to the Garrett-Munk wave model, and the other based on turbulence theory.

INTRODUCTION

The purpose of this paper is to review the knowledge and understanding of the structure of atmospheric noise. By "noise" I refer in general to all disturbances outside of a mean zonal flow, but the principal emphasis here is to the atmospheric mesoscales, that is from a few to a thousand kilometers in wavelength. Although many important meteorological phenomena are represented in this scale range, knowledge of its statistical properties has been somewhat limited. Recently, however, analysis of both direct (aircraft) and remote (Doppler radar) measurements has solidified the observational foundations to an extent. Two principal theories have been proposed in an attempt to satisfy the observational structure. One of these, due to Van Zandt (1982), is essentially an adaptation of the Garrett-Munk (1972, 1975, 1979) model of the statistical effects of internal gravity waves on the oceanic noise spectra. The other is a turbulent theory due to Gage (1979) and Lilly (1983). At this time strong grounds for acceptance or rejection of either of these models do not seem available.

THE OBSERVED SPECTRA OF ATMOSPHERIC MOTIONS ABOVE THE BOUNDARY LAYER

The most comprehensive set of measurements of atmospheric motions above the boundary layer has been obtained by use of sondes, balloon-borne sensors measuring temperature and pressure and tracked by radio signals. Sonde stations in continental areas are typically spaced several hundred kilometers apart and the sondes are launched at 6- or 12-hour intervals. They are much more widely spaced over the oceans. Statistics have generally been computed from objective analyses of the observed and geostrophic winds, and are therefore subject to some

286

smoothing at scales near the observational resolution. Another source
of data is the wind velocity measured by large commercial or military
aircraft with inertial navigation systems. Although this data is not
produced mainly for meteorological purposes, it is usually of good
quality. Flight tracks are widespread but by no means uniform in their
global coverage, and most of the data is confined to the levels between
10 and 13 km ASL. An increasingly important third source is Doppler
radar, especially the fixed array type becoming known as "profilers."
These are at present rather sparsely distributed as research tools, but
are capable of producing vertical soundings at very frequent intervals.
Data from the sonde nets are suitable for large-scale spatial and
temporal spectra and finer scale (tens to hundreds of meters resolution)
vertical spectra of horizontal winds. The aircraft data can be used to
obtain broad-band horizontal spectra of both horizontal and vertical
wind components and also temperature fluctuations. The radar profilers
produce data suitable for broad-band temporal and vertical spectra of
both horizontal and vertical motions.

Figure 1 shows several summarized horizontal spectra of horizontal
winds, as observed by the kinds of observing systems described above.
At the large-scale end the dash-dotted line spectrum from Chen and Wiin-
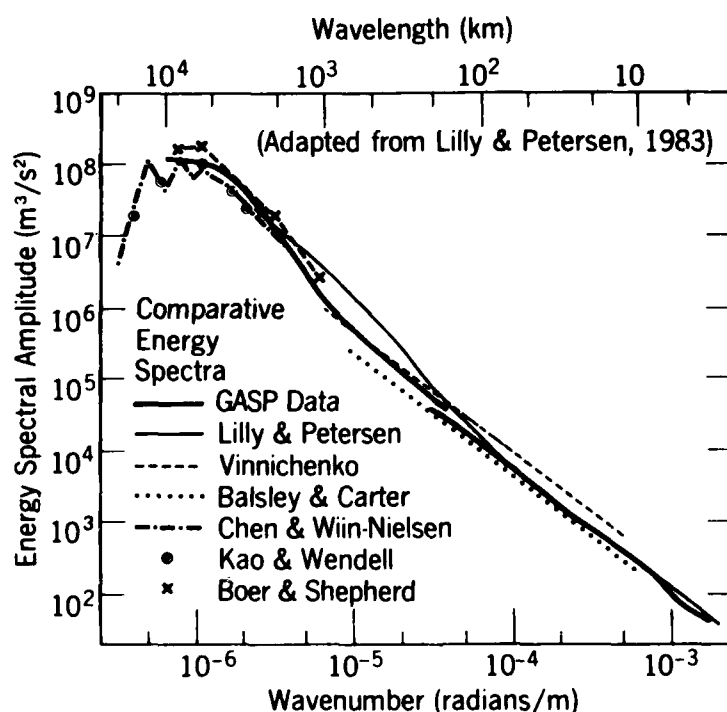Nielsen (1978) was derived from sonde sources, after intermediate

Figure 1. Horizontal spectra of horizontal kinetic energy from
various sources. The large scale values are mostly from sonde
data, and the meso- and small-scale values from aircraft and
Doppler radar. This version was produced by Nastrom and Gage
(1984).

analysis and interpretation. The dotted line is a slightly smoothed version of a temporal spectrum computed from Doppler radar data over central Alaska in summer by Balsley and Carter (1982). The conversion to spatial form was made by Lilly and Petersen (1983) using a Taylor hypothesis that the flow is turbulent and advected by the mean flow with the long-term mean wind. The solid lines are spectra obtained from aircraft sources by Lilly and Peterson (1983) and Nastrom and Gage(1983, 1984). While not all the spectra are in agreement and the circumstances and methods by which they are obtained vary substantially, a general pattern emerges. From wavelengths of about 4000 to 1000 km a rather steep spectrum exists, with a logarithmic slope apparently near -3, while at the smaller mesoscales, from say 200 down to 10 km the slope is closer to -5/3. The region between is apparently transitional. Nastrom and Gage (1984) show that spectral amplitudes and slopes are fairly consistent with changes of scales and locations. It is unclear whether a gap or hump in the mean spectrum occurs at scales between 10 km and the presumed -5/3 range of the 3-d turbulent microscales, 500 m and less, but if so it is not likely to involve a shift of more than a factor of two in the otherwise continuous slope (Lilly, 1983).

Vertical spectra of horizontal motions have been obtained from analysis of high-resolution balloon soundings. Figure 2, from Endlich
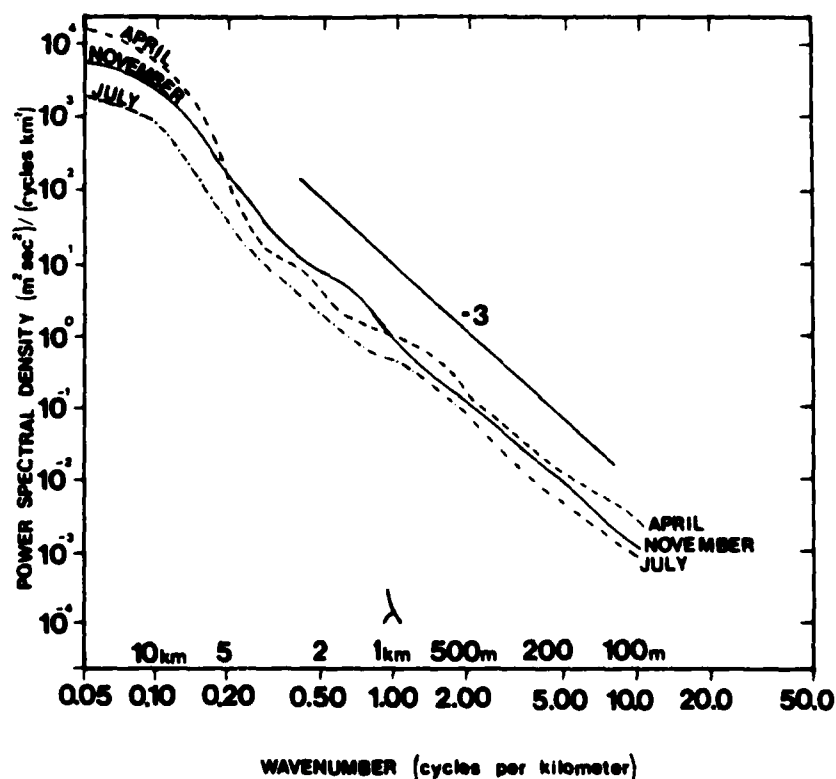

Figure 2. Vertical spectra of the horizontal wind
in the troposphere and lower stratosphere, based
on high-resolution balloon tracking. From Endlich
et al. (1979).

et al. (1979) summarizes vertical spectra, showing an approximately -2.5 slope for wavelengths less than 5 km.

Temporal spectra of horizontal velocities, from sondes and Doppler radar, have generally not been considered as independent of the horizontal spatial spectra; that is, wave propagation through the atmosphere has generally been neglected, except at the larger planetary scales (see Vinnichenko, 1970). Brown and Robinson (1979) showed that the Taylor hypothesis, using mean winds, was suitable for converting from temporal to spatial spectra for scales of hundreds of kilometers.

Spectra of vertical motions have been slow to appear. At horizontal scales larger than about 10 km, vertical velocities are very small and hard to measure directly. At the microscale end, on the other hand, they become isotropic with the horizontal motions. Balsley et al. (1983) showed a temporal spectrum of vertical motion measured by Doppler radar which was essentially flat for time scales longer than the Brunt-Vaisala frequency under circumstances of weak mean flow. For stronger mean flow the spectrum was redder, but thought to be contaminated by horizontal motions.

In a stratified atmosphere vertical displacements can be estimated from temperature fluctuations. Large-scale horizontal temperature spectra are similar in shape to those of horizontal velocity components (Chen and Wiin-Nielsen, 1978). Nastrom and Gage (1984) find that this is also true for the mesoscales. A horizontal spectrum function proportional to the -5/3 power of wavenumber is consistent with a horizontal vertical velocity spectrum proportional to the +1/3 power. This is in rough agreement with the Balsley flat spectrum.

THEORIES FOR MAINTENANCE OF THE NOISE SPECTRUM

Van Zandt's (1982) application of the Garrett-Munk model to atmospheric spectra is a plausible hypothesis, due to the at least superficial similarity of the atmospheric spectra and processes to their oceanic analogues. The horizontal spectrum of horizontal winds in the troposphere, indicated above as having a -5/3 logarithmic slope between 10 and 200-500 km, can be about as well fit with a -2 slope, as observed for the ocean. The vertical spectrum of horizontal motions is also similar in shape to that of the oceans. The intrinsic (Doppler shifted, following the mean flow) frequency spectrum is not well observed in the atmosphere, because of the effects of the large horizontal mean flows. Nevertheless, Van Zandt found that a fairly straightforward application of the Garrett-Munk model produces spectra that follow the observations to at least an order of magnitude.

Gage (1979) suggested that the mesoscale energy spectrum is produced by two-dimensional turbulence, transferring energy upscale from initially three-dimensional small-scale sources, such as convection, shearing instability, and orography. This suggestion has been further explored by Lilly (1983). It is assumed that motion is excited by an

isotropic injection of kinetic energy of an average amplitude $V^2/2$ at a characteristic length scale H. If the disturbance Froude number, $F = V/NH$, is initially much greater than unity, the isotropic motion field will lose energy through an inertial energy cascade at a rate proportional to V^3/H. Here N is the Brunt-Vaisala frequency. Integration of the equation $d(V^2/2)/dt = -V^3/H$, holding H constant, shows that F will decrease below unity in a time scale of order N^{-1}, regardless of its initial value. This is consistent with the results of a 3-d numerical simulation of turbulence in a stratified environment by Riley et al. (1981). In this context Riley et al. then present a scale analysis and other arguments which show that for F<<1 the initially 3-d turbulence decomposes into a mixture of internal gravity waves and a quasi-two-dimensional non-linear flow which I call "stratified turbulence." The scale analysis is repeated below.

I start with the Boussinesq equations of incompressible flow, buoyancy deviation from the mean, and continuity, written with dissipation terms neglected in the form

$$\frac{d\vec{V}_H}{dt} + \nabla_H \pi + f\vec{k} \times \vec{V}_H = 0 \tag{1}$$

$$\frac{dw}{dt} + \frac{\partial \pi}{\partial z} - b = 0 \tag{2}$$

$$\frac{db}{dt} + N^2 w = 0 \tag{3}$$

$$\nabla_H \cdot \vec{V}_H + \partial w/\partial z = 0 \tag{4}$$

where $d/dt = \partial/\partial t + \vec{V}_H \cdot \nabla_H + w\partial/\partial z$ and $N^2 = \partial \bar{b}/\partial z$, with $\bar{b}$ and b the mean and deviation buoyancy variables and $\pi = p/\bar{\rho}$. The direction pursued by Riley, et al. was to separate the flow into a component with wave-like behaviour and a component similar to turbulence. They did this by introducing a length scale H, a horizontal disturbance velocity scale V, a wave time scale N^{-1} and an advective (turbulent) time scale H/V. They assumed that π is scaled by V^2 and that the vertical pressure gradient and buoyancy terms in (3) are of the same magnitude, so that b is scaled by V^2/H. Introducing these scaling parameters into the variables generates dimensionless equations as follows. For the wave system they are

$$\frac{\partial \vec{V}_H}{\partial t} + F(\vec{V}_H \cdot \nabla_H \vec{V}_H + w \frac{\partial \vec{V}_H}{\partial z}) + \nabla_H \pi + (f/N)\vec{k} \times \vec{V}_H = 0 \tag{5}$$

$$\frac{\partial w}{\partial t} + F(\vec{V}_H \cdot \nabla_H w + w \frac{\partial w}{\partial z}) + \frac{\partial \pi}{\partial z} - b \qquad = 0 \qquad (6)$$

$$\frac{\partial b}{\partial t} + F(\vec{V}_H \cdot \nabla_H b + w \frac{\partial b}{\partial z}) \qquad + w \qquad = 0 \qquad (7)$$

$$\nabla_H \cdot \vec{V}_H + \partial w / \partial z \qquad = 0 \qquad (8)$$

The turbulent motions are described by the dimensionless system

$$\frac{\partial \vec{V}_H}{\partial t} + \vec{V}_H \cdot \nabla_H \vec{V}_H + F^2 w \frac{\partial \vec{V}_H}{\partial z} + \nabla_H \pi + R^{-1} \vec{k} \times \vec{V}_H \qquad = 0 \qquad (9)$$

$$F^2 (\frac{\partial w}{\partial t} + \vec{V}_H \cdot \nabla_H w + F^2 w \frac{\partial w}{\partial z}) \frac{\partial \pi}{\partial z} - b \qquad = 0 \qquad (10)$$

$$\frac{\partial b}{\partial t} + V_H \cdot \nabla_H b = F^2 w \frac{\partial b}{\partial z} \qquad + w \qquad = 0 \qquad (11)$$

$$\nabla_H \cdot \vec{V}_H + F^2 \frac{\partial w}{\partial z} \qquad = 0 \qquad (12)$$

where $R = V/fH$ is the Rossby number.

For small F the two systems are distinct, which is reasonable since F is the ratio of the two time scales. The wave system, eqs. (5)-(8) is effectively linearized, and after neglecting the Coriolis term $(f/N \sim 10^{-2}$ in the atmosphere) is identical to the equations describing internal gravity waves. In the system defined by eqs. (9)-(12), the lowest order solution for small F^2 and moderate or large R is horizontal nonlinear flow, for which vertical vorticity is conserved. This flow has similar dynamics to two-dimensional turbulence, but may have vertical structure. Given knowledge of the horizontal flow field at each level, pressure may be obtained from solution of the horizontal divergence equation, and buoyancy is then determined by the hydrostatic approximation to eq. (10). A vertical velocity field is obtained from diagnostic solution of the buoyancy equation, eq. (11). Feedback of buoyancy to the motion field only occurs through order F^2 terms.

A simple argument suggests that an initially isotropic velocity field divides itself roughly equally into the two kinds of motion

defined by the above scale analysis. If a velocity vector $\vec{V}$ (x,y,z) is transformed through a three-dimensional Fourier integral into the Fourier components $\hat{\vec{V}}(\vec{k})$, where $\hat{\vec{k}}$ is a three-dimensional wavenumber, then the continuity equation requires that $\vec{k} \cdot \vec{V} = 0$, i.e. the velocity vector must lie in a plane normal to the wavenumber. This is illustrated by figure 3 in which the velocity vector is decomposed into a horizontal component and an orthogonal tilted component. The stratified turbulence flow, here designated by V_ψ, is horizontal and horizontally non-divergent, so its Fourier component is normal to both $\vec{n}$ and $\vec{k}$ and must lie along the horizontal line shown in the figure. The wave flow component, $\vec{V}_\phi$, must be irrotational, so its Fourier component lies along the tilted axis. Since isotropy implies that a forced wavenumber vector is equally likely to lie in any direction on the normal plane, equal amplitudes of wave and turbulence energy are predicted.

The wave and turbulence motions not only differ in their time scales, but their energy propagation characteristics are very different. A gravity wave group or packet tends to propagate and disperse in space with the group velocities characteristic of spatial and temporal frequencies in it. Regions or patches of two-dimensional turbulence do not propagate in space except in a slow diffusive way, but their amplitudes migrate to larger horizontal scales in accord with Kraichnan's (1967) upscale inertial range prediction . I assume that the vertical component of wave propagation will transport wave energy to layers where dissipation is strong enough to destroy it. This is
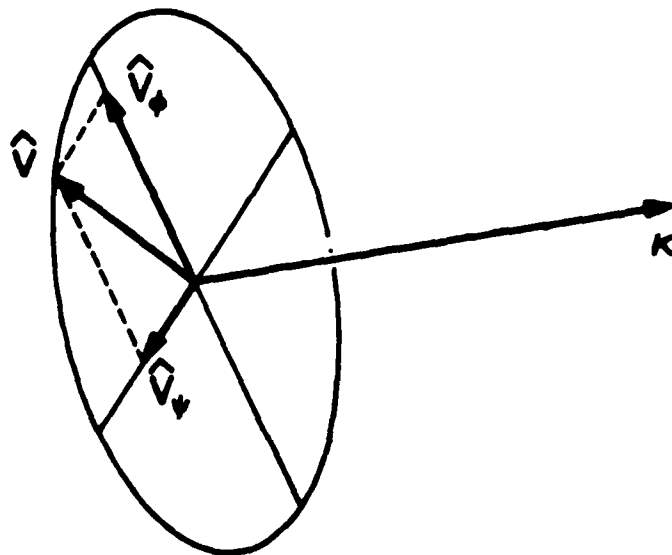

Figure 3. Illustration of the decomposition of the Fourier velocity mode $\hat{\vec{V}}(\vec{k})$ into horizontal and tilted modes.

292

perhaps more likely in the atmosphere than the ocean because the
compressional decrease of density with height leads to increased
kinematic amplitude and therefore increased nonlinearity of upward
propagating waves.

Kraichnan's upscale inertial range is predicted to have a $-5/3$
spectral slope. It is suggested, therefore, that the observed
atmospheric noise spectrum may be produced from initially three-
dimensional turbulent energy, some of which effectively escapes from its
normal dissipative fate and propagates to large scales. A more complete
analysis (Lilly, 1983) suggests that only a few percent of the initially
small-scale turbulent energy need to escape in order to produce the
observed spectrum. The analysis also indicates, however, that secondary
instability produced by vertical shear between adjacent evolving layers
may continue to remove much of the energy before it has propagated to
large scales. After the turbulence becomes effectively geostrophic,
i.e., after a few hours of life, it is protected from this secondary
shearing loss, since geostrophic turbulence tends to have a more
organized vertical structure. Detailed calculations from a closure
model or a more complete theory to predict the quantitative fate of a
3-d turbulent event in an unbounded stratified flow have not, I believe,
been carried out.

Definitive comparisons of observational data with the above
theoretical predictions are also yet lacking. It is not helpful to
measure the heat flux, since it tends to disappear for both wave and
two-dimensionally turbulent motions. Direct measurements of group
velocity or energy propagation sufficient to determine the relative
amounts of upward and downward propagating energy would be very
enlightening, however, since these are apparently almost equal in the
oceans. Some evidence exists that in the stratosphere the slowly
propagating inertio-gravity modes are mostly carrying energy upward, as
evidenced by clockwise rotating hodographs in high-resolution sonde
ascents. Doppler radar is capable of evaluating momentum flux and mean
flow components but not energy flux, at least not directly.

An indirect statistic of a possibly determining nature is the ratio
of the spectral amplitudes of kinetic to available potential energy
($b^2/2N^2$ in my notation). For waves one expects equipartation, i.e.
kinetic equals potential energy, and this should presumably hold for all
wavenumber components. For geostrophic turbulence Charney (1971)
proposed that each component of the two-dimensional kinetic energy
should be equal to potential energy, so that the ratio of kinetic to
potential energy would be 2:1. I await the appearance of a more
complete analysis of aircraft data by Nastrom and Gage to test these
predictions.

REFERENCES

1. Balsley, B. B., M. Crochet, W. L. Ecklund, D. A. Carter, A. C.
   Riddle, and R. Garello, 1983: Observation of vertical motion in
   the troposphere and lower stratosphere using 3 closely spaced
   radars. Preprint volume, 21st Conference on Radar Meteorology of
   the American Metreological Society, pp. 148-152.

2. Balsley, B. B. and D. A. Carter, 1982: The spectrum of atmospheric
   velocity fluctuations at 8 km and 86 km. Geophys. Res. Ltrs., 9,
   pp. 465-468.

3. Brown, P. S., Jr. and G. D. Robinson, 1979: The variance spectrum
   of tropospheric winds over Eastern Europe. J. Atmos. Sci., 36,
   pp. 270-286.

4. Charney, J. G., 1971: Geostrophic turbulence. J. Atmos. Sci., 28,
   pp. 1087-1095.

5. Chen, T.-C. and A. Wiin-Nielsen, 1978: On nonlinear cascades of
   atmospheric energy and enstrophy in a two-dimensional spectral
   index. Tellus, 30, pp. 313-322.

6. Endlich, R. M., R. C. Singleton, and J. W. Kaufman, 1979: Spectral
   analysis of detailed vertical wind speed profiles. J. Atmos.
   Sci., 26, pp. 1030-1041.

7. Gage, K. S., 1979: Evidence for a $k^{-5/3}$ law inertial range in
   mesoscale two-dimensional turbulence. J. Atmos. Sci., 36,
   pp. 1950-1954.

8. Garrett, C. and W. Munk, 1972: Space-time scales of internal
   waves. Geophys. Fluid Dyn., 2, pp. 225-264.

9. _____ and _____, 1975: Space-time scales of internal waves: a
   progress report. J. Geophys. Res., 80, pp. 291-297.

10. _____ and _____, 1979: Internal waves in the ocean. Ann. Rev.
    Fluid Mech., 11, pp. 339-369.

11. Kraichnan, R., 1967: Inertial ranges in two-dimensional
    turbulence. Phys. Fluids, 10, pp. 1417-1423.

12. Lilly, D. K., 1983: Stratified turbulence and the mesoscale
    variability of the atmosphere. J. Atmos. Sci., 40, pp. 749-761.

13. _____ and E. L. Petersen, 1983: Aircraft measurements of
    atmospheric kinetic energy spectra. Tellus, 35A, pp. 379-382.

14. Nastrom, G. D. and K. S. Gage, 1983: A first look at wavenumber
    spectra from GASP data. Tellus, 35A, pp. 383-388.

294

15. _____, 1984: Climatology of atmospheric wavenumber spectrum observed by commercial aircraft. Submitted to J. Atmos. Sci.

16. Riley, J. J., R. W. Metcalfe, and M. A. Weissman, 1981: Direct numerical simulation of homogeneous turbulence in density-stratified fluids. American Institute of Physics Conference Proceedings, Conference on Non-Linear Properties of Internal Waves. Ed. Bruce J. West.

17. Van Zandt, T. E., 1982: A universal spectrum of buoyancy waves in the atmosphere. Geophys. Research Ltrs., 9, pp. 575-578.

18. Vinnichenko, N. K., 1970: The kinetic energy spectrum in the free atmosphere--1 second to 5 years. Tellus, 22, pp. 158-166.
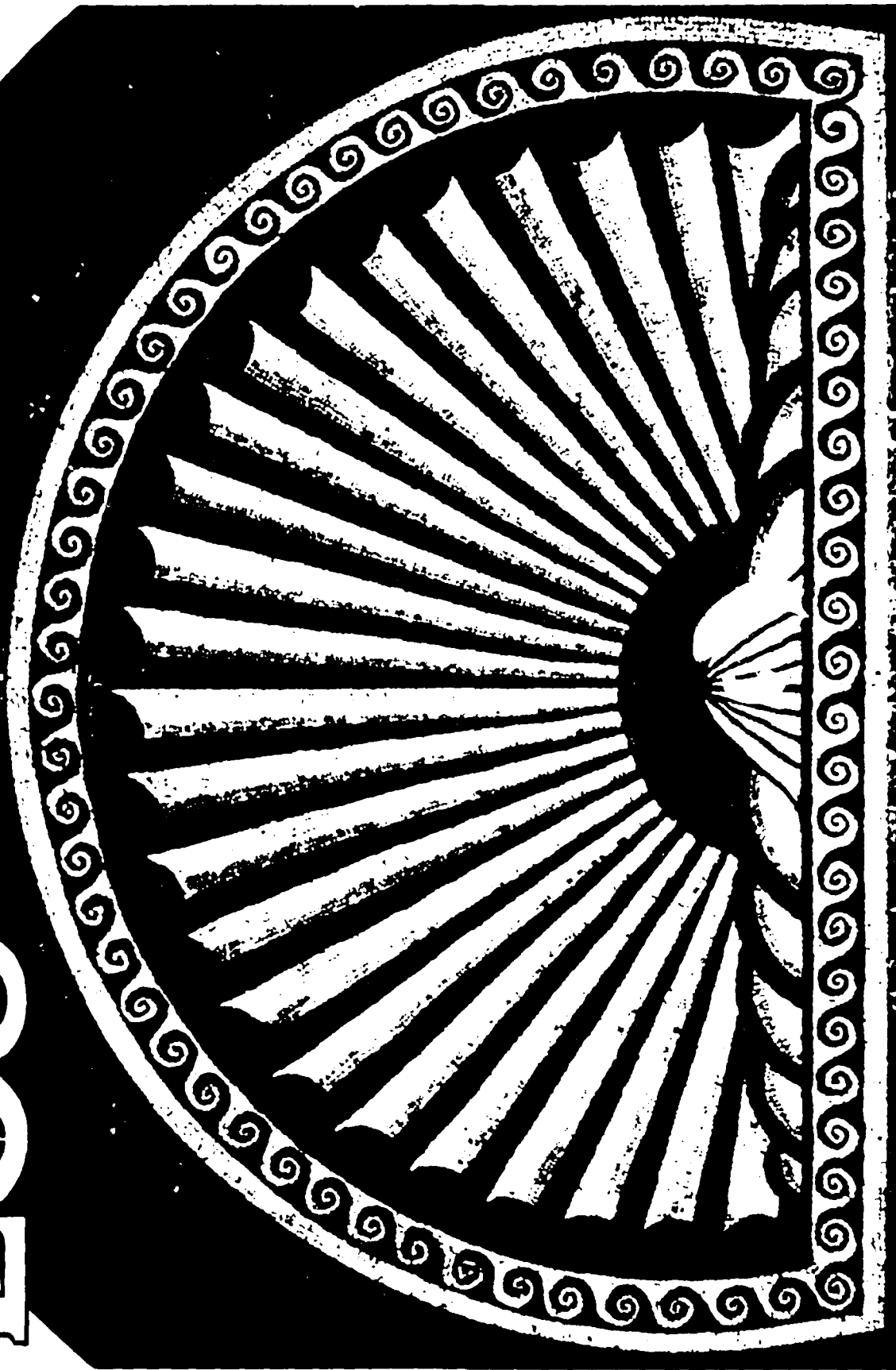
295

The Oceanography Report

The Oceanography Report
Dit is a part is private communication geologic al and biological oceanographic

Editor: Arnold L. Gordon, Lamont-Doherty Geological Observatory, Palisades, NY 10964 (telephone 914-359-2900, ext. 325)

Meetings

New Directions in Internal Wave and Microstructure Research

Collaboration of oceanographers across traditional boundaries always results in exciting new insights into the complex processes which govern oceanic motions. Such collaboration was evident at the second annual 'Aha Huliko'a Hawaiian Winter Workshop, held in Honolulu, Hawaii, January 18-20, 1984. This year's topic was Internal Gravity Waves and Small Scale Turbulence. Participants from Europe, Canada, and the United States reviewed recent developments and proposed *intriguing studies in the kinematics and dynamics of internal waves, fine structure, and microstructure.* Here we summarize the

highlights of the meeting and identify some of the emerging trends, all subject to the participants' biases.

Internal Waves

Internal waves are viewed as an important link in the overall oceanic energy cascade from the large scales of generation to the small scales of dissipation. Although the dominant sources and sinks for internal waves have not been identified, the following concept is generally accepted: Energy enters the internal wave field at large scales and cascades down to small scales by nonlinear wave-wave interactions. When the shear reaches a critical value, the waves break and generate small-scale turbulence and microstructure. At microscales energy is dissipated by molecular processes. Research that led to this picture has been dominated by the concept of a universal internal wave spectrum, an idea introduced over a decade ago by *Garrett and Munk* [1972]. During the workshop, the concept of a universal spectrum was challenged, whereas the link between internal waves and microstructure was substantiated.

"Universal" Spectrum Observed spectra usually fit the "universal" spectrum to within a factor of 3 for frequencies significantly above the inertial and less so in the near-inertial band [*Wunsch*, 1976, Briscoe; Levine]. (Note: Undated references refer to talks given at the workshop. These talks will be published in the proceedings. Copies may be obtained from Peter Muller, University of Hawaii, Department of Oceanography, 1000 Pope Road, Honolulu, HI 96822.) This means that there is an order of magnitude variation in the spectral levels. These variations are likely the dynamical signatures of the sources, sinks, and internal transfers of the internal wave field. It is these dynamical features that have become the object of internal wave research.

The deviations of the internal wave field from the universal form exhibit definite patterns. Energy in the near-inertial frequency band varies in response to storms and to mesoscale features (D'Asaro), as well as geographically and with depth [*et al.*, 1981]. The energy in the higher frequency continuum varies seasonally and geographically (Briscoe, Levine, and Figure 1) and near topographic features (Eriksen). Clear patterns exist in the data; explanation of their dynamics is a challenge for future research.

New measurement techniques like Doppler sonars reveal local spectra that are not smooth but show an irregular structure with ridges and shoulders (Pinkel and Figure 2).

Nonlinear Interactions Nonlinear interactions among internal waves have primarily been analyzed by using the weak resonant interaction approach. Detailed calculations have been made by using this technique, and an inertial range theory has emerged similar to the one in turbulence theory [*McComas and Muller*, 1981]. Nonlinear interactions cascade energy down the spectrum from the generation to the dissipation scale. The level of the energy spectrum adjusts itself so the energy flux through the spectrum. The downscale

cascade is associated with an energy transfer from high to low frequencies, somewhat opposite to conventional wisdom. The appropriateness of the weak resonant interaction approach for small-scale waves has been questioned because interaction times are often much shorter than the periods of the waves [*Holloway*, 1980].

Now, nonlinear interactions are investigated by two new methods: numerical integration of the Navier-Stokes equations in two dimensions (Holloway and Figure 3) and Monte-Carlo simulation of the Eikonal equations that describe the evolution of a small-scale wave in a background wave field (Henyey). Their preliminary calculations show unexpected and exciting results: an upward mass flux (mixing) at low wave numbers in Holloway's calculation and preferred layers of breaking "patches" in the Eikonal approach. Unlike the weak interaction calculations, the new approaches produce space-time results that will eventually allow direct comparison with experimental data. Such comparison certainly will stimulate a greater interaction between theoretical and observational oceanographers.

Sources and Sinks

Numerous sources and sinks have been proposed for the internal wave field [see, e.g., *Olbers*, 1983]. Observationally, the situation might be summarized as "a little bit of evidence for everything" (Briscoe). No dominant generation or dissipation mechanism has been identified, although some progress is occuring on some mechanisms.

Theoretical and observational evidence is emerging that the wind generates near-inertial frequency waves at large vertical scales (D'Asaro) and that internal waves and the mesoscale flow strongly interact (Watson).

Classically, it has been assumed that the internal wave field dissipates its energy pre-
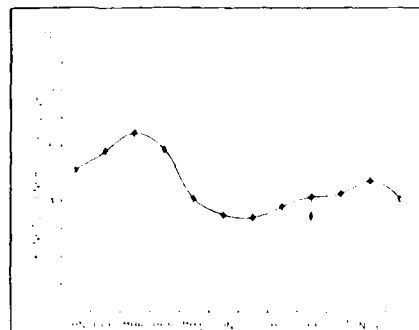

Fig. 1. Seasonal variability of the internal wave continuum. The data points represent the high frequency (0.1-2.0 cph) horizontal kinetic energy from 13 moorings in the North Atlantic over a 10-year period. The moorings are all subsurface. The instrument depths are 114-306 m, and the locations range from 16°-50°N and 12°-71°W. The error bars are plus and minus one standard deviation (courtesy of M. Briscoe).
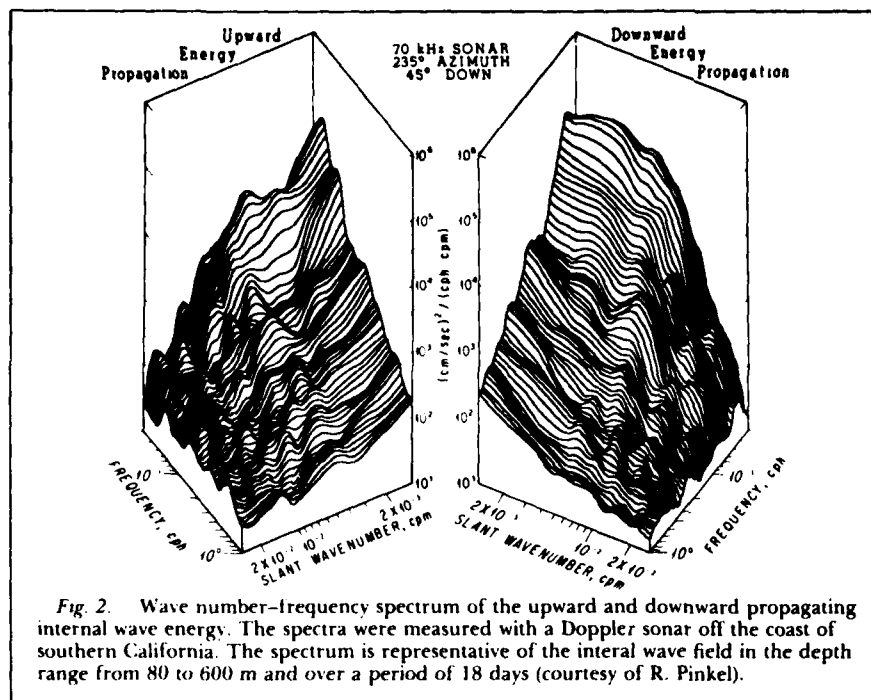
Fig. 2. Wave number–frequency spectrum of the upward and downward propagating internal wave energy. The spectra were measured with a Doppler sonar off the coast of southern California. The spectrum is representative of the interal wave field in the depth range from 80 to 600 m and over a period of 18 days (courtesy of R. Pinkel).

tical" motions is also a problem in the atmosphere. In meterology, the "vortical" mode is called "stratified two-dimensional (2-D) turbulence." The observed atmospheric mesoscale spectra are roughly consistent with theories of upscale inertial ranges in stratified 2-D turbulence (Lilly).

The implications of the existence of the vortical mode for the dynamics have not yet been explored, but we expect the vortical mode to be intimately connected and intertwined with the internal gravity mode of motion (Holloway). A distinction between the internal gravity and vortical mode of motion requires the measurement of vorticity on small scales, a measurement that to date has not been possible because of lack of suitable instruments; however, a "vorticity meter" is now being developed by Sanford (personal communication, 1984), so that such distinction might soon become possible.

Small-Scale Turbulence

If double diffusive effects are ignored, small-scale turbulence measurements are almost always discussed within the following, now classical, framework: Estimates of oceanic mixing rates can be made from velocity and temperature measurements that resolve the small scales on which molecular dissipation occurs. Measurements of the Richardson number on the meter scale commonly show values of the order of 1 or less, suggesting that shear instability is a major mechanism for mixing. Assuming that the shear responsible for the small values of the Richardson number is due to internal waves, dissipation driven by shear instability becomes an energy sink for the internal wave field. Accordingly, the rate of mixing and the properties of the internal wave field are related. If this link were understood, the rate of mixing could be parameterized in terms of the energy sources and environmental parameters of the internal wave field.

Studies of the relationship between small-scale turbulence and the internal wave field clearly require measurements of both the turbulence, using microstructure instruments, and the internal wave shear and density fields, using larger scale measurements. Existing evidence suggests that the internal wave field is highly random, so many measurements are required. Instrument systems capa-

Current Fine Structure

Existing velocity and temperature measurements clearly show that linear internal waves alone cannot explain all of the observed structure within the internal wave frequency band [Muller et al., 1978]. In particular, the coherence between current meters as a function of vertical separation drops rapidly with-

in the first few meters and then decays more slowly on a scale of many tens of meters. The rapid drop is traditionally attributed to current fine structure. At frequencies well above inertial frequency, current fine structure has an energy density comparable to that of internal wave motions. The kinematical and dynamical character of current fine structure is unclear. The traditional view is that it represents internal wave currents concentrated at small vertical scales because of the fine structure in the Brunt-Väisälä profile. A different view (Müller) holds that current fine structure is an entirely different type of motion with well-defined, distinct dynamics. Unlike internal waves, this "vortical mode" of motion [Riley et al., 1981] carries potential vorticity. Current fine structure might, hence, be the small-scale realization of the same mode that represents quasigeostropic flows at mesoscales.

The separation of internal waves and "vor-

dominantly in the interior of the ocean, through small-scale turbulence. Calculations (Eriksen) indicate, however, that the loss of internal wave energy at a sloping boundary might be substantial and could be the major energy sink of internal waves. Significant sinks of energy also may occur in critical layers when near-inertial waves become trapped within fronts or eddies [Kunze and Sandford, 1984]. These losses would be concentrated at particular locations in the ocean and not spread uniformly throughout its volume.
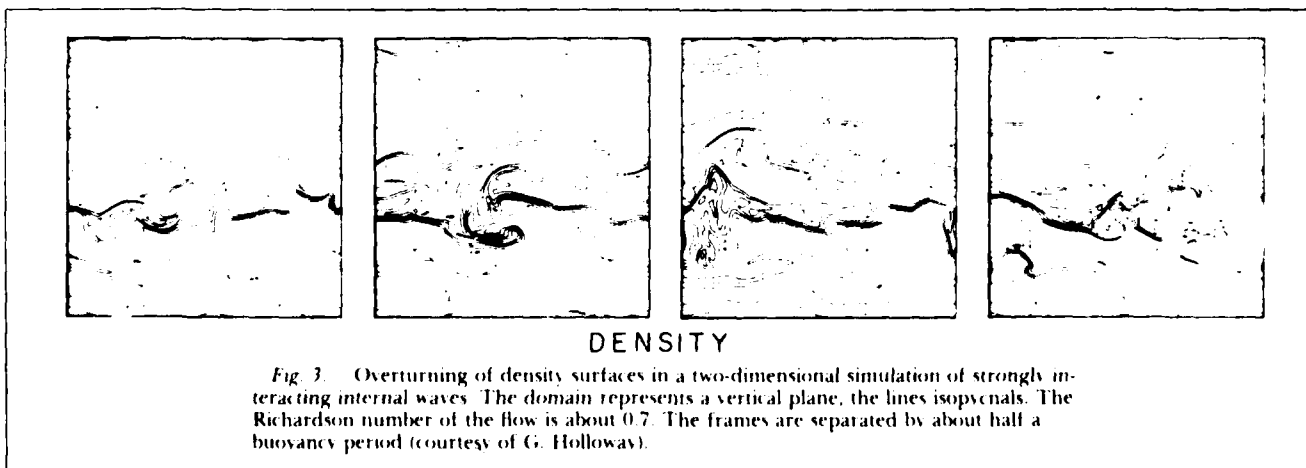

DENSITY

Fig. 3. Overturning of density surfaces in a two-dimensional simulation of strongly interacting internal waves. The domain represents a vertical plane, the lines isopycnals. The Richardson number of the flow is about 0.7. The frames are separated by about half a buovancy period (courtesy of G. Holloway).
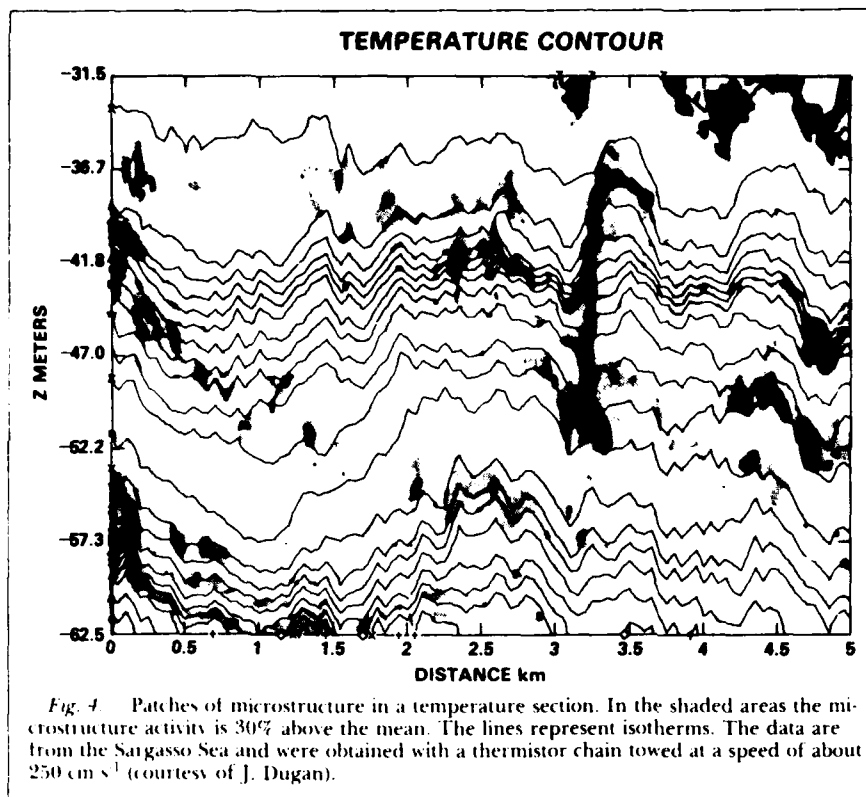
TEMPERATURE CONTOUR

Fig. 4. Patches of microstructure in a temperature section. In the shaded areas the microstructure activity is 30% above the mean. The lines represent isotherms. The data are from the Sargasso Sea and were obtained with a thermistor chain towed at a speed of about 250 cm s⁻¹ (courtesy of J. Dugan).

ble of repeated measurements of both microstructure and internal wave scales have only recently become available (Gregg, Osborn) and are limited to use in the upper few hundred meters. Simultaneous measurements of the internal wave spectrum and microstructure over periods long enough for significant changes in the internal wave field to occur are not yet available. It is, therefore, not surprising that the research in this field is still exploratory.

If, as hypothesized, small-scale turbulence is driven by the internal wave field, its structure should reflect the structure of the wave field. Observationally, this issue is complicated by the possibility of turbulence caused by double diffusion which is ignored here. Nevertheless, several promising links between internal wave field and oceanic turbulence are emerging.

Patchiness Measurements of small-scale turbulence generally show that the individual mixing events are not randomly distributed, but concentrated into "patches" of high activity. These "patches" vary in size from centimeters to 10–20 m (Gregg, Dugan, Osborn, and Figure 4), with the smaller patches being more common.

Two theoretical approaches based on internal waves predict such a structure. Calculations of the vertical distribution of the Richardson number, *Ri*, made assuming a Garrett and Munk internal wave spectrum, and Gaussian statistics (Desaubies). If a turbulent patch is assumed to occur whenever *Ri* < 1/4, a range of "patch" sizes comparable to that observed, is computed. A more detailed comparison with the observed "patch" statistics would be interesting. Eikonal calculations, which trace individual waves in a background internal wave spectrum, have also been used

to model the spatial distribution of small-scale turbulence (Henyey). It is assumed that an individual wave breaks when it reaches a sufficiently high wave number. One such calculation shows the persistent clustering of the breaking events at a particular level, suggesting the formation of a turbulent "patch." This calculation suggests that it may be possible to formulate general criteria for the location of such patches as a function of the background shear field.

Recent experimental work suggests a link between the larger patches and near-inertial frequency shear. One such patch, which persisted for nearly a day, occurred at the same depth as a small inertial jet (Gregg).

Shear Statistics. The universal internal wave spectra have dominantly been energy spectra and have not accurately described the statistics of the shear and density gradient fields, particularly on scales smaller than 10 m. Such a description is needed if accurate models of the link between microstructure and internal waves are to be developed. A "universal" shear spectrum has been proposed by *Gargett et al.* [1981], but it is not complete. There is still uncertainty as to whether the shear at 10 m scales is dominantly inertial, as at larger scales (D'Asaro) or dominantly high frequency (Pinkel). This particular question is complicated by Doppler-shifting of small-scale velocity features. Basic descriptive work is needed on the shear and density gradient distribution, spectrally, spatially, and temporally.

Kelvin Helmholtz Billows A variety of ingenious arguments developed in the last decade allow *K*, the vertical diffusivity for mass, to be estimated from microstructure parameters; however, a clear picture of the three-dimensional structure and evolution of these

mixing events has not yet emerged. Generally, mixing is envisioned as being caused by Kelvin-Helmholtz billows. The structure of these billows was very nicely depicted by the artist of the Roman scallop shell mosaic shown on the cover. These billows have been extensively studied in the laboratory and have been observed at one location in the upper ocean [Woods, 1968]. The extrapolation of laboratory studies to the ocean may be difficult, due to side-wall effects in the laboratory studies (Thorpe). A variety of other stratified shear flow instabilities with structures distinct from Kelvin-Helmholtz billows, such as wave breaking and critical layer absorption, have been observed in the laboratory [Thorpe, 1973] and may also occur in the ocean. Turbulence research in other fields has benefited greatly from flow visualization studies that aim to identify the dominant structures of the turbulent flow. Once the structures of a flow have been identified in this way they can usually be identified in point measurement. It seems likely that similar studies using dye or high-frequency acoustics would likewise increase our understanding of oceanic turbulence.

On the theoretical side, the nonlinear stability of stratified flows has been investigated by using a constrained energy method due to V. I. Arnol'd (Abarbanel). Applied to the customary parallel shear flow in the presence of stratification, one proves that the flow is nonlinearly stable for Richardson numbers greater than unity. The theoretically interesting regime is hence 1/4 < *Ri* < 1 where the flow is stable to infinitesimal perturbations, but may be unstable to finite perturbations. Shear-generated turbulence in homogeneous fluids is being studied with new second-order closures. Employed in numerical models, these yield good predictions of the observed Reynolds stress tensors evolving in strained and sheared wind tunnel flows (Gallagher).

Parameterization

Many oceanographers prefer to study the large-scale motions of the ocean. These oceanographers regard internal waves and small-scale turbulence as subgrid-scale noise and ask for the parameterization of subgrid fluxes in terms of large-scale flow characteristics. They ask for eddy diffusion and viscosity coefficients. Here the state of affairs is still not satisfactory. Most work on parameterization has been concerned with the vertical diffusion coefficient *K*. A typical value of 0.1 cm² s⁻¹ seems not to be inconsistent with microstructure measurements and the kinematics and dynamics of internal waves (Garrett). A similar value is obtained when the observed large-scale hydrographic field is fitted by beta-spiral methods (Olbers) but that value includes an artificial contribution due to averaging of the data. Basic questions are still unanswered. For example, how much of the vertical mixing is done in the interior of the ocean and how much is done in boundary layers? Does the value *K* have a strong depth dependence? The answers to these questions could have dramatic implications. Changing the depth dependence of the dissipation rate changes the direction of the meridional circulation in an advective-diffusive model of the thermohaline circulation (Gargett).

The momentum fluxes are even less established. There are only spotty measurements.

Some of them imply significant eddy viscosity coefficients [e.g., *Brown and Owens*, 1981], but no coherent picture has emerged from the sparse data.

Conclusions and Trends

Internal gravity waves and small-scale turbulence are the motions by which the ocean mixes momentum and mass. The specific way in which this mixing is done has pronounced effects on geostrophic eddies and the general circulation. To understand these grander scales of motions, we must understand the smaller-scale mixing processes.

Internal wave research is presently undergoing a transition from a dominantly kinematic study of spectral slopes to a dominantly dynamic study of sources, sinks, and internal fluxes. The link between internal waves and oceanic turbulence is becoming more apparent, and the glimmers of a dynamical understanding are emerging. The parameterization of the internal wave and turbulent fluxes, which is a major goal of these studies, has not yet been achieved.

Further progress will come from simultaneous measurements of internal waves and microstructure and from a detailed comparison of experimental data with the results of numerical models. These experiments and studies require collaboration of oceanographers across specific areas of interest, a beginning of which was witnessed at the Hawaiian Winter Workshop.

Acknowledgments

References

Brown, A. D., and W. B. Owens, Observations of the horizontal interactions between the internal wave field and the mesoscale flow, *J. Phys. Oceanogr.*, *11*, 1474–1480, 1981.

Fu, L., Observations and models of inertial waves in the deep ocean, *Rev. Geophys. Space Phys.*, *19*, 141–170, 1981.

Gargett, A. E., T. J. Hendricks, T. B. Sanford, T. R. Osborn, and A. J. Williams III, A composite spectrum of vertical shear in the upper ocean, *J. Phys. Oceanogr.*, *11* 1258–1271, 1981.

Garrett, C. J. R., and W. H. Munk, Space-time scales of internal waves, *Geophys. Fluid Dyn.*, *2*, 225–264, 1972.

Holloway, G., Oceanic internal waves are not weak waves, *J. Phys. Oceanogr.*, *10*, 906–914, 1980.

Kunze, E., and T. B. Sanford, Observations of near inertial waves in a front, *J. Phys. Oceanogr.*, in press, 1984.

McComas, C. H., and P. Müller, The dynamic balance of internal waves, *J. Phys. Oceanogr.*, *11*, 970–986, 1981.

Müller, P., D. J. Olbers, and J. Willebrand, The Iwex spectrum, *J. Geophys. Res.*, *83*, 479–500, 1978.

Olbers, D. J., Models of the oceanic internal wave field, *Rev. Geophys. Space Phys.*, *21*, 1567–1606, 1983.

Riley, J. J., R. W. Metcalfe, and M. A. Weissman, Direct numerical simulations of homogenous turbulence in density-stratified fluids in *Nonlinear Properties of Internal Waves*, edited by B. J. West, vol. 76, pp. 79–112, American Institute of Physics Conference Proceedings, New York, 1981.

Thorpe, S. A., Turbulence in stably stratified fluid: A review of laboratory experiments, *Boundary Layer Meteorol.*, *5* 95–119, 1973.

Wunsch, C., Geographical variability of the internal wave field: A search for sources and sinks, *J. Phys. Oceanogr.*, *6* 471–485, 1976.

Woods, J. D., Wave induced shear instability in the summer thermocline, *J. Fluid Mech.*, *32* 791–800, 1968.

REPORT DOCUMENTATION PAGE		READ INSTRUCTIONS BEFORE COMPLETING FORM
1 REPORT NUMBER	2. GOVT ACCESSION NO. AD-A149 510L	3. RECIPIENT'S CATALOG NUMBER
4 TITLE (and Subtitle) Internal Gravity Waves and Small-Scale Turbulence		5. TYPE OF REPORT & PERIOD COVERED
		6. PERFORMING ORG. REPORT NUMBER
7. AUTHOR(s) Peter Muller, Rita Pujalet (Eds.)		8. CONTRACT OR GRANT NUMBER(s) N-00014-84-G-0008
9 PERFORMING ORGANIZATION NAME AND ADDRESS Hawaii Institute of Geophysics 2525 Correa Road Honolulu, Hawaii 96822		10. PROGRAM ELEMENT, PROJECT, TASK AREA & WORK UNIT NUMBERS
11 CONTROLLING OFFICE NAME AND ADDRESS Office of Naval Research		12. REPORT DATE 1984
		13. NUMBER OF PAGES
14 MONITORING AGENCY NAME & ADDRESS(if different from Controlling Office) Office of Naval Research Department of the Navy 800 N. Quincy Street Arlington, VA 22217		15. SECURITY CLASS. (of this report) Unclassified
		15a. DECLASSIFICATION/DOWNGRADING SCHEDULE

16. DISTRIBUTION STATEMENT (of this Report)

Approved for public release; distribution unlimited

17. DISTRIBUTION STATEMENT (of the abstract entered in Block 20, if different from Report)

18. SUPPLEMENTARY NOTES

Proceedings, 'Aha Huliko'a, Hawaiian Winter Workshop, January 1984, Honolulu, Hawaii.

19. KEY WORDS (Continue on reverse side if necessary and identify by block number)

Internal gravity waves, turbulence, mixing, finestructure, microstructure, inertial oscillations, vortical motion, shear instability, Kelvin Helmholtz billows, patchiness, cross-isopycnal mixing, bottom reflection, non-linear interactions.

20. ABSTRACT (Continue on reverse side if necessary and identify by block number)

These proceedings contain the lectures given at the 'Aha Huliko'a Hawaiian Winter Workshop on "Internal gravity waves and small-scale turbulence" and a summary, "New directions in internal wave and micro-structure research", which appeared in EOS (Transactions, American Geophysical Union). The lectures and the summary cover the major aspects of the state of the art and the plans for future research in the field of internal gravity waves, turbulence and mixing in the ocean.

END

FILMED

2-85

DTIC